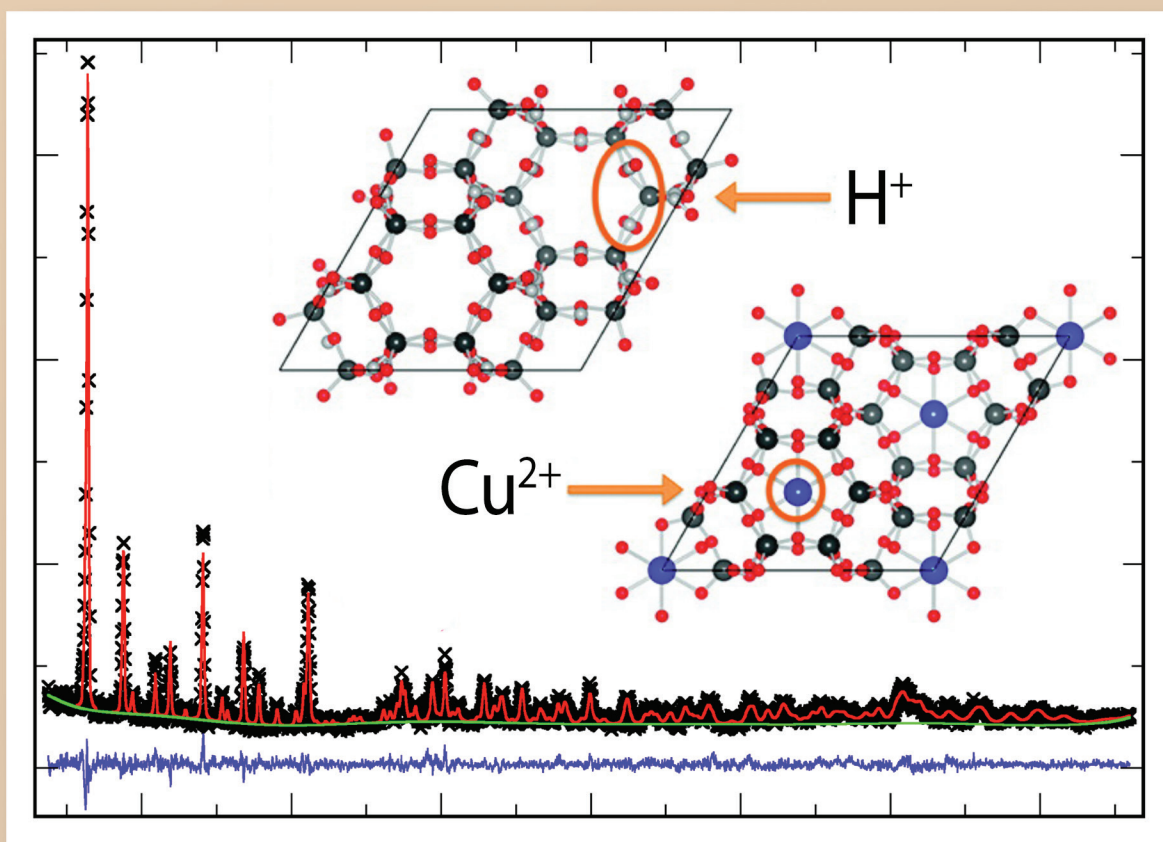
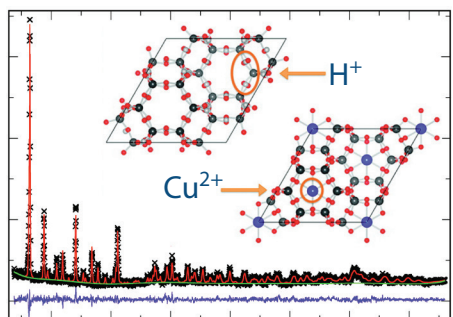


2012

Accomplishments and Opportunities

**NIST**

National Institute of
Standards and Technology
U.S. Department of Commerce



ON THE COVER

Neutron powder diffraction pattern of a chabazite zeolite that is a good candidate for CO_2 absorption, indicating high selectivity sites.

See the highlight article by Hudson *et al.* on p.16

NIST Center for Neutron Research

2012 Accomplishments and Opportunities

NIST Special Publication 1143

Robert M. Dimeo, Director

Ronald L. Cappelletti, Editor

December 2012

National Institute of Standards and Technology

*Patrick Gallagher, Under Secretary of Commerce
for Standards and Technology, Director*

U.S. Department of Commerce

Rebecca Blank, Acting Secretary



DISCLAIMER

Certain commercial entities, equipment, or materials may be identified in this document in order to describe an experimental procedure or concept adequately. Such identification is not intended to imply recommendation or endorsement by the National Institute of Standards and Technology, nor is it intended to imply that the entities, materials, or equipment are necessarily the best available for the purpose.

National Institute of Standards and Technology
Special Publications 1143

Natl. Inst. Stand. Technol. Spec. Publ. 1143, 92 pages
(December 2012)

CODEN: NSPUE2

U.S. GOVERNMENT PRINTING OFFICE-
WASHINGTON: 2012

For sale by the Superintendent of Documents,
U.S. Government Printing Office

Internet: bookstore.gpo.gov
Phone: 1.866.512.1800
Fax: 202.512.2104
Mail: Stop SSOP
Washington, DC 20402-0001

Table of Contents

FOREWORD	iii
THE NIST CENTER FOR NEUTRON RESEARCH	1
NIST CENTER FOR NEUTRON RESEARCH INSTRUMENTS	2
NCNR IMAGES 2011	4
HIGHLIGHTS	
ARCHEOLOGY	
Foreigners or not: new data prior to the Maya collapse in the western lowlands of mesoamerica, R. Bishop, <i>et al.</i>	6
BIOLOGY	
Walking the line between life and death: membrane binding and regulation of the PTEN tumor suppressor, S. S. Shenoy, <i>et al.</i>	8
Towards the elucidation of antibiotoxic resistance transfer in bacteria: structural studies of the Trl protein, N.T. Wright, <i>et al.</i> (CHNRNS)	10
Structures and conformations of voltage-sensor domains and voltage-gated K ⁺ channel proteins, S. Gupta, <i>et al.</i>	12
The role of electrostatic interactions in the local dynamics of biological and synthetic polyelectrolytes, J.H. Roh, <i>et al.</i> (CHNRNS)	14
CHEMICAL PHYSICS	
Powder neutron diffraction reveals new CO ₂ adsorption interactions in chabazite zeolites, M.R. Hudson, <i>et al.</i> (CHNRNS)	16
Evolving structure of the solid electrolyte interphase in Li-ion batteries characterized by <i>in situ</i> neutron reflectometry, J.A. Dura, <i>et al.</i>	18
Activated dihydrogen bonding to a supported organometallic compound, J.M. Simmons, <i>et al.</i> (CHNRNS)	20
CONDENSED MATTER	
Electronic delocalization in the correlation gap insulator LaMnPO, J.W. Simonson, <i>et al.</i>	22
Spin-orbital short-range order on a honeycomb-based lattice, S. Nakatsuji, <i>et al.</i> (CHNRNS)	24
Common origin of the two types of magnetic excitations in iron chalcogenide superconductors, Songxue Chi, <i>et al.</i> (CHNRNS)	26
Correlation between spin-flop transition and enhanced spin polarized supercurrents in ferromagnetic Josephson junctions, C. Klose, <i>et al.</i>	28
Charge ordering and magnetic frustration in the fluoride pyrochlore, RbFe ²⁺ Fe ³⁺ F ₆ , S.W. Kim, <i>et al.</i>	30

Table of Contents

ENGINEERING

Measuring yield stresses in biaxial deformation, T. Gnäupel-Herold, <i>et al.</i>	32
---	----

NEUTRON PHYSICS

A new limit on time-reversal violation in beta decay, H.P. Mumm, <i>et al.</i>	34
--	----

SOFT MATTER

Self-assembling organohydrogels: liquid dispersions with solid-like behavior, M.E. Helgeson, <i>et al.</i> (CHRRNS)	36
Thickness fluctuations in model membranes, A.C. Woodka, <i>et al.</i> (CHRRNS)	38
Electrochemical Small-Angle Neutron Scattering (eSANS) for studies of nanoparticle redox reactions, V.M. Prabhu, <i>et al.</i> (CHRRNS)	40
Identifying the shape of copper-seamed nanocapsules in solution, H. Kumari, <i>et al.</i> (CHRRNS)	42
Characterizing dense polymer-nanoparticle mixtures by neutron scattering, S.Y. Kim, <i>et al.</i> (CHRRNS)	44

ADVANCES IN MEASUREMENT

A Liquid Deuterium Cold Neutron Source for the NBSR, R.E. Williams, <i>et al.</i>	46
---	----

EXPANSION ACTIVITIES DURING THE PLANNED OUTAGE	47
---	----

NEUTRON SOURCE OPERATIONS	52
--	----

FACILITY DEVELOPMENT	53
---------------------------------------	----

SERVING THE SCIENCE AND TECHNOLOGY COMMUNITY	57
---	----

THE CENTER FOR HIGH RESOLUTION NEUTRON SCATTERING (CHRRNS)	60
---	----

2012 AWARDS	64
------------------------------	----

PUBLICATIONS: AUGUST 1, 2011 TO JULY 31, 2012	66
--	----

INSTRUMENTS AND CONTACTS	86
---	----

NIST CENTER FOR NEUTRON RESEARCH CONTACTS	(inside back cover)
--	---------------------

Foreword



It is with pleasure that I present this year's annual report for the NIST Center for Neutron Research. When looking back over the last year, the only word that I can use to describe this time period is dynamic. User operations were successful and productive, the reactor operating for 142 days out of a scheduled 142 days. The cold source continued to operate reliably and deliver neutrons 99 % of the scheduled operating time. This period was marked by considerable scientific productivity and impact as the highlights in this report illustrate. The productivity is due to many factors, but it is worth noting that the number of user experiments on the MACS spectrometer continued to grow as the amount of time available to the user community was increased, industrial research participation on many of the neutron instruments, especially uSANS, was strong, and research opportunities with other laboratories grew, particularly in the area of biology and biosciences. Moreover, significant progress was made towards bringing the isotope labeling laboratory on line which will certainly prove to be a valuable resource for NCNR users.

This year was also marked by a period of many facility enhancements that can best be described as historic. On April 3, the reactor shut down, as planned, for a period of 11 months. As I described in last year's annual report this outage was scheduled in order to execute many tasks towards the expansion of our cold neutron measurement capability and enhance the reliability of the reactor. A few of the activities include installation of a new neutron guide system in our expanded guide hall which will hold new and relocated instruments, installation of a new cold source dedicated to the MACS instrument, relocation of MACS, and installation of a new cooling system for the reactor's thermal shield. In addition significant construction in and around the site has taken place during the outage, including the construction of a new secondary cooling system, the addition of a new cooling tower cell, and additional electrical capacity. The commencement and execution of this outage marks the culmination of a significant amount of planning and coordination as well as the hard work and diligent efforts of our staff, especially those from Reactor Operations and Engineering and Research Facility Operations. You can read more about the progress we have made during the outage within this report and on our website: <http://www.ncnr.nist.gov/expansion2/> where you will find technical details and photos. I am also pleased to inform you of the release this year of an informal history, "The NIST Center for Neutron Research: Over 40 Years Serving NIST/NBS and the Nation", by Jack Rush and Ron Cappelletti, NIST Special Publication 1120. Contained therein is an account of major events of the NCNR spanning the period from conception of the NIST reactor to the NCNR Expansion Project.

As of this writing we just announced our first call for proposals for experiments to be run upon restart of the reactor. In just a few short months the reactor will restart and users will return to the NCNR. The reason for the outage and expansion is for you, our users. I am looking forward to restoration of user operations and especially offering new measurement capabilities that our expansion project will provide through the coming year. I invite you to take a look at the research highlights from the past year as well as the description of what we have been up to during the outage. As you read through this report, I hope you get the same sense of excitement and opportunity that we are all feeling here.



A view of new guides emerging into the guide hall in a Nov. 6, 2012 photo. The group of people is standing by NG-D, emerging through the square hole just to their right. Behind them are shields blocking the view of the newly installed PBR and MAGik instruments, taking beams off the side of NG-D. The guide visible just behind the striped safety marker is NG-C, and to its right, emerging from NG-B_{lower}, is the tank of the 10 m SANS instrument being installed. NG-B_{upper} is behind the two grey shields to the left of the tank. Not visible is NG-A, to the right of the 10 m SANS, still under development.

The NIST Center for Neutron Research

Neutrons provide a uniquely effective probe of the structure and dynamics of materials ranging from water moving near the surface of proteins to magnetic domains in memory storage materials. The properties of neutrons (outlined at left) can be exploited using a variety of measurement techniques to provide information not otherwise available. The positions of atomic nuclei in crystals, especially of those of light atoms, can be determined precisely. Atomic motion can be directly measured and monitored as a function of temperature or pressure. Neutrons are especially sensitive to hydrogen, so that hydrogen motion can be followed in H-storage materials and water flow in fuel cells can be imaged. Residual stresses such as those deep within oil pipelines or in highway trusses can be mapped. Neutron-based measurements contribute to a broad spectrum of activities including in engineering, materials development, polymer dynamics, chemical technology, medicine, and physics.

The NCNR's neutron source provides the intense, conditioned beams of neutrons required for these types of measurements. In addition to the thermal neutron beams from the heavy water or graphite moderators, the NCNR has a large area liquid hydrogen moderator, or cold source, that provides long wavelength guided neutron beams for the major cold neutron facility in the U.S.

There are currently 27 experiment stations: four provide high neutron flux positions for irradiation, and 23 are beam facilities most of which are used for neutron scattering research. The subsequent pages provide a schematic description of our instruments. More complete descriptions can be found at www.ncnr.nist.gov/instruments/. Construction of a second guide hall is now complete (see p. 47) and five new instruments are under development.

The Center supports important NIST measurement needs, but is also operated as a major national user facility with merit-based access made available to the entire U.S. technological community. Each year, about 2000 research participants from government, industry, and academia from all areas of the country are served by the facility (see p.57). Beam time for research to be published in the open literature is without cost to the user, but full operating costs are recovered for proprietary research. Access is gained mainly through a web-based, peer-reviewed proposal system with user time allotted by a beamtime allocation committee twice a year. For details see www.ncnr.nist.gov/beamtime.html. The National Science Foundation and NIST co-fund the Center for High Resolution Neutron Scattering (CHRNS) that operates six of the world's most advanced instruments (see p. 60). Time on CHRNS instruments is made available through the proposal system. Some access to beam time for collaborative measurements with the NIST science staff can also be arranged on other instruments.

Why Neutrons?

Neutrons reveal properties not readily probed by photons or electrons. They are electrically neutral and therefore easily penetrate ordinary matter. They behave like microscopic magnets, propagate as waves, can set particles into motion, losing or gaining energy and momentum in the process, and they can be absorbed with subsequent emission of radiation to uniquely fingerprint chemical elements.

WAVELENGTHS – in practice range from ≈ 0.01 nm (thermal) to ≈ 1.5 nm (cold) ($1 \text{ nm} = 10 \text{ \AA}$), allowing the formation of observable interference patterns when scattered from structures as small as atoms to as large as biological cells.

ENERGIES – of millielectronvolts, the same magnitude as atomic motions. Exchanges of energy as small as nanoelectronvolts and as large as tenths of electronvolts can be detected between samples and neutrons, allowing motions in folding proteins, melting glasses and diffusing hydrogen to be measured.



SELECTIVITY – in scattering power varies from nucleus to nucleus somewhat randomly. Specific isotopes can stand out from other isotopes of the same kind of atom. Specific light atoms, difficult to observe with x-rays, are revealed by neutrons. Hydrogen, especially, can be distinguished from chemically equivalent deuterium, allowing a variety of powerful contrast techniques.

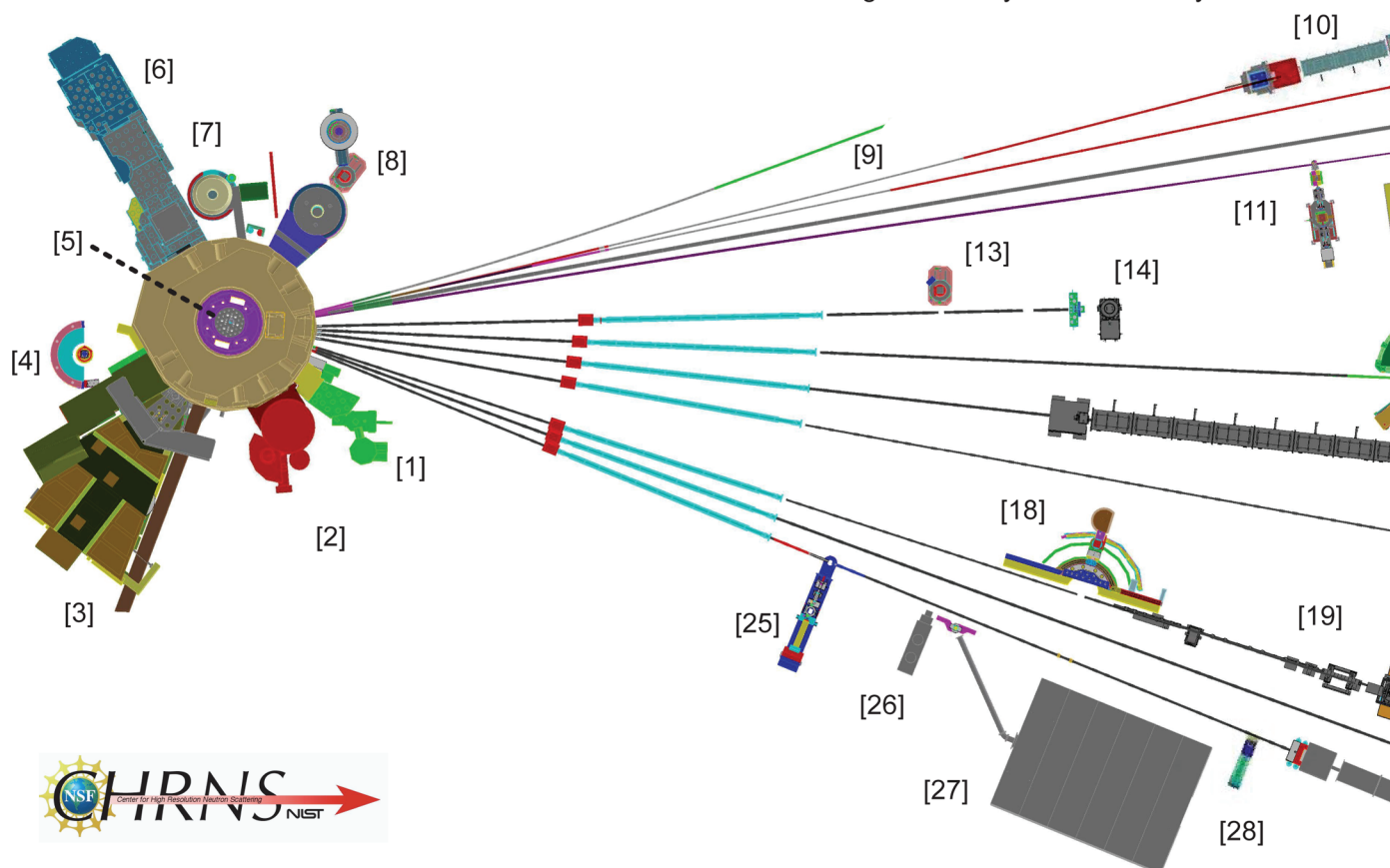
MAGNETISM – makes the neutron sensitive to the magnetic moments of both nuclei and electrons, allowing the structure and behavior of ordinary and exotic magnetic materials to be detailed precisely.

NEUTRALITY – of the uncharged neutrons allows them to penetrate deeply without destroying samples, passing through walls that condition a sample's environment, permitting measurements under extreme conditions of temperature and pressure.

CAPTURE – characteristic radiation emanating from specific nuclei capturing incident neutrons can be used to identify and quantify minute amounts of elements in samples as diverse as ancient pottery shards and lake water pollutants.

NIST Center for Neutron Research Instruments

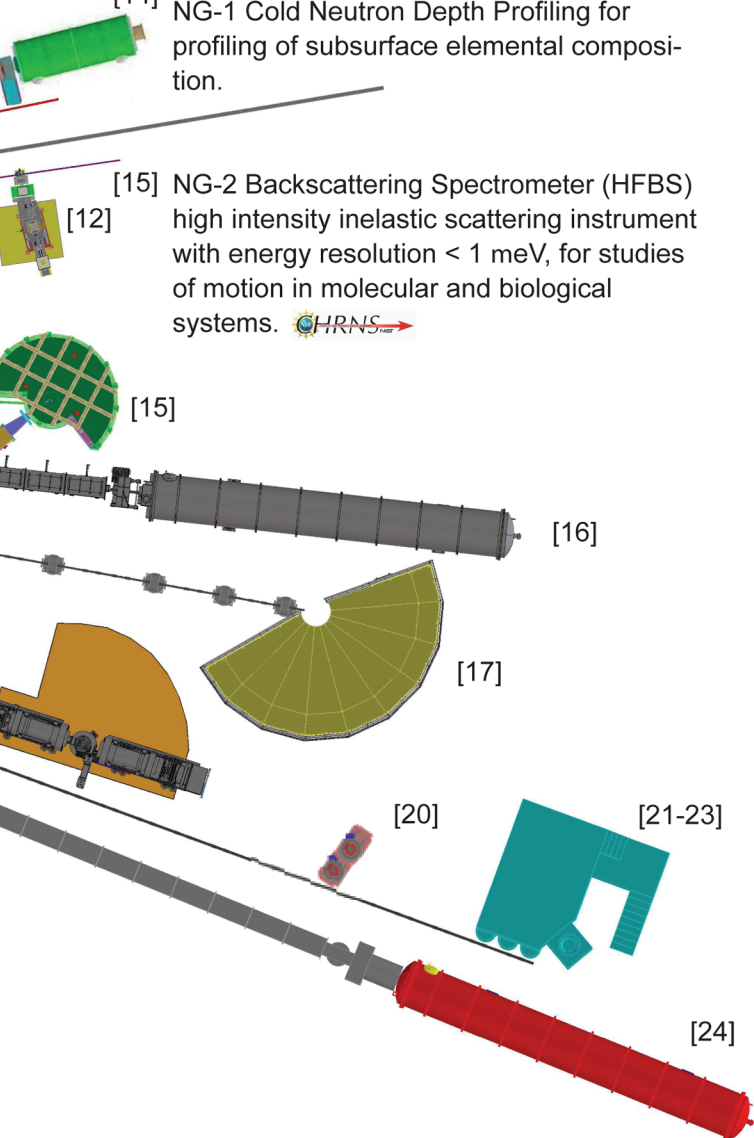
- [1] BT-5 Perfect Crystal Ultra-Small Angle Neutron Scattering (USANS) Diffractometer for micro-structure up to 10^4 nm. 
- [2] BT-4 Filter Analyzer Neutron Spectrometer with cooled Be/Graphite filter analyzer for chemical spectroscopy and thermal triple axis spectrometer.
- [3] BT-2 Neutron Imaging Facility for imaging hydrogenous matter in large components such as water in fuel cells and lubricants in engines, in partnership with General Motors and DOE.
- [4] BT-1 Powder Diffractometer with 32 detectors; incident wavelengths of 0.208 nm, 0.154 nm, and 0.159 nm, with highest resolution of $\delta d/d \cong 8 \times 10^{-4}$.
- [5] VT-5 Thermal Neutron Capture Prompt Gamma-ray Activation Analysis Instrument with a neutron fluence rate of $3 \times 10^8 \text{ cm}^{-2} \text{ s}^{-1}$ used for quantitative elemental analysis of bulk materials. Generally used for the analysis of highly hydrogenous materials ($\cong 1\% \text{ H}$) such as foods, oils, and biological materials.
- [6] BT-9 Primary spectrometer and shielding for MACS II. 
- [7] BT-8 Residual Stress Diffractometer optimized for depth profiling of residual stresses in large components.
- [8] BT-7 Thermal Triple Axis Spectrometer with large double focusing monochromator, and interchangeable analyzer/detectors systems.



The Center for High Resolution Neutron Scattering (CHRNS) is a partnership between NIST and the National Science Foundation that develops and operates neutron scattering instrumentation for use by the scientific community. The following instruments are part of the Center: 1 (USANS), 6 (MACS II), 15 (HFBS), 16 (NG-3 SANS), 17 (DCS), 18 (SPINS), and 19 (NSE). In late 2012 CHRNS will no longer include SPINS.

(as of Dec. 2012)

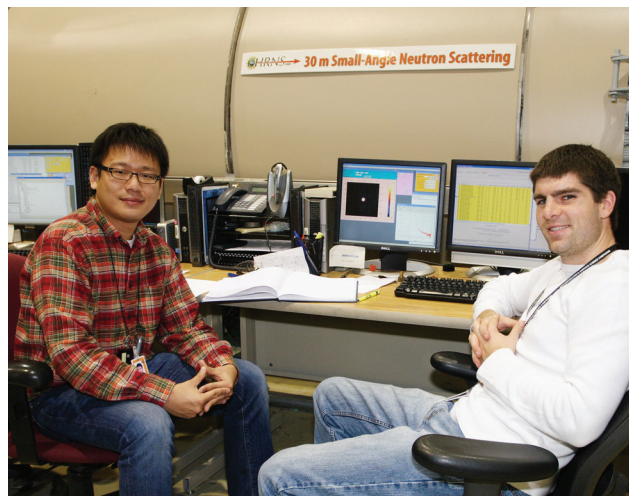
- [9] NG-A,B,C and D Cold neutron guides being installed into the expansion west wing of the guide hall.
- [10] NG-B 10 m SANS for macromolecular structures. *nSoft*
- [11] NG-D Polarized Beam Reflectometer (PBR) for measuring reflectivities down to 10^{-8} to determine subsurface structure.
- [12] NG-D MAGIK off-specular reflectometer for studies of thin-film samples with in-plane structure.
- [13] NG-1 Detector development station.
- [14] NG-1 Cold Neutron Depth Profiling for profiling of subsurface elemental composition.
- [15] NG-2 Backscattering Spectrometer (HFBS) high intensity inelastic scattering instrument with energy resolution < 1 meV, for studies of motion in molecular and biological systems. *HRNS*
- [16] NG-3 30 m SANS for microstructure measurements. *HRNS*
- [17] NG-4 Disk Chopper Time-of-Flight Spectrometer for diffusive motions and low energy dynamics. Wavelengths from ≈ 0.18 nm to 2.0 nm and energy resolutions from ≈ 2 meV to < 10 meV. *HRNS*
- [18] NG-5 Spin-Polarized Triple Axis Spectrometer (SPINS) using cold neutrons with position sensitive detector capability for high-resolution studies.
- [19] NG-5 Neutron Spin-Echo Spectrometer (NSE) for measuring dynamics from 100 ns to 10 ps. *HRNS*
- [20] NG-6A Neutron Physics Test Bed for developing accurate measurements techniques of the neutron magnetic dipole moment.
- [21-23] NG-6 Neutron Physics Station offering three cold neutron beams having wavelengths of 0.5 nm, 0.9 nm, and "white" for neutron physics experiments, including aCORN.
- [24] NG-7 30 m SANS for microstructure measurements, in partnership with ExxonMobil and University of Minnesota's IPrime.
- [25] NG-7 Horizontal Sample Reflectometer allows reflectivity measurements of free surfaces, liquid/vapor interfaces, as well as polymer coatings.
- [26] NG-6 Neutron Physics Interferometry Test Bed for developing novel interferometry techniques.
- [27] NG-7 Neutron Interferometry and Optics Station with perfect crystal silicon interferometer. A vibration isolation system provides exceptional phase stability and fringe visibility.
- [28] NG-7 Cold neutron capture Prompt Gamma Activation Analysis, for quantitative elemental analysis of bulk materials, especially of hydrogenous ones.



NCNR Images 2012



Takoma Park (MD) Middle Schoolers jump for joy on their NCNR tour.



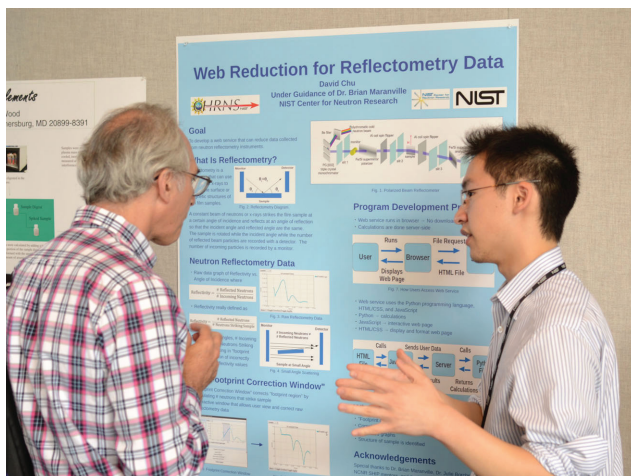
Hao Shen and Doug Godfrin, University of Delaware, take a break for a photo-op at NG-3 SANS.



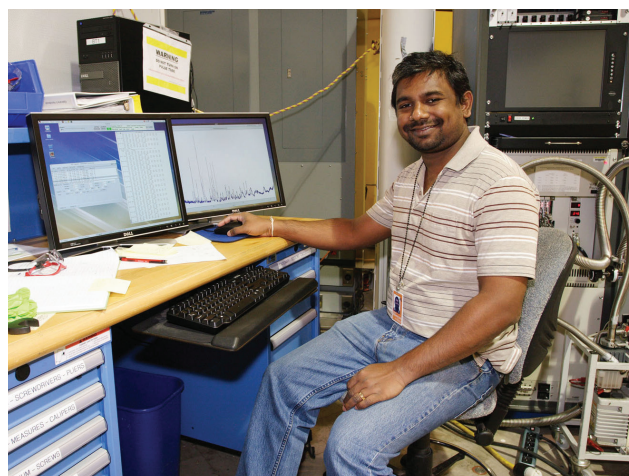
NCNR's Kate Ross at the DCS console listens to comment by former advisor Bruce Gaulin, McMaster University.



NCNR's Cedric Gagnon (front) guides University of Maryland researchers Hyuntaek Oh and Nick Yraghi on NG-3 SANS.



Zach Levine (NIST Sensor Science Div.) takes a few pointers from NCNR SHIP student David Chu.



Sachith Disnayake, University of Virginia, appears pleased with his powder diffraction results visible on the High Resolution Powder Diffraction instrument display.



New guide hall with 10 m SANS being placed. Also visible at left are enclosed guides NG-D and NG-C.



Shingo Maruyama, University of Maryland, records data at the FANS instrument console.



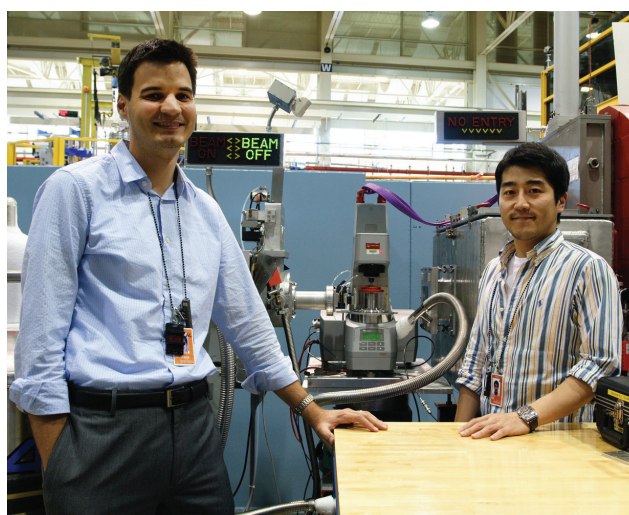
Andrey Podleznyak, ORNL, at the Neutron Spin Echo instrument console.



NCNR's Juscelino Leao works his personal magic with future scientists at the NSF booth of the 2012 Science Tech Expo.



NCNR's Michael Dimitriou is just as intrigued as participant TingTing Liu about reflectometry results while Marilia Cabral ponders her data at the NCNR Summer Workshop.



Matt Helgeson (University of California Santa Barbara) with Ph.D. student Juntae Kim anticipate excellent rheo-SANS results. (See Helgeson's article on p. 36)

Foreigners or not: new data prior to the Maya collapse in the western lowlands of mesoamerica

R. Bishop¹ and M.J. Blackman^{1,2}

In 1952 Robert Oppenheimer suggested the use of neutron activation analysis (NAA) to chemically analyze archaeological artifacts as a possible peaceful application of nuclear energy under the Atoms for Peace program. The thought was to use the chemical composition of artifacts to identify the source of raw materials or site of manufacture. By the early 1970s instrumental neutron activation (INAA) became, and still is, the preferred method for the analysis of archaeological ceramics. Among the first archaeological ceramics analyzed by INAA were orange fine paste pottery made by the ancient Maya. Today, Maya Fine Orange pottery continues to be analyzed, as part of collaboration between the NIST Center for Neutron Research and the Smithsonian Institution. The data provide a new window into the events concerning one of the great mysteries of the past — the “collapse” of the lowland Maya civilization in the ninth century AD.

From approximately 1100 BC to the mid-800s AD a highly complex society developed, reaching its apogee in the rain forests of southern Mexico, Guatemala, Belize and western Honduras. The society’s achievements in art, monumental architecture, mathematics—independently inventing the concept of zero—, and astronomy rivals other great civilizations of the world. Religious and civic administration rested in the hands of elite members of the society, headed by a grand lord or king, sometimes ruling grand city states, exemplified by such well-visited archaeological ruins today as Tikal, Calakmul, Palenque and Copan (Fig. 1). Hieroglyphic texts tell of kingly succession, marriages, alliances, and especially warfare for territorial expansion and celebrated in grand public ceremonies.

By the middle of the eight century AD, beginning with sites in the far west, and expanding to those in the upper reaches of the great Usumacinta River and in the Central Peten state of Guatemala, ties to the civic and ceremonial centers and to the grand lords were slipping. By 830 many of the great centers had only remnant populations and by 1000 vast areas of the Maya lowlands were depopulated—remaining that way until recent times. So what happened? Among the more prominent, somewhat sensationalistic explanations are ones that involve a peasant revolt against the elite, soil exhaustion, drought, disease, earthquakes, expansionistic warfare, and foreign invasion.

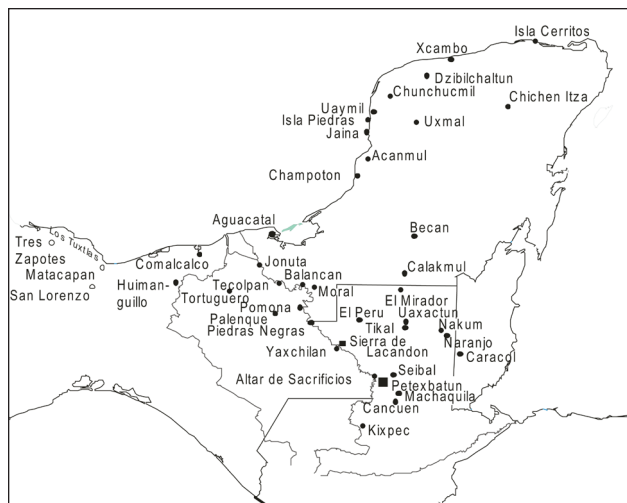


FIGURE 1: Map showing major sites in the Maya region and southern Veracruz from which pottery has been analyzed using INAA.

No single cause however can explain the loss of cohesion of the political system and decline of the power of the divine lords. Studies of ceramic composition, including sources of manufacture and patterns of dispersion, are providing some new insights into changes that were taking place.



FIGURE 2: Left: Maya ceramic; Provincia Plano Relief showing long-haired figure. Middle: Maya ceramic; Pabellon Modeled-carved. Right: Non-Maya Campamento Fine Orange, imported to Cancun from southern Veracruz.

Photo credits: Ronald L. Bishop

The original use of INAA to characterize Fine Orange pottery was directly related to the possibility that foreign invaders were involved in the dramatic changes of the late eighth century. The construction of buildings ceased, as did the erection of monuments, and use of polychrome pottery. It was sometime during these changes that a distinctive, orange, finely textured ceramic appeared which carried “non-Maya images,” conceivably

¹ Smithsonian National Museum of Natural History, Washington, DC, 20013

² NIST Center for Neutron Research, National Institute of Standards and Technology, Gaithersburg, MD 20899

from the Southern Veracruz or Tabasco plains to the north: the lands of the Putun (Fig. 2 left: Fine Orange with long hair image; middle: non-Maya features.) Our long term application of NAA to this distinctive ceramic, obtained from national and international collections and through recent excavation, has yield significant information.

We have established that the Usumacinta River, which arises in the mountains of Guatemala and flows for more than 1000 km (600 miles) into the Gulf of Mexico, is the “source” of the Fine Orange pottery. With our use of 18 elemental concentrations, 12 of which are quantified to less than 4 % analytical error, we have been able to accurately locate a subregion for Fine Orange pottery along this great riverine artery. The locus of early manufacture is determined to lie within an approximately 50 km zone located between the small modern town of Balancan and the archaeological site of Jonuta (see Fig.1). Sedimentary features including levees, oxbows and hydrological events including annual inundation have sorted the weathered silts and fine sands into highly localized resources that are only slightly different but can be distinguished use the neutron activation data (Fig. 3).

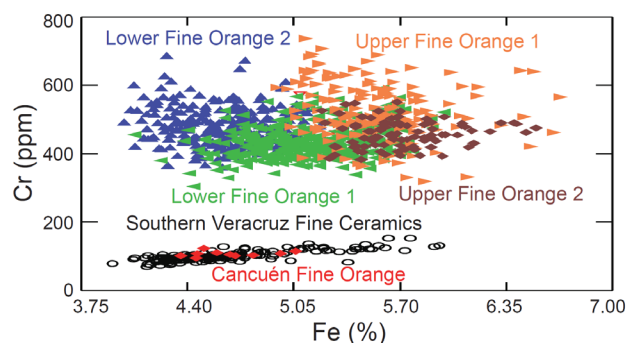


FIGURE 3: Plot of Fine Orange ceramic data relative to the concentration of chromium and iron to show separation between major Fine Orange group and pottery from Southern Veracruz. Groups have formed according to similarity using 18 elemental concentrations obtained by neutron activation analysis. Groups have been refined using their Mahalanobis distances from the individual group multivariate centroid. All groups are separate at a 95 % confidence interval.

Later, perhaps sometime in the ninth century, makers of Fine Orange moved downstream closer to the Usumacinta delta region. Whereas the earlier Fine Orange had been moved/traded to sites of the interior of the Maya lowlands, the latter pottery was circulated to sites along the coast, and around the Yucatan Peninsula. This may be a reflection of changing trading habits that responded to the movement of western and central Maya inhabitants toward the coast. Also in the late eight century there appears to be another major producer of Fine Orange that placed heavy emphasis on the strange designs found on pottery of the earliest analyses (Fig. 2 middle). A subregion for the manufacture of that pottery appears to be centered upstream on the

Usumacinta about the site of Yachixlan. From there, Fine Orange was moved to the east and even copied and traded by groups at the declining great city of Tikal.

Recent excavations at the site of Cancuén resulted in a surprising find: a Fine Orange vessel (Fig. 2, right) recovered in good context under a sealed floor along with a distinctive type of Fine Gray ceramics. The problem was the association, namely, that it placed Fine Gray and Fine Orange together some 50 years before the “collapse” and the time that Fine Orange was to become abundant. We analyzed the Fine Orange vessel and several other similar ceramic fragments, only to find that it did not match the usual paste composition of other Maya Fine Orange ceramics. Searching the accumulated database of more than 36,000 analyses of Maya ceramics we found a match with recent data from pottery in Southern Veracruz. The use of neutron activation data demonstrated that both the Fine Gray and the Fine Orange vessels were not strictly speaking “Maya” but rather has been made from the resources in southern Veracruz. The INAA data represented contact with people in the southern Veracruz – Tabasco plain region in the mid 700s. We revisited our neutron activation data base and have been able to identify other ceramics from southern Veracruz pottery that were present at several other sites along the Usumacinta more toward the interior of Guatemala.

The “strange designs” on the Maya Fine Orange pottery was originally thought to be evidence of non-Maya people and thereby being threatening to dwellers of the Maya cities or perhaps part invasion. However, later study suggested that the designs were more or less within “Maya” canons. The chemical data has allowed us to determine that there was secure evidence of contact between the southern Veracruz and Maya regions, that it occurred at several population centers, and it occurred well before the major events that precipitated the Maya collapse. The designs and personages found on the ceramics coming into the core area of the Maya are slightly different because they represent a fusion of ideas that came together over at least half a century. Sites on the western edge of the Maya area, for example have several ceramic traditions that break with other Maya centers and reflect strong, influences of people in the Gulf coastal area.

Rather than considering the southern Veracruz – Tabasco region being a home of foreign invaders, we can begin to appreciate that it combined with the Western Maya area as an interaction zone involving trade in such items as cotton, quetzal feathers, cacao, and jade. An interaction zone is quite different conceptually than a hostile border between socially different groups. The interpretations based on the neutron activation data of fine paste pottery are forcing us to re-evaluate the interactions of neighboring groups during the decades immediately prior to the societal changes that are known as the Maya Collapse.

Walking the line between life and death: membrane binding and regulation of the PTEN tumor suppressor

S. S. Shenoy¹, P. Shekhar¹, F. Heinrich^{1,2}, H. Nanda^{1,2}, A. Gericke⁴, M.-C. Daou⁵, A. H. Ross⁵ and M. Lösche^{1,2,3}

In recent decades, biology made tremendous progress in determining how cells – the smallest viable units that support life and form large organisms, such as ourselves – cast critical decisions whose outcomes often discriminate death from survival. For example, after completing their useful life cycle, cells are signaled to “shut off”, so that they can be replaced by fresh cells – a process called apoptosis, or controlled cell death. If worn-out cells lose their ability to be “shut off” because of malfunctions of the underlying cell signaling machinery, they transform into cancer cells, *i.e.*, immortalized cells that divide beyond control – the start of tumor growth.

Many cell signaling processes occur on cell membranes – nanometer-thin, fluid lipid bilayers and their associated proteins that enclose each cell. One such bilayer forms the plasma membrane that separates inside from out. Lipid membranes are disordered assemblies of their constituent molecules, held together by weak intermolecular forces but not through the much stronger, and much more inflexible, covalent chemical bonds. As a result, membranes respond dynamically to changes in their environment, be it within the cell or at the outside. However, cell membranes are extremely difficult to characterize by physical techniques such as x-ray crystallography, and biochemical techniques are often only indirect and non-quantitative. This is where neutron scattering enters the game.

Our collaboration studied PTEN (short for *phosphatase and tensin homologue deleted on chromosome 10*) [1], a protein that plays a key role in the apoptosis cell signaling pathway, and its interaction with membranes. PTEN is a tumor suppressor [2], *i.e.*, it shifts the balance between life and death for an individual cell toward cell clearance. At the plasma membrane PTEN finds a specialized signaling molecule, a lipid of the phosphoinositolphosphate (PIP) family, which it cleaves in an enzymatic reaction [3]. PTEN has been identified as one of the most frequently mutated proteins in human tumors [4], *i.e.*, if PTEN cannot fulfill its function properly, the result is almost always cancer. There is yet little understanding of how the tumor suppressor associates with the membrane, finds its target substrate and processes it to shift the balance toward cell death.

Most importantly, it is not clear how the tumor suppressor is regulated, *i.e.*, by which physical mechanisms the cell decides whether its activity should increase or decrease.

Recently, a low-resolution structure of PTEN on a bilayer using *sparsely-tethered bilayer lipid membranes* (stBLMs) [5] was obtained with neutron reflectometry (NR) [6] (see Fig. 1a). The structure shows that the protein associates closely with the membrane without penetrating deeply. Although NR on its own does not provide sufficient resolution to determine atomic-scale details, it characterizes the structure in its biologically relevant membrane-bound state, including disordered parts of the protein that are invisible in the PTEN crystal structure [7]. A second breakthrough came by combining the NR results with molecular dynamics (MD) simulations of the membrane-bound protein and of the protein in solution. Without any cross-reference to the experimental results, the membrane-bound MD simulations settled exactly into the NR structure (see Fig. 1b). This is strong evidence that both the NR and the MD simulations independently describe the structure correctly at their different levels of resolution.

NR and MD simulations in combination unlock a wealth of previously inaccessible information (see Fig. 2). The MD simulations of the membrane-bound PTEN show that two distinct regions of the protein, located at the phosphatase (PD) and the C2 domain, tie the protein peripherally to the membrane surface. In between the two contact points and buried within the PD, is the catalytic site, which cleaves the headgroup of a specific PIP lipid, thus shifting the regulatory chemical circuit toward cell death. A comparison between the solution structure and the membrane-bound structure of the protein shows that both are slightly distinct and in turn different from the crystal structure. In the membrane-bound state, the PD is rearranged, such that the body of the PTEN protein flattens somewhat against the bilayer surface, thus gaining easier access to its substrate.

The most significant difference between the membrane-bound and solution states of the PTEN protein, however, concerns the disordered C-terminal tail. Because of anionic charges

¹ Department of Physics; Carnegie Mellon University; Pittsburgh, PA 15213

² NIST Center for Neutron Research; National Institute of Standards and Technology; Gaithersburg, MD 20899

³ Department of Biomedical Engineering; Carnegie Mellon University; Pittsburgh, PA 15213

⁴ Worcester Polytechnic Institute; Worcester, MA 01609

⁵ University of Massachusetts Medical School; Worcester, MA 01605

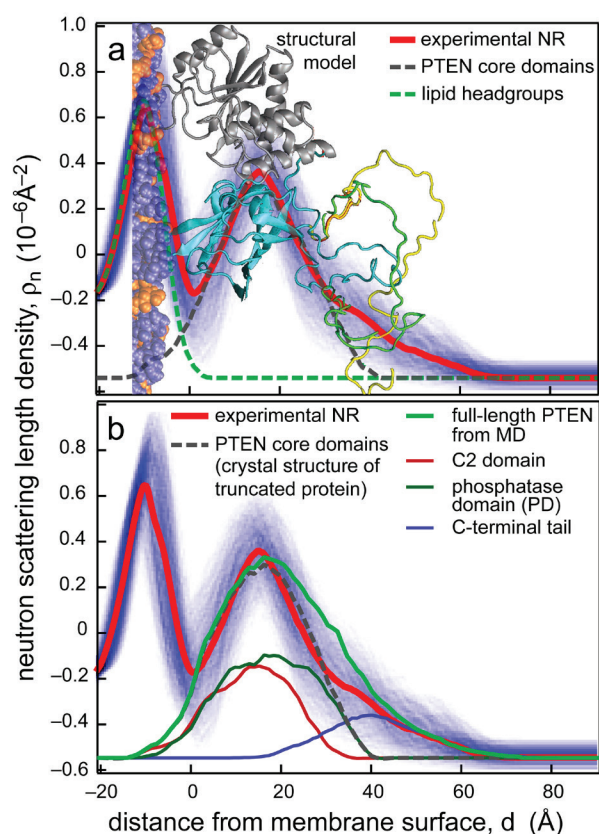
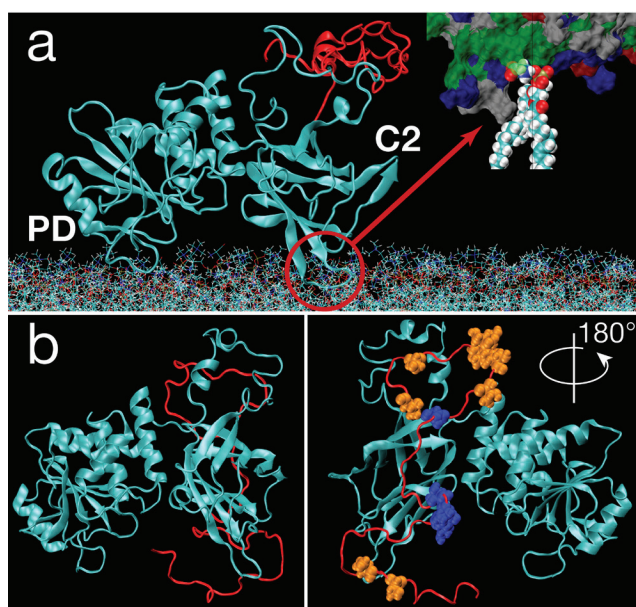


FIGURE 1: The low-resolution structure of the membrane-bound PTEN phosphatase as a neutron scattering length density (nSLD) distribution across the membrane. The bilayer, only partially shown, extends to the left. The high nSLD around $d = -10$ Å shows the lipid headgroups. Experimentally determined nSLD (red) and its interpretation (a) by accommodating the crystal structure of a truncated PTEN variant [7] and (b) from MD simulations of the full-length protein. Shaded blue band indicates the confidence intervals around the best-fit model (red line). The image in (a) shows a structural model represented by this nSLD profile [6].



along the peptide chain, the tail is repelled by the anionic membrane surface in the membrane-bound state of the protein. In contrast, in solution this tail wraps around the C2 domain where it partially obstructs the membrane-binding interface. This conformation could be locked in place if the C-terminal tail itself becomes phosphorylated, a chemical modification that has been reported to interfere with the membrane binding of the protein [8].

A detailed view of the duty cycle of PTEN, a key regulator in the cell signaling pathway that controls apoptosis, has been uncovered using neutron scattering techniques and MD simulations. For the first time, this provides a high-resolution structure of a supra-molecular complex comprised of a disordered lipid membrane and a peripherally associated protein. Functionally important disordered parts of the protein were determined in their distinct organization on and off the membrane, and it became clear that the crystal structure is neither an entirely appropriate description of the solution structure nor the membrane-bound structure of PTEN. Thus, atomic-scale details become available which are crucial for in-depth understanding of the fine line that separates life from death.

References

- [1] J. Li, *et al.*, *Science* **275**, 1943 (1997).
- [2] N. R. Leslie and C. P. Downes, *Biochem. J.* **382**, 1 (2004).
- [3] F. Vazquez, *et al.*, *Proc. Natl. Acad. Sci. USA* **103**, 3633 (2006).
- [4] L. Simpson and R. Parsons, *Exp. Cell Res.* **264**, 29 (2001).
- [5] D. J. McGillivray, *et al.*, *Biointerphases* **2**, 21 (2007).
- [6] S. Shenoy, *et al.*, *PLoS ONE* **7**, e32591 (2012).
- [7] J. O. Lee, *et al.*, *Cell* **99**, 323 (1999).
- [8] F. Vazquez, *et al.*, *Mol. Cell. Biol.* **20**, 5010 (2000).

FIGURE 2: MD simulations of PTEN on a membrane (a) and in solution (b). The inset in panel (a) shows the interaction of amino acid sidechains with lipids. The two core domains, C2 and PD, organize similarly in solution and on the bilayer, where the protein is slightly more flattened against the membrane surface. At the membrane, the flexible C-terminal tail (red), is electrostatically repelled by the anionic bilayer. In distinction, it wraps around C2 in solution and obstructs the membrane binding interface (left in panel b). In the rotated view (right), amino acid side chains are highlighted that may play a role in controlling PTEN's membrane association.

Towards the elucidation of antibiotic resistance transfer in bacteria: structural studies of the TraI protein

N.T. Wright¹, M. Raththagala², E. Bruenger², J. Schildbach², J.E. Curtis³ and S. Krueger³

Approximately 70 % of bacteria responsible for hospital-acquired infections are resistant to at least one antibiotic commonly used to treat the infection, which presents a serious public health problem. Bacterial conjugation, or lateral gene transfer, plays an important role in the spread of genes, leading to increased abundance of pathogenic or antibiotic-resistant bacteria. The mechanism of bacterial conjugation can be elucidated by understanding the regulation of its components. One component, TraI, is a protein that is essential for the unilateral transfer of DNA from donor to recipient bacterium. In order to pass through the conjugative pore, TraI likely unfolds, at least partially, prior to transfer, though the mechanism and extent of unfolding is unknown. We are interested in studying the orientation of the domains in combination with large-scale structural changes of TraI that are responsible for the regulation of TraI functionality and hence the transfer of antibiotic resistance. In this report we have combined high-resolution nuclear magnetic resonance spectroscopy (NMR) and small-angle neutron scattering (SANS) to screen models in order to elucidate the structure of portions of the TraI protein.

TraI is a 1,756 residue protein containing several functional domains. The functional domains of TraI include: a N-terminal nickase domain that binds and nicks (cleaves one strand of) plasmid DNA at the origin of transfer (*oriT*); a non-specific single-stranded DNA (ssDNA) binding domain; a helicase domain; and a C-terminal domain. A schematic of the domain structure of TraI is shown in Fig. 1. While structures have been solved for several domain fragments, there is currently no high-resolution structural data available for the full-length TraI protein. Obtaining structural information is necessary for determining how conformation regulates TraI function during DNA transfer.

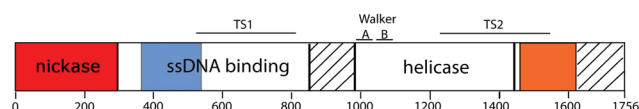


FIGURE 1: Schematic of TraI protein. Regions of known structure are colored in red, blue (current report), and orange. TS1 and TS2 stand for Translocation Sequences 1 and 2, which are regions containing sequences necessary for protein transfer to the recipient cell. Walker A/B identifies the ATP binding site in the helicase domain. Hash marks indicate no currently known structure or function.

We combined structural data from NMR and SANS measurements. Structural models were developed using both molecular dynamics and molecular Monte Carlo simulations. Models were screened by comparing synthetic SANS profiles to experimental data. In the first part of the study we determined the structures of the residues 306-381. In the second part we studied a larger fragment of TraI composed of residues 1-569. Small-angle neutron scattering experiments were performed on the 30 m SANS instruments at the NCNR.

TraI model structures were generated by combining known x-ray and NMR structures along with molecular dynamics simulations. Molecular Monte Carlo simulations were performed using the program SASSIE [2] where intrinsically disordered regions were permitted to sample allowed conformational space. Model SANS profiles corresponding to each of these model structures were calculated using Xtal2sas. Chi squared analysis and protein density map calculations were generated using SASSIE. In Fig. 2, we show an ensemble of structures obtained by combining analysis of NMR and SANS data for residues 306-381 of TraI combined with the known x-ray structure of residues 1-305. This result indicates that residues 306-381 are only partially disordered and the region is slightly compact. We extended our analysis to study residues 1-569 of TraI as shown in Fig. 3. We find through analysis of small-angle scattering data that two domains that are known to exhibit negative cooperativity to binding DNA are found to be adjacent in three dimensional space.

¹ James Madison University; Harrisonburg, Virginia 22807

² Johns Hopkins University; Baltimore, MD 21218

³ NIST Center for Neutron Research; National Institute of Standards and Technology; Gaithersburg, MD 20899-8562

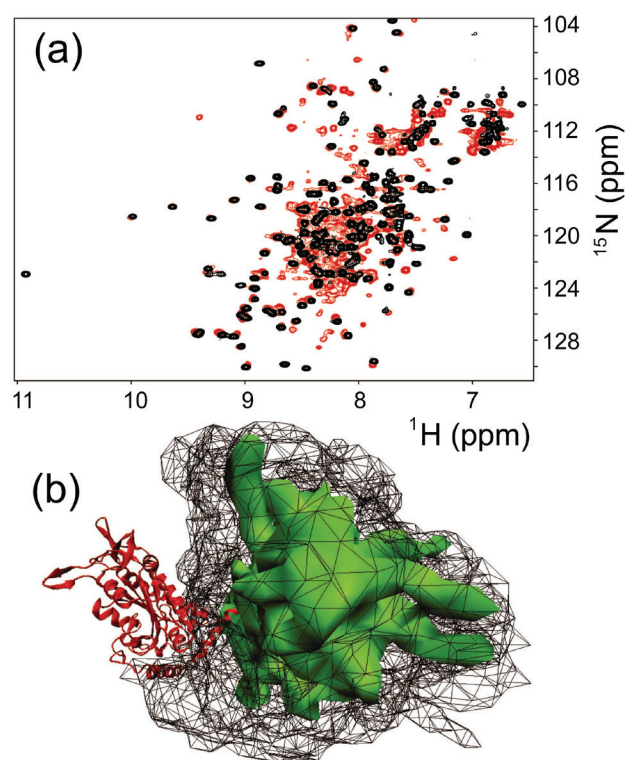


FIGURE 2: Structure of the first Tral linking region (306 to 381). (a) NMR spectra overlay between F-Tral (381-569) in black and F-Tral (309-569) in red. The red spots suggest that part of this construct is well-folded (mostly, those whose peaks overlay with (381-569)), while part of this construct is poorly folded or unfolded. (b) shows a composite image arising from SANS data collected on Tral (1-330). Residues 1 to 305 of the modified 1P4D crystal structure are represented in red. Using the program SASSIE [2], 5795 structures were generated by Monte Carlo sampling the backbone dihedral angles for residues 306 to 330. The protein shell of residue 306 to 330 from this simulation is represented in black mesh. The SANS profiles of these structures were then back-calculated and compared to actual SANS data of Tral (1-330). The protein shell of residues 306 to 330 from those models that most closely agreed to the actual SANS data ($\chi^2 < 5$) is represented in green. This shows that residue 306 to 330 does not exist in a well-formed structure in this construct.

In summary we have determined the solution structures of the N-terminal fragment of the F Tral helicase-associated ssDNA binding domain. We determined that this structure forms a well-folded globular motif consisting of a core of four parallel β strands that are surrounded by helices. We also determined how this region of Tral is situated in the context of the entire N-terminal third of the Tral molecule.

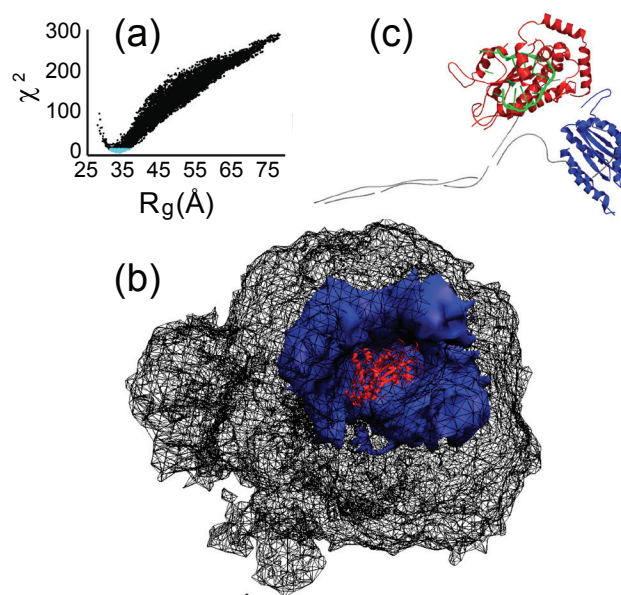


FIGURE 3: Orientation of domains within Tral (1-569). 8755 models of Tral (1-569)-*oriT*, ssDNA, and small-angle scattering profiles were generated using SASSIE, where residues 306 to 389 were allowed to randomly move. (a) A plot of the χ^2 versus radius of gyration. Data colored in blue represent those models with a χ^2 value of less than 15. (b) Tral (1-305) is shown in red, with the protein shell of residues 306 to 569 of all models represented in black mesh. Those models with a low χ^2 value (240 models) are depicted in blue. (c) shows the model that most closely agrees with the scattering data. In this and all other well-agreeing models, the nickase (red) and (390-569) (blue) are close to each other in physical space. In green is the 12 bp ssDNA from the crystal structure of nickase-ssDNA, which is the fragment that was bound to the nickase domain in these experiments.

Although Tral is a modular protein, the nickase and ssDNA binding domains are in close proximity to each other, and are apparently oriented not through direct domain-domain interaction but instead through the partial folding of a linker region. This orientation of domains may have functional consequences, in that it gives the apparent negative cooperativity of ssDNA binding a structural basis.

References

- [1] N.T. Wright, M. Raththagala, C.W. Hemmis, S. Edwards, J.E. Curtis, S. Krueger, and J.F. Schildbach, *Proteins: Struct., Funct., Bioinf.* **80**, 2250 (2012).
- [2] J.E. Curtis, S. Raghunandan, H. Nanda, and S. Krueger, *Comp. Phys. Comm.* **183**, 382 (2012).

Structures and conformations of voltage-sensor domains and voltage-gated K⁺ channel proteins

S. Gupta¹, J.A. Dura², D.L. Worcester^{2,3,5}, J.A. Freites⁴, D.J. Tobias⁴ and J.K. Blasie¹

Ion channel proteins control the diffusion of ions such as K⁺, Na⁺ and Ca²⁺ across plasma membrane of cells, thereby affecting numerous cellular signaling processes, especially those involving the electrochemical potential across the membrane, called the membrane potential. These ion channels change conformations from one structure to another (within a few milliseconds) in order to open or close the channel in response to stimuli. Important channels which are responsive to changes in membrane potential are the voltage-gated potassium (Kv) and sodium (Nav) channels which have fundamental roles in propagating action potentials along nerve axons, thereby providing nerve cell signaling in all animals. These channels are also sites for effects of both general and local anesthetics. In addition to open and closed conformations, some ion channels have an inactivated conformation, which ensures that the electrical signals propagate in only one direction along a nerve axon. Details of these different conformations and the switching between them are crucial to understanding the function of voltage-gated ion channels.

Voltage-gated ion channel proteins are large structures with domains that perform distinct roles, such as the channel pore containing the selectivity filter, generally four voltage sensor domains (VSD), and an inactivation gate to block the pore. Channel responses to changes in membrane potential require electromechanical coupling between VSDs and the pore domain (PD), the mechanism of which remains unknown. X-ray crystal structures of a few voltage-gated potassium (Kv) channels and a voltage-gate sodium (Nav) channel have been determined and provide much basic structural information, but these pertain to only the open state. Furthermore, the channel proteins in these crystals are in a non-native environment since there is no lipid bilayer. The importance of lipids was demonstrated by experiments showing that without certain lipids (phospholipids) the channels do not function.

In the present work, methods have been developed to obtain structural and conformational information on channel proteins all oriented in the same direction, and their separate domains in phospholipid membrane environments similar to nerve cells. These methods include the possibility of applying membrane potentials and monitoring protein conformational changes in

response to changes in the potential. Neutron reflectometry is utilized to characterize the membrane protein conformation in detail at the sub-molecular level using a single membrane that contains oriented channels, tethered to a special substrate [1]. The use of neutron reflectometry has inherent advantages arising from solvent contrast variation (H₂O/D₂O) coupled with the deuteration of selected membrane molecular or sub-molecular components, especially important for the solid/liquid interface. A new approach is used to form the tethered membrane. Instead of forming a lipid bilayer tethered to the substrate, the protein channels themselves are tethered to the substrate and phospholipids, such as 1-palmitoyl-2-oleoyl-sn-glycero-3-phosphocholine, (POPC) are added to form the bilayer, with the lipid bilayer attaining its equilibrium location with respect to the tethered protein. By tethering the whole protein, or a protein domain of interest, to the substrate, its orientation with respect to the substrate is assured. Therefore it is possible to more accurately determine its unique location and conformation in SLD profiles. This is an advantage over other techniques that lose information by averaging over the two possible orientations of the protein across the membrane [2]. To achieve protein tethering, the proteins of interest are expressed with a modified carboxyl terminus that has six histidine residues added. These provide linking to an alkylated substrate by co-ordination chemistry.

Another essential technique is to utilize a known reference multilayer of high scattering length density (SLD) in the substrate to enhance features of the reflectivity by neutron interferometry. The reference multilayer also provides a marker of the position of the membrane with respect to the substrate surface and can be used to “phase” the reflectivity data. As a result, unique SLD profiles can be derived whose spatial resolution (minimum wavelength Fourier component) is limited by the accessible Q_z -range. These resolution-limited SLD profiles can be modeled with error functions. Such modeling effectively fits both the modulus and phase of the reflectivity data, unlike the more traditional refinement of such “slab-models” which utilize only the modulus data.

Omitting details [1] for brevity, we present only the error-function, or “slab-models” of the experimental SLD profiles

¹ University of Pennsylvania, Philadelphia, PA 19104

² NIST Center for Neutron Research, National Institute of Standards and Technology, Gaithersburg, MD 20899-6102

³ Dept. of Physiology & Biophysics, University of California, Irvine, CA 92697

⁴ Dept. of Chemistry, University of California, Irvine, CA 92697

⁵ University of Missouri, Columbia MO 65201.

derived by phasing the reflectivity data. Figure 1 (top) shows the profile structure of the precursor, tethered VSD:OG monolayer (*i.e.*, VSD solvated by a detergent, *n*-octyl- β -D-glucopyranoside (OG)), fully hydrated with bulk aqueous media for 100 % D₂O (blue) and (60 % D₂O)/(40 % H₂O) (green). The water slabs at either surface of the membrane are removed to reveal the VSD itself. Figure 1 (middle) shows the profile structure of the POPC bilayers within the reconstituted VSD:POPC membrane fully hydrated with bulk aqueous media for (60 % D₂O)/(40 % H₂O) for D4-POPC (blue) vs. H-POPC (red). The former contains four deuterium atoms within the phospholipid's polar head group. The differences in the slab-model profiles, here due to hydration with bulk H₂O or D₂O (top) and D4-POPC or H-POPC (middle), are statistically significant, exceeding the propagated experimental error. Figure 1 (bottom) shows the H-D exchange profile for the reconstituted VSD:POPC membrane (blue), and for the VSD (red) itself within the membrane. This is in good agreement with that predicted by a molecular dynamics simulation. A cut-away view of the simulation system (Fig. 1 bottom inset) shows that when the VSD is embedded in a lipid bilayer, water molecules penetrate throughout the VSD profile via a "pore" forming an internal hydrogen bond network with a set of highly-conserved basic and acidic side chains.

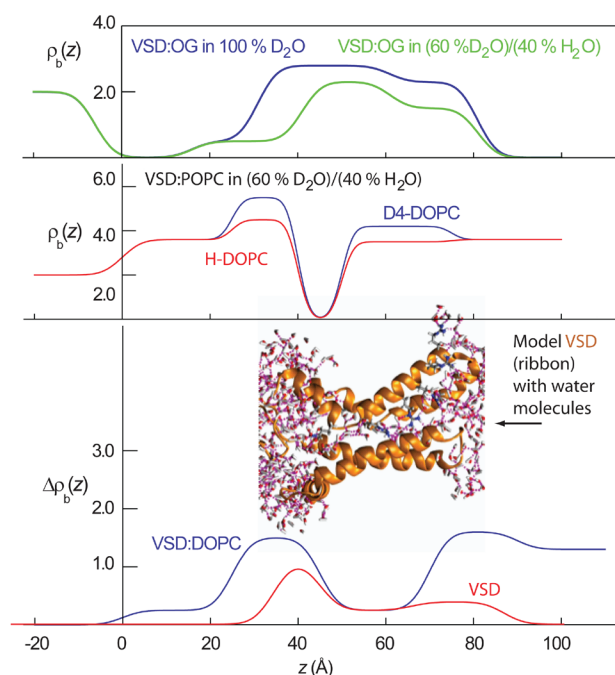


FIGURE 1: Summary of the slab-model profiles as described in the text. The inset is from a MD simulation where the voltage-sensitive domain is shown in ribbon (orange) representation, the lipid bilayer has been deleted for clarity, and waters are colored by atom (oxygen, red; hydrogen, white).

These results are in much greater sub-molecular detail than previously achieved. They demonstrate the unidirectional orientation of the VSD and the retention of its molecular conformation (secondary and folded 3-D tertiary structure) manifest in the asymmetric profile of the protein within this

reconstituted single bilayer membrane system. They describe the structure of the phospholipid bilayer solvating the lateral surfaces of the VSD protein. The profile structures of both the VSD protein and the phospholipid bilayer also demonstrate significant dependence on the hydration state of the membrane (not shown). They also provide the distribution of hydration water and exchangeable hydrogen throughout the profile structure of both VSD itself and the VSD:POPC membrane for the fully hydrated case. The two experimentally determined water and exchangeable hydrogen distribution profiles are consistent with the existence of a water pore within the core of the VSD, as first indicated by MD simulations.

The structural detail obtained is derived not only from neutron interferometry coupled with solvent contrast variation and selective deuteration in the polar headgroup of the POPC component, but also because of the unidirectionality of the VSD protein within the membrane. Such results cannot be achieved utilizing more typical membrane reconstitution approaches that generally result in an average orientation of the protein with equally populated opposed directions. This average orientation results in the determined profile structures of both the protein and the phospholipid being symmetric about the center of the membrane profile structure.

Some results (not shown) were obtained for the full-length KvAP protein for both the tethered KvAP:DM monolayer and the subsequently reconstituted KvPA:POPC membrane. While these results are not as extensive as those described for the VSD, they demonstrate a successful reconstitution of a phospholipid bilayer environment for the unidirectional KvAP protein, more similar to that of a pure phospholipid bilayer than that for only the VSD itself.

This work on unidirectional channel proteins in lipid bilayers provides a basis for the investigation of the profile structures as a function of the applied transmembrane voltage. In such studies, the substrate to which the reconstituted membrane is tethered also serves as the working electrode in the electrochemical cell. Neutrons can easily penetrate the solid/liquid materials forming the cell, but the relatively low incident neutron flux will likely limit such studies to profile structures at steady-state values of the potential. High-energy (> 20 keV) x-rays are required to penetrate solid/liquid materials complicating the cell design, but the much higher incident photon flux provided by synchrotron radiation sources can allow time-resolution of the response of the profile structure to a step-wise change in the potential.

References

- [1] S. Gupta, J.A. Dura, J.A. Freites, D.J. Tobias, and J.K. Blasie, *Langmuir* **28**, 10504 (2012).
- [2] D. Krepiak, M. Mihailescu, J.A. Freites, E.V. Schow, D.L. Worcester, K. Gawrisch, D.J. Tobias, S.H. White and K. Swartz, *Nature* **462**, 473 (2009).

The role of electrostatic interactions in the local dynamics of biological and synthetic polyelectrolytes

J.H. Roh^{1,2}, M. Tyagi^{2,3}, R.M. Briber², S.A. Woodson⁴, A.P. Sokolov^{5,6}

RNA is the only known biomolecule capable of both self-replication and enzymatic activity. Recent research has shown that there is a broad diversity of classes of RNA molecules, the knowledge of which is leading to advances in the understanding of basic biochemical processes in the cell and which holds significant promise for biotechnology applications. Understanding conformational dynamics of RNA is critical for mapping out the microscopic mechanism of biological events such as self-assembly, folding, ligand recognition and catalysis [1]. RNA folds to the compact native state in presence of Mg^{2+} ions which screen the negative charges on the RNA backbone arising from the phosphate groups. Folding allows for the formation of long-range tertiary interactions and results in a concomitant decrease in the radius of gyration and stabilization of the native state. In this work we describe our recent quasielastic neutron scattering studies using the HFBS instrument to examine the effect of Mg^{2+} counterions on the picosecond to nanosecond local dynamics and structure of hydrated tRNA in comparison to sulfonated polystyrene (SPS) [2]. This work provides insight into the role of electrostatic interactions on the dynamical fluctuations and structural stabilization of RNA and synthetic polyelectrolytes.

Figure 1a exhibits the dynamic transition (T_d) which is associated with the onset of anharmonic motion and which appears in both unfolded (u-) and folded (f-) tRNA between $T \approx 180$ K and 200 K. Another transition occurs at $T \approx 325$ K and is associated with the melting of secondary (2°) and tertiary (3°) structures. Interestingly, the mean squared displacement, $\langle r^2 \rangle$, values for the more compact f-tRNA were observed to be greater than those for the more extended u-tRNA at all temperatures up to 350 K. The more rapid change of $\langle r^2 \rangle$ in f-tRNA between 200 K and 250 K implies that the observed dynamics are not controlled solely by the hydrating water, but are significantly affected by the electrostatic nature of the RNA surface.

To separate how Mg^{2+} influences the flexibility of tRNA through stabilization of the tertiary structure and by altering the electrostatic environment, we also characterized the dynamical flexibility SPS with and without Mg^{2+} . As a synthetic polyelectrolyte, SPS does not have the tertiary interactions which are present in RNA. Like f-tRNA, SPS screened by Mg^{2+}

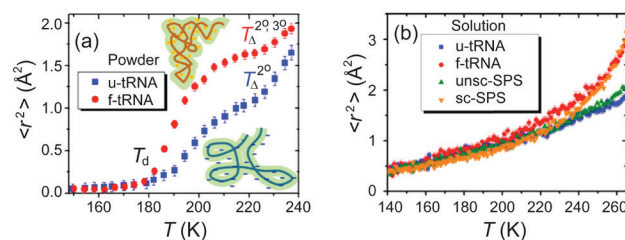


FIGURE 1: Temperature dependence of the mean-squared displacement, $\langle r^2(T) \rangle$, obtained from a Gaussian approximation, $\langle r^2(T) \rangle = -3Q^{-2} \ln[I_{el}(Q,T)/I_{el}(Q,50\text{ K})]$ for Q between 0.25 \AA^{-1} and 1.00 \AA^{-1} . (a) Powder unfolded (u-) and folded (f-) tRNA samples were hydrated to 42 % mass fraction corresponding to completion of the first hydration layer. The dynamic transition ($T_d \approx 200$ K) and melting transition ($T_{\Delta}^{2^\circ/3^\circ} \approx 325$ K) are indicated. (b) D₂O solutions of u- and f-tRNA and unscreened (unsc-) and screened (sc-) SPS.

(sc-SPS) showed larger local motion compared to unscreened SPS (unsc-SPS) (Fig. 1b). The larger $\langle r^2 \rangle$ values of sc-SPS and f-tRNA indicate that the Mg^{2+} induced electrostatic neutralization leads to larger and more thermal fluctuations of the polyelectrolyte. It is striking that $\langle r^2 \rangle$ of biological RNA and a synthetic polyelectrolyte, SPS, increase similarly with temperature, in both the unscreened and Mg^{2+} screened conditions.

Because the materials in this study have similar hydration levels, the differences we observe are primarily due to Mg^{2+} . Together with our earlier results [2], this suggests that the dynamical properties of both biological and synthetic polyelectrolytes are mainly controlled by solvation and electrostatics, rather than by specific macromolecular structure.

To understand the details of the dynamics, we analyzed the dynamic structure factor, $S(Q,E)$, of hydrated unfolded and folded tRNA powder at different temperatures. The total scattering spectra can be represented as:

$$S(Q,E) = DW(Q)[(1-QISF(Q))\delta(E) + QISF(Q)S_{QENS}(Q,E)] \otimes R(E) \quad (1).$$

Here $DW(Q)$ is the Debye-Waller factor, $QISF(Q)$ is the quasielastic incoherent scattering factor defined as the ratio of quasielastic scattering to the total scattering intensity, $S_{QENS}(Q,E)$ is the quasielastic scattering function, and $R(E)$ is a resolution function. The amplitude of $QISF$ is directly proportional to the mobile fraction of hydrogen atoms associated with the relaxation.

¹ Naval Research Laboratory; Washington, DC 20375

² University of Maryland; College Park, MD 20742

³ NIST Center for Neutron Research; National Institute of Standards and Technology; Gaithersburg, MD 20899

⁴ Johns Hopkins University; Baltimore, MD 21218

⁵ Oak Ridge National Laboratory; Oak Ridge, TN 37831

⁶ University of Tennessee; Knoxville, TN 37996

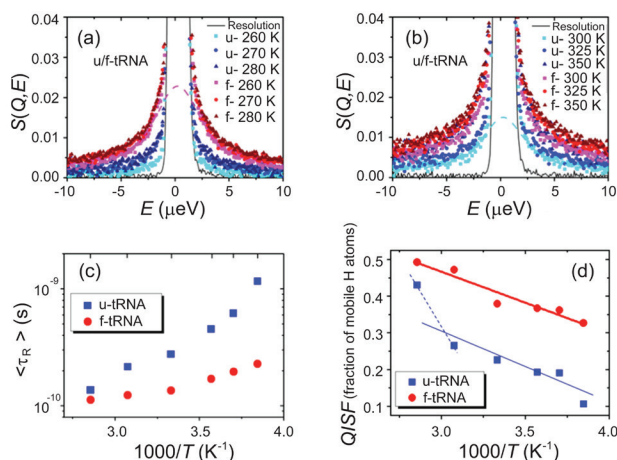


FIGURE 2: Dynamic structure factor, $S(Q=0.56 \text{ \AA}^{-1}, E)$, of u- and f-tRNA at various temperatures in (a) and (b). Resolution functions are $S(Q=0.56 \text{ \AA}^{-1}, E)$ at 10 K. Dashed lines are representative Lorentzian fits of quasielastic scattering of f-tRNA at 260 K and u-tRNA at 300 K. (c) Averaged relaxation time, $\langle \tau_R \rangle$, was estimated from the half-width at half-maximum of a Lorentzian peak. No significant Q -dependence of the $\langle \tau_R \rangle$ values was found, indicating that the relaxation is localized. (d) Quasielastic incoherent scattering factor as obtained from analysis of the peaks.

Figure 2a and 2b show that $S(Q, E)$ exhibits about a factor of two larger quasielastic scattering from f-tRNA than u-tRNA from 260 K to 320 K over the given energy range. This indicates that f-tRNA experiences a larger mobile fraction with faster local motions. The quasielastic scattering of u-tRNA at 350 K becomes similar in magnitude to that of f-tRNA at 300 K, which agrees with the sharp increase in $\langle r^2 \rangle$ for u-tRNA between 325 and 350 K as the secondary structure begins to melt.

The characteristic relaxation time, $\langle \tau_R \rangle$, of the tRNA motion was estimated from the half-width at half-maximum of $S_{QENS}(Q, E)$. Although a single Lorentzian fit is not the best analysis for a stretched relaxation spectra, a qualitative comparison of $\langle \tau_R \rangle$ values within the limit of the given time window is reasonable, especially for RNA which lacks methyl groups (as compared to proteins). The relaxation time of u-tRNA is slower and more temperature-dependent than $\langle \tau_R \rangle$ of f-tRNA (Fig. 2c). The average relaxation rate of u-tRNA becomes about one order of magnitude slower than that of f-tRNA at $T \approx 260$ K. Likewise, the QISF of u-tRNA is also lower than that of f-tRNA, suggesting the local relaxation is more suppressed (Fig. 2d). This suggests that, u- and f-tRNA explore different dynamical pathways. These results indicate that water likely serves as a plasticizer that lubricates the local motion of the hydrophilic macromolecules.

It has been observed that the compact folded yeast f-tRNA^{phe} ($R_g \approx 20 \text{ \AA}$ for f-tRNA^{phe}) having long-range tertiary interactions shows greater dynamical flexibility than unfolded extended yeast RNA ($R_g \approx 30 \text{ \AA}$ for u-tRNA^{phe}) [3]. This result is opposite to the relationship between structural compactness and global dynamics observed for folded proteins which have been shown to be more rigid than denatured proteins. The estimate of the persistence length, l_p , obtained from solution small-angle x-ray scattering (Fig. 3) shows that l_p is 1.7 times larger for u-tRNA compared to

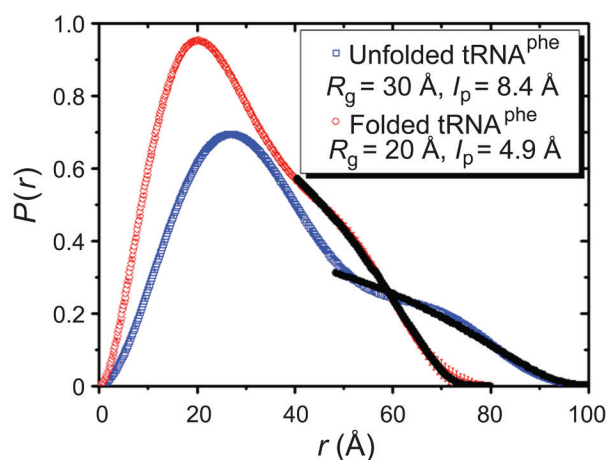


FIGURE 3: Analysis of pair distance distribution functions, $P(r)$, of unfolded and folded tRNA^{phe}. $P(r)$ was obtained from indirect inverse Fourier transform of small-angle x-ray scattering intensity using GNOM program [3]. The radius of gyration, R_g , and persistence length, l_p , were estimated from $P(r)$. Black lines are the fit of $P(r)$ to the exponential equation at $r > R_g$ on the basis of a worm-like chain model [4].

that of f-tRNA (8.4 \AA vs. 4.9 \AA), indicating significantly higher flexibility for the folded tRNA [2]. The difference in persistence length is in good agreement with the difference in $\langle r^2 \rangle$ between f- and u-tRNA at $T = 300$ K (Fig. 1a).

Our study demonstrates that charge screening by counterions greatly increases the local motion of tRNA and a synthetic polyelectrolyte. The increase in the magnitude of the displacement, relaxation rate and fraction of mobile atoms is consistent with the shorter persistence length of the folded tRNA. However, the mechanism by which Mg^{2+} increases the flexibility of coupled dynamics between the compact folded tRNA and hydrating water remains unclear. Possible reasons include 1) increased electrostatic fluctuations caused by the diffusion of hydrated cations and 2) increased fluctuations of the hydrogen bond network. Interestingly, NMR, birefringence, and molecular dynamics simulation studies reported that divalent cations suppress the mobility of single-stranded RNA segments, compared to monovalent cations. More details about the electrostatic origins controlling hydrating water-coupled tRNA dynamics will be developed through the comparison of the dynamics in the presence of monovalent cations with different ionic densities, such as Na^+ and K^+ .

References

- [1] D.E. Draper, D. Grilley, A.M. Soto, Annu. Rev. Biophys. Biomol. Struct. **34**, 221 (2005); S.A. Woodson, Curr. Opin. Chem. Biol. **9**, 104 (2005).
- [2] J.H. Roh, M. Tyagi, R.M. Briber, S.A. Woodson, A. Sokolov, J. Am. Chem. Soc. **133**, 16406 (2011).
- [3] X.W. Fang, K. Littrell, X. Yang, S.J. Henderson, S. Siefert, P. Thiagarajan, T. Pan, T.R. Sosnick, Biochemistry, **39**, 11107 (2000).
- [4] G. Caliskan, C. Hyeon, U. Perez-Salas, R.M. Briber, S.A. Woodson, D. Thirumalai, Phys. Rev. Lett. **95**, 268301-1 (2005).

Powder neutron diffraction reveals new CO₂ adsorption interactions in chabazite zeolites

M.R. Hudson^{1,2}, W.L. Queen¹, J.A. Mason³, D.W. Fickel⁴, R.F. Lobo⁴, and C.M. Brown^{1,5}

One of the most pressing issues facing the energy sector is the mitigation of global warming-implicated greenhouse gases through pre- and post-combustion capture applications. The efficient and selective capture of CO₂ from industrial flue gas streams is of particular interest. The current strategy, involving absorption in alkanolamine solutions, has several disadvantages, namely a lack of corrosion control and significant energy requirements for regeneration [1]. Typical flue gas streams have N₂:H₂O:CO₂ mass ratios of 6.5:1:1 and up to 15 % CO₂ volume fraction at atmospheric pressure. The high gas flow rates make porous materials, such as zeolites, promising options for separation/sequestration of CO₂. These framework materials exhibit high internal surface areas allowing them to physically adsorb large amounts of gas. Neutron powder diffraction (NPD) is a useful tool for studying these materials [2]. Here, we highlight our recent investigation of low-pressure CO₂/N₂ sorption in the acidic (H-SSZ-13) and copper-exchanged (Cu-SSZ-13) derivatives of zeolite SSZ-13 utilizing NPD combined with *in situ* CO₂ and N₂ adsorption [3].

Cu-SSZ-13 is unique among copper-exchanged zeolites in that there is only one location for the copper cation in the host framework at high silicon/aluminum ratios, thereby simplifying the discussion of cation-exchange effects on the uptake and selectivity. Additionally, Cu-SSZ-13 has shown improved hydrothermal stability over other copper-exchanged zeolites, an important property for post-combustion capture of CO₂ in flue streams with the presence of water [4]. The CO₂ and N₂ adsorption data for both H-SSZ-13 and Cu-SSZ-13 were collected at 298 K, and the maximum uptake at 1 bar is lower for the Cu²⁺ exchanged derivative: 3.75 mmol/g, compared to the acidic form: 3.98 mmol/g. In terms of the number of moles of CO₂ adsorbed at STP, H-SSZ-13 and Cu-SSZ-13 are in-line with the best sorbents for CO₂ uptake, and only significantly bested by Mg-MOF-74 (5.4 mmol/g at 0.1 bar) [5]. Adsorption selectivities for CO₂ over N₂ were estimated using Ideal Adsorbed Solution Theory (IAST) for an idealized flue gas mixture composed of 0.15 bar CO₂ and 0.75 bar N₂, to be 72.0 and 73.6 for Cu-SSZ-13 and H-SSZ-13, respectively [3]. Gas uptake measurements indicate that the low-pressure CO₂ capacity and IAST selectivity relative to N₂ are not significantly impacted upon exchanging Cu-cations into the host SSZ-13 framework. We have further determined the key structural features of the host framework that result in the high uptake and selectivity.

SSZ-13 is composed of corner-sharing Al/SiO₄ tetrahedra that form double six-membered ring cages (see inset, Fig. 1). The cages are further connected to form a cavity with 8-membered windows (consisting of 8 O and 8 Si/Al) approximately 3.8 Å across, providing size-exclusion in the adsorption of gas molecules. Based on the potential bond distances and coordination, there are four suitable sites for Cu²⁺. The 6-ring window has been determined to be the only copper location in Cu-SSZ-13 (SiO₂/Al₂O₃ = 12) from NPD with a refined occupancy of 25 % Cu²⁺, as indicated by nuclear scattering density only in this region (Fig. 1). Rietveld refinement of NPD data obtained on the bare Cu-SSZ-13 reveals a Cu-O(1) distance of 2.24(1) Å to the three coordinate oxygen atoms. The potential of a second copper site at higher Cu²⁺ loadings than that presented here has been suggested from TPR and FTIR spectroscopy [6].

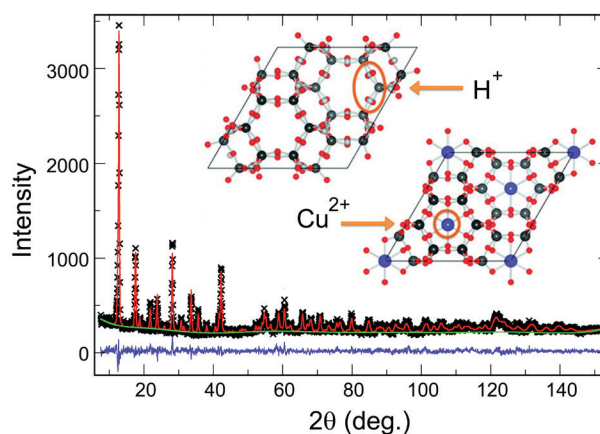


FIGURE 1: Representative NPD Rietveld refinement of the *in situ* gas loaded zeolite at a loading of 0.5 CO₂ per Cu²⁺ at 4 K (final goodness-of-fit $\chi^2 = 1.048$).

NPD data were further collected at sequential, *in situ* loadings of 0.5, 0.75, 1.0, 1.5, and 4.0 CO₂ molecules per Cu²⁺ cation [3]. Fourier difference maps allowed elucidation of CO₂ site positions and Rietveld refinements provided a final determination of atomic coordinates and CO₂ occupancy as a function of gas loading. At low CO₂ loadings there is preferential occupancy of the gas molecules at a single site (Site A) located in the center of the 8-ring window (Fig. 2). The CO₂ carbon is centered in the window such that O_{ring}-(C)-O_{ring} angle is equal to 180°. The closest CO₂-framework interactions include carbon to O_{framework}

¹ NIST Center for Neutron Research; National Institute of Standards and Technology; Gaithersburg, MD 20899-6102

² University of Maryland; College Park, MD 20742

³ University of California; Berkeley, CA 94720

⁴ University of Delaware; Newark, DE 19716

⁵ The Bragg Institute; Australian Nuclear Science and Technology Organisation; PMB1 Menai, NSW, Australia

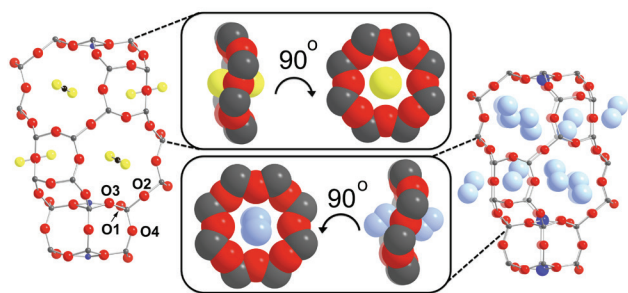


FIGURE 2: CO₂ adsorption at Site A (left, with oxygen labeling scheme) and N₂ adsorption site (right) as determined from NPD measurements of Cu-SSZ-13 at 4 K (yellow = oxygens; black = carbons; pale blue = nitrogens) for one complete cage. The positions of CO₂ and N₂ relative to the 8-ring cage windows are shown as a space-filling representation. It should be noted that figure represents only the adsorption sites and does not quantify the amounts of gas at each location; the actual occupancy is much greater for CO₂.

between approximately 3.2 Å to 3.5 Å. The CO₂ molecules, which are canted with respect to the c-axis, point towards the center of the small pore and away from the secondary adsorption site (Site B). Site B has end-on CO₂ coordination to the Cu²⁺ with Cu²⁺...O=C=O equal to 2.69(3) Å (at a 4.0 CO₂ per Cu²⁺ loading, Fig. 3). The observed canting angle allows the largest possible degree of separation between the CO₂ and framework oxygen atoms minimizing repulsive interactions between the framework and adsorbate. The O-O distances found between the ring window and CO₂ range from ≈ 3.4 Å to 3.8 Å for O_{framework} to O_{CO2}. The isotropic atomic displacement parameters (ADP) for CO₂ increase as the occupancy of the CO₂ in the window increases, which is likely indicative of some static disorder with higher loadings. Increasing the gas concentration from 0.5 to 1.5 CO₂ per Cu²⁺, increases the concentration of CO₂ in the window, but reveals no evidence of any nuclear density directly above the Cu²⁺, indicating that the window site is the preferred adsorption site. NPD of CO₂ in H-SSZ-13 loaded with 2.0 CO₂ per H⁺ (equivalent to ≈ 3.0 CO₂ per Cu²⁺) also results in CO₂ adsorption at the window site and is canted similarly into the pore. This type of CO₂-framework interaction is novel compared to that observed in other zeolites, such as cation-exchanged Y-zeolite, which have end-on CO₂ interacting with the cations, or NaX and H/Na-ZSM-5 where CO₂ molecules form carbonate-like species with framework oxygen atoms [3].

To determine specifics of the separation properties, we performed additional *in situ* N₂ diffraction for a loading of 1.5 N₂ per Cu²⁺ [3]. The N₂ is located to the side of the window at an angle of approximately 128° (O_{ring}-(N₂)-O_{ring}) whereas the CO₂ was centered (*i.e.*, 180°, Fig. 2). The closest N₂-framework interactions are approximately 3.1 Å to 3.5 Å from nitrogen to O_{framework}. The N₂ molecules, unlike the CO₂ molecules, do not orient perpendicular to the symmetry center of the 8-ring window. The ADPs for N₂ are large, suggesting that there is more disorder in the location of the N₂.

The origins of the overall high affinity for CO₂ versus N₂ in both forms of the zeolites determined here may stem from several

key factors. They are: (1) the small pore size in zeolite SSZ-13 restricts diffusion, (2) the pore window is an ideal diameter for adsorption of CO₂ and unoccupied by cations, and (3) the difference in electrostatic interactions between the gases and both the H⁺ and Cu²⁺ frameworks. In SSZ-13, the 3.8 Å pore window is too small for easy diffusion of N₂ (kinetic diameter, 3.64 Å), while CO₂ (3.30 Å) can more freely diffuse into the pores. This, coupled with the fact that the framework-CO₂ interaction is the ideal distance for adsorption in the window sites based on the van der Waals radii, leads to very high CO₂:N₂ selectivity in SSZ-13. Additionally, if we consider the difference in the quadrupole interactions between framework and CO₂ (quadrupole moment = 13.4×10^{-40} C m², polarizability = 26.3×10^{-25} cm³) and N₂ (quadrupole moment = 4.7×10^{-40} C m², polarizability = 17.7×10^{-25} cm³) over the “length” of the guest molecule, the result is a much stronger affinity for CO₂ over N₂ in the window site. This was demonstrated with density functional theory (DFT) calculations [3].

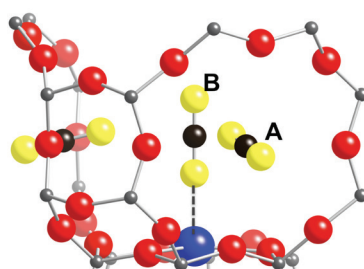


FIGURE 3: A cut-away view of the cage showing the primary (A) and secondary (B) CO₂ adsorption sites (black = carbons, yellow = oxygens) for the highest CO₂ dosing.

This newfound knowledge of CO₂-framework interaction directly mediated in the center of the 8-ring window has potentially broad applicability. The quadrupolar interactions should also be valid in the description of other zeolites with high selectivities and 8-ring windows. In the analogous zeolite CHA, albeit at differing Si/Al ratios, the CO₂ and N₂ adsorption in the Li, Na, and K exchanged derivatives follows a trend that is based on the properties of the cations (size and polarizability) [7]. Diffraction experiments, such as these, are able to determine the extent of this effect, if any, with different alkali metal content controlled by varying Si/Al₂ ratios. Through varying the Si/Al ratio, it may be possible to modify the Cu²⁺ content of SSZ-13, further tuning and enhancing the overall uptake *and* separation capacity. NPD combined with *in situ* gas dosing has proven ideal for systematic tuning of materials for industrial gas separation applications.

References

- [1] D.M. D'Alessandro, B. Smit, J.R. Long, *Angew. Chem. Int. Ed.* **49**, 6058 (2010).
- [2] E.D. Bloch, W.L. Queen, R. Krishna, J.M. Zadrozny, C.M. Brown, J.R. Long, *Science* **335**, 1606 (2012).
- [3] M.R. Hudson, W.L. Queen, J.A. Mason, D.W. Fickel, R.F. Lobo, C.M. Brown, *J. Am. Chem. Soc.* **134**, 1970 (2012).
- [4] D.W. Fickel, R.F. Lobo, *J. Phys. Chem. C* **114**, 1633, (2009).
- [5] W.L. Queen, C.M. Brown, D.K. Britt, P. Zajdel, M.R. Hudson, O.M. Yaghi, *J. Phys. Chem. C* **115**, 24915 (2011).
- [6] J.H. Kwak, H. Zhu, J.H. Lee, C.H.F. Peden and J. Szanyi, *Chem. Commun.* **48**, 4758, (2012).
- [7] F.N. Ridha, P.A. Webley, *Micro. Meso. Mater.* **132**, 22 (2010).

Evolving structure of the solid electrolyte interphase in Li-ion batteries characterized by *in situ* neutron reflectometry

J.A. Dura¹, J.E. Owejan², J.P. Owejan², and S.C. DeCaluwe³

Electrochemical energy storage is a critical component in efforts to transform our energy base from fossil fuels to modern renewable energy sources. Lithium ion batteries in electric and hybrid automobiles present the greatest potential for its large scale application. In these, economic considerations are driving ongoing research and development to improve durability and prevent capacity fade. At the extremely high anode chemical potential which provides Li-ion batteries with high energy and power density, the electrolyte decomposes, coating the electrode surface with a layer of lithium-containing compounds called the Solid Electrolyte Interphase (SEI). This reduces the available amount of active lithium and therefore the capacity of the cell. The SEI, however, passivates the surface, greatly reducing (though not completely eliminating) further electrolyte decomposition.

Despite its critical significance, structural characterization of the SEI is currently incomplete because of the highly reactive and delicate nature of both the SEI and the electrolyte. Many previous investigations have sought to understand the SEI layer, primarily by *ex situ* spectroscopy or microscopy techniques. It is essential to expand these measurements to study the growth, composition, thickness, and porosity of the SEI *in situ* as a function of operating conditions such as potential, temperature, age, depth and number of cycles, or selection of material components including electrolyte additives. Neutron reflectometry (NR) determines the depth profile of the scattering length density (SLD) which can be related to the composition profile. In particular, since it is sensitive to the light elements in SEI compounds, NR is ideal for *in situ* Li-ion battery studies. Additionally, isotopic differences in SLD for H and Li allow their accurate depth profiles and/or isotopic labeling of sources of these elements. Similarly, exchange of working fluids with different SLDs allows direct measurement of the porosity depth profile. This study highlights the first use of *in situ* NR to measure the SEI structure in a lithium battery [1].

NR data were taken using AND/R at the NCNR, first of the as-grown Cu cathode in the electrolyte-filled cell at open circuit voltage (OCV), *i.e.*, no current that would cause an SEI to grow was allowed (test point a-OCV). An SEI was then produced by running 10 cyclic voltamograms (CV), in which current is measured during a cyclic voltage sweep, followed by a hold at 250 mV during which NR data were again taken (test point

b-250). These two data sets (Fig. 1) show distinct differences in oscillation peak amplitude and position vs. Q_z due to the effects of the SEI layer on the scattering. A simultaneous fit of these data sets reveals that a temporary copper carbonate/hydroxide layer had formed on the initial unoxidized Cu surface. After the CV scans, the copper carbonate/hydroxide layer is removed and a single 4.0 nm (3.6 to 4.2) nm thick SEI layer is deposited with an SLD well below the level of the electrolyte, seen at the left in the inset to Fig. 1. (Numbers in parentheses are the 68 % confidence range).

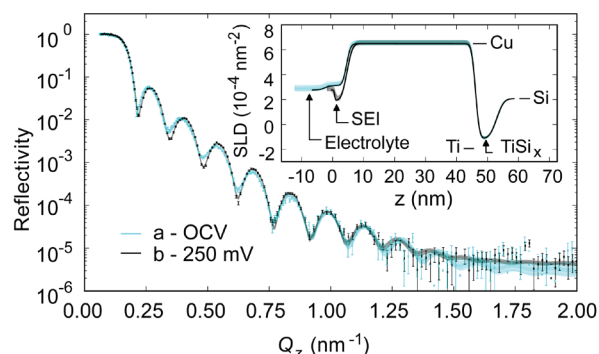


FIGURE 1: Neutron reflectivity vs. Q_z at a-OCV, open circuit voltage, and b-250 during a hold at 250 mV after 10 cyclic voltamograms. Solid lines are the best simultaneous fit to the two data sets. Inset – the best fits SLD profiles. Dark and lighter shaded regions are 68 % and 95 % confidence intervals, respectively.

The next test point c-150 was taken after 10 more CV cycles were run, followed by a hold at 150 mV. The SEI layer at test point c-150 is remarkably similar to the previous test point, b-250, but slightly thicker at 4.5 nm (4.0 to 4.7) nm due to the lower reduction potential and/or additional 10 CV cycles. Subsequently, six data sets (d-1000 through i-7) were taken at various potentials without further CV cycling, as summarized in the right inset to Fig. 2 which also shows representative CV curves taken throughout the experiments. The NR data for test points c-150 through i-7 each had excellent fits to a model that held all parameters at the same values determined from the simultaneous fit (Fig. 1), except the Cu and SEI thicknesses, the SEI SLD, and both interface widths surrounding the SEI. The resultant SLD profiles from these fits (along with test point b-250) are shown in Fig. 2. Key fitting parameters are summarized in Fig. 3.

¹ NIST Center for Neutron Research, National Institute of Standards and Technology, Gaithersburg, MD 20899-6102

² Electrochemical Energy Research Laboratory, General Motors, Honeoye Falls, New York 14472

³ Colorado School of Mines, Golden, CO, 80401

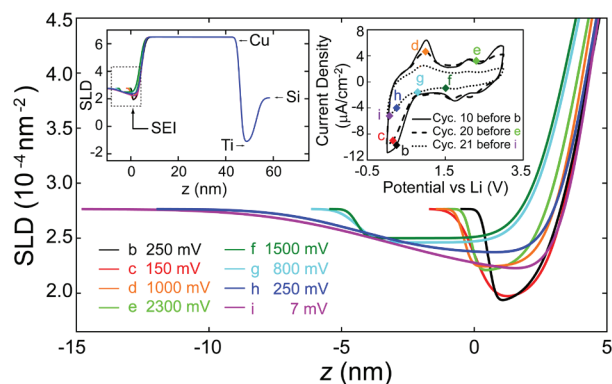


FIGURE 2: The SLD as a function of depth for the SEI region. The left inset shows the full SLD profile with the fits co-aligned on the Ti layer. The right inset shows selected CV scans. Test points b-250 to i-7 denote the location of potentiostatic holds for NR testing.

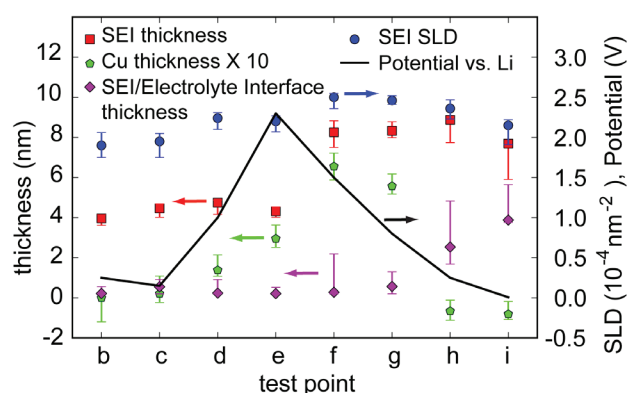


FIGURE 3: Selected fitting parameters and hold potential as a function of test point. Cu thickness is plotted relative to the thickness measured in test point a-OCV.

These fits and associated uncertainties clearly show that the SEI on the copper surface changes in both composition and thickness as a function of voltage. The SEI thickness grows steadily from b-250 to d-1000, from 3.96 nm to 4.75 nm, while the SLD increases, demonstrating that the SEI, originally rich in lithium, incorporates molecules with relatively less lithium. The layer shrinks slightly at e-2300 (*i.e.*, at 2300 mV), presumably due to the oxidation current and/or solubility of several molecules. After e-2300, stable for carbonate-based electrolytes, to f-1500, the SEI doubles in thickness and increases in SLD. There is little change when the potential is decreased at test point g-800.

The next two test points, h-250 and i-7, demonstrate increasing reduction of the SLD as the potential is lowered, indicating a net gain of lithium-containing or low density molecules. The large SLD gradients seen at the SEI/electrolyte interface in these last two test points can be interpreted in two ways. A one-layer interpretation shows the layer thickness roughly constant or slightly decreasing as the SLD decreases (in going from test point g-800 through i-7), which can be interpreted as that the SEI layer as a whole is substituting high SLD material (Li-poor or dense) with lower SLD material (Li-rich or less dense). Alternatively, examination of the SLD profile indicates a layer that increases in thickness from g-800 to h-250 and less so to i-7, wherein the low SLD material is added near the Cu interface. This composition

gradient interpretation would indicate that Li-rich material is added near the Cu interface while the already deposited material remains adjacent to the electrolyte and is roughened. This view is supported by the net charge accumulation (not shown) during these potential holds, indicating that molecules were added to the SEI. Future measurements employing Li isotopic substitution will be able to distinguish between these two possibilities.

The composition of the SEI was determined by x-ray photoelectron spectroscopy, XPS, obtained after the NR experiment. The amount of each component was adjusted within XPS variability to provide a composition model of the SEI consistent with the NR SLD and thickness. From the amount of each molecule the charge required to produce the SEI is calculated. The measured charge divided by modeled charge increases from 1.85 at test point b-250 to 5.39 at test point i-7. This is most likely due to the SEI molecules which have contributed to the charge accumulation and then have subsequently re-dissolved into the electrolyte.

In sum, a well-functioning electrochemical cell with electrode materials compatible with NR measurements has been developed and used to successfully measure the SEI for a range of potentiostatic holds. It has been demonstrated that NR is highly effective for investigating *in situ* growth and evolution of the SEI. These results are the first direct measurements of critical SEI properties (such as thickness, porosity, layer structures, gradients, and chemical composition) on an operating Li cell, without confounding experimental artifacts associated with ex situ techniques. These results include an SEI thickness of 4.0 to 4.5 nm for 10 to 20 CV cycles growing to 8.9 nm after a series of potentiostatic holds that approximates a charge/discharge cycle. The SLD profile of several test points indicates a lack of significant gradients, contrary to proposed structures in the literature. The SEI thickness grew most rapidly at the first test point that lies in the region of electrolyte instability. Due to its passivating nature, growth of the SEI thickness slowed subsequent to this, even at the lowest potentials examined. However, Li-rich molecules having a lower SLD substitute into the SEI at lower potentials, as demonstrated when moving from test points g-800 through i-7.

Future implications of this study include the capability to directly and quantitatively study SEI properties as a function of electrolyte composition (including additives), temperature, voltage, current, cycling and time, etc. In addition, the direct measurement of critical SEI parameters, both presented herein and in the future under various conditions, will lead to marked improvements in the accuracy of numerical simulations of processes in Li batteries involving the formation of and ion transport within the SEI. Taken together, such NR investigations will enable future systematic improvements for commercial device performance, affordability, and sustainability.

References

- [1] J.E. Owejan, J.P. Owejan, S.C. DeCaluwe, J.A. Dura, *Chem. Mater.* **24**, 2133 (2012).

Activated dihydrogen bonding to a supported organometallic compound

J.M. Simmons¹, T. Yildirim¹, A. Hamaed², D.M. Antonelli^{2,3}, M.I. Webb⁴, C.J. Walsby⁴

On-board hydrogen storage in fuel-cell-powered vehicles is a major component of the national need to achieve energy independence and protect the environment. Fundamental breakthrough discoveries in materials science will be required to achieve light-weight, low-volume, safe, economical and recyclable storage technology. The main obstacles in hydrogen storage are slow kinetics, poor reversibility and high dehydrogenation temperatures for the chemical hydrides, and very low desorption temperatures/energies for the physisorption materials such as metal-organic-frameworks or porous carbons. The optimum conditions for viable room temperature hydrogen storage require materials that possess isosteric heats of adsorption in between that of standard physisorbers and chemisorbers, typically in the (20 to 30) kJ/mol regime. Theoretical efforts have shown that the incorporation of transition metal atoms onto a porous support can provide such binding energies at multiple hydrogen molecule adsorption sites [1]. The origin of this surprising finding can be traced back to dihydrogen Kubas complexes in which charge transfer from metal d-orbitals to hydrogen antibonding orbitals controls the strength of the dihydrogen metal interaction and causes the H-H bond to elongate [2]. However, despite a very large number of theoretical efforts, there has been no direct experimental proof of these predictions. Here we highlight our work [3] presenting such evidence for dihydrogen-Ti binding on a silica-supported Ti(III) organometallic complex using detailed sorption and inelastic neutron scattering (INS) measurements. Our experimental findings are further supported by extensive density-functional theory (DFT) and reaction path calculations.

The sample (Ti-HMS) is formed by grafting tetrabenzyl-titanium onto a porous silica by attachment to the surface hydroxyls, then slowly heating to reduce the titanium to the +3 oxidation state as confirmed by electron paramagnetic resonance spectroscopy. Prompt Gamma Neutron Activation Analysis (PGAA) indicates 0.6 mmol titanium per gram of Ti-HMS. Given the highly heterogeneous nature of silica surfaces, there are a number of ways the titanium could bond to the surface, each of which can have important effects on the final dihydrogen state. To better understand the starting chemistries, we have studied the vibrational structure of Ti-HMS using the Filter Analyzer Neutron Spectrometer, and have compared the measurements to spectra calculated for energy minimized structures in several possible bonding motifs using DFT.

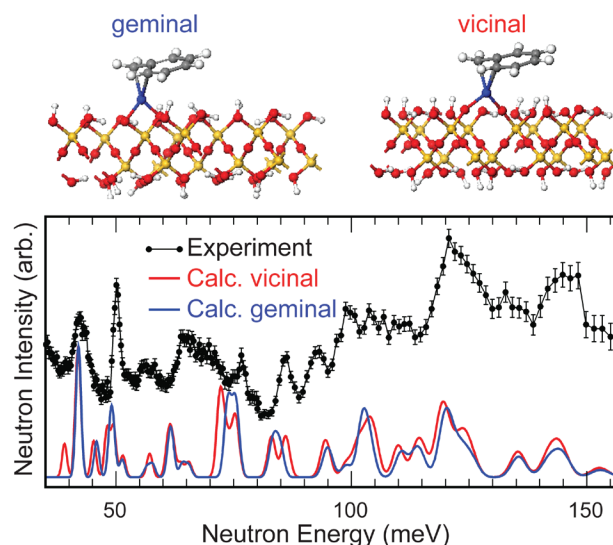


FIGURE 1: Experimental INS spectrum of the host Ti-HMS measured at 4 K as compared to the DFT calculated spectra. The computed energy-minimized structures are shown for two bonding arrangements, geminal and vicinal. In both structures, the highly reactive Ti(III) ion is protected by the benzyl ligand bending towards the ion, creating a steric hindrance to incoming reactants and acting like a gate.

In Fig. 1, we show two cases: geminal bonding, where the starting hydroxyls are attached to the same silicon atom, and vicinal bonding where the oxygens are on adjacent silicon atoms. Though the INS spectrum is dominated by the scattering from the benzyl ligand, it is subtly affected by the surface attachment. In both structures, the initially vertical benzyl ligand bends over to cover the Ti(III) ion, acting like a gate. It is believed that this shielding stabilizes the Ti(III) ion against surface hydrolysis reactions and is a critical component to the dihydrogen formation discussed below. For clarity, we will focus on the geminal attachment; other cases are presented in Ref. [3].

As shown in Fig. 2, low temperature adsorption of hydrogen leads to simple physisorption, with complete reversibility, modest isosteric heat of adsorption, ≈ 5.5 kJ/mol, and uptakes that are consistent with the ≈ 1100 m²/g apparent surface area. Physisorption is also apparent by INS investigations in which the Ti-HMS sample is exposed *in situ* to hydrogen at 50 K. After subtracting the bare Ti-HMS spectrum, the signal due to the adsorbed hydrogen shows weak molecular rotational peaks near 12.0 meV and 14.7 meV atop a large recoil background that

¹ NIST Center for Neutron Research; National Institute of Standards and Technology; Gaithersburg MD 20899

² University of Windsor; Windsor, ON, N9B 3P4 (Canada)

³ University of Glamorgan; Pontypridd CF37 1DL (UK)

⁴ Simon Fraser University; Burnaby, BC, V5A 1S6 (Canada)

comes from billiard-like scattering of weakly bound hydrogen molecules. Though hydrogen sorption is slightly improved over that of the bare silica, there is nothing to indicate the presence of a dihydrogen complex.

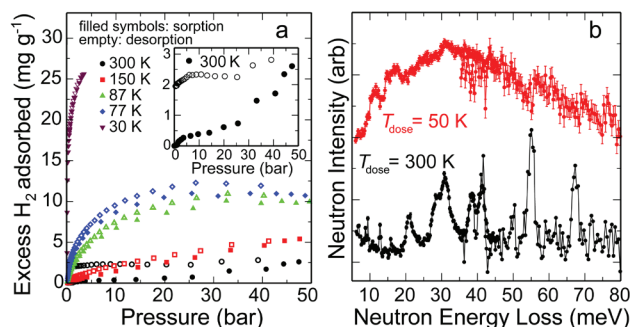


FIGURE 2: (a) Hydrogen sorption isotherms, and (b) background-subtracted INS spectra showing fully reversible physisorption at low temperature and partially irreversible sorption near room temperature. In (b), the INS spectrum of the low temperature adsorbed hydrogen is dominated by a weak rotational peak on top of a large recoil background, while the room temperature adsorbed hydrogen shows well-defined modes.

Surprisingly, sorption at room temperature shows *irreversible* behavior with a significant amount of hydrogen remaining after evacuation (Fig. 2a, inset). Approximately 1 mmol of H_2 per gram of Ti-HMS is retained corresponding to ≈ 1.6 hydrogen molecules per titanium atom, based on PGAA measurements. To confirm the irreversibility, Ti-HMS was exposed to room temperature hydrogen, briefly evacuated at room temperature to remove all physisorbed gas, and then cooled to 4 K for INS measurements. The difference is readily apparent in Fig. 2: the spectrum of the low temperature adsorbed hydrogen is dominated by hydrogen recoil, whereas the room temperature adsorbed hydrogen spectrum shows several well defined rotational/vibrational modes. Further, INS shows no loss of signal arising from the benzyl ligands and thus the additional features are due only to the adsorbed hydrogen. Critically for potential applications, the final complex is stable for long periods of time when stored near room temperature but can be removed under mild conditions. After storing the sample at room temperature for 40 days and evacuating to remove any desorbed hydrogen, the INS spectrum was quantitatively unchanged, and attempts to add more hydrogen at room temperature showed no increase in uptake. However, evacuating the sample at 350 K led to the release of all adsorbed hydrogen [3].

To understand the reversible physisorption at low temperature and irreversible adsorption at room temperature with mild desorption temperatures, and to probe the possibility that this behavior corresponds to the sought after dihydrogen complex, we turn again to DFT. In Fig. 3 we present reaction path calculations of the structure and relative energy as the hydrogen adsorbs from the gas phase. A hydrogen molecule starts far from the titanium and retains the unperturbed 0.76 Å bond length. As the hydrogen moves toward the titanium, there is an appreciable increase in the total energy of the system due largely to the

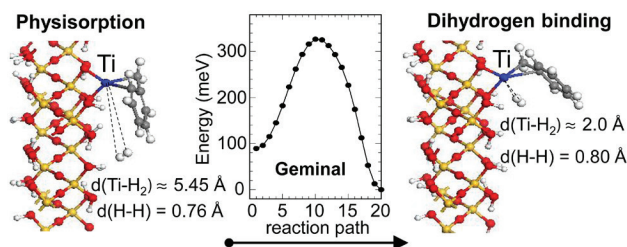


FIGURE 3: Relaxed molecular structures and relative energy as hydrogen adsorbs to form the dihydrogen complex. The short Ti—H₂ distance and H—H bond elongation are consistent with dihydrogen bonding. The dihydrogen complex is more stable than a physisorbed molecule and the calculated activation barrier is consistent with room temperature adsorption.

flexure of the benzyl ligand away from the titanium, opening the “gate”, leaving the highly reactive Ti(III) more exposed. Once the hydrogen is close enough to directly interact with the titanium, the energy sharply decreases and is accompanied by an elongation of the H—H bond from 0.76 Å to 0.8 Å. The final Ti—H₂ distance is around 2 Å and is much smaller than would be expected for physisorbed H₂. The H—H bond elongation and close proximity of the adsorbed hydrogen to the titanium are signatures of dihydrogen bonding. It is notable that the ≈ 240 meV activation barrier effectively prohibits low temperature formation of the dihydrogen state but allows for room temperature adsorption, and the dihydrogen state is more stable by ≈ 100 meV, enabling hydrogen release under modest heating.

To summarize, we have used inelastic neutron scattering, gas sorption and first principles DFT to show that specially prepared light transition metal complexes can support dihydrogen bonding, providing experimental support for earlier predictions. The close correlation between first principles DFT and INS lends strong support for the formation of the dihydrogen complex. The key obstacle to dihydrogen formation is the creation of a reduced transition metal adsorption site that is sufficiently stabilized through ligand control while not inhibiting the adsorption of hydrogen. In Ti-HMS, the flexibility of the benzyl ligand is important for stabilizing the Ti(III) ion, acting as a trap door/gate-keeper to the adsorption of hydrogen near room temperature. Once formed, the dihydrogen complex is quite stable, persisting for at least 40 days without loss of hydrogen but able to release the hydrogen under mild heating conditions. In light of these results, it is worth noting that in the search for new hydrogen storage materials, one should not limit measurements to 77 K (a common procedure) but should also check adsorption isotherms at room or higher temperatures for possible activated binding.

References

- [1] T. Yildirim and S. Ciraci, Phys. Rev. Lett. **94**, 175501 (2005).
- [2] G. J. Kubas, J. Organomet. Chem. **635**, 37 (2001).
- [3] J. M. Simmons, T. Yildirim, A. Hamaed, D. M. Antonelli, M. I. Webb, C. J. Walsby, Chem. – Eur. J. **18**, 4170 (2012).

Electronic delocalization in the correlation gap insulator LaMnPO

J. W. Simonson¹, D. E. McNally¹, Z. P. Yin^{1,2}, M. Pezzoli^{1,2}, J. Guo³, J. Liu⁴, K. Post⁵, A. Efimenko⁶, N. Hollmann⁶, Z. Hu⁶, H.-J. Lin⁷, C. T. Chen⁷, C. Marques¹, V. Leyva¹, G. Smith¹, J. W. Lynn⁸, L. Sun³, G. Kotliar², D. N. Basov⁵, L. H. Tjeng⁶, and M. C. Aronson^{1,9}

The unexpected discovery of high T_C superconductivity in cuprates suggests that the highest T_C s occur when pressure or doping transform the localized and moment-bearing electrons in antiferromagnetic insulators into itinerant carriers in a metal, where magnetism is preserved in the form of strong correlations. The absence of this transition in Fe-based superconductors may limit their T_C s, but even larger T_C s may be possible in their isostructural Mn analogs, which are antiferromagnetic insulators like the cuprates. LaMnPO is isostructural to superconducting LaFeAsO, with an insulating gap of ≈ 0.8 eV and a moment of $3.2 \mu_B/\text{Mn}$ attesting to strong Hund's rule correlations. Electronic structure calculations indicate that charge fluctuations are surprisingly large, suggesting proximity to electronic delocalization, and indeed delocalization occurs under quite modest pressures via two steps [1]. The insulating gap vanishes near 9 GPa, and the resulting antiferromagnetic metal is driven to a quantum critical point where the Mn moment collapses at ≈ 30 GPa (Fig. 1a). While these seem like large pressures, they correspond to a volume reduction of only 10 %, similar to the values required to induce superconductivity itself in some Fe-pnictide compounds.

Neutron diffraction and inelastic scattering show intriguing similarities of the magnetic structure and excitations of LaMnPO to those of its Fe-based superconducting relatives. Figure 1b shows that the Néel temperature T_N of LaMnPO is (375 ± 5) K. However, unlike the iron-based superconductors, charge doping in $\text{LaMnPO}_{1-x}\text{F}_x$ has little effect on either T_N or the ordered moment, which at $T = 0$ is $3.28 \mu_B/\text{Mn}$ in LaMnPO. The magnetic structure of tetragonal LaMnPO consists of ab planes where the Mn moments are arranged in an antiferromagnetic checkerboard pattern as shown in the inset of Fig. 1(b). Nearest-

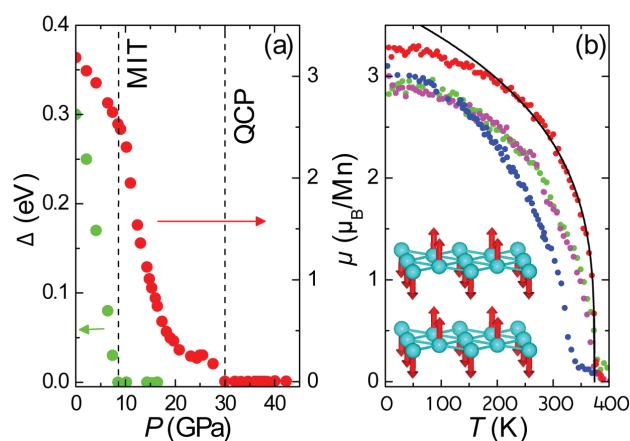


FIGURE 1: (a) The pressure dependencies of the band gap (green circles) and ordered Mn moment (red circles) in LaMnPO from LSDA calculations. Dashed line at 9 GPa indicates the metal-insulator transition (MIT) where the charge gap vanishes. Dashed line at 30 GPa (QCP) indicates full electronic delocalization, where the Mn moment and also antiferromagnetic order collapse. (b) Temperature dependencies of the ordered Mn moment μ_{AF} in $\text{LaMnPO}_{1-x}\text{F}_x$ for $x = 0$ (red), 0.07 (magenta), 0.10 (green), and 0.21 (blue), taken from the temperature dependence of the (100) magnetic peak in neutron diffraction measurements. The solid curve is a least-squares fit to the power law $M \sim (T_N - T)^\beta$ with an Ising-like exponent $\beta = 0.28 \pm 0.02$ (solid line). Inset: the magnetic structure of antiferromagnetic LaMnPO, where only the moment-bearing Mn moments are shown.

neighbor spins along the c -axis are parallel (ferromagnetic alignment) as previously reported [2]. This magnetic structure of tetragonal LaMnPO is more like that of the cuprates than the ones that are found in Fe-based superconductors, where the antiferromagnetic phase is orthorhombic and the magnetic order is stripe-like [3].

The magnetic susceptibility of LaMnPO is nearly temperature-independent up to 800 K, with no sign of antiferromagnetic

¹ Stony Brook University; Brook, NY 11794

² Rutgers University; , NJ 08854

³ Institute of Physics and Beijing National Laboratory for Condensed Matter Physics; Chinese Academy of Sciences; 100190, P. R. China.

⁴ Institute of High Energy Physics; Academy of Sciences; 100039, P. R. China

⁵ University of California San Diego; Jolla, CA 92093

⁶ Max-Planck-Institut für Chemische Physik fester Stoffe; D-01187 Dresden, Germany

⁷ National Synchrotron Radiation Research Center (NSRR); 101 Hsin-Ann Road; Hsinchu 30077, Taiwan

⁸ NIST Center for Neutron Research; National Institute of Standards and Technology; Gaithersburg, MD 20899

⁹ Brookhaven National Laboratory; Upton, NY 11973

order at 375 K. This suggests that LaMnPO is a system with very strong exchange interactions, and so inelastic neutron scattering measurements were carried out on a polycrystalline sample of LaMnPO using BT-7 to test this hypothesis. Energy scans performed around the antiferromagnetic wave vector $Q = 1.55 \text{ \AA}^{-1}$ are shown in Fig. 2(a). At low temperature we find a spin gap Δ of $\approx 7.5 \text{ meV}$, while the magnetic intensity above this energy is constant up to the highest energy of 25 meV probed in our experiment. This indicates a very steep spin wave dispersion in LaMnPO, consistent with an exchange interaction that is much larger than 25 meV. With increasing temperature the data in Figure 2a show that the intensity of the spin wave scattering increases as expected for the Bose population factor, while the spin gap decreases and vanishes at the Néel temperature. Thus in the paramagnetic state ($T > T_N$) the gapped spin wave scattering is replaced by strong quasielastic scattering centered at the antiferromagnetic wave vector, as is found in some of the Fe-pnictide superconductors [4]. Figure 2b demonstrates that strong short-ranged correlations persist well into the paramagnetic state, indicating that this paramagnetic scattering in LaMnPO is emphatically not that of individual Mn moments, but rather reflects the dynamical correlations of strong exchange coupled Mn-moments.

Pressure dependent x-ray diffraction measurements of the structure have been carried out, and electronic band calculations based on these crystallographic results were performed to determine the effects of pressure on the electronic structure and charge and spin correlations. Surprisingly, it was revealed that only modest pressures of 9 GPa are required to transform LaMnPO from an antiferromagnetic insulator to a metallic antiferromagnet [1]. Moreover, the calculated magnetic moment above an orthorhombic distortion observed at 16 GPa becomes less than $1 \mu_B$. These properties are in striking analogy to the isostructural metallic iron-based superconducting host LaFeAsO, which undergoes a tetragonal-to-orthorhombic structural transition with temperature followed by antiferromagnetic ordering with an ordered moment of only $0.35 \mu_B$ [3]. A second transition is predicted to occur at 30 GPa, where the complete collapse of the magnetic moment occurs [1]. The proximity to these charge and moment delocalization transitions in LaMnPO results in a metallic state with highly correlated electrons, the familiar breeding ground of superconductivity.

How promising are Mn-based compounds as potential superconductors? Superconductivity is achieved in compounds where the interactions are exquisitely balanced between metal and insulator, and where magnetic order is on the verge of complete destruction. Our neutron scattering measurements show an unexpected degree of similarity between the magnetic structure and spin excitation spectrum of LaMnPO and the

Fe-pnictide superconductors. Achieving higher T_C may require something more. Perhaps the cuprates have higher T_C s than the Fe-pnictides because the spin correlations in the cuprates are strong enough to make them insulating in the absence of doping. The present work suggests that electron correlations in the Mn-pnictides are very strong and may be even stronger than the cuprates, indicating that Mn-based compounds like LaMnPO could provide a new avenue to superconductivity, and perhaps with higher T_C s than currently available.

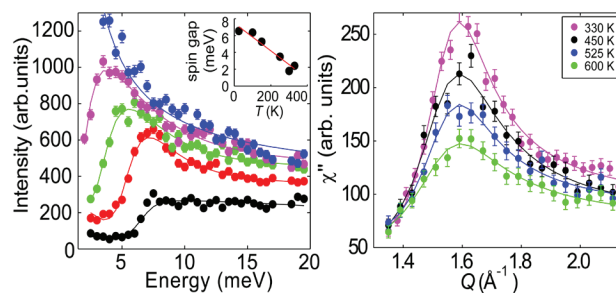


FIGURE 2: (a) Energy dependence of the magnetic intensity for $Q_{AF} = 1.55 \text{ \AA}^{-1}$ (the (100) antiferromagnetic wave vector) at different temperatures (black: 25 K, red: 150 K, green: 250 K, purple: 330 K, blue: 355 K). At low T there is a spin gap of 7.5 meV, while the magnetic intensity above this energy is constant indicating very steep spin wave dispersion. The intensity increases with increasing temperature due to the thermal population factor, while the gap decreases. Inset: temperature dependence of spin gap Δ . (b) Wave vector dependencies of the scattered intensity for fixed $E = 15 \text{ meV}$ at different temperatures above and below the antiferromagnetic order temperature $T_N = 375 \text{ K}$, indicating that very strong spin correlations persist in the paramagnetic state. The observed asymmetry of the scattering is due to a second antiferromagnetic wave vector (101) at 1.71 \AA^{-1} . Data were obtained using the BT-7 triple axis spectrometer.

References

- [1] J.W. Simonson, Z. Yin, M. Pezzoli, J. Guo, J. Liu, K. Post, A. Efimenko, N. Hollmann, Z. Hu, H.-J. Lin, C.T. Chen, C. Marques, V. Leyva, G. Smith, J.W. Lynn, L. Sun, G. Kotliar, D.N. Basov, L.H. Tjeng, and M.C. Aronson, *Proceedings National Academy of Science* **109**, 10751 (E1815) (2012).
- [2] H. Yanagi, T. Watanabe, K. Kodama, S. Iikubo, S-I. Shamoto, T. Kamiya, M. Hirano, and H. Hosono, *J. Appl. Phys.* **105**, 093916 (2009).
- [3] C. de la Cruz, Q. Huang, J.W. Lynn, J. Li, W. Ratcliff II, J.L. Zarestky, H.A. Mook, G.F. Chen, J.L. Luo, N.L. Wang, and P. Dai, *Nature* **453**, 899 (2008).
- [4] M. Wang, X.C. Wang, D.L. Abernathy, L.W. Harriger, H.Q. Luo, Y. Zhao, J.W. Lynn, Q.Q. Liu, C.Q. Jin, Chen Fang, J. Hu, and P. Dai, *Phys. Rev.* **B83**, 220515(R) (2011).

Spin-orbital short-range order on a honeycomb-based lattice

S. Nakatsuji¹, K. Kuga¹, K. Kimura¹, R. Satake², N. Katayama², E. Nishibori², H. Sawa², R. Ishii³, M. Hagiwara³, F. Bridges⁴, T. U. Ito⁵, W. Higemoto⁵, Y. Karaki⁶, M. Halim⁷, A. A. Nugroho⁷, J. A. Rodriguez-Rivera^{8,9}, M. A. Green^{8,9}, C. Broholm^{8,10}

A spin liquid within a solid is a state of matter without static spin order at low temperatures, despite strong interactions between local magnetic moments on a lattice. It is thought that competing (frustrated) interactions can lead to this order, but no definite realization on a 2D honeycomb lattice has been documented. Magnetically frustrated $\text{Ba}_3\text{CuSb}_2\text{O}_9$ has some of the anticipated characteristics. Inelastic neutron scattering is gapless at a resolution of 0.2 meV but shows no temperature dependent elastic scattering between 25 K and 1.5 K. This indicates that spins in $\text{Ba}_3\text{CuSb}_2\text{O}_9$ do not develop static order but remain in a fluctuating quantum state to the lowest temperatures [1].

The structure of $\text{Ba}_3\text{CuSb}_2\text{O}_9$ was determined by synchrotron x-ray and neutron diffraction from single crystals and powder samples to be $P6_3/mmc$, different from a previously reported structure [2,3]. Inside, there is a 6H perovskite substructure with Cu-Sb “dumbbell” ordering (Fig. 1). This structure is oriented along the c axis connected through corner-sharing SbO_6 octahedral and Ba counterions.

The dominant super-exchange interactions in the resulting structure are associated with Cu-O-O-Cu pathways. In Fig. 1 we identify $J(1)$ and $J(2)$ as the largest interactions, thanks to the σ bonding component of O 2p-2p hybridization. For the same reason, $J(3)$ is an order of magnitude smaller due to the absence of O-O σ bonding. The resulting interactions give us a quasi-two-dimensional spin orbital system with the Cu^{2+} forming a honeycomb lattice with identical nearest-neighbor interactions. The out of the plane Cu' site in the “dumbbell” structure forms a frustrated isosceles spin triangle interacting via $J(2)$ with two Cu atoms in the hexagonal (honeycomb) structure.

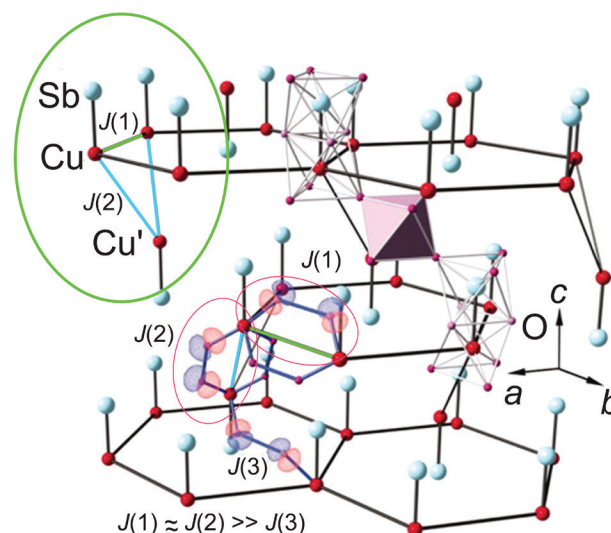


FIGURE 1: $\text{Ba}_3\text{CuSb}_2\text{O}_9$ structure (Ba removed for clarity) showing the 2D honeycomb lattice with Cu-Sb “dumbbells”. The O 2p orbitals controlling $J(1)$ (green) and $J(2)$ (blue) super-exchange magnetic coupling between Cu ions (within the pink circles) are shown as colored blobs. The disordered structure results from frozen-in frustrated interactions between the Cu and Cu' ions on the isosceles triangles (in the green circle) that propagate the disorder into the Cu ions on the honeycomb.

Depending of the stoichiometry, the sample is susceptible to a Jahn-Teller (JT) type transition. For example, if the Cu/Sb stoichiometry differs from 2/1 by $\approx 10\%$, the compound displays a JT type transition from hexagonal to orthorhombic at $T \approx 200$ K. Those samples become orthorhombic at low temperatures. For samples with $\text{Cu/Sb} \approx 1$ the synchrotron x-ray diffraction data show that the majority phase is hexagonal at $T = 12$ K. The same data for $T < 30$ K show subtle remnants of the JT- distorted orthorhombic phase.

¹ University of Tokyo; Kashiwa, Chiba 277-8581, Japan

² Nagoya University; Nagoya 464-8603, Japan

³ KYOKUGEN; Osaka University; Toyonaka, Osaka 560-8531, Japan

⁴ University of California; Santa Cruz, CA 95064

⁵ Advanced Science Research Center; Japan Atomic Energy Agency; Tokai, Ibaraki 319-1195, Japan

⁶ University of the Ryukyus; Nishihara, Okinawa 903-0213, Japan

⁷ Institut Teknologi Bandung, Jl; Ganesha 10, Bandung 40132, Indonesia

⁸ NIST Center for Neutron Research; National Institute of Standards and Technology; Gaithersburg, MD 20899

⁹ University of Maryland; College Park, MD 20742

¹⁰ Johns Hopkins University; Baltimore, MD 21218

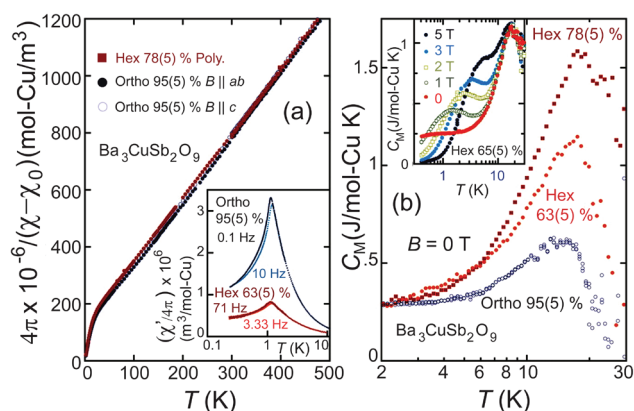


FIGURE 2: (a) Inverse susceptibility $1/(\chi - \chi_0)$ as a function of temperature for polycrystalline hexagonal and single crystal orthorhombic samples for applied fields along [100] and [001]. The diamagnetic contribution is $\chi_0 \approx -4\pi \times 10^{-10} (\text{m}^3/\text{mol-Cu})$. Inset: χ vs T at two frequencies for these samples. (b) Magnetic specific heat C_M as a function of T at zero field and (inset) non-zero fields. The data indicate that hexagonal samples have more degrees of freedom than orthorhombic ones, consistent with enhanced spin fluctuations.

Susceptibility measurements for the hexagonal samples (Fig. 2a) indicate magnetic isotropy. In the hexagonal phase for $300 \text{ K} < T < 600 \text{ K}$, the Curie-Weiss fitting consistently yields an effective moment, $P_{\text{eff}} = 1.87 \mu_B$ and $g \approx 2.15$ for both single crystal and polycrystalline samples. The single crystal samples shows a Curie-Weiss temperature $\Theta_W = -42 \text{ K}$ in both field directions and $\Theta_W = -47 \text{ K}$ for polycrystalline samples. Using $[(-z)/3]/S(S+1)$ with $-z = 10/3$ and $S = 1/2$, this yields $J(1) \approx J(2) = 52 \text{ K}$ which are typical values for Cu-O-O-Cu super-exchange. Fig. 2b shows the electronic specific heat C_M as a function of the temperature. At 5 T, the field induces a Schottky anomaly, which indicates that a significant part of the low- T specific heat can be associated with orphan spins found in all samples. The zero-field peak at 20 K, in the hexagonal samples indicates enhanced fluctuations on an energy range that approximately matches the spin exchange constants.

Fig. 3 shows inelastic neutron scattering data taken at MACS on a powder sample at different temperatures. $\tilde{S}(Q, \omega)$ is the spherically averaged dynamic spin correlation function. The data (Fig. 3e) shows direct evidence for a peak in the magnetic excitation at $\approx 6 \text{ meV}$ (70 K) near the values of $J(1) \approx J(2) = 54 \text{ K}$ indicated by the susceptibility data. The low T spectrum (Fig. 3c) appears to be gapless at the MACS resolution of $\approx 0.2 \text{ meV}$. Low T (1.4 K) elastic neutron scattering data subtracted from high T (25 K) data do not show a frozen moment developing between these temperatures. Figure 3d solid lines are the fit to a single-dimer correlation function. The wave vector dependence was obtained under the assumption of a separable dynamic correlation function, $\tilde{S}(Q, \omega) = \tilde{S}(Q) f(\omega)$, and averaging the data from 1.5 meV to 10 meV.

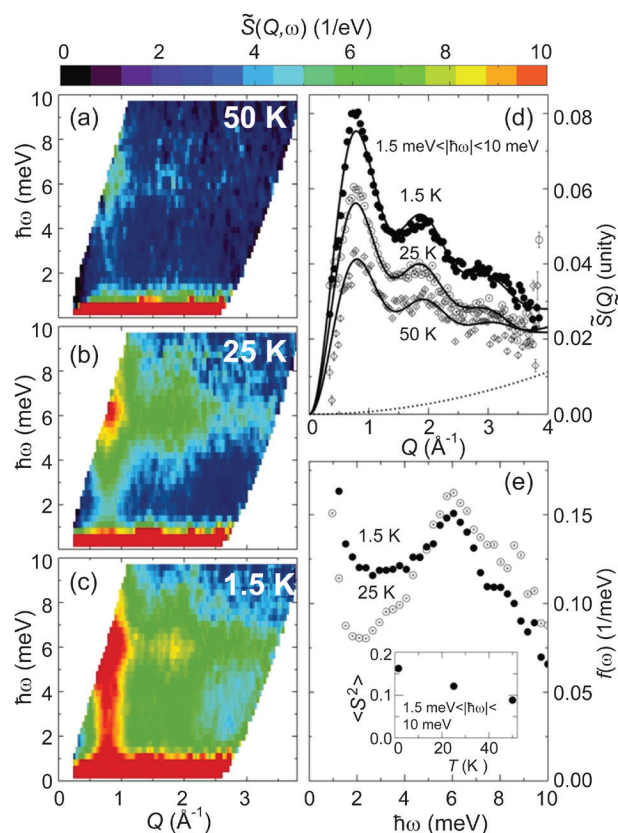


FIGURE 3: Inelastic neutron scattering from polycrystalline $\text{Ba}_3\text{CuSb}_2\text{O}_9$ at $T = 1.5 \text{ K}$, 25 K and 50 K (with inferred diffuse scattering subtracted). $\tilde{S}(Q, \omega)$ is the spherically averaged dynamic spin correlation function, Q the wave vector and $\hbar\omega$ the energy transfer. The data in (e) show direct evidence for a peak in the magnetic excitation spectrum at $\approx 6 \text{ meV}$ (70 K), near the values of $J(1) \approx J(2) = 54 \text{ K}$ indicated by the susceptibility data.

We conclude that the unit cell averaged spin and orbital configuration for $\text{Ba}_3\text{CuSb}_2\text{O}_9$ retains hexagonal symmetry and does not develop a frozen moment at very low temperatures despite its being magnetically and structurally anisotropic on atomic length scales. The neutron scattering data also show a near-neighbor singlet formation with a range of coupling strengths that peaks near $J(1) \approx J(2)$. One explanation of this behavior is local static JT distortions not affecting the overall hexagonal geometry with a static orbital disorder that is seeded by the Cu'-Cu coupling; another explanation would be a dynamic JT distortion. The experiments done cannot identify which explanation is correct, but they have unveiled a new disordered magnetic structure on a honeycomb lattice.

References

- [1] S. Nakatsuji *et al.*, Science **336**, 559 (2012).
- [2] V.P. Köhl, Z. Anorg. Allg. Chem. **442**, 280 (1978).
- [3] H.D. Zhou *et al.*, Phys. Rev. Lett. **106**, 147204 (2011).

Common origin of the two types of magnetic excitations in iron chalcogenide superconductors

Songxue Chi,^{1,2} J. A. Rodriguez-Rivera,^{1,2} J. W. Lynn,¹ Chenglin Zhang,³ D. Phelan,¹ D. K. Singh,^{1,2} R. Paul,⁴ and Pengcheng Dai^{3,5}

To participate in superconductivity, electrons need help to overcome their natural repulsion for each other to form bound Cooper pairs. In conventional superconductors, this help comes from lattice vibrations, or phonons, but for the superconductivity found in ‘high- T_C ’ copper oxides (cuprates), the transition temperature to superconductivity, T_C , below which superconductivity sets in, is too high to be supported by phonons. The parent compounds of cuprates are insulating and antiferromagnetically (AFM) ordered, while superconductivity arises when holes or electrons are introduced through doping, with the AFM order suppressed. Mounting evidence has pointed to robust spin fluctuations as the pairing glue, yet how the electrons pair up in the high- T_C superconductors (HTSCs) has yet to be resolved despite three decades of research. In 2008 a new class of Fe-based HTSCs was discovered, and again magnetism was found to play an essential role in the superconductivity, while the nature of the magnetism itself remains controversial. The work highlighted here explores the character of the magnetic spin fluctuations of the iron chalcogenides, and reveals two different components of the excitations that are found to be intimately connected to each other rather than separate as previously thought.

The Fe superconductors can be classified into two groups: the ferropnictides (iron plus a column VB element of the periodic table) and ferrochalcogenides (iron plus a VIB element). The parent compounds of the two groups have many things in common: They have similar crystal structures; both are metallic and have similar Fermi surface (FS) topologies that control both the magnetic and electrical properties. Yet the AFM magnetic structures, and the associated spin excitations, of the two classes are quite different. The pnictides have a single stripe collinear AFM arrangement characterized by the vector $(0.5, 0.5, 0.5)$ in momentum space. This is expected for the type of magnetism originating from itinerant conduction electrons through the mechanism of FS nesting. Fe_{1+y}Te , on the other hand, has a diagonal double-stripe bicollinear order modulated along the $(0.5, 0, 0.5)$ direction [1], which is 45° away from FS nesting wave vector. Additionally, the ordered moment in Fe_{1+y}Te is much bigger— $2 \mu_B$ in contrast to less than $1 \mu_B$ in the pnictides. Such a large moment has fueled debates over whether the nature of the

magnetism in ferrochalcogenides originates from local moments, itinerant electrons, or both.

The Fe_{1+y}Te ‘parent’ system becomes superconducting when Te is replaced by Se. With doping the magnetic long range order is suppressed, while two types of collective spin excitations are observed. One set of excitations occurs in the low energy regime at the commensurate (CM) $(0.5, 0, 0)$ wave vector position, while the other type consists of very energetic incommensurate (ICM) excitations (up to 200 meV) located around the $(0.5, 0.5, 0)$ position. It was thought that these two types of excitations might arise from separate phases due to chemical inhomogeneity, impurity, or phase separation that exists in these materials, but we found that both types of excitations have a common origin and occur in the same phase.

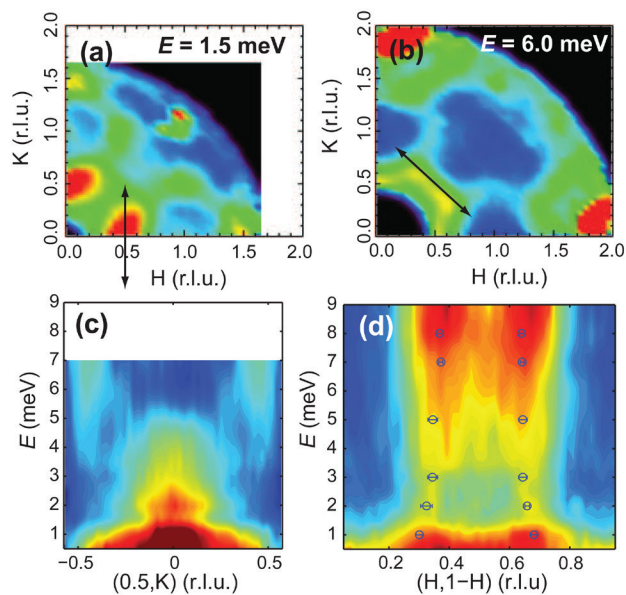


FIGURE 1: Contour plots of neutron scattering intensity in the $(H, K, 0)$ plane at energy transfers of (a) 1.5 meV (b) 6.0 meV. The data were collected at $T = 1.5$ K on MACS. The arrows in (a) and (b) show the directions of the spectral intensities plotted in (c) and (d), respectively. The open circles (d) are high resolution SPINS data that reveal the ‘hour-glass’ dispersion characteristic of high temperature superconductors.

¹ NIST Center for Neutron Research, National Institute of Standards and Technology, Gaithersburg, Maryland, 20899-6102

² Department of Materials Science and Engineering, University of Maryland, College Park, Maryland, 20742

³ Department of Physics and Astronomy, The University of Tennessee, Knoxville, Tennessee 37996-1200

⁴ Materials Measurement Laboratory, National Institute of Standards and Technology, Gaithersburg, Maryland, 20899-6102

⁵ Beijing National Laboratory for Condensed Matter Physics, Institute of Physics, Chinese Academy of Sciences, Beijing, 100190, China

In order to investigate the relationship between the two types of magnetic excitations, single crystals of moderately doped non-superconducting $\text{Fe}_{1.01}\text{Te}_{0.72}\text{Se}_{0.28}$ were used for this study. The actual compositions of the samples were determined with prompt gamma activation analysis (PGAA). Neutron scattering measurements were performed on the cold neutron MACS and SPINS spectrometers and the BT-7 thermal triple axis spectrometer.

At low-energy transfers the CM type excitation is dominant with a broad peak at $(0.5,0,0)$, as shown Fig. 1(a). As the energy increases the CM type scattering quickly diminishes in intensity while the two ICM peaks around $(0.5,0.5,0)$ start to appear and intensify (Fig. 1(b)). At various energies, we performed cuts along $[0.5,K]$ through the centers of both $(0.5,0,0)$ and $(0.5,0.5,0)$, which enabled us to track the evolution of the two excitations simultaneously. Constant- E cuts in the transverse $[H,1-H]$ direction through $(0.5,0.5,0)$ were also conducted, which yielded two symmetric ICM peaks, giving the dispersion of the ICM excitation. The combinations of these two cuts as a function of energy are shown in Figs. 1(c) and 1(d). Remarkably, the data reveal that there is a clear reciprocal interplay between the two types of spin excitations; the sudden disappearance of the CM excitation at around 6 meV is directly correlated with the energy where the twin ICM peaks increase spectral weight. Above about 7 meV the spectral weight is constant, which indicates that the gap of the ICM excitations below 7 meV is not compensated by spectral gain at higher energies at the same wave vector. This again indicates that spectral weight is transferred between the two wave vectors and that the CM spectrum is at the cost of the ICM spectrum. Clearly, the spectral weight for these two types of excitations is inversely correlated, which rules out electronic phase separation or magnetic inhomogeneity as the origin of the two types of magnetic correlations.

The connection of the CM and ICM excitations is clearly revealed by the behavior as a function of temperature. The $(H,K,0)$ planar maps have been obtained at different temperatures between 1.5 K and 308 K for four typical energy transfers, one of which is shown in Fig. 2. Both types of magnetic correlations are so robust that they maintain their well-defined features up to the highest measured temperature for all the energy transfers. On warming, the CM spectrum at $E = 1$ meV (Fig. 1(a)) starts to gain intensity at about 60 K, where the static order disappears, reaches its maximum at about 80 K and gradually decreases at higher temperatures. The ICM spectrum around $(0.5,0.5)$, however, is clearly gapped below the transition temperature of the static AFM order. The similar T dependencies of the scattering in the paramagnetic phase ($T > 60$ K) further confirms that these two types of spin excitations are of the same nature.

Another conspicuous feature in Fig. 1(d) is the dispersion toward $(0.5,0.5,0)$ below 3 meV before its steep outward dispersion. The result of high wave vector resolution measurements on SPINS is over-plotted in Fig. 1(d), which confirms this hourglass-shaped

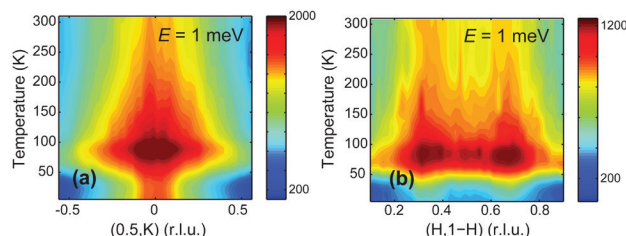


FIGURE 2: Temperature dependence of the (a) CM and (b) ICM spectra at an energy transfer of 1 meV.

dispersion as a characteristic feature of the highly correlated spin excitations found in the high- T_C class of superconductors.

Now that we know that the two types of excitations have a common origin, suppressing the CM-type correlations through doping Se cannot be simply understood as eliminating a coexisting phase. Rather, one has to treat the two excitations as one problem when trying to reveal the driving force for magnetism and superconductivity. In this sense, itinerant conduction electrons alone may not be able to provide a complete answer. The FS nesting describes the main features of the ICM excitations such as the hourglass dispersion near $(0.5,0.5,0)$, but the FS near the X point does not appear to support the nesting scenario for the CM excitation. In a local moment picture, the magnetic ground state is governed by the coupling between magnetic ions through non-magnetic ions. The contest between the collinear and bi-collinear order is controlled by the competition between magnetic couplings at different sites, which have different Te/Se height dependencies. As Se replaces Te, the chalcogen height is reduced, which results in a less-favored bi-collinear CM order. The spin-wave spectrum centered at $(0.5,0,0)$ that extends up to 60 meV in undoped FeTe is suppressed to lower energies, and is completely taken over by the ICM magnetism as the Se content increases well into the superconducting region. This scenario is supported by the reciprocal interplay between the two types of excitations and the temperature dependence presented in this study. However, it is not possible to understand the low-energy features such as the hourglass dispersion and the abnormal change of intensity and linewidth for the $(0.5,0,0)$ CM spectrum with just a local spin picture. Our results call for a more unified mechanism that reconciles these features and embraces the two types of excitations as having a common origin.

References

- [1] W. Bao, Y. Qiu, Q. Huang, M. A. Green, P. Zajdel, M. R. Fitzsimmons, M. Zhernenkov, S. Chang, M. Fang, B. Qian, E. K. Vehstedt, J. Yang, H. M. Pham, L. Spinu, and Z. Q. Mao, *Phys. Rev. Lett.* **102**, 247001 (2009).
- [2] O. J. Lipscombe, G. F. Chen, C. Fang, T. G. Perring, D. L. Abernathy, A. D. Christianson, T. Egami, N. Wang, J. Hu, and P. Dai, *Phys. Rev. Lett.* **106**, 057004 (2011).
- [3] M. D. Lumsden, A. D. Christianson, E. A. Goremychkin, S. E. Nagler, H. A. Mook, M. B. Stone, D. L. Abernathy, T. Guidi, G. J. MacDougall, C. de la Cruz, A. S. Sefat, M. A. McGuire, B. C. Sales and D. Mandrus, *Nature Phys.* **6**, 182 (2010).

Correlation between spin-flop transition and enhanced spin polarized supercurrents in ferromagnetic Josephson junctions

C. Klose¹, T.S. Khair¹, Y. Wang¹, W.P. Pratt¹, N.O. Birge¹, B. J. McMorran^{2,3}, J. A. Borchers⁴, T. Ginley⁵, B.J. Kirby⁴, B.B. Maranville⁴, J. Unguris²

Production of spin-polarized superconducting currents (“supercurrents”) that can propagate over long distances opens up new possibilities for the development of low-energy, magnetoelectronic devices that combine magnetic storage and data manipulation with conventional semiconductor electronics. Though the typical penetration depth of a superconducting current into a normal metal is on the order of microns, the Cooper pair correlations persist for only a few nanometers when a conventional, spin-singlet (*i.e.*, zero total spin) superconductor is brought in contact with a strong ferromagnet. Recent experiments, however, have demonstrated that the addition of magnetic inhomogeneities at the superconductor/ferromagnet interface give rise to a spin-polarized supercurrent with spin-triplet (*i.e.*, total spin of one) symmetry that can be sustained over large lengthscales. In particular, research performed at Michigan State University [1] focused on a multilayer Josephson junction with a central Cu/Co/Ru/Co/Cu block surrounded by thin ferromagnetic alloy (PdNi or CuNi) layers adjacent to the superconducting Nb electrodes at the top and bottom. The misalignment of the ferromagnetic Co layers relative to the alloy layers was the source of the magnetic non-uniformity, and the Co sandwich also acted to suppress the spin-singlet current, even though it has no net magnetization due to the antiparallel alignment of the Co across the intervening Ru. The simple device design provided a means to reproducibly create a spin-triplet supercurrent at low temperatures that can be easily tuned by changing parameters such as the thickness of the Co or alloy layers.

More recent experiments on similar junctions revealed that the supercurrent can be enhanced by up to a factor of 20 simply by applying a large (> 0.1 T to 0.2 T), in-plane magnetic field [2]. Since misalignment of the ferromagnet magnetizations is crucial to the production of the spin-triplet state, the speculation was that the dramatic increase originates from a field-induced change in the magnetic configuration of the antiferromagnetically-coupled Co/Ru/Co sandwich in the junction center. To explore this enhancement we used the complementary techniques [2] of polarized neutron reflectivity (PNR) and scanning electron microscopy with polarization analysis (SEMPA) to characterize the magnetic structure of half junctions [Si substrate/Nb(150 nm)/Cu(10 nm)/Co(X nm)/Ru(0.6 nm)/Co(X nm)/Cu(10 nm)] before, during, and after applying magnetic fields of

varying strength. PNR nondestructively probes the ensemble average of the net in-plane magnetization for each ferromagnetic layer, even in the presence of a field. When combined with ion milling, SEMPA images the remanent magnetization of the in-plane domains within each ferromagnetic layer. Together these measurements revealed that the large magnetic field acts to flip a large fraction of the magnetization in the Co layers nearly perpendicular to the field and to the magnetizations of the thin alloy layers in the full Josephson junction. The local magnetic environment is thus more ideal for producing, sustaining and propagating the spin-polarized supercurrent.

Several samples were examined for this study, and all showed qualitatively similar behavior. For illustration, we focus here on a sample with $X = 6$ nm that was characterized fully at room temperature before and after applying a 0.3 T field. In the PNR measurements performed on the NG-1 Reflectometer, the nonspin-flip cross sections (R^{++} and R^{--}) are sensitive to the nuclear structure as well as the projection of the net magnetization parallel to the guide field direction. The spin-flip cross sections (R^{+-} and R^{-+}) originate solely from the projection of the total magnetization perpendicular to the field. The data were all fit (solid lines) using the REFL1D software package [3] in order to extract the depth-dependent structure and vector magnetization.

Figures 1a and 1b show the PNR data for the as-grown sample, both upright (*i.e.*, bare sample edge vertical) and rotated by approximately 90° , in a guide field of 0.003 T. For the upright configuration, the spin-flip cross sections in Fig. 1a are small, but nonzero, consistent with a slight canting of the Co layer magnetizations relative to the field. The R^{++} and R^{--} cross sections are dominated by structural scattering, but exhibit an unexpected splitting resulting from a small net magnetization along the guide field. In order to remove the structural scattering contribution, we rotated the sample relative to the guide field (Fig. 1b) in order to transfer the scattering from the magnetization component parallel to the bare edges from the non-spinflip to the spin-flip channels. The shape of the resultant spin-flip scattering is distinct and can only be reproduced by a model [3] with nearly perfect antiparallel alignment of the two Co layers. Simultaneous fits to the data in Figs. 1a and 1b reveal that the magnitude of the net magnetizations of the top and bottom Co layers are (822 ± 25)

¹ Michigan State University; East Lansing, MI 48824

² Center for Nanoscale Science and Technology; National Institute of Standards and Technology; Gaithersburg, MD 20899

³ University of Oregon; Eugene, OR 97403

⁴ NIST Center for Neutron Research; National Institute of Standards and Technology; Gaithersburg, MD 20899

⁵ Juniata College; Huntingdon, PA 16652

kA/m and (722 ± 25) kA/m, respectively. The magnetization axes, shown in the schematics, are tilted at an angle of approximately 25° relative to the sample edge, suggestive of a growth-induced anisotropy direction.

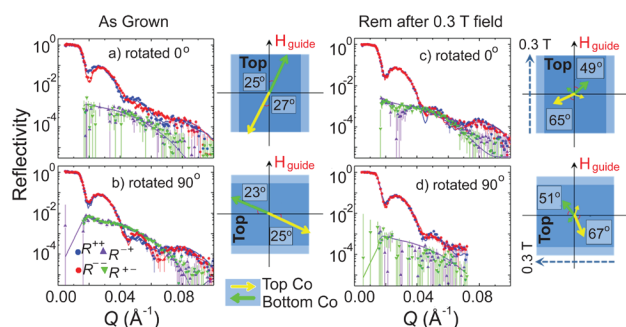


FIGURE 1: PNR data and fits in a field of < 0.002 T: (a) as-grown with sample upright, (b) as grown with sample rotated by 90° , (c) remanence after 0.3 T field with sample upright and (d) with sample rotated by 90° . The arrows in the schematics (*i.e.*, light blue designates bare sample edges) correspond to the average Co layer magnetizations.

The PNR measurements were repeated in remanence after applying a 0.3 T field parallel to the bare edge of the sample. In this magnetic state, the spin flip scattering from the sample in the upright position (Fig. 1c) is more than double that obtained from the rotated sample (Fig. 1d). It is clear that the Co layer magnetizations have reoriented such that the majority of the moments are perpendicular to the field. Motivated by SEMPA results discussed below, these data were fit simultaneously with a model that includes an incoherent addition of scattering from two distinct domain states in which the antiparallel-aligned Co layers are rotated to either side of the applied field direction, as shown in the schematics. The magnetizations of the top and bottom Co layers in the dominant state are (381 ± 20) kA/m and (273 ± 20) kA/m, respectively, and the top and bottom layers in the secondary state have a reduced magnetization of (38 ± 15) kA/m and (52 ± 20) kA/m, respectively. Overall, the net magnetizations of each layer are significantly reduced from that obtained in the as-grown state indicating that a large fraction of the Co magnetization is distributed into in-plane domains with dimensions smaller than the coherence length of the neutron beam ($\approx 100 \mu\text{m}$).

SEMPA characterization of the same sample, both before and after application of the 0.3 T field, corroborated the PNR findings and provided specific details regarding the nature of the in-plane magnetic domains within each Co layer. For these measurements, images were obtained within a 1 mm^2 window of the sample that was ion milled with 800 eV Ar ions to first reveal the top and bottom Co layer magnetizations sequentially. The corresponding images for the as-grown state are shown in Figs. 2a and 2b, and the magnetization distribution in each image is summarized in the corresponding polar plot. The average directions of the layer magnetizations obtained from SEMPA match those obtained from PNR, confirming that the top and bottom Co layers are aligned antiparallel. The Co moments, however, are distributed about their average direction with an

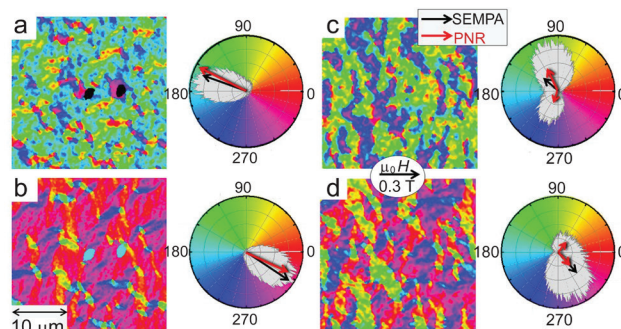


FIGURE 2: SEMPA images of the in-plane remanent magnetization in the top (a), (c) and bottom (b), (d) layers before (a), (b) and after (c), (d) a field of 0.3 T. Polar histograms show the distribution (in grey) of magnetization angles in the image. The average magnetizations from the image (standard arrow) and from PNR (diamond-head arrow) are also shown. The magnitude of the small diamond-head arrows in (c) and (d), corresponding to the second domain state, has been scaled by a factor of 5.

angular spread of approximately 30° . After application of a 0.3 T field, the angular spread of the in-plane moment distribution broadens substantially (Figs. 2c and 2d), with a bimodal domain distribution that is most pronounced in the top Co layer. Though the layer moments have now broken up into smaller domains, their average directions, which are consistent with those obtained from PNR measurements, are nearly perpendicular to the applied field.

The field-dependent evolution of the magnetic structure was also characterized using PNR, since SEMPA can only be performed in residual fields. These data reveal that antiferromagnetic coupling between the Co layers persists in fields up to approximately 0.1 T at which point the moments form a scissors-like state symmetric about the applied field direction. The angle between the layer moments gradually decreases with increasing field. In remanence at high fields, both PNR and SEMPA (Figs. 1 and 2) indicate that the original antiparallel alignment between the Co layer moments is restored, but the original anisotropy direction is not recovered. Instead the high field induces a “spin flop” magnetic state, though with a broad distribution of in-plane magnetic domains. These investigations thus indicate that the spin-triplet supercurrent can be strongly enhanced by maximizing the misalignment between the magnetizations of the ferromagnetic outer and center layers in a Josephson junction. Full optimization of the polarized current in actual devices can potentially be achieved simply by tuning the competing magnetic interactions of the central antiferromagnetically-coupled sandwich.

References

- [1] T.S. Khaire, M.A. Khasawneh, W.P. Pratt, N.O. Birge, Phys. Rev. Lett. **104**, 137002 (2010).
- [2] C. Klose, T.S. Khaire, Y. Wang, W.P. Pratt, N.O. Birge, B.J. McMorran, T.P. Ginley, J.A. Borchers, B.J. Kirby, B.B. Maranville, and J. Unguris, Phys. Rev. Lett. **108**, 127002 (2012).
- [3] P.A. Kienzie, J. Krycka, N. Patel, and I. Sahin, computer software REFLID (Version 0.6.19), University of Maryland, 2011. Available from <http://reflectometry.org/danse>.

Charge ordering and magnetic frustration in the fluoride pyrochlore, $\text{RbFe}^{2+}\text{Fe}^{3+}\text{F}_6$

S.W. Kim,¹ S-H. Kim,¹ P.S. Halasyamani,¹ M.A. Green,^{2,3} K.P. Bhatti,⁴ C. Leighton,⁴ H. Das,⁵ and C.J. Fennie⁵

The discovery of new materials possessing magnetic frustration is essential to further our understanding of these complex magnets, which have future applications in the next generation of electronics. Oxide pyrochlores have played an important role in this goal, particularly with the discovery of “spin-ice” materials [1]. Fluoride pyrochlore have been less prominent, mainly as a result of problems with controlling stoichiometry; a key factor in studying model magnets. However, a new low temperature route to producing fluoride pyrochlore offers new opportunities to the field. In a recent paper, we have used neutron diffraction, combined with magnetization measurements and computational techniques, to study the properties of β -pyrochlore, RbFe_2F_6 [2].

Powder neutron diffraction measurements were performed on RbFe_2F_6 at several temperatures in the range, 4 K to 300 K. RbFe_2F_6 crystallizes in the $Pnma$ space group with lattice parameters of $a = 7.02134(7) \text{ \AA}$, $b = 7.45093(7) \text{ \AA}$ and $c = 10.1795(1) \text{ \AA}$ at room temperature. This represents a reduced orthorhombic cell of the conventional β -pyrochlore lattice with the $Fd-3m$ symmetry. It is related to the more common α -pyrochlore lattice, with the general formula, $\text{A}_2\text{B}_2\text{X}_6\text{X}'$, through two ordered vacancies. Firstly, one of the two A cations is vacant, which reverts the kagome network of the A sites in α -pyrochlore into a diamond lattice with Td point symmetry. Secondly, the anion, X' , that does not contribute to the BX_6 octahedra is vacant; removing this apical anion reduces the 8 coordination of the A cation and leaves an open cage site (see Fig. 1).

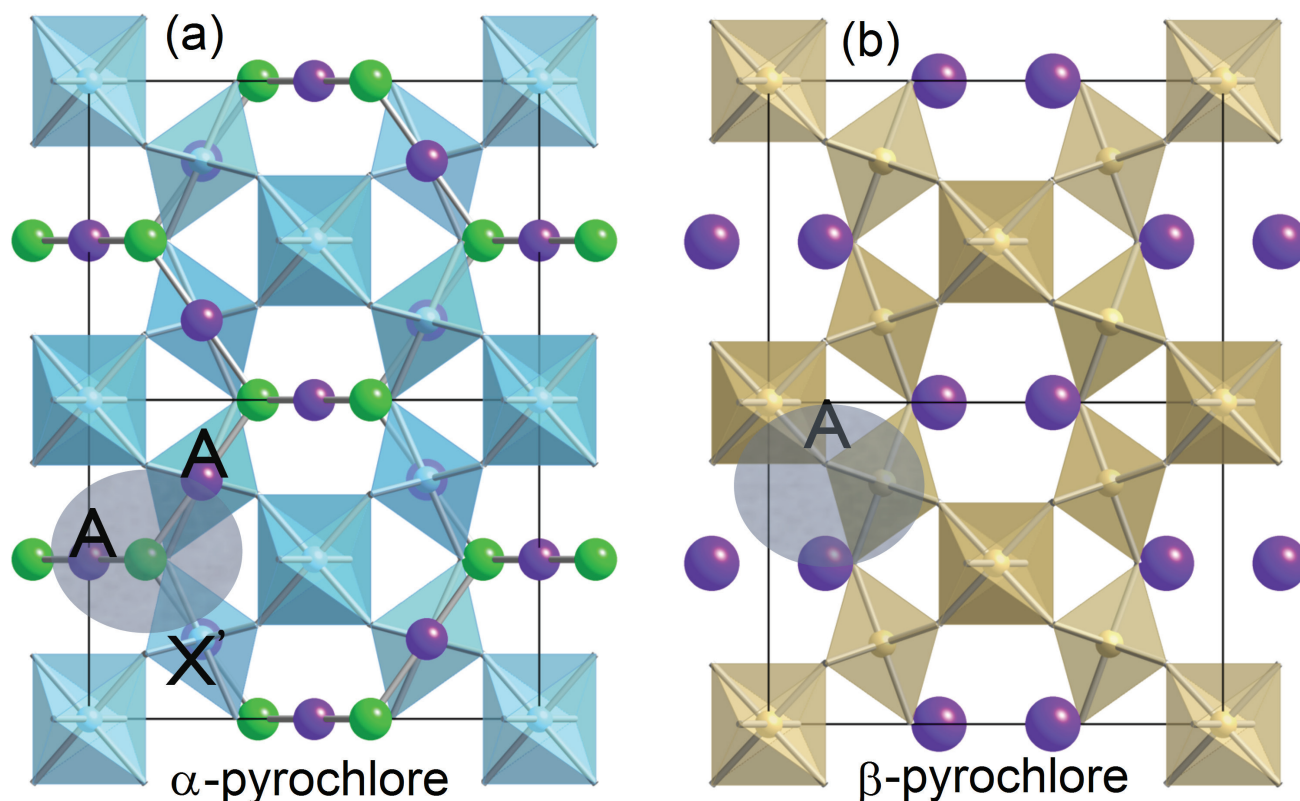


FIGURE 1: (a) α -pyrochlore has a $\text{A}_2\text{X}'$ network that is simple A in the (b) β -pyrochlore.

¹ University of Houston; Houston, TX, 77204-5003

² University of Maryland; College Park, MD, 20742-2115

³ NIST Center for Neutron Research; National Institute of Standards and Technology; Gaithersburg, MD, 20899-6103

⁴ University of Minnesota; Minneapolis, MN, 55455

⁵ Cornell University; Ithaca, NY, 14853

One key feature of β -pyrochlores that has greatly hindered their usefulness as model magnetic systems is their tendency for both site disorder and partial occupancy. To evaluate these possibilities a number of models were tested and no evidence could be found for such issues in RbFe_2F_6 .

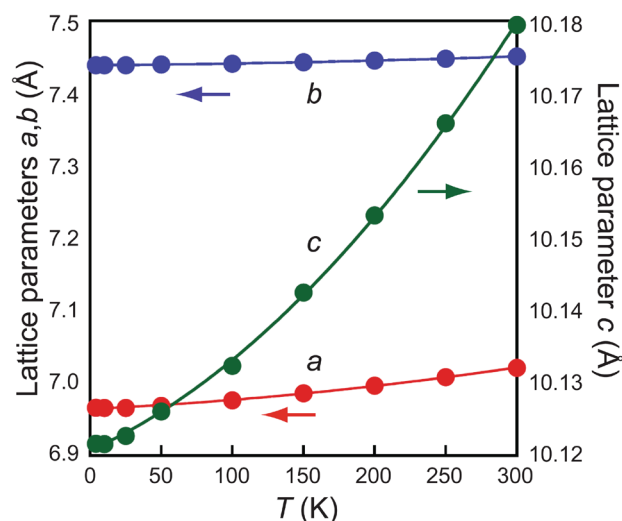


FIGURE 2: Lattice parameters of RbFe_2F_6 as a function of temperature.

Figure 2 shows the lattice parameters as a function of temperature. All three lattice parameters show a modest contraction down to the magnetic ordering temperature, below which there is negative thermal expansion, particularly within the ab plane. No structural phase transition was found on cooling and RbFe_2F_6 remained orthorhombic with $Pnma$ symmetry to the lowest temperature measured. One central structural feature was the difference between thermal factors of the constituent elements.

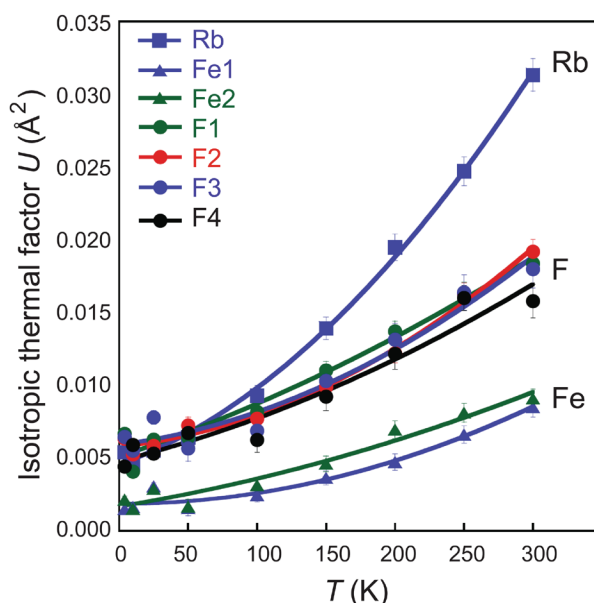


FIGURE 3: Thermal parameters for RbFe_2F_6 .

Figure 3 shows the isotropic thermal factor for all 6 atoms as a function of temperature. Although each atom has a typical temperature dependence, the absolute value of U for Rb is ≈ 5 times that of the lighter Fe, and even twice that of F that is over four times lighter. The rattling effect of A site cations within the β -pyrochlores is well documented and results from a gross mismatch between the ionic radii of the cations and the space available.

A new charge-ordered magnetically frustrated mixed-metal fluoride with a pyrochlore-related structure has been synthesized and characterized. The material exhibits a three-dimensional pyrochlore-related structure consisting of corner-shared Fe^{2+}F_6 and Fe^{3+}_6 octahedra. Magnetization measurements reveal strong antiferromagnetic interactions (a Curie-Weiss temperature of -270 K) but the structure is sufficiently frustrated to suppress long range ordering until 16 K.

References

- [1] M.J. Harris, S.T. Bramwell, D.F. McMorrow, T. Zeiske and K.W. Godfrey, *Phys. Rev. Lett.* **79**, 2554 (1997).
- [2] S.W. Kim, S.H. Kim, P. S. Halasyamani, M.A. Green, K.P. Bhatti, C. Leighton, H. Das, and C.J. Fennie *Chemical Science* **3**, 741 (2012).

Measuring yield stresses in biaxial deformation

T. Gnäupel-Herold^{1,2}, T. Foecke³, A. Creuziger³, M. Iadicola³, L. Hu⁴

Sheet metal forming is a tricky business even after a century of mass production typical for the automotive industry. This is in good part due to the difficulties in predicting springback. Everyone who has ever bent a long, thin piece of metal is familiar with the phenomenon – the metal piece springs back after releasing the applied force. The amount of this ‘springback’ at the release of the stamping tool must be known precisely if doors, hoods and handles are to fit together. Predicting the magnitude of springback for such complex shapes has proven to be a lasting challenge because of the side effects of automotive light weighting – thinner gages at higher strength (high strength steels) and lighter materials (aluminum and magnesium alloys), all of which strongly increase springback. Contrary to expectation, the poor predictability is caused less by a lack in computing power for running finite element codes than by insufficient knowledge of the materials constants that govern multi-axial straining, not just of advanced steels but almost any structural material. The measurement of these constants, called the yield stresses, is described in the following.

The key in obtaining these much needed properties is the measurement of plastic strains and stresses *while* the material is being deformed. Stress can only be determined through the elastic strains it causes. This requires three steps: (1) the capability for biaxial deformation with a prescribed strain by applying a (unknown) stress; (2) *in situ* measurement of lattice strains during forming and (3) the conversion of the thus measured lattice strains into the previously unknown stresses applied in step (1). The key fact to know is that diffraction only measures lattice strains which represent the elastic part of the strains from which the stresses can be obtained – if the elastic constants are known. The combination of the technologies in (1) and (2) have been implemented over the past decade at NIST. Plastic strains are measured during straining using digital image correlation with precisions of $\approx 10^{-3}$. The measurement of elastic strains needed to determine stress needs a precision at least one order of magnitude better ($\approx 5 \times 10^{-5}$) which is realized through an x-ray diffractometer integrated into the forming machine for *in situ* measurements. Using established analysis methods, a proof-of-concept was delivered through the measurement of the yield surface of an aluminum alloy. However, advancing this concept

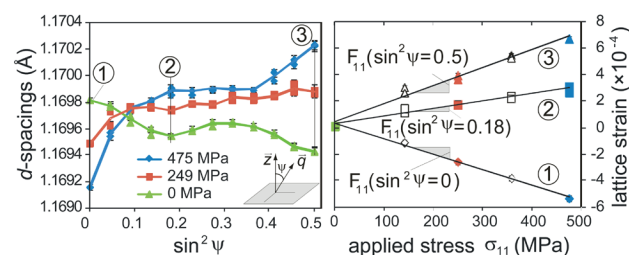


FIGURE 1: Left: *d*-spacings as measured for different stresses; right: lattice strains for fixed directions ψ and different stresses (①: $\sin^2 \psi = 0$, ②: $\sin^2 \psi = 0.18$, ③: $\sin^2 \psi = 0.5$). The color code in the legend applies to both graphs; empty symbols are for stresses not shown on the left graph. Strains are referenced to the green curve on the left, thus, all strains are zero at zero stress. Without elastic anisotropy, each curve on the left would be a straight line; without intergranular strains, the green curve at zero stress would be flat. Intergranular strains are dealt with by referencing to the zero-stress *d*-spacings, elastic anisotropy requires measurement of elastic constants in each direction (the slopes in the linear regressions on the right).

to steels has proven to be challenging because of its strongly non-linear behavior caused by large elastic anisotropy (Fig. 1).

The challenge to the data analysis is to reproduce the *d*-spacings in Fig. 1, left, for known stresses. However, the comparison of results from modeling of diffraction elastic constants (DEC) with neutron diffraction measurements has shown that at this point no model is able to predict with *sufficient accuracy* the evolution of DEC with texture and grain shape. This includes advanced models that use quantitative texture information from neutron diffraction together with grain-morphology data. Only the use of measured DEC produced satisfactory agreement between known and calculated stresses while also allowing a statement of accuracy of the measurement rather than its precision. For example, the use of measured DEC gave average accuracies $\approx 2\%$ while the best model yielded accuracies $\geq 10\%$. With the scale clearly tilting in favor of an all-around measurement of DEC, the question remains how many DEC measurements are necessary before the actual quantities of interest – the flow stresses – can be determined. Typically, during sample deformation the plastic straining is halted 10 to 15 times for the x-ray measurements of lattice strain. If elastic constants were to be measured for each level of plastic strain it would require 10 000+ measurements to completely characterize a material. This is clearly prohibitive,

¹ University of Maryland; College Park, MD 20704

² NIST Center for Neutron Research; National Institute of Standards and Technology; Gaithersburg, MD 20899-6102

³ NIST Metallurgy Division; National Institute of Standards and Technology; Gaithersburg, MD 20899

⁴ Carnegie Mellon University; Pittsburgh, PA 15213

and for that reason a hybrid method was developed in which a more limited set of measured DEC is used to fit a function that approximates the theoretical evolution of the DEC with plastic strain. Plastic deformation occurs through slip and grain rotation, both of which affect the DEC through changes of morphology and orientation of grains. The evolution of DEC with plastic strain is simulated first through a visco-plastic self-consistent (VPSC) crystal plasticity model which puts out the grain orientation distribution function (ODF) for a given level of plastic strain. Second, DEC are calculated from a grain-aggregate interaction model that uses the ODF to simulate the behavior of the polycrystal. The simulations confirm the expectation that in materials without stress-induced phase transformations texture and texture-derived properties change with strain in a monotonic fashion. The precise nature of this strain-property correlation cannot be established as a closed-form expression because the entire model is far too complex to be reduced analytically in this way; it must be approximated itself by a fit. It was found that the crystal-elastic behavior reflected in the DEC is described better by a linear correlation than by a type of power law that can be inferred from the uniaxial stress-strain behavior of the aggregate (Fig. 2, green curve).

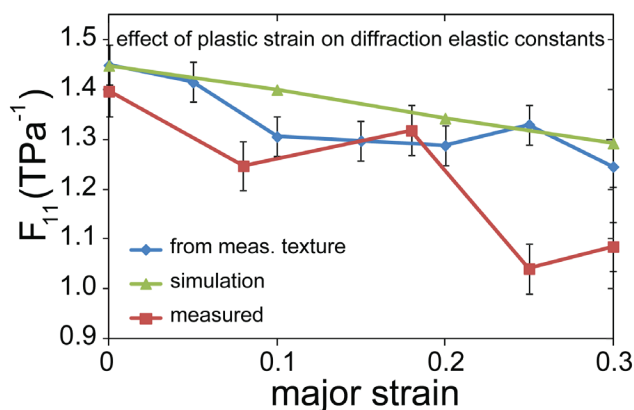


FIGURE 2: Dependence of diffraction elastic constants on plastic strain for one orientation of the scattering vector. The blue and green curves are simulated but each data point in the blue was obtained from a DEC model together with an ODF from three measured neutron diffraction pole figures. Each data point in the red curve represents the linear regression of five measurements (elastic) lattice strain vs applied stress (see Fig. 1).

A comparison between measured and simulated DEC for a multitude of directions and plastic strains has shown that the quantitative agreement between the DEC is generally not sufficient for an all-around use of calculated DEC for stress determination. Instead, a first-order polynomial is fitted to the measured DEC for each direction and each strain level. This procedure solves the problem to obtain DEC at plastic

strains where DEC have not been measured with the useful side effect that the overall uncertainties are somewhat reduced (Fig. 3: $\sigma \approx 10$ MPa). The final result, obtained from (stress = DEC \times strain), is shown in Fig. 3 which represents the first-ever measured biaxial yield stresses for steel using diffraction. Figure 3 shows summarily the steps that are necessary in order to obtain biaxial yield stresses: from lattice strains measured during plastic straining to measurements of diffraction elastic constants (DEC) done on pre-strained samples but under elastic loading. The recognition that, through texture, DEC evolve in a nearly linear fashion with plastic strain is the basis for a procedure that allows us to obtain stresses at any of the intermediate plastic strains in Fig. 3, bottom.

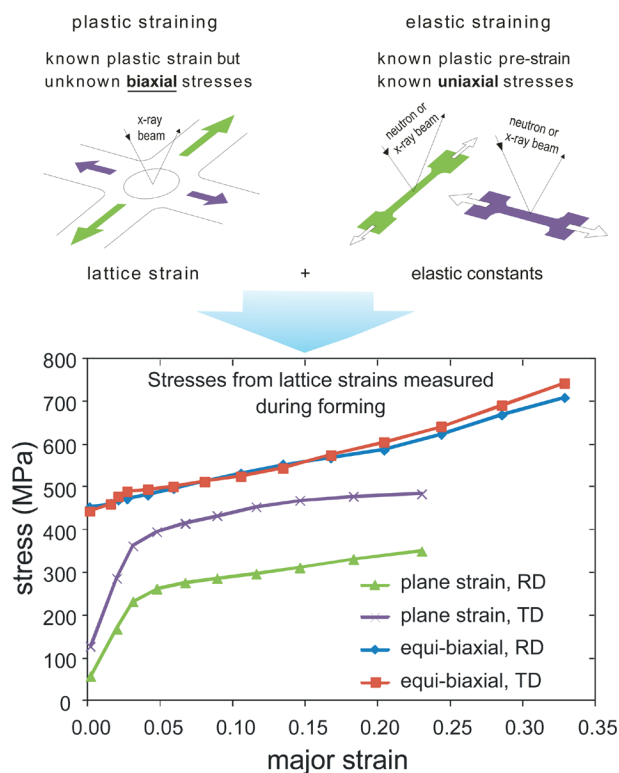


FIGURE 3: General outline of the procedure to measure biaxial yield stresses. Lattice strains are measured at an unknown biaxial stress (top, left), with unknown elastic constants. Diffraction elastic constants (DEC) are measured on separate samples that were extracted at pre-defined plastic strains (top, right). Both lattice strains and DEC together allow the determination of the stresses shown in the lower graph.

References

- [1] T. Gnäupel-Herold, A. Kreuziger, M. Iadicola, J. Appl. Cryst. **45**, 197 (2012).

A new limit on time-reversal violation in beta decay

H. P. Mumm¹, T. E. Chupp², R. L. Cooper², K. P. Coulter², S. J. Freedman³, B. K. Fujikawa³, A. Garcia⁴, G. L. Jones⁵, J. S. Nico¹, A. K. Thompson¹, C. A. Trull⁶, J. F. Wilkerson⁶, and F. E. Wietfeldt⁷

The stars and galaxies that make up our universe can only form if, during the initial moments after the Big Bang, there existed a slight dominance of matter over antimatter. It has been understood for some time that such an imbalance can only be explained if three conditions are met; a departure from thermal equilibrium, a violation of baryon (*i.e.*, three quark states) number, and a violation of charge-conjugation-parity (CP) symmetry in the physical laws that govern particle interactions (charge conjugation turns particle states into the corresponding anti-particle states and parity is essentially a mirror reflection of the state). Thus far, CP violation has been observed only in the K and B meson systems (*i.e.*, quark-antiquark states) and can be entirely accounted for within the Standard Model of particle physics (SM). However, the extent of SM CP violation is many orders of magnitude too small to account for the known asymmetry in the context of Big Bang cosmology, so there is compelling reason to search for CP violation in other systems. As CP and Time-reversal symmetry (T) violation can be theoretically related to one another, experimental limits on T-odd observables in nuclear beta decay place strict constraints on possible sources of new CP violation. We have recently reported the results of an improved experiment that limits time-reversal invariance violation in the beta decay of polarized neutrons and thus constrains extensions to the Standard Model.

The decay probability distribution for neutron beta decay, dW , can be written in terms of the neutron spin-state $\vec{\sigma}_n$, the momenta (energy) of the electron $\vec{p}_e(E_e)$ and antineutrino $\vec{p}_\nu(E_\nu)$ as [1]

$$dW \propto 1 + a \frac{\vec{p}_e \cdot \vec{p}_\nu}{E_e E_\nu} + b \frac{m_e}{E_e} + \vec{\sigma}_n \cdot \left(A \frac{\vec{p}_e}{E_e} + B \frac{\vec{p}_\nu}{E_\nu} + D \frac{\vec{p}_e \times \vec{p}_\nu}{E_e E_\nu} \right). \quad (1)$$

A contribution of the parity-even (P-even) triple correlation D above the level of calculable final-state interactions (FSI) unambiguously indicates a violation of T symmetry. While the FSI for the neutron are $\approx 1 \times 10^{-5}$, previous D measurements had reached $\approx 7 \times 10^{-4}$ [2]. Thus, improved measurements of D probe non-SM sources of T-violation. Various theoretical models that extend the SM, such as left-right symmetric theories, leptoquarks, and certain exotic fermions could cause observable effects that are as large as the present experimental limits [3]. In small-scale experiments the neutrino is effectively unobservable,

however in the neutron rest frame, the triple correlation from Eq. 1 can be expressed as $D \vec{\sigma}_n \cdot (\vec{p}_p \times \vec{p}_e)$ (*i.e.*, involving protons and electrons). Thus, one can extract D from the spin dependence of proton-electron coincidences in the decay of cold polarized neutrons.

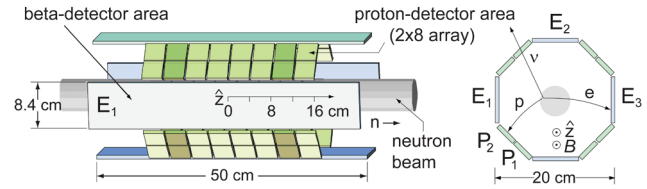


FIGURE 1: A schematic of the emiT detector illustrating the alternating electron and proton detector segments. The shaded detectors show the example of the paired-ring at $z \pm 10$ cm. The cross section view illustrates, in a greatly exaggerated manner, the effect of the magnetic field on the particle trajectories. A P_2E_2 coincidence event is shown.

Our measurement was carried out at the NCNR NG-6 beamline. The detector, shown schematically in Fig 1, was built to be highly symmetric and consisted of an octagonal array of four electron-detection planes and four proton-detection planes concentric with the longitudinally polarized beam. The beam, with a neutron capture fluence rate at the detector of $1.7 \times 10^8 \text{ cm}^{-2} \text{ s}^{-1}$, was polarized to $> 91\%$ (95 % C.L.) by a double-sided bender-type supermirror. A 0.56 mT (5.6 G) guide field maintained the polarization direction, while a current-sheet spin-flipper was used to periodically reverse the neutron spin direction, allowing for first order cancellation of detector efficiency variations. The octagonal geometry was chosen to maximize sensitivity to D , and the highly symmetric arrangement allows for the approximate cancellation of systematic effects stemming from residual coupling to the relatively large spin-correlations A and B (≈ 0.1 and ≈ 1 respectively) in Eq.1. Each of the four proton segments consisted of a 2×8 array of silicon surface-barrier diode detectors (SBDs). Because the maximum proton energy from the decay is very low, approximately 750 eV, protons were accelerated through grounded wire-mesh boxes and onto SBDs mounted within an electrode normally held between -25 kV and -32 kV. The beta detectors were slabs of plastic scintillator with sufficient thickness to stop electrons at the decay endpoint energy of 782 keV. Scintillation photons were detected by photomultiplier tubes (PMTs) at each end of the slab. Details of the apparatus can be found elsewhere [4].

¹ National Institute of Standards and Technology; Gaithersburg, MD 20899

² University of Michigan; Ann Arbor, MI 48104

³ University of California at Berkeley and ; Lawrence Berkeley National Laboratory,; Berkeley, CA 94720

⁴ University of Washington; Seattle, WA 98195

⁵ Hamilton College ; Clinton, NY 13323

⁶ Tulane University ; New Orleans, LA 70118

⁷ University of North Carolina; Chapel Hill, NC 27599

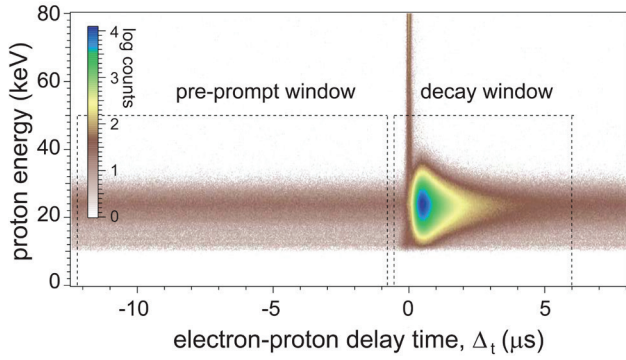


FIGURE 2: Log plot of SBD-scintillator coincidence data showing proton energy vs delay time. Events near $\Delta_t = 0$ are prompt coincidences due primarily to beam-related backgrounds.

Neutrons have a relatively long lifetime of 881 s, thus, even with a high fluence beam and a very efficient detector, the typical count rate for the entire array was only 25 s^{-1} . After various instrumental cuts were applied to improve data quality, the final data set, taken over roughly one year of running, consisted of approximately 300 million coincidence events. These events were divided into two timing windows based on the proton time-of-flight, a pre-prompt window, and the decay window, as shown in Fig. 2 (The recoil proton is delayed by approximately $0.5 \mu\text{s}$ on average). The pre-prompt background was subtracted from the spectrum in the decay window. Because of the tight coincidence requirement in time, the average signal-to-background was excellent, approximately 30/1. Integrating these energy spectra then gives the total number of decay events for a particular proton-detector electron-detector pair. A non-zero D would manifest itself as a slight asymmetry in the number of coincidence events seen between a given proton-detector and the two opposing electron detectors, *i.e.*, P_2E_2 and P_2E_1 in Fig. 1. To extract D , coincident events are first combined in approximately efficiency-independent asymmetries

$$w^{p_i e_j} = \frac{N_+^{p_i e_j} - N_-^{p_i e_j}}{N_+^{p_i e_j} + N_-^{p_i e_j}}, \quad (2)$$

where $N_+^{p_i e_j}$ is the integrated number of coincident events in proton detector p_i , beta detector e_j , with neutron spin + (-) aligned (anti-aligned) with the field. For a uniform polarization vector, \vec{P} , the w can be written in terms of decay correlations as

$$w^{p_i e_j} \approx \vec{P} \cdot (\vec{A} \vec{K}_A^{p_i e_j} + \vec{B} \vec{K}_B^{p_i e_j} + \vec{D} \vec{K}_D^{p_i e_j})$$

where the \vec{K} vectors are obtained from Eq. 1 by integrating each term over the phase space of the decay, the neutron beam volume, and the acceptance of the indicated detectors. As \vec{K}_B and \vec{K}_A are proportional to $\langle \vec{p}_v / E_v \rangle$ and $\langle \vec{p}_e / E_e \rangle$ respectively, both have small longitudinal components and thus the parity-violating correlations A and B in Eq. 2 lead to a w at the level of 1×10^{-3} , an order of magnitude larger than the desired sensitivity. Fortunately, one can choose appropriate combinations of detectors that are sensitive to the D -correlation but that largely cancel the effect of A and B . One such combination is $v^{p_i} = 1/2(w^{p_i R} - w^{p_i L})$ where R and L label the electron-detector at approximately 135° giving a positive and negative cross-product $\vec{p}_p \times \vec{p}_e$ respectively (P_2E_2 vs P_2E_1 as shown

in Fig. 1). We define \bar{v} as the average of the values of v from the sixteen proton-cells at the same z , *i.e.*, $(\pm 2, \pm 6, \pm 10, \text{ and } \pm 14)$ cm. Each set corresponds to paired-rings with the same symmetry as the full detector; the shaded detectors in Fig. 1. We then obtain $\bar{v} = P \vec{K}_D D$, where \vec{K}_D is determined by a Monte Carlo calculation, and the experiment provides four independent measurements of D corresponding to the four paired-rings.

Systematic effects fall into two categories; those that change the sensitivity to D , and those that result in a false asymmetry. Variations in flux, polarization, spin-flip frequency, and uncertainty in the constant \vec{K}_D , can be shown to produce asymmetries proportional to D . Due to the high signal-to-noise, errors in background subtraction, as well as possible spin-dependent asymmetries in this background, have a negligible effect. Other effects alter the symmetry of the detector and can therefore lead to a false asymmetry. For example, proton detector efficiencies were not uniform due to lower energy thresholds that varied slightly across the detector. The thresholds combined with the spin-dependence of the accelerated proton energy spectra resulted in a significant, but measureable, error in w . Beam expansion from a radius of ≈ 2.5 cm to ≈ 2.75 cm combined with the weak magnetic field also breaks the detector symmetry because the average proton-electron opening angle for each detector pair is modified. Monte Carlo calculations using measured density profile maps were used to calculate a correction. Finally, for a symmetric beam, contributions to v due to transverse components of the polarization cancel for opposing paddles; however small azimuthal beam asymmetries on the order of even millimeters affect this cancellation. To study this effect transverse-polarization calibration runs were taken over the course of the experiment. In these runs the effect was amplified by ≈ 200 . The false D from the transverse runs was then scaled to the observed polarization misalignment. Other effects of polarization non-uniformity are small. Finally, a blind analysis was performed by adding a constant hidden factor to Eq. 2. that was only removed once all analyses of systematic effects were complete.

The final result, including all corrections, is $D = (-0.96 \pm 1.89 \text{ (stat)} \pm 1.01 \text{ (sys)}) \times 10^{-4}$ [5,6]. Prior to this measurement, the most sensitive measurement of D was in ^{19}Ne , with $D = 1 \pm 6 \times 10^{-4}$ [7]. Thus, our result represents the most sensitive measurement of the D -coefficient in nuclear β -decay and improves constraints on CP-violation in leptoquark and certain exotic fermion extensions to the SM.

References

- [1] J.D. Jackson, S.B. Treiman and H.W. Wyld, Jr., Phys. Rev. **106**, 517 (1957).
- [2] T. Soldner, *et al.*, Phys. Lett. B, **581**, 49 (2004).
- [3] P. Herczeg, Proc. of the 6th Int. PASCOS-98, World Scientific, Singapore, (1998).
- [4] H.P. Mumm, *et al.*, Rev. Sci. Instrum. **75**, 5343 (2004).
- [5] H.P. Mumm, *et al.*, Phys. Rev. Lett. **107**, 102301 (2011).
- [6] T.E. Chupp, *et al.*, Phys. Rev. C, **86**, 035505 (2012).
- [7] F. Calaprice, Hyperfine Interactions, Springer, Netherlands **22**, 83 (1985).

Self-assembling organohydrogels: liquid dispersions with solid-like behavior

M.E. Helgeson¹, S.E. Moran², H.Z. An², P.S. Doyle²

Gels comprised almost entirely of water (hydrogels) or oil (organogels) have become important to a number of technologies that take advantage of their combined liquid-like transport and solid-like mechanical properties. However, the ability to create gels containing both water and oil, allowing encapsulation and transport of both polar and non-polar solutes, could lead to significant advances in these applications.

We recently discovered a novel class of such “organohydrogels” based on oil-in-water nanoemulsions [1]. These nanoemulsions are metastable liquid dispersions typically formed from high-energy processing techniques [2]. The nanoemulsions contain four primary components – water, silicone oil, a surfactant stabilizer, and poly(ethylene glycol) diacrylate (PEGDA) – and exhibit the ability to reversibly self-assemble from a low-viscosity liquid to a gel over a narrow range of temperature (Fig. 1). The small-strain mechanical properties of these materials resemble those of a linear elastic solid, with elastic (G') and viscous (G'') moduli that are nearly independent of the applied rate of deformation. This is remarkable, given that the organohydrogels form with compositions up to 90 % oil and water.

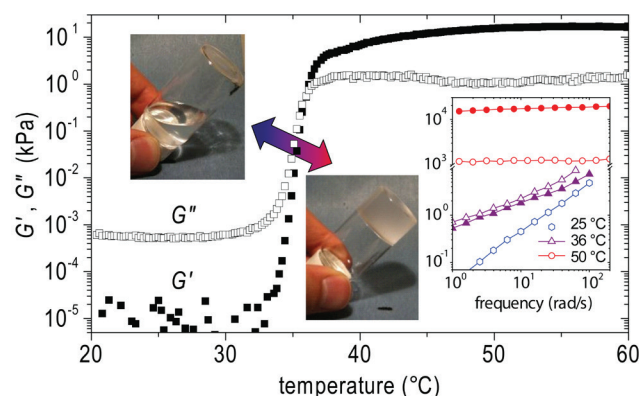


FIGURE 1: Linear viscoelastic moduli, G' (closed symbols) and G'' (open symbols), of a nanoemulsion containing 33 % oil droplets (radius = 17 nm) in 44 % D_2O and 22 % PEGDA undergoing a transition from a low-viscosity liquid to a highly elastic solid at high temperatures (see also inset photographs). Inset plot shows linear viscoelastic spectra of the sample through the gel transition.

To understand the mechanisms of self-assembly and solid-like behavior in these new materials, we used SANS and USANS to characterize the microstructure and interactions of the gelling nanoemulsions. In particular, the use of contrast variation

allowed us to independently interrogate the behavior of the different material constituents. First, we performed SANS on dilute nanoemulsions in aqueous PEGDA solutions over temperatures spanning well below and above the gel transition (Fig. 2). The low- q scattering, dominated by the nanoemulsion droplets, shows a significant increase in intensity with temperature, indicating changes in interdroplet interactions. Furthermore, increases in high- q scattering, dominated by PEGDA, with increasing temperature suggest self-association of PEGDA in solution. Separate measurements of the polymer conformation in solution show no significant changes in solvent quality during this process [1], indicating that PEGDA association is primarily driven by the functional end-groups, as shown previously for other chemistries [3]. The overall scattering of the dilute nanoemulsions was fit to a combined model including both the polymer conformation and square-well interdroplet attractions, revealing an abrupt transition in the attractive well depth near the gel transition temperature (Fig. 2).

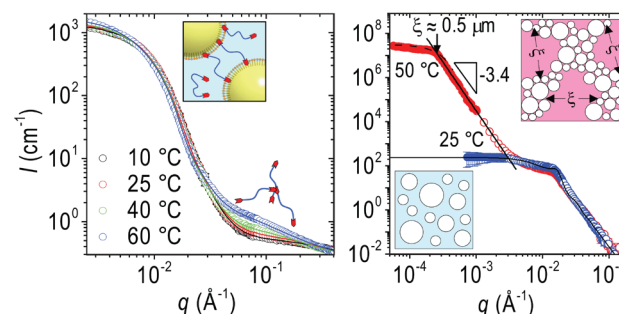


FIGURE 2: (Left) SANS spectra from nanoemulsion containing 1 % oil droplets (radius = 17 nm) in 44 % D_2O and 22 % PEGDA for temperatures spanning the gel transition, indicating interdroplet attractions mediated by polymer end-group solubility. (Right) Combined SANS/USANS spectra from a nanoemulsion containing 33 % oil droplets (radius = 17 nm) in 44 % polymer matching solvent (82/18 H_2O/D_2O) and 22 % PEGDA.

These results suggest that formation of the organohydrogels is driven by changes in polymer-mediated interdroplet attractions. Specifically, we hypothesize that the moderately hydrophobic polymer end-groups are driven to the oil-water interface at elevated temperatures, resulting in interdroplet bridging of the polymer (Fig. 2). This was corroborated by rheological measurements of the dependence of gel formation on the polymer chemistry, in which both the gel temperature and modulus were found to vary significantly according to the hydrophobic character of the polymer end-groups [1].

¹ University of California, Santa Barbara, Santa Barbara, CA 93106

² Massachusetts Institute of Technology, Cambridge, MA 02139

SANS and USANS measurements were then performed on more concentrated nanoemulsions where thermogelation occurs in order to elucidate the organohydrogels' microstructure (Fig. 2). These experiments were made under solvent conditions in which PEGDA was contrast-matched to specifically isolate the droplet microstructure. At low temperatures, the scattering is indicative of a well-dispersed droplet suspension, and is in quantitative agreement with that predicted from the dilute droplet interactions.

Above the gel temperature, no changes in high- q scattering occur, indicating that spherical droplets remain upon gelation, and do not fuse or transform into other morphologies. By contrast, significant increases in low- q scattering are observed, indicating the formation of large droplet aggregates. The power-law dependence of the scattered intensity at moderate q -values indicates fractal droplet clusters, much like those found in hard sphere colloidal gels [4]. The slope of -3.4 indicates dense clusters with a combination of mass and surface fractal contributions. Furthermore, a shoulder in the scattering at low q -values indicates limited cluster growth. We believe this limited growth is due to arrested phase separation of the droplets, whereby the q -value of the associated shoulder marks a characteristic length scale of droplet-lean "pores", as has been predicted for attractive near-hard sphere colloidal gels [5].

From this, we surmise that the solid-like behavior of the gels arises from the effective "bonds" between dense droplet clusters mediated at the molecular level by the polymer-induced interdroplet attractions (Fig. 2). Thus, the gel strength can be enhanced through the use of a polymer with more hydrophobic end-groups, thereby increasing polymer bridging and the cluster bond strength [1]. In this regard, the elasticity of the nanoemulsion gels is very similar to that of hard particle colloidal gels, but where the polymer self-assembly provides a convenient route for controlling the gelation process.

The ability to make self-assembled structures such as organohydrogels permanent can be critical for their processing and end use. Here, this is achieved by photoinitiated free radical polymerization of PEGDA to form a crosslinked polymer network in the aqueous phase, providing encapsulation of the nanoemulsion in a semi-permanent matrix. Contrast variation SANS and USANS measurements were thus used as a critical test of the ability to "freeze" targeted droplet microstructures within a polymer network (Fig. 3). Nanoemulsions in a polymer contrast-matched solvent were photocrosslinked at temperatures both below and above the gel transition. These samples (Fig. 3) exhibit scattering that is nearly identical to that before crosslinking (Fig. 2), indicating that both well-dispersed and gelled droplet microstructures can be successfully encapsulated.

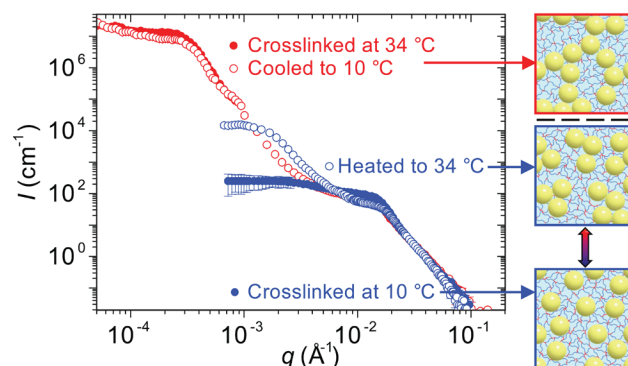


FIGURE 3: Combined SANS/USANS spectra from crosslinkable nanoemulsions. A nanoemulsion photocrosslinked above the gel temperature (red) exhibits similar droplet microstructure at temperatures both above (open) and below (closed) the gel temperature, whereas a nanoemulsion photocrosslinked below the gel temperature (blue) exhibits changes in droplet microstructure between the same temperatures (see insets at right).

The temperature of the samples crosslinked below and above the gel transition, respectively, was then switched to the opposite end of the gel transition in order to test whether the encapsulated droplet microstructures remained intact. Interestingly, we find that while emulsions crosslinked above the gel transition temperature retain their percolated cluster microstructure, those crosslinked below the transition temperature exhibit increased low- q scattering at elevated temperatures, suggesting limited ability of the droplets to form clusters in spite of the large steric barrier to self-assembly provided by the crosslinked polymer network. These composites exhibited significantly different strains required to break the material [1], suggesting that droplet microstructure is a key parameter governing the mechanical properties of such composites.

In summation, we have presented a fascinating new class of solid-like gels from entirely liquid dispersions. Our neutron scattering measurements give critical insight into the mechanisms of thermoreversible gel formation and elasticity. These results will motivate predictive multi-scale models that capture the interdependence of polymer self-assembly and gel formation, providing means by which to rationally engineer the structure and properties of organohydrogels at the molecular level. Furthermore, the ability to "freeze" the nanoemulsion into a crosslinked polymer gel provides new ways by which to create soft nanocomposites with highly controlled microstructure.

References

- [1] M.E. Helgeson, S.E. Moran, H.Z. An, P.S. Doyle, *Nature Materials* **11**, 344 (2012).
- [2] T.G. Mason, J.N. Wilking, K. Meleson, C.B. Chang, S.M. Graves, *J. Phys.: Condensed Matter* **18**, R635 (2006).
- [3] B. Hammouda, D.L. Ho, S. Kline, *Macromolecules* **37**, 6932 (2004).
- [4] H. Wu, J.J. Xie, M. Lattuada, M. Morbidelli, *Langmuir* **21**, 3291 (2005).
- [5] E. Zaccarelli, *J. Phys.: Condensed Matter* **19**, (2007).

Thickness fluctuations in model membranes

A.C. Woodka¹, P.D. Butler^{1,2}, L. Porcar³, B. Farago³, M. Nagao^{1,4}

Biological membranes are complex structures whose role is to provide selective permeability: allowing necessary nutrients in while excluding toxins, and allowing waste to exit while preventing vital intracellular components from escaping. The highly dynamic nature of these membranes plays a critical role in maintaining this delicate balance. These motions range from individual lipid oscillation, to the undulation of large (micron size) patches of the membrane. At atomic to molecular length scales the diffusion of individual lipids within the membrane have been shown to affect cell signal transduction while at the large length scales membrane stiffness and fluidity have been shown to have a significant impact on cellular uptake and release. The dynamics at intermediate length scales are collective movements of dozens of molecules, and thus, fundamental to understanding how the large scale motions emerge from atomic and molecular movements and interactions, yet remain experimentally elusive. At this intermediate length scale thickness fluctuations have been suggested theoretically and even proposed as a mechanism for membrane pore formation.

In the study highlighted here, we use Neutron Spin Echo Spectroscopy (NSE) to probe the thickness fluctuations in lipid membranes [1]. We report the experimentally measured thickness fluctuations in a single component phospholipid model membrane as a function of both lipid tail length and temperature. Unilamellar vesicles (ULVs) composed of a single lipid dimyristoyl-, dipalmitoyl-, or distearoyl-phosphocholine (DMPC = 14 carbon tail, DPPC = 16 carbons, or DSPC = 18 carbons) were prepared and their dynamics characterized using NSE complemented with Small Angle Neutron Scattering (SANS) to fully characterize each system.

In order to highlight the thickness fluctuations, tail deuterated and fully hydrogenated lipids were mixed in an appropriate ratio so that the membrane tail region was contrast-matched with D₂O. Saturated phosphocholine lipids undergo a first order phase transition known as the melting transition at temperature T_m , resulting in a change in membrane thickness and density. T_m was determined for each lipid to be 20.5 °C, 37.5 °C, and 50.5 °C (± 0.2 °C) for our DMPC, DPPC, and DSPC systems, respectively, using densitometry. Relatively monodisperse 100 nm lipid vesicles were prepared by heating each lipid solution above T_m and extruding through a polycarbonate filter.

Initially SANS is measured to determine membrane thickness. Figure 1a shows the SANS from DPPC ULVs at 30 °C, 40 °C, and 50 °C. The scattering from the bilayer is modeled as vesicles with a Schulz distribution of radii and composed of three layers, each with a corresponding scattering length density (SLD). The two outer layers of the membrane represent the hydrogenated lipid headgroup regions and were constrained to have equal thickness and SLD, the third (center) layer represents the contrast matched deuterated lipid tail region. The lines in Fig. 1a represent the vesicle fits. The change in membrane thickness, d_m , on crossing T_m is clearly visible in the shift of the SANS dip position, q_{min} .

The normalized intermediate scattering functions, $I(q,t)/I(q,0)$, for each lipid were measured by NSE (see Fig. 1b). Since the single membrane undulational motion is the primary dynamic in the present system, the theory of Zilman and Granek [2] for the bending motion of a single membrane should be applicable as:

$$\frac{I(q,t)}{I(q,0)} = \exp[-(\Gamma t)^{2/3}], \quad (1)$$

where Γ is the decay rate which scales as q^3 .

The data for the fluid phase (above T_m) of each lipid system shown in Fig. 1c, d, and e (DMPC, DPPC, and DSPC respectively) clearly exhibit a deviation from the expected q^3 behavior. This excess in dynamics is observed as a peak in Γ/q^3 at the q_{min} observed in the SANS measurement (DPPC shown in Fig. 1a) indicating that the length scale of the enhancement in the dynamics signal is that of the membrane thickness and thus due to membrane thickness fluctuations. In the gel phase (below T_m) the lipid tails are much more ordered leading to a much more rigid membrane which translates into the much smaller Γ observed here. Interestingly, in this regime there is no observable excess in the dynamics (no peak in Γ/q^3).

In order to further characterize the excess in dynamics at the membrane thickness length scale, we assume that the decay rate contains two additive terms and can be expressed by the following empirical equation:

$$\frac{\Gamma}{q^3} = 0.0058 \frac{k_B T}{\eta_{D_2O}} \sqrt{\frac{k_B T}{\kappa}} + \frac{\Gamma_{TF}}{q_0^3} \frac{1}{1 + (q - q_0)^2 \xi^{-2}}, \quad (2)$$

¹ NIST Center for Neutron Research; National Institute of Standards and Technology; Gaithersburg, MD 20899-6102

² University of Delaware; Newark, DE 19716

³ Institut Laue Langevin; Grenoble Cedex 9, FRANCE

⁴ Indiana University; Bloomington, IN 47408

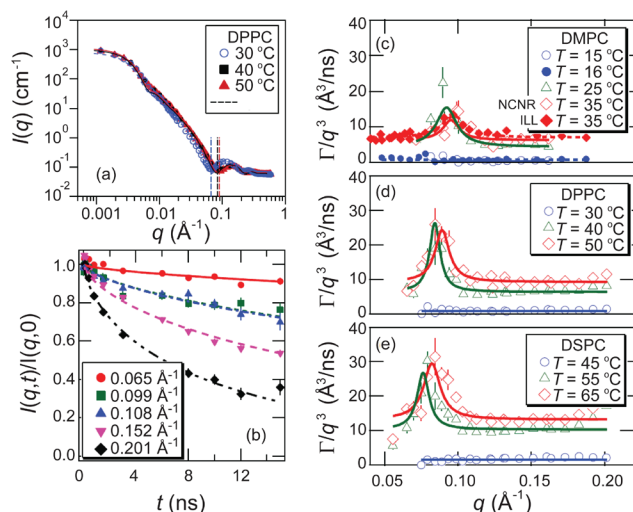


FIGURE 1: (a) Temperature variation SANS of DPPC vesicles. Vertical lines represent q_{min} , fits are to the three shell vesicle model described in the text. (b) $I(q,t)/I(q,0)$ of DPPC vesicles at $T = 50$ °C, fits are to Eq. 1. q -dependence of Γ/q^3 for (c) DMPC (d) DPPC and (e) DSPC vesicles, fits above T_m are to Eq. 2. Error bars represent ± 1 standard deviation.

where the first term represents the bending fluctuations. κ and η_{D20} are bending modulus and solvent viscosity, and Γ_{TF} represents the decay rate due to the thickness fluctuations leading to the excess dynamics observed at $q = q_0$. Γ_{TF}/q_0^3 is the peak height of the Lorentzian where q_0 is the peak position of the Lorentz function, and ξ^{-1} is the width of the Lorentzian. Here η_{D20} and $k_B T$ are known quantities and q_0 comes from the SANS measurements. κ is plotted in Fig. 2a as a function of the reduced temperature, $T - T_m$. The expected transition in κ as T_m is crossed is clearly visible and agrees well with literature values within the uncertainty of our measurements.

The temperature dependence of the thickness fluctuation decay rates, Γ_{TF} , is shown in Fig. 2b. Within our experimental uncertainty these rates appear independent of either lipid tail length or temperature above T_m . The computed relaxation time,

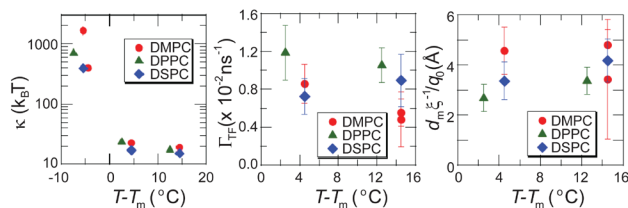


FIGURE 2: (a) The bending modulus, κ , (b) relaxation rate, Γ_{TF} and (c) amplitude of thickness fluctuations, $d_m \xi^{-1}/q_0$, plotted against the reduced temperature, $T - T_m$.

$\tau = 1/\Gamma_{\text{TF}}$ is on the order of 100 ns, which is much smaller than those found in surfactant membrane systems (which are only a few ns) [3]. Such a significant slowdown of thickness fluctuation might originate from larger membrane viscosities, increased membrane stiffness, or differences in compressibility of membranes. One explanation for the lack of observed thickness fluctuations below T_m is that if the decay times are slower (due for example to the higher bending rigidity) they will no longer be within our accessible time window.

The amplitudes of the thickness fluctuations are related to the observed peak width, ξ^{-1} , and can be estimated from $d_m \xi^{-1}/q_0$ [3]. As shown in Fig. 2c, this value is also essentially independent of either tail length or temperature above T_m . The average thickness fluctuation amplitude was estimated to be (3.7 ± 0.7) \AA , approximately 8 % of the membrane thickness, in remarkably good agreement with estimates based on both theory [4] and simulations [5,6], lending further support to our empirical model. Further, the amplitude is not significantly smaller than found that for surfactant membranes, suggesting the amplitude may be controlled more by the bilayer's geometrical constraints such as volume conservation, rather than dynamical ones. If this holds below T_m then the lack of observed fluctuations would indeed be due to extremely slow relaxations.

While these findings experimentally demonstrate the existence of thickness fluctuations in lipid membrane systems and provide some quantitative insights into them, there remains significant theoretical work on the physics of lipid bilayers in order to fully understand their dynamics. We hope that these findings will lead to other theoretical and experimental investigations of local intra-membrane dynamics to improve our understanding of these interesting systems. In particular exactly how these fluctuations might enable pore formation, membrane protein insertion, or other biological functions remain open questions. Fully understanding the dynamics in these systems will be key to, for example, designing therapies to control dysfunctions in membrane permeability and pore formation which can lead to cellular death.

References

- [1] A.C. Woodka, P.D. Butler, L. Porcar, B. Farago, and M. Nagao, Phys. Rev. Lett. 109, 058102 (2012).
- [2] A.G. Zilman and R. Granek, Phys. Rev. Lett. 77, 4788 (1996).
- [3] M. Nagao, S. Chawang, and T. Hawa, Soft Matter 7, 6598 (2011).
- [4] H.W. Huang, Biophys. J. 50, 1061 (1986).
- [5] E. Lindahl and O. Edholm, Biophys. J. 79, 426 (2000).
- [6] B. West and F. Schmid, Soft Matter 6, 1275 (2010).

Electrochemical Small-Angle Neutron Scattering (eSANS) for studies of nanoparticle redox reactions

V.M. Prabhu¹ and V. Reipa²

The redox properties of nanomaterials are crucial to applications such as in photocatalytic materials and in matching electronic band gaps for photovoltaic devices. Moreover, redox properties are also important to nanomaterial toxicology [1, 2]. With particle sizes of nanomaterials approaching the quantum confinement range and with conjugation to organic ligands (*e.g.*, to stabilize dispersions for magnetic resonance imaging), their redox properties are governed by the position of their electronic band edges and may differ from the tabulated thermodynamic properties of bulk materials.

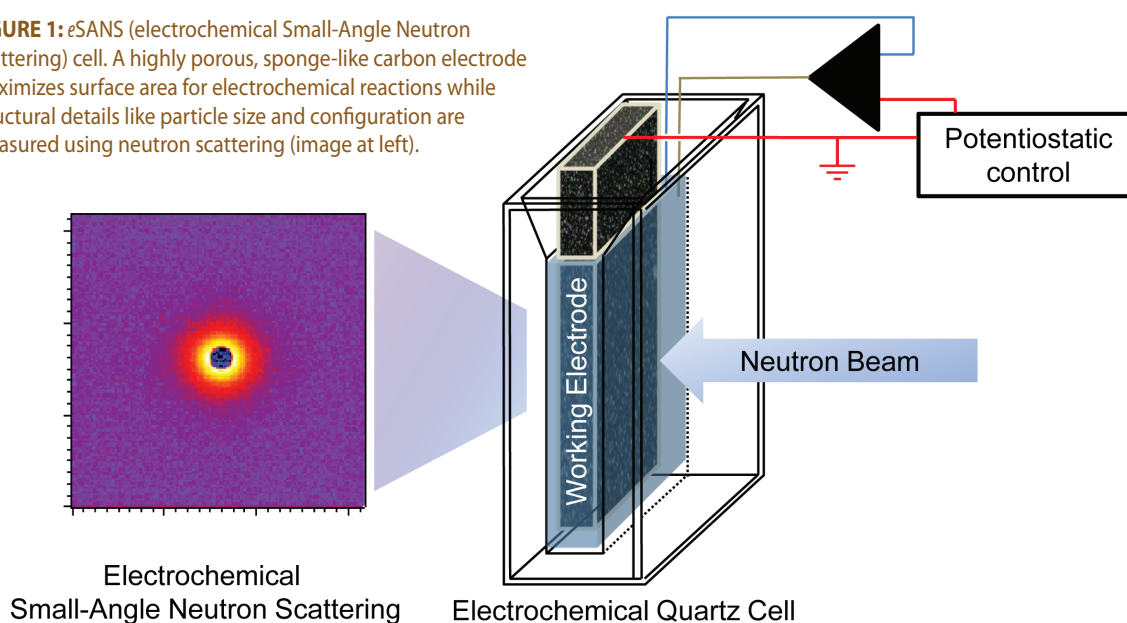
Redox reactions can be controlled in electrochemical cells via changes in electrostatic potential. Optical spectroscopies (ultraviolet-visible, infrared, fluorescence, Raman) are the most common analytical techniques to follow species undergoing redox reactions in electrochemical cells. However, these methods do not provide the nanoscale structure (size and shape) or thermodynamic interactions (virial coefficients) under the reaction conditions, as can be obtained directly through scattering methods. Neutron scattering provides a unique capability to probe transformational kinetics for organic, inorganic, as well as composite particles with wide sensitivity at the nanoscale. Here we highlight our work demonstrating *in situ* electrochemical small-angle neutron scattering (eSANS)

measurements on ZnO nanoparticles undergoing reduction at potentiostatic conditions at an inert electrode [2].

The eSANS method was tested for feasibility with ZnO nanoparticles in a 50 mmol/L NaCl deuterium oxide solution undergoing bulk electrolysis at negative potentials. A potentiostat and eSANS cell with working porous carbon electrode in the beam and counter and reference electrode (Ag/AgCl) out of the beam was used on the NG-3 and NG-7 30 m SANS instruments (Fig. 1).

The macro to nanoporous vitreous carbon electrode with high surface area is highly conductive with negligible neutron absorbance and incoherent scattering. However, the nanoporous structure does give rise to small-angle scattering and Porod scattering arising from micropores. Contrast variation SANS with mixtures of D₂O and H₂O show an open-pore structure comprised of polydisperse nanopores of 6 Å radius and 0.05 % volume fraction. This choice of electrode material meets a critical criterion for electrochemical analysis in aqueous solutions, namely low probability for electrolysis of water (high overpotential). Unlike platinum working electrodes, carbon may be used at potentials to investigate the reduction of ZnO in aqueous solutions. The bulk Pourbaix phase diagram for zinc

FIGURE 1: eSANS (electrochemical Small-Angle Neutron Scattering) cell. A highly porous, sponge-like carbon electrode maximizes surface area for electrochemical reactions while structural details like particle size and configuration are measured using neutron scattering (image at left).



¹ Polymers Division and

² Biochemical Sciences Division ; Material Measurement Laboratory ; National Institute of Standards and Technology; Gaithersburg, MD 20899

shows where the stable oxidation states lie in the potential-pH plane. These diagrams, devised by corrosion science, also show that the reduction of zinc occurs at energetic potentials that are relevant to biochemical processes [1].

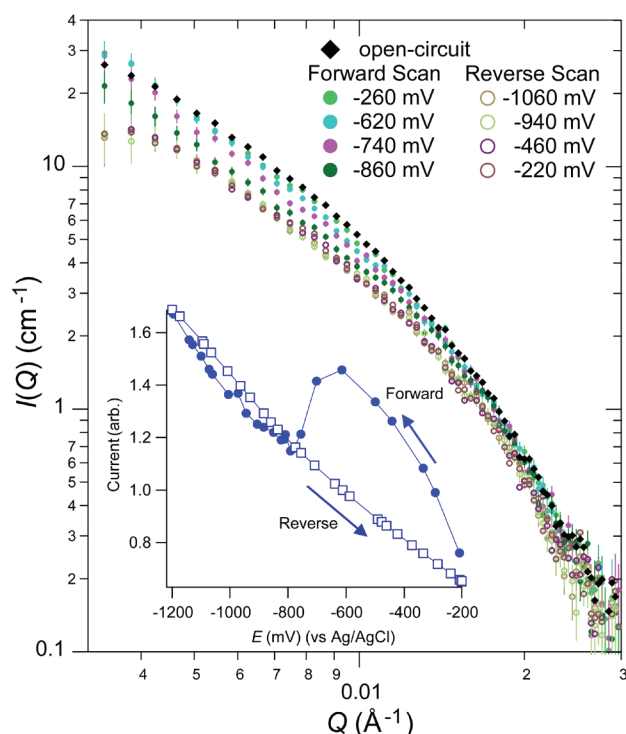


FIGURE 2: Selected *e*SANS data under forward and reverse potential scans. The inset shows current reading of the potentiostat vs controlled potential (vs Ag/AgCl).

A slow linear cathodic scan from -200 mV to -1200 mV (vs Ag/AgCl, 3 mol/L KCl electrode) at 6 mV/min was applied to a solution of ZnO in 50 mM NaCl in D_2O . *e*SANS data were collected in 20 min intervals in average 120 mV increments for the forward and reverse scans. The D_2O solvent-filled electrode was subtracted from the data to yield several *e*SANS curves at various potentials. A selection of *e*SANS data are shown in Fig. 2 to illustrate the trends. The potential range covers an expected reduction of ZnO into Zn according to bulk Pourbaix diagrams. Figure 2 shows an increase in scattering intensity as the reductive current peak at ≈ -600 mV (shown in the inset) is approached in the forward scan, followed by a decrease in intensity across a broad Q -range and meeting towards high- Q beyond the peak. The scattering pattern remains unchanged with voltage during the reverse scan, indicative of an irreversible structural change. This irreversible signature is also observed in the current readout from the potentiostat, shown in the Fig. 2 inset, whereby a reductive peak appears in the forward scan, but no change upon reversal.

The scattering was analyzed using Ornstein-Zernike plots to provide the correlation length, ξ , and scattered intensity at zero angle, $I(0)$. The correlation length for fluctuations (Fig. 3) shows an irreversible structural change with a midpoint potential ≈ -650 mV. The correlation length is on the order of

the nanoparticle radius of gyration without applied potential (open-circuit point) and increases near the current maximum during the forward potential scan, followed by a gradual drop consistent with an overall particle cluster-size decrease expected by partial ZnO to Zn transition. The complete reduction of Zn^{2+} to Zn^0 nanoparticles is unlikely, but the peak in ξ shows that clustering of multiple nanoparticles takes place, illustrating that the solution structure is dependent upon the redox potential. The reverse potential scan did not produce appreciable *e*SANS data variation, as shown in ξ plots vs E , implying an irreversible change in nanoparticle cluster size, but stable dispersion. The independent electrochemical readout and *e*SANS prove that the ZnO structure is coupled to the redox state changes quantitatively.

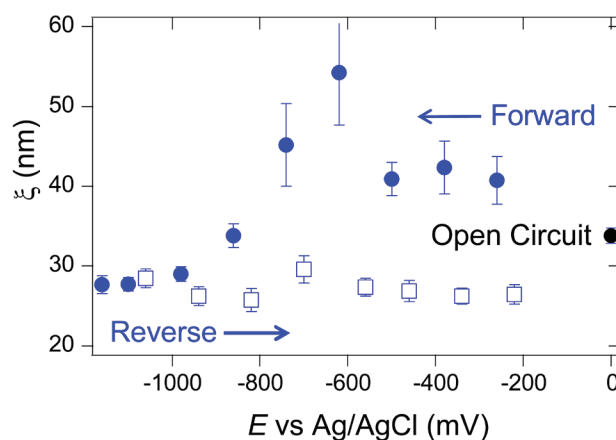


FIGURE 3: Correlation length from an Ornstein-Zernike plot as a function of voltage during forward (closed symbols) and reverse (open symbols) scans, and open-circuit (black symbol) before the scans.

Neutron scattering can follow these complex changes *in situ* under conditions that would be challenging for electron microscopy and optical spectroscopy. Combining SANS with electrochemical methods via porous vitreous carbon electrodes reduces observing an interfacial redox event into a bulk scattering method. It also allows monitoring redox structural changes in the dark, eliminating potential photochemical effects that are present when conducting optical spectroscopy of light sensitive nanoparticles, such as ZnO. The approach outlined here is extendable to contrast variation strategies. Importantly for *e*SANS, vitreous carbon has negligible neutron absorption and incoherent scattering contributions. Moreover, unlike platinum and gold working electrodes, carbon does not activate under direct beam exposure to high-flux neutrons, which makes it safer to use. This *e*SANS technique thus provides many opportunities to understand redox-related structural features of dispersed nanoparticle solutions.

References

- [1] E. Burello and A.P. Worth, *Nanotoxicology* **5**, 228 (2011).
- [2] V.M. Prabhu and V. Reipa, *J. Phys. Chem. Lett.* **3**, 646 (2012).

Identifying the shape of copper-seamed nanocapsules in solution

H. Kumari,¹ S.R. Kline,² N.J. Schuster,¹ C.L. Barnes,¹ and J.L. Atwood¹

Nanoscale materials based on the bowl-shaped members of the calixarene extended family continue to capture the imagination of the scientific community with potential applications in pharmaceuticals, catalysis, and as molecular magnets [1, 2]. One particularly robust, yet less investigated member of this family is the C-alkylpyrogallol[4]arene (PgC_n). Recent studies have shown that PgC's self-assemble into a wide range of supramolecular capsules based on both inter- and intra-molecular hydrogen bonding, as well as metal ion coordination. The guests in such capsules are generally small, polar molecules, but larger entities such as substituted pyrenes may also be housed in tubular structures and hexameric capsules.

In the discussion of a complex supramolecular solid-state structure, a question always arises: what does the solid-state structure teach about the species present in solution? The answer to this question is typically based on nuclear magnetic resonance (NMR) evidence or sheer speculation. Small-angle neutron scattering (SANS), however, is capable of providing insight into the geometry of the species present in solution, regardless of the suitability of the sample for NMR or crystallographic analysis.

Our interest in metal-seamed hexamers bearing long alkyl chains stems from the previously reported ellipsoidal assembly of C-undecylpyrogallol[4]arene hydrogen-bonded (PgC₁₁) hexamers [3]. The solid-state structure of the PgC₁₁ hexamer was obtained by a single crystal x-ray diffraction study in which it was found that the C₁₁ alkyl chains were interdigitated in two-, not three-dimensions. This deviation from a 3-D spherical arrangement of the alkyl chains for carbon chains shorter than $n = 11$ to a two-dimensional arrangement of the $n > 11$ alkyl chains led us to consider using longer alkyl chain hexamers as building blocks for even larger supramolecular assemblies. However, using single crystal x-ray diffraction for structure elucidation of nanocapsules with longer alkyl chains ($n > 11$) has proven difficult due to complexities in refining the long hydrocarbon chains. Thus, beyond the (PgC₁₁) hydrogen-bonded hexamer, no long chain hexamer has been characterized in the solid state [3].

In the current study [4], copper-seamed nanocapsules of PgCs with long side chains were prepared (Fig. 1a and 1b). However, obtaining single crystals of the copper-seamed capsules suitable for diffraction has not been possible. In this case, SANS provides the only means to measure the structure. SANS from each of the nanocapsules was measured on the NG7 30 m SANS instrument by dissolving the previously isolated nanocapsules in an appropriate solvent. Crystals of PgC₁₁Cu or PgC₁₃Cu were dissolved in CDCl₃ at a concentration of 3 % mass fraction, while PgC₁₇Cu was dissolved in deuterated o-xylene at 1 % and 5 % mass fractions.

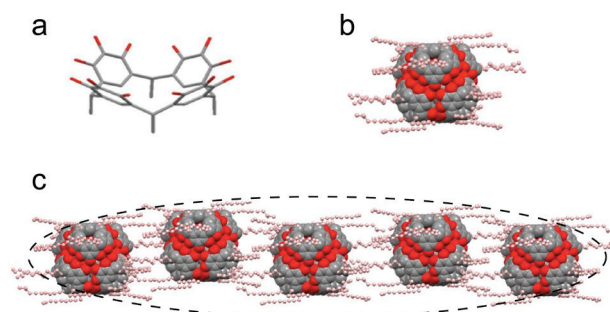


FIGURE 1: (a) Structure of pyrogallol[4]arene. Pendant alkyl chains are not drawn. (b) Hydrogen-bonded nanocapsule composed of a single C-heptadecylpyrogallol[4]arene (PgC₁₇Cu) hexamer in the solid state. (c) A model of C-heptadecylpyrogallol[4]arene (PgC₁₇Cu) hexameric nanocapsules assembled into an ellipsoid in solution, as measured using SANS (ellipse with axis ratio 4.79 to guide the eye).

The scattering from PgC₁₁Cu and PgC₁₃Cu is shown in Fig. 2, and each curve was fitted very well with a monodisperse core-shell structure, with the core comprised of the pyrogallol[4]arene + Cu, and the shell of alkyl chains. Both capsules have an overall diameter of (44 ± 0.5) Å. It is not surprising for both nanocapsules to have similar dimensions since there is little difference in the alkyl chain length.

The PgC₁₇Cu capsules, however, show a very different structure in solution as seen in Fig. 3. For PgC₁₇Cu in deuterated o-xylene, the SANS measurements are best fitted with a model of a prolate ellipsoid. The ellipsoids have a shorter axis of

¹ University of Missouri-Columbia; Columbia, MO 65211

² NIST Center for Neutron Research; National Institute of Standards and Technology; Gaithersburg, MD 20899-6102

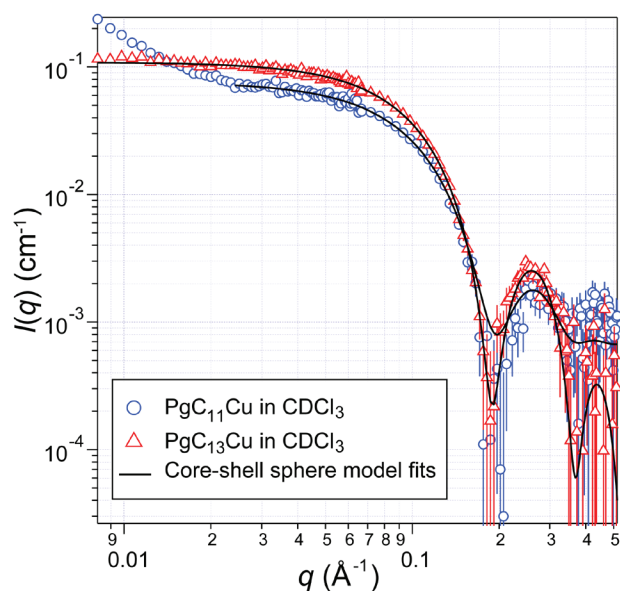


FIGURE 2: SANS data for copper-seamed hexamers of C-undecylpyrogallol[4]arene (PgC_{11}Cu ; blue circles) and C-tridecylpyrogallol[4]arene (PgC_{13}Cu ; red triangles) in CDCl_3 . The solid lines are resolution-smeared core-shell sphere model fits, and error bars on the data represent one standard deviation of the intensity.

(48 ± 0.02) Å diameter and a major axis of (230 ± 0.2) Å. The ellipsoid diameter is larger compared to the 44 Å diameter of the spherical PgC_{11}Cu and PgC_{13}Cu copper-seamed hexamers, as expected. The long axis dimension indicates the presence of one nanocapsule along the minor axis and approximately 5 nanocapsules chained together along the long axis of the ellipsoid, held together through the interdigitation of the C_{17} alkyl chains. Such a solution phase ellipsoidal nanocapsular assembly is drawn in Fig. 1c from the dimensions fitted to the data in Fig. 3. The ellipsoidal shape of PgC_{17}Cu does not change with concentration (1 % or 5 %) mass fractions, indicating that the ellipsoidal assembly is an equilibrium structure rather than just aggregation or incomplete dissolution of the hexamers. These results reveal, to some extent, the limits to which self-assembled entities can stabilize in solution without aggregation, although it is reasonable to expect more complex assemblies to crystallize out.

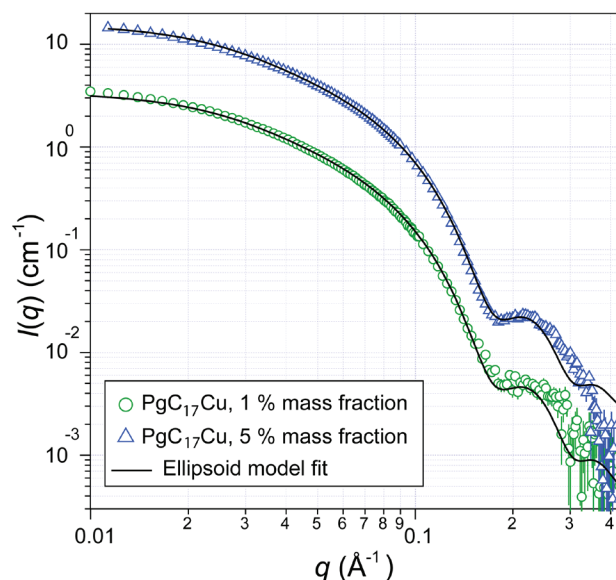


FIGURE 3: SANS data for PgC_{17}Cu in deuterated o-xylene. The solid line is a global fit to both data sets using a resolution-smeared prolate ellipsoid model.

In summary, the current study has revealed the stability of PgC_{11}Cu and PgC_{13}Cu hexamers in solution, which form core-shell spheres, and the formation of interdigitated ellipsoidal assemblies for PgC_{17}Cu containing longer alkyl side chains. Such interlocking side chains facilitate the formation of larger multi-capsule assemblies that mimic biological membranes connecting two adjacent cells or nanocapsules. SANS measurements have proven valuable in determining the solution structure of species that are difficult to crystallize, making solid-state structure determination impractical. This detailed structural characterization provided by SANS will help in understanding the limits of guest inclusion and the mechanisms of metal-organic nanocapsule formation, eventually allowing synthesis directed towards specific applications.

References

- [1] J.W. Steed, J.L. Atwood, *Supramolecular Chemistry*, 2nd Ed., Wiley, Chichester, 2009.
- [2] J.L. Atwood, E.K. Brechin, S.J. Dalgarno, R. Inglis, L.F. Jones, A. Mossine, M.J. Paterson, N.P. Power, S.J. Teat, *Chem. Commun.* **46**, 3484 (2010).
- [3] G. W.V. Cave, S.J. Dalgarno, J. Antesberger, M.C. Ferrarelli, R.M. McKinlay, J.L. Atwood, *Supramol. Chem.* **20**, 157 (2008).
- [4] H. Kumari, S.R. Kline, N.J. Schuster, C.L. Barnes, J.L. Atwood, *J. Am. Chem. Soc.* **133**, 18102 (2011).

Characterizing dense polymer-nanoparticle mixtures by neutron scattering

S.Y. Kim,¹ K.S. Schweizer,^{1,2,3} and C.F. Zukoski^{1,2,3}

Achieving desirable properties in colloidal suspensions and polymer nanocomposites depends on controlling particle spatial organization and material microstructure. In concept, good dispersion of nanoparticles can be obtained by coating them with polymer layers in order to induce a repulsive inter-particle potential between them. Understanding the nature of, and what controls, the structure and properties of these bound layers remains a challenge. Obstacles limiting progress include (i) developing experimental tools for measuring the attraction strength of a polymer coated surface, (ii) differentiating polymer segments adsorbed on the nanoparticle surface from bulk polymer in the dense polymer solutions or melts, and (iii) measuring the packing structure of *both* segments and particles over a wide range of length scales and volume fractions. In this highlight we present experimental results addressing the above issues using contrast matching small angle neutron scattering (SANS) techniques in a thermodynamically stable system that is a mixture of short chain polymers, nanoparticles and solvent. By measuring the intensity of scattered neutrons while varying the scattering contrast between components using D₂O/H₂O mixtures, all three partial coherent structure factors arising from polymer-polymer, particle-particle, and interfacial concentration fluctuations can be determined.

Silica nanoparticles of diameter $D = 40$ nm are synthesized via the standard Stöber process and suspended in dense polymer solutions composed of poly(ethylene glycol) (PEG) of molecular weight 400 Da and D₂O and H₂O solvents. Polymer concentration, defined as the ratio of PEG to (PEG-plus-solvent) volumes (R_{PEG}), is fixed at a high value of 0.45. This ensures physical behavior representative of melts since the monomer collective density fluctuation correlation length is of order of the nanometer segment size. Silica volume fraction (ϕ_c) is varied from 0.05 to 0.30. All experiments are performed at room temperature, and we find no evidence of aggregation or phase separation. Intensities of scattered neutrons were measured in the range of $0.004 \text{ \AA}^{-1} < q < 0.04 \text{ \AA}^{-1}$, which corresponds to a reduced wave vector range of $1.6 < qD < 13$.

The intensity of scattered neutrons at wave vector q , $I(q)$, has three contributions:

$$I(q) = n_c \Delta \rho_c^2 P_c(q) S_{cc}(q, \phi_c) + 2 \Delta \rho_c \Delta \rho_p \sqrt{n_c n_p} P_c(q) S_{pc}(q) + n_p \Delta \rho_p^2 S_{pp}(q), \quad (1)$$

where $n_j = \beta_j V_j^2$, and β_j and V_j are the number density and unit volume of the j^{th} component, respectively. $\Delta \rho_j$ is the difference

in scattering length density (SLD) between component j and the medium, $P_c(q)$ is the silica particle form factor, and $S_{ij}(q)$ is the partial structure factor associated with different components and their cross correlation terms (pp , pc , cc) where the subscript p stands for polymer and c for silica particles [1].

In order to extract all three partial structure factors $S_{ij}(q)$ at a fixed silica particle volume fraction ϕ_c , the D₂O/H₂O ratio of the solvent is varied so that the SLD contrast of different components is changed accordingly. For example, when the D₂O/H₂O ratio is chosen to match the SLD of polymer ($\Delta \rho_p = 0$) the measured scattering intensity is caused only by the silica particles, so that Eq. (1) reduces to $I(q) = n_c \Delta \rho_c^2 P_c(q) S_{cc}(q, \phi_c)$. The form factor $P_c(q)$ of the silica particles is determined at a low particle volume fraction. Then $S_{cc}(q)$ at large concentrations is obtained by dividing the scattering intensity by $n_c \Delta \rho_c^2 P_c(q)$ [1]. Using the results from three D₂O/H₂O ratios, we solve the multiple linear equations simultaneously by multiple linear regression fitting methods to obtain the polymer-polymer $S_{pp}(q)$ and polymer-particle $S_{pc}(q)$ partial structure factors. The technical details are given in [1].

Measured scattering patterns are compared with the standard polymer nanocomposite version of the *PRISM* integral equation theory where the solvent enters implicitly, details of which are thoroughly documented in the literature [1-3]. All species interact via pair decomposable site-site hard core repulsions. The chemical nature of the mixture enters via an exponential monomer-particle interfacial attraction, $U_{pc}(r) = -\epsilon_{pc} \exp\{-[r - (D+d)/2]/\alpha d\}$, where ϵ_{pc} is the net energy released when transferring a polymer segment (diameter, d) of the freely jointed chain from a concentrated polymer solution environment to the nanoparticle surface (diameter, D), and $\alpha = 0.5$ is a spatial range parameter. A chain length $N = 100$ is used as representative of the equilibrium behavior of polymers [2]. With all the information, the partial structure factors ($S_{ij}(q)$) can be calculated using *PRISM* theory [2].

Experimental partial structure factors at various ϕ_c are shown in Fig. 1. The partial structure factor of silica particles $S_{cc}(q)$ has a form characteristic of a correlated fluid. Both $S_{cc}(q)$ and $S_{pp}(q)$ display peaks near $qD \approx 4$ to 6. The peak in $S_{cc}(q)$ is associated with a liquid-like nanoparticle packing, while the intense “microphase-like” peak in $S_{pp}(q)$ occurs at a length scale which greatly exceeds that of the PEG radius-of-gyration. Its physical origin is spatial correlations mediated by adsorbed polymers with non-bulk-like properties mediated by nanoparticles [1].

¹ Department of Chemical & Biomolecular Engineering; University of Illinois; Urbana, Illinois 6180

² Department of Materials Science; University of Illinois; Urbana, Illinois 61801

³ Frederick Seitz Materials Research Laboratory; University of Illinois; Urbana, Illinois 61801, USA

Experimental $S_{cc}(q)$ and $S_{pp}(q)$ were compared with theoretical calculations for interfacial attraction strengths: $0.25 \text{ k}_B T < \varepsilon_{pc} < 1.05 \text{ k}_B T$ (not shown, see [1]). Good agreement between theory and experiment is found for both $S_{cc}(q)$ and $S_{pp}(q)$ with a common value of $\varepsilon_{pc} = 0.45 \text{ k}_B T$ for all particle volume fractions.

In Fig. 1, increasing ϕ_c suppresses long wavelength ($qD < 4$) nanoparticle concentration fluctuations $S_{cc}(q)$, but enhances polymer fluctuations $S_{pp}(q)$ in the same range. At larger qD the increased height and shift of the first peak in $S_{cc}(q)$ indicates a more ordered first neighbor shell, while increased coherency of polymer segment density fluctuations on the nanoparticle length scale is deduced from the form of $S_{pp}(q)$. The right inset shows that the cross partial structure factors $S_{pc}(q)$ are negative, and with increasing wave vector they decrease and goes through a minimum at $qD \approx 4$ to 6. These features indicate anti-correlation of particle and polymer segment concentration fluctuations over a wide range of length scales. As ϕ_c increases, the minimum in $S_{pc}(q)$ grows in magnitude and occurs at larger qD , tracking the increased local interparticle correlation and also the growth of the $S_{pp}(q)$ peak. Taken together, there is remarkable agreement between *all three* experimental structure factors and *PRISM* theory over a wide range of wave vectors and all volume fractions based on a *volume fraction independent* value of ε_{pc} . This provides significant support for the intrinsic material origin of ε_{pc} , the dominance of the interfacial attraction strength in determining both polymer and particle microstructures.

To characterize adsorbed polymer layers on the nanoparticles *in situ*, a system is investigated when the SLD of silica particles is matched by the solvent ($\Delta I_c = 0$). Hence, the scattering intensity is due to non-bulk-like polymer concentration fluctuations from shells of adsorbed polymer (cartoon in Fig. 2). The polymer partial structure factor in Eq. (1) can then be approximated as $S_{pp}(q) \approx S_{pp}^*(q) P_s(q)$, where $P_s(q)$ is the form factor of the polymers adsorbed on a silica particle surface. The adsorbed polymer forms a shell around a silica particle. $S_{pp}^*(q)$ is the structure factor associated with correlations between the centers-of-mass (CM) of these polymer shells. We argue that the CMs of the adsorbed polymer shells to a good approximation have the same correlations as that among the silica particles ($S_{pp}^*(q) \approx S_{cc}(q)$). Under this assumption, an experimental form factor of the polymer shell $P_s^*(q)$ can be defined and obtained.

Figure 2 presents the experimental $P_s^*(q)$, and the *PRISM* theory analog determined in the same manner. We note that $P_s^*(q)$ results from well-defined adsorbed polymer layers (cartoon) that are structurally distinct from bulk polymers. Varying ϕ_c , the resulting $P_s^*(q)$ values overlap well. Using scattering length density parameters at a match condition and a core-shell model form factor [4], the adsorbed shell thickness is determined [1] to be $\approx 0.7 \text{ nm}$ to 1 nm , which is modestly larger than the PEG segment length. $S_{pp}(q)$ and $S_{pc}(q)$ contain critical information that allows the determination of the thickness of the polymer layer adsorbed on the silica nanoparticles under dense conditions.

In summary, using contrast matching neutron scattering we have measured and compared to the theory, for the first time, all collective partial structure factors in concentrated polymer-nanoparticle mixtures. We established the existence and size of adsorbed polymer layers and their consequences on dense solution microstructures.

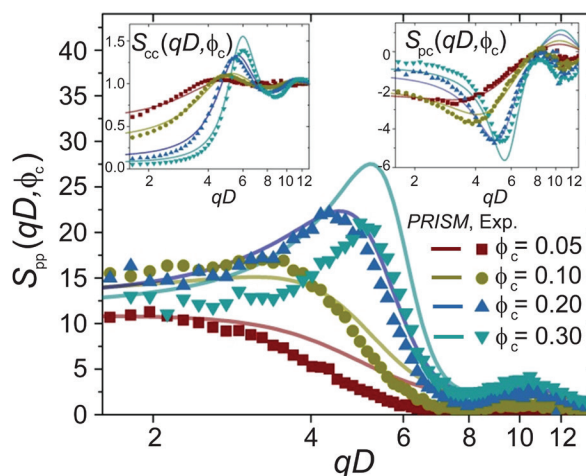


FIGURE 1: Polymer collective structure factor S_{pp} at different nanoparticle volume fractions, ϕ_c . Corresponding curves are the *PRISM* theory results for $\varepsilon_{pc} = 0.45 \text{ k}_B T$. Left and right insets: S_{cc} and S_{pc} under the same conditions.

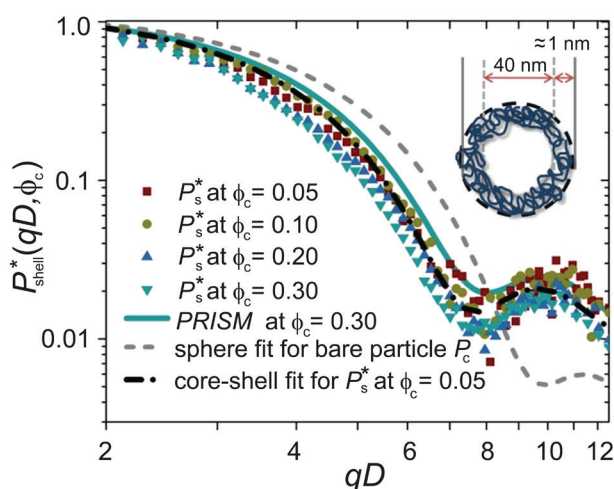


FIGURE 2: Adsorbed polymer shell form factor ($P_s^*(q)$) from *PRISM* theory (solid curve) and experiment (dots). The dash-dot line is a fit to the form factor of a core-shell model. The bare spherical-particle form factor, $P_c(q)$, is shown as the short dashed curve for comparison to $P_s^*(q)$.

References

- [1] S.Y. Kim, K.S. Schweizer, C.F. Zukoski, *Phys. Rev. Lett.* **107**, 225504 (2011).
- [2] L.M. Hall, B.J. Anderson, C.F. Zukoski, K.S. Shweizer, *Macromolecules* **42**, 8435 (2009).
- [3] S.Y. Kim, L.M. Hall, K.S. Schweizer, C.F. Zukoski, *Macromolecules* **43**, 10123 (2010).
- [4] S.R. Kline, *J. Appl. Cryst.* **39**, 895 (2006).

A Liquid Deuterium Cold Neutron Source for the NBSR

R. E. Williams, P. Kopetka, J. M. Rowe and M. Middleton

A liquid deuterium cold neutron source is being designed and built to replace the existing liquid hydrogen source installed in 2002. The LD₂ source will shift the neutron spectrum to lower energies, with gains of 1.4 to 1.8 for neutrons with wavelengths between 4 Å and 9 Å. This project has received funding from the National Nuclear Security Administration Global Threat Reduction Initiative (DOE) as a mitigation strategy to offset the expected 10 % flux decrease in NBSR beams when the reactor is converted to low-enriched uranium (LEU) fuel.

Work on the deuterium source actually began a few years ago but was suspended for lack of sufficient funding for a new helium refrigerator. Monte Carlo simulations using MCNP indicated that a very large volume source was needed to realize the above mentioned gains, and the anticipated nuclear heat load would exceed the capacity of the existing refrigerator. The earlier work showed that the bigger the LD₂ volume the greater the gain, but the gains increase more slowly than the heat load. As a result, it was decided a 40 cm long by 40 cm ID vessel would provide excellent gains with a modest heat load of about 3500 W. At this power, it is expected that the void fraction in the boiling liquid deuterium will be 13 % ± 5 %. The gain as a function of wavelength is shown in Fig. 1 for the 40 x 40 source. “Fine-tuning” of the gains can be accomplished by varying the re-entrant hole depth, with a deeper hole favoring short wavelengths, and vice versa; a 18 cm depth maximizes the gain between 4 Å and 8 Å. The hole diameter, 22 cm ID, assures full illumination of all of the neutron guides to at least 10 Å.

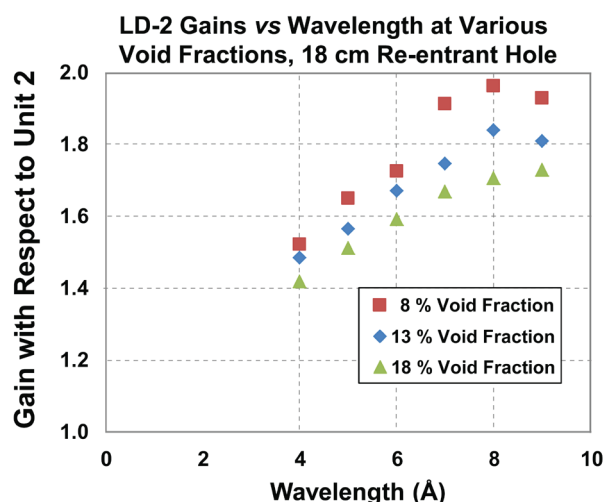


FIGURE 1: Expected gains of the LD₂ cold source with respect to the existing LH₂ source.

Figure 2 is an MCNP geometry plot of the source (plan view) in the cryogenic thimble of the NBSR. The source will be surrounded by insulating vacuum and a helium containment

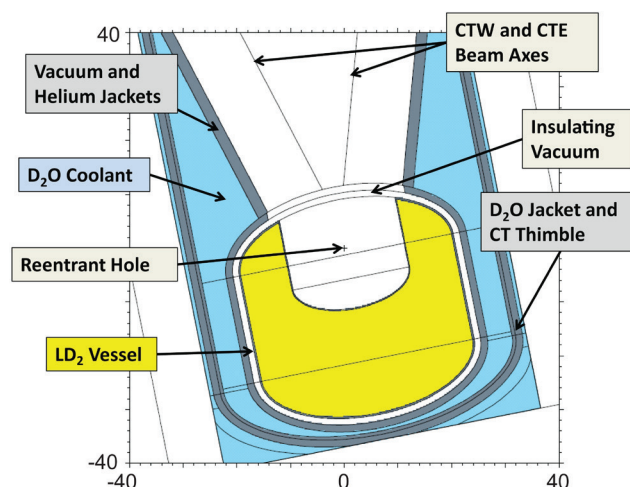


FIGURE 2: A plot of the MCNP geometry used for cold neutron optimization and nuclear heat load calculations showing the major features of the 40 x 40 cm LD₂ source.

jacket strong enough to withstand the pressure of the maximum hypothetical accident (these jackets are combined in the model). The cryostat assembly must also be cooled with D₂O. This water jacket serves as part of the core reflector, so it will surround the source to the greatest extent possible without cutting into the cold neutron beams. The assembly will be installed horizontally in the CT cavity and a deuterium condenser will replace the existing LH₂ condenser on the north face of the biological shield.

The thermal-hydraulic design of the LD₂ source is based on the very successful horizontal source at ILL in Grenoble. Its designers published the results of their pressure and temperature measurements on a full-scale LD₂ mockup of that source, which has a slightly lower heat load, 3000 W, but a much smaller volume. By scaling up the inside diameters of the liquid supply line to 22 mm and the two-phase return line to 31 mm, the NBSR source can easily operate as a thermosiphon with the available driving head of about 2 m between the condenser and the source. A perforated section of the return line at the top of the vessel allows a two-phase mixture of LD₂ and the vapor generated in the source to flow back to the condenser, ensuring that the vessel remains full of liquid. The source will operate at 23 K, the boiling point of deuterium at 1.0 bar.

The conceptual design of the LD₂ source is nearly complete. A contract for a 7 kW refrigerator was awarded in April; its delivery is scheduled for early 2014. Specifications for a 6 kW deuterium condenser and a 16 m³ ballast tank have been sent to procurement. The mechanical design of the moderator vessel is complete so it will soon be possible to build and pressure-test a prototype. The goal is to build or procure all the major components in the next 3 years and install the source shortly thereafter.

Expansion Activities During the Planned Outage

In April 2011, the reactor shut down for an extended outage in order to accomplish the many tasks associated with the multi-year NCNR Expansion Project and infrastructure enhancements. Planning for all of the activities in this major outage began well over a year prior to the shutdown and involved organization and planning across Reactor Operations and Engineering (ROE) and the Research Facility Operations (RFO) Groups. Major construction work in building 235 (supported through the American Recovery and Reinvestment Act) included a number of reliability enhancements to the facility. This work was carried out by independent contractors and it imposed specific scheduling constraints requiring detailed coordination with the work carried out by the NCNR staff. This period included the most complex set of activities undertaken by the NCNR in any single reactor shutdown period. The results of the detailed planning and coordination were that all planned projects were completed successfully and the facility was able to restart for user operations in April 2012. This section describes some of the major activities carried out by ROE and RFO during the extended outage.

Reactor Operations and Engineering Activities

Reactor Spent Fuel Storage Pool Refurbishment

The spent fuel storage pool contains 125 m³ (33 000 gallons) of water with trace levels of radioactivity requiring disposal as hazardous waste or temporary storage in tank trucks for any work requiring the pool to be emptied. Hence, the NCNR evaluated several contractors and chose to use a commercial diver company that could perform all the activities, including recoating the pool, without draining the original pool water. The selected dive company had extensive experience doing similar projects at nuclear power plants. Performance of the refurbishment with divers added a degree of complexity but this was outweighed by the benefits of significantly reduced personnel radiation doses and lowered safety risk (working around the empty pool). One of the functions of the water in the pool is to provide radiation shielding from the radioactive materials stored within the pool. Removal of the water prior to commencing the refurbishment work would likely have increased the radiation exposure to the individuals working within the drained pool until the stored equipment and loose radioactive materials were removed.

Initial work required plasma cutting of several large storage racks so they could be removed and placed into waste disposal



FIGURE 1: Diver (right) exiting the spent fuel storage pool.

containers. When the divers began to remove the original coating on the concrete walls of the pool, they found that removal was unexpectedly difficult due to the concrete surface not being trowel finished as per the original building specification. Because of the rough finish, the divers had to hand scrape the material off the concrete instead of using a power washer to do so. Application of the new coating also was more difficult than expected due to the rough texture of the pool walls. Nonetheless, the dive team completed the recoating of the pool and the installation of new fuel storage containers without impacting the overall restart schedule.

Replacement Secondary Cooling System

It was noted while planning the expansion project that the new neutron guides would pass over the existing secondary cooling pump rooms and block an access hatch used to remove pumps and motors for maintenance or replacement. Due to the age of the secondary cooling system and the expected access problems, the decision was made to replace the system, installing it in a new building. The original secondary cooling system used six, constant speed pumps but the new system has four variable frequency drive pumps with only three needed to cool the reactor and auxiliary systems. The additional cooling provided by a new 7 MW cooling tower beside the original 20 MW tower supported the future installation of a liquid deuterium cold neutron source and added supplemental heat removal for the hot and humid Maryland summers. The power for these new systems came from a new electrical substation also installed behind the NCNR. The substation reduced the load on the NCNR electrical system which would then support the increased electrical demand from the neutron instrumentation growth in the expanded guide hall.

Commissioning and Operational Phase of the Thermal Shield System

The reactor is equipped with a radiation shield (the “thermal shield”) to absorb radiation, allowing closer access around the reactor vessel for experimental equipment and less concrete biological shielding protecting personnel. It is located immediately around the vessel and consists of a 15 cm (6 inch) thick steel tube clad on the inside with a 5 cm (2 inch) thick lead layer. Soldered onto the inside diameter of the steel tube (thus surrounded by the lead) are 188 copper cooling lines which circulate water to allow the removal of heat that is deposited into the thermal shield by intense gamma radiation generated in the reactor core, in order to keep the shield at a temperature where it does not change shape under its own weight. Over the many years of pumping water under pressure, the thermal shield plumbing has developed tiny leaks which are impossible to repair. The upgrade converted the previously pressurized coolant-flow system into a vacuum operated system that “pulls” the coolant through the copper lines. The operating vacuum is created by an aspirator which maintains the entire cooling system at a pressure lower than atmospheric and prevents liquid from leaking from the small holes in the copper lines. The upgraded system was prototyped at the NCNR by Paul Brand and Tony Norbedo over several years to evaluate the flow method and develop chemistry controls.



FIGURE 2: Tony Norbedo and Paul Brand inspecting headers of the thermal shield cooling system.

The complete upgrade design was fully mocked-up at the factory and tested prior to any demolition of the original NCNR system to minimize the risk to the NCNR and the Outage schedule. Some cooling lines had been isolated because the leaks were found to be too large and temporary repairs were not successful. The upgrade to the thermal shield system has allowed some of these lines to be returned to service and increase the cooling to these locations in the thermal shield. The upgrade for the thermal shield cooling system included a full digital monitoring and

control system. This system acquires flow rate data from all 188 cooling lines and many other process parameters, permitting detailed system performance analysis and automatic protection action when certain parameters are out of specification. The data acquired helped identify flow oscillations on some lines early during the testing phase which were eliminated by the installation of a bypass line to reduce local flow starvation. The trending of process data to identify system design problems or potential equipment failures is a powerful diagnostic tool that has not been previously available for many of the NBSR systems but will eventually be available for nearly all NBSR parameters as the reactor control console is upgraded to a full digital monitoring system.

Reactor Control Room Upgrade

The NBSR reactor control console is in a continuous state of evaluation and upgrade to assure the equipment is maintained at a high level of reliability. Systems are upgraded if repairs are not successful or parts are no longer available. A complete replacement of the reactor control console was planned prior to the Outage but resource limitations and unacceptable scheduling risk convinced NCNR management that a longer term console replacement project schedule was preferred. During the Outage, a majority of the indications, alarms and process (non-reactor) controls were replaced with systems that could communicate via the dedicated, isolated control room network. These systems could now provide data to an acquisition system where it would be stored for analysis or be used for real-time reactor plant monitoring. A new facility was constructed near the NBSR Control Room to house the data acquisition system servers and allow prototyping of upgraded control systems and the HMI (Human-Machine Interface) screens.

Installation of Second Hydrogen Cold Source in BT-9

The addition of new neutron guides during the Expansion required moving the MACS (Multi-Angle Crystal Spectrometer) instrument. MACS uses cold neutrons so the instrument movement project included the installation of a second, smaller liquid hydrogen cold source. Unexpected conditions and material degradation within the beam tube required machining of the inner beam tube walls to permit the installation of the cold source unit. Cooldown and liquefaction of hydrogen in both cold sources finally occurred in mid-March because the testing of both cold sources and operating the reactor above 1 MW required the new secondary cooling system to be functional. Initial testing of the cold sources at full power (20 MW) occurred on April 12 with the new systems accepted for normal operation on April 24. Neutron spectrum measurements from the BT-9 cold source will be performed when MACS is fully installed and operating sometime in early 2013.



FIGURE 3: Robert Williams monitoring the first cool down of the two cold sources that use the same refrigerating system.

Research Facility Operations Activities

Installation of the new guide network

A central feature of the Expansion Initiative is the addition of a new guide network to accommodate instruments in the new guide hall. Installation of these five new guides presented a series of engineering, technical, and logistical challenges that are described here.

Precise alignment of individual guide elements is critical to the transmission efficiency and ultimate performance of any neutron optics system and installation of the Expansion guide network posed specific new challenges. Whereas the existing guides at NCNR (NG-1 through 7) have straight flightpaths and are of rectangular cross-section, the new NG-A through D guides are designed to capitalize on major developments and improvements in neutron guide optics and design technology over the past 20 years. They are curved to help reduce spectrometer background arising from gamma rays and fast neutrons by siting instruments beyond the line-of-sight of the source and, in the case of NG-A and NG-D, have quasi-elliptical cross-sections when viewed from the side to improve transmission efficiency and beam reshaping.

Moreover, installation of the new guides had to be achieved within the tight constraints imposed by existing Facility installations. The guides traverse a path from the cold neutron source situated in the confinement building, through the D-wing - a former utility area - and then, finally, into the G-100 guide hall. These factors were compelling in the decision by the in-house engineering and technical installation staff to switch from conventional analogue alignment methods, which typically use theodolites, and adopt new techniques that use laser-tracker and digital level technology coupled with a portable co-ordinate measuring machine to characterize each guide section.

Prior to installation, each of over 360 individual sections comprising the 260 m long guide network was first characterized (fiducialized) using the measuring arm (see Fig. 4). At key stages

of the installation, local control networks were set up using the laser tracker to define co-ordinate measurement systems in the confinement building, the D-wing, and the guide hall. These three discrete areas were then linked-or "tied in"-to form a Facility-wide coordinate system by employing optimized line-of-sight penetrations that were bored between each area as part of the outage construction activities. Local area coordinate networks were also set up in a high bay assembly area and a portion of the new guide hall to enable pre-assembly and alignment of a large percentage of the guide network prior to final installation. These pre-assembly and alignment activities enabled the final installation to proceed smoothly and with minimal delay. This efficiency during installation ultimately proved critical in maintaining the outage schedule.



FIGURE 4: Doug Ogg (left) and Mike Rinehart use a measuring arm to characterize an element of guide NG-C.

At the start of the outage, technical staff removed hundreds of tonnes of steel and wax shielding from the confinement building to expose the Cold Tube West (CT-W) viewport to the hydrogen cold source required by the new guides. This location was formerly occupied by the multi-angle crystal spectrometer (MACS) and so the spectrometer also required dismantling. A full three months of preparatory work was required before installation of the new guides could begin in the confinement building.

The origin of the guides is the "in-pile" plug (Fig. 5). This element required alignment inside the biological shield of the source to within a fraction of a degree in order to ensure that the resulting guide flight paths were correctly aligned and conformed to tight constraints imposed by existing Facility building infrastructure.

The in-pile guide monolith is constructed using highly-polished aluminum rather than a conventional glass substrate material. Recent advances in supermirror technology have enabled this use of metal substrates which offer considerable advantages



FIGURE 5: The in-pile plug containing the metal-substrate supermirror guides comprising the first section of the new guide network.

given their ability to withstand the high levels of neutron bombardment received close to the source. The shutdown also provided an ideal opportunity to replace the CT-E plug, serving the existing NG-5 through 7 guides, with metal in-pile guides so as to promote reliable operations for those guides in the future.

Once the in-pile plug had been set, a series of steel vacuum vessels containing sections of glass guide were then installed. All the new guides have curved flightpaths and so, as the beamlines diverge, the guides transition from a monolithic housing to discrete vacuum jackets and dedicated shutter mechanisms before leaving the confinement building. Although the confinement building houses only some 25 % of the total guide network, it was arguably the most challenging phase of the installation with the addition of the in-pile plug, shutter, vacuum and other ancillary systems in this area. Today, the unremarkable shielding that can be seen covering this area belies the true complexity of the guide system housed inside.

Construction activities played a major role in the guide installation project, not least in the conversion of the D-wing utility area into a structurally reinforced chamber capable of supporting the new guide and shielding infrastructure and with the necessary wall penetrations through which the steel vacuum-jacketed guides pass from the confinement building and into the guide hall. Physical access into the D-wing was extremely limited. During construction and installation, all building materials and components of the guide network had to pass either through the wall penetrations (see Fig. 7 below) or enter via a personnel door of standard dimensions. These restrictions were skillfully overcome by first constructing sidewall shields with poured-in-place concrete before individual approximately 7.6 m (25 ft) long steel vacuum-jacketed guide sections for each guide were rolled into place from the guide hall side. The guide sections were all pre-aligned and, by virtue of the smooth transport mechanism designed, needed only minimal adjustment once installed within the confines of the D-wing. The D-wing was completed by installation of a 61 cm (2 ft) thick roof shield. In this case the execution owed less to ingenious design and more to brute force with the 25.4 t (65 000 lb) shield constructed using over 2700 pavers — all stacked by hand!



FIGURE 7: Danny Ogg and Mike Rinehart work with Dan Adler (center) in aligning the vacuum-jacketed NG-D guide inside the D-wing.



FIGURE 6: A view of the new guides and shields in the latter stages of installation in the confinement building, coming from the reactor on the right and entering D-wing on the left. (The apparent curvature is an artifact arising from the fisheye-lens camera.)



FIGURE 8: Guide installation in G-100. Viewing left to right, the completed NG-D and NG-C guides are seen emerging from end windows of the blue shielding while installation of the as-yet unshielded NG-B guides continues behind.

The final installation phase in the guide hall brought the relief of an essentially open and vacant site in the new (East) guide hall. Design and installation challenges remained however, not least along the boundary region between old and new guide halls where guide and shield components are located outside the reach of the overhead cranes of both halls. This required using a forklift truck to carefully maneuver massive shielding blocks to within inches of the now exposed glass — in G-100 the guide sections are no longer housed in steel vacuum jackets. It is testimony to the skill of the installation team that throughout the project, despite multiple handling activities, not a single segment of guide glass was damaged.

The final sections of the NG-D through B guides were installed rapidly once the network entered within the reach of the crane in the new guide hall. On NG-D, local instrument shutters and monochromator tables were installed in sequence with the guides. Since the fit-up of electrical and instrument controls proceeded in parallel with the guide installation, the Polarized Beam and MAGIk reflectometers were already being installed on NG-D while the NG-B guides were being completed. With the 10 m SANS instrument already pre-staged for installation on the lower NG-B guide, the first three instruments on the new guides are poised for the start of commissioning activities.

TABLE 1: Guide installation facts and figures

Total Guides installed length (m)	261
Total Guide elements aligned	361
C-100 Shielding installed (t/lbs)	136/300 000
D-100 Shielding hand-stacked (t/lbs)	29.5/65 000
G-100 Shielding installed (t/lbs)	453.6/1 000 000

Neutron Source Operations

The first startup to 100 kW of the neutron source from the extended shutdown occurred on February 8, 2012 for low power testing. Higher power testing required the new secondary cooling system to be functional and 1 MW operation for radiation surveys occurred on March 15. The following month was required to bring systems back into service and to commission new equipment such as the secondary system, thermal shield cooling system, and the BT-9 cold source. The NBSR officially started normal user operations on April 26 and the Outage was declared over after 389 days. Although Users were now able to perform experiments, the NCNR staff continued working hard behind the scenes to complete the installation and continue testing of some equipment not considered essential for initial User operations but necessary for long-term, reliable operation. Essentially, the first few cycles after the Outage were used to evaluate and operate new systems or those that had not been used for over a year while providing neutrons to the User program. Relatively few unplanned shutdowns of the neutron source occurred from equipment problems after the restart of user operations. The NCNR neutron source achieved a remarkable 92 % reliability in 2012 owing to the high quality of the maintenance and upgrades performed by the Reactor Operations and Engineering group (ROE) and their ability to safely make modifications to systems without requiring the reactor to be shutdown.

A system that had not been installed on April 26 was the fuel transfer system (FTS). The system is used to move spent fuel

from the reactor into the storage pool and, occasionally, back to the reactor. The FTS had been partially refurbished during the Outage but could not be tested until it was returned to the pool area in late March. The FTS did not operate correctly during testing and it was found that the hydraulic seals that actuated the mechanism leaked excessively. Waiting for the new seals to arrive would have delayed the return to normal User operations by several weeks. NCNR management chose to startup the facility and return to 20 MW operations as scheduled and install the FTS in the spent fuel pool during the next shutdown. Additional problems with the FTS were discovered over the next month and the system was not ready for installation as expected. The neutron source was started up without refueling to support the annual neutron scattering school and then shutdown again after one week of operation. The FTS was finally tested and reinstalled on July 2.

The upgraded thermal shield system performed remarkably well but some problems were noted during testing in the first two cycles after the Outage. Cooling water flow rate to each of the 188 lines is an important parameter to assure protection of the thermal shield. If lines in a particular area have no flow or significantly reduced flow it could damage the lead of the thermal shield. The thermal shield instrumentation system prevents damage to the lead if cooling flow is lost by causing an automatic reactor power reduction (reactor rundown). Using the new trending function of the digital control system it was noted that flow in some lines dropped after the reactor reached

full power and this sometimes caused a reactor rundown. The ROE engineers and operators developed several mitigation methods including scouring out the tubing with a mild, non-reactive abrasive to remove loose debris clogging the lines and this improved flow rates on some lines. There have been no low-flow rundowns since the implementation of these improvements on the system but the ROE continues to monitor the performance.



Senior Reactor Operator
Jeff Burmeister starts up the
NCNR reactor.

Facility Development

Facility support staff met the end of the long outage by successfully bringing the existing complement of instruments back into operation after nearly a year shutdown. In addition to activities directly associated with the Expansion Initiative described earlier (p. 47) progress was also made in many other areas.

Instrument Development

NCNR has two major new instrument projects running: CANDoR, a white beam reflectometer, and the Very Small Angle Neutron Scattering spectrometer (vSANS). Detector procurement and development for these instruments has been a major component in their programs this year.

NCNR has initiated a development program for solid state scintillation detectors that are needed to replace conventional ^3He gas tubes due to the projected shortage of ^3He . Scintillator technology is also advantageous for instrumental applications where more compact devices are required as is the case with the energy sensitive neutron detector in design for first use on CANDoR. The Facility was awarded NIST intramural funding to support staff for the development of the CANDoR detector which utilizes a sliver of $^6\text{Li}/\text{ZnS}(\text{Ag})$ scintillator as the neutron-sensitive element and wavelength shifting fibers to conduct the scintillator light to silicon photomultiplier devices (SiPMs). This construction allows detectors to be very thin ($\approx 1\text{mm}$), permitting many more channels of crystal-analyzed neutron detection than a similar arrangement using gas-filled pencil detectors. This year, as part of this development program, a detector development station has been commissioned on the NG-1 beamline (Fig. 1) providing a monochromatic neutron beam (4.75 \AA wavelength, with a fractional wavelength resolution of approximately 1 %) to establish the performance properties of the scintillator and optimize the configuration and type of fiber optics and electronics used.

The design of the vSANS spectrometer calls for two types of detectors: a high resolution area detector typical of most instruments of this type and arrays of linear position sensitive tubes. While no candidate has been positively identified for the high resolution detector, NCNR took delivery of eight panels of “8-pack” linear position sensitive ^3He proportional counters for incorporation into the spectrometer (Fig. 2). Since delivery, facility staff members have been working to characterize the readout electronics based on the Spallation Neutron Source data acquisition standard.



FIGURE 1: Nick Maliszewskyj, Chuck Majkrzak (mostly hidden), Brian Maranville, and Jeff Ziegler assess data from the new detector development station at NG-1.

Neutron Spin Filters

The NCNR's program to provide and develop ^3He neutron spin filters (NSFs) is operated in collaboration with the Physical Measurement Laboratory at NIST. In the current reporting period, which includes the outage period, user experiments were only performed during two reactor cycles prior to the long shutdown. Nevertheless, the spin filter program serviced 14 user experiments, for a total of 43 beam days requiring about 76 bar-liters of polarized ^3He gas. Polarized beam experiments are routinely carried out on the thermal neutron triple-axis spectrometer BT-7, on small-angle neutron scattering instruments, on the Multi-Axis Crystal Spectrometer (MACS), and on the reflectometers. Results from the first user experiment to employ wide-angle polarization analysis on MACS have now been published [1].



FIGURE 2: Assembled “8-pack” ^3He proportional counter arrays for vSANS.

^3He gas is polarized by spin-exchange optical pumping (SEOP), in which alkali-metal atoms are polarized by optical pumping and the resulting electronic polarization is transferred to ^3He nuclei in spin-exchange collisions. The performance of the SEOP systems, ^3He cells, and ^3He polarization continues to improve and, to address increasing user demand, a third SEOP system will be implemented shortly. A major technical barrier in fabricating large (over 1 L), high-pressure ^3He cells has been successfully overcome and three such cells have been produced to enable efficient polarization of 50 meV neutrons on BT-7. Characterization of the polarized neutronic performance for these cells is underway. In addition, two new SANS cells are now available for user experiments.

Standard protocols have been developed and are now available for routine use in polarized neutron scattering measurements at the NCNR. A standardized measurement sequence is necessary for measurement of ^3He polarization and flipping ratio versus time, polarization efficiency calibration, and spin-transport configurations for user experiments. The goal is to provide an integrated, user-friendly ^3He NSF package and hence to better service users in polarized neutron scattering.

The break from user operations during the recent outage provided an opportunity to develop and establish an EPR (electron paramagnetic resonance) measurement facility used to determine the ^3He polarization by measuring the shift in the alkali metal's EPR frequency in the magnetic field arising from the ^3He magnetization. During the EPR measurement, the intensity of a collimated portion of the optical pumping laser beam passing through the center of the ^3He cell is monitored by a photodiode. This development has been very successful and in tests of wide-angle cells for MACS, we have found the ^3He polarization results from EPR agree with the neutron-based values to within 1 %.

There is a sustained drive to make the hardware and software used to control ^3He NSFs user-friendly, incorporating it into the instrument software. Continuing the previous development of the ^3He nuclear magnetic resonance (NMR) hardware and software for use on specific beam-lines, a universal method has been developed for NMR on all instruments using ^3He NSFs. Taking a modular approach, integrated hardware and software resides on a dedicated ^3He NMR computer and communicates with neutron instrument computers via a mini-PYTHON server. The software can control several free induction decay (FID) measurements and ^3He adiabatic fast passage (AFP) based spin flipping for both the polarizer and analyzer. The integrated device is user-friendly so that the instrument scientist or user can handle the complicated ^3He NMR flipper just like a conventional neutron spin flipper. The ^3He flipping information such as time stamps, number of flips, and the state of the ^3He spin is recorded for use by polarization efficiency correction software.

During the year significant improvements in the ^3He polarization-flipping efficiency have been realized. Using an amplitude-modulated radio-frequency (RF) field when performing a frequency-sweep AFP NMR for ^3He spin flipping, ^3He polarization losses of 3×10^{-5} per flip for a magnetically shielded solenoid and 1×10^{-5} per flip for a magic box on the beam-lines have been achieved. The enhanced ^3He spin-flipping capability for the magic box is a particular success and provides over one order of magnitude improvement in ^3He spin flipping efficiency for the solenoid compared to the constant RF field scheme. This amplitude-modulated RF scheme has been integrated into the NMR software for routine use on every instrument.

Significant efforts have been made to advance polarized neutron instrumentation for each instrument class. The aim is to improve the polarized neutronic performance and detection efficiency for magnetic materials. For BT-7, one of the most important advances was to develop polarized inelastic neutron instrumentation. Building on the success of the polarized inelastic experiments just before the long shutdown in 2011 [2], a re-optimized setup for BT-7 polarized beam for both the vertical field (\mathbf{P} perpendicular to \mathbf{Q}) and horizontal configuration (\mathbf{P} parallel to \mathbf{Q}) has been designed. Successful development of automated and nearly lossless (on the order of 10^{-5} per flip) ^3He spin flipping capability on the beam line as described above is essential for the new polarized beam setup. To achieve automated neutron spin control, it is necessary to have one adiabatic $\pi/2$ spin rotation for \mathbf{P} perpendicular to \mathbf{Q} and three adiabatic $\pi/2$ spin rotations for \mathbf{P} parallel to \mathbf{Q} . Ultra-compact spin rotation devices using permanent magnets and magnetic coils have been designed, which fit the constrained space on the BT-7 spectrometer. Simulations indicate that these spin rotation devices allow for efficient spin transport up to 50 meV. The new design of the spin rotation devices has also improved the relaxation time of the ^3He analyzer from 220 h to 330 h for a cell with an intrinsic relaxation time of 390 h. Optimization of the polarizer is in progress. Since flipping the ^3He spin on the order of every minute on the beam-line is a completely new development, tests are still required of the reliability and stability of the fast- ^3He -spin-flipping scheme for both the polarizer and analyzer. The new design of the entire polarized beam instrumentation will significantly improve the long-term provision of a polarized beam setup on BT-7 and increase the reliability of operation of polarized beam experiments.

For the SANS instruments, major improvements in polarization analysis have been made, which are important for scientific research at the forefront of nanomagnetism and other condensed matter applications. By improving the magnetic shielding of the 1.6 T electromagnet and developing a double-shielded solenoid, a higher sample field can now be provided as well as

higher maximum Q . The modified electromagnet is available for SANS and possibly also reflectometry experiments and provides a transverse horizontal field for the sample. The magnetic shielding is important for efficient spin transport and for improving the lifetime of the ^3He analyzer cells. A double-shielded solenoid has been developed for improving the maximum Q range and the lifetime of the ^3He analyzer cells. Extensive polarized beam tests on SANS have confirmed that an adiabatic $\pi/2$ spin rotation from transverse horizontal (sample) to longitudinal (^3He analyzer) can be achieved even when the ^3He analyzer solenoid is only 10 cm (gap) away from the magnet.

Finally, substantial improvements have been made in all aspects of the MACS polarized beam apparatus. Most notable is the success in fabricating wide-angle cells blown from GE180 glass that provide the required 110 degrees of angular coverage. The cells have yielded ^3He polarizations of 75 % and relaxation times longer than 100 h. Additional RF shielding and use of an amplitude-modulated RF frequency sweep for adiabatic fast passage NMR have reduced ^3He polarization loss to 0.03 % per flip for the polarizer and 0.006 % per flip for the analyzer. Full testing of the new apparatus will await the re-commissioning of MACS at its new location at BT-9.

Sample Environment

During the NCNR outage, sample environment and laboratory staff focused on maintenance and repair projects seeking to provide reliable equipment and facilities at the restart of Facility research activities. Overhaul of the entire fleet of bottom-loading closed-cycle refrigerators was completed. The 10 T cryogen-free magnet was outfitted with a cryogen-free variable-temperature insert and is now being used for experiments. Cryostat sample sticks were repaired and refurbished with the addition of overpressure devices and concentricity spacers. New capabilities include the development and preliminary testing of a computer-controlled gas-loading rig to support research across a range of areas including hydrogen storage, hydrate clathrate, and zeolite systems.

The outage period also provided opportunity to fit out a new sample preparation laboratory for users. This laboratory vaunts a new wet glove box, ovens, and a microscope along with standard equipment and supplies necessary for sample preparation. New Dynamic Light Scattering and UV-VIS sample characterization apparatuses has also been installed and are ready for use—more information can be found in the CHRNS section (pp. 60-63).

Data Acquisition

The instrument suite was brought back on line with a controls package updated, rationalized, and standardized for manageability. All instrument computers are now enterprise managed using the Red Hat Enterprise distribution of Linux.

Development of the New Instrument Control Environment (NICE) software system has followed the project plan initiated last year and successfully completed an alpha version which was deployed for testing on the pre-staged 10 m SANS in March 2012. The alpha release, which includes only core features required for instrument control and data acquisition, has since been deployed in triple-axis mode on BT-4 and on a simulated neutron spin echo spectrometer.

Data Analysis

In the last decade, the Data Analysis and Visualization Environment (DAVE) project has been the primary vehicle through which software support has been provided for the inelastic instruments at the NCNR. Staff members at the NCNR and visiting research scientists use the software for various purposes including experiment planning, data reduction, visualization and data analysis. Although DAVE is fully functional, developers and instrument scientist continue to maintain and extend the software suite to accommodate user requests, changes to neutron scattering instrumentation or to take advantage of new techniques in software engineering. This brief report highlights examples of recent developments in reduction, visualization and analysis in the project, further details can be found at <http://www.ncnr.nist.gov/dave/>.

Work on the initial phase of new data reduction modules for MACS and BT-7 are now complete. These two instruments represent the state-of-the-art in triple axis spectroscopy and hence require appropriate software that allows the scientists to fully explore the data generated from them. BT-7 and MACS respectively make use of a multichannel detector and a multi-detector system and hence enable sophisticated scans to be performed in more than one independent variable. Furthermore, when multiple scans are grouped, volumetric data are produced. The challenge for the data reduction software is to automate the conversion of the raw data into physical units, taking into account instrument calibration parameters and, in the case of multiple files, stitching the data so that overlapping points are appropriately handled. The software supports single crystal or powder samples measured in either diffraction or inelastic mode. For BT-7, there is also a raw view mode that serves as a flexible tool for examining the data to look for patterns which, for example, can help the instrument scientist determine whether the instrument is operating as expected.

As mentioned earlier, in most cases, the data produced by these instruments can be a function of more than two independent variables (volume data) and the DAVE Mslice tool is very effective at visualizing such data and performing basic analysis. A new feature in Mslice makes it even easier to perform planar slices of volumetric data and cuts of planar data. Using mouse controls, it is now possible to interactively manipulate the plane of interest from a volume or the line of interest from a plane and

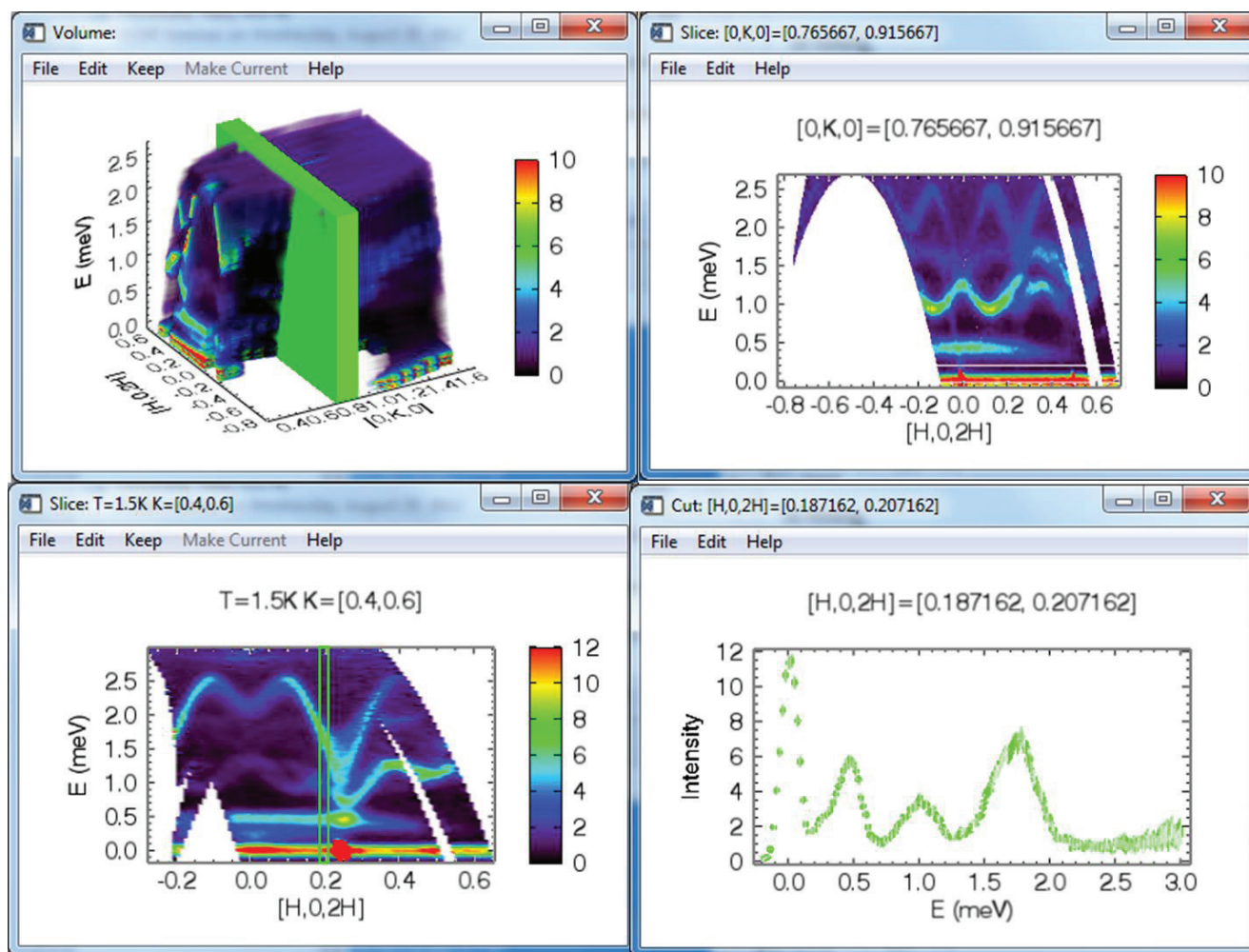


FIGURE 3: Mouse controls, depicted by the green slab and rectangle in the two left plots, are used to quickly select a region of interest which is then extracted, processed and displayed as shown by the plots to the right. The intensity is integrated along the width of the slab or rectangle.

view the results instantaneously. These are illustrated in the Fig. 3 where the contour plot is a slice of data from the volume plot represented by the green slab and the line plot is a cut from the contour plot represented by the green rectangle. If the slab or the rectangle is manipulated using the mouse, the sliced or cut visualization is automatically updated.

The Peak Analysis (PAN) module in DAVE enables modeling of experimental data. The user can either take advantage of built-in functions or specify custom analytical expressions using IDL. PAN uses the Levenberg-Marquardt (LM) least-squares fitting algorithm to optimize the parameters of the model. LM uses a gradient search procedure that is fast and works well as long as the problem domain with respect to the model parameters has a simple topology with a single minimum or that the starting point is in the neighborhood of the global minimum. In some cases therefore, LM may fail to converge to the best solution. For PAN to be used for more challenging problems, a new algorithm is being developed as an alternative to LM. The technique is a genetic algorithm known as differential evolution (DE). DE

is a population based stochastic search approach. It makes use of mutation strategies to evolve from an initial population (trial solution) to future generations that provide a better solution to the problem. While the basic algorithm has been developed, there is still work to be done before it can be made generally available. Genetic algorithms are notoriously difficult to use because the choice of mutation strategy, and associated control parameter values, that can be employed is inherently problem dependent. Our goal is to try to create an automated environment that will be as seamless to use as the LM currently in PAN. Consequently, we are still working to automate the selection of mutation strategies using adaptive feedback techniques, fine tuning the convergence criteria and calculating uncertainties in the best fit model parameters.

References

- [1] V. Thampy *et al.*, Phys. Rev. Lett. 108,107002 (2012).
- [2] Discovery of a New Type of Magnetic Mode in $\text{YBa}_2\text{Cu}_3\text{O}_{6+x}$, H.A. Mook, J.W. Lynn, M.B. Stone, M.D. Lumsden, and A.D. Christianson, (submitted).

Serving the Science and Technology Community

The mission of the NIST Center for Neutron Research is to assure the availability of neutron measurement capabilities to meet the needs of U.S. researchers from industry, academia and from other U.S. government agencies. To carry out this mission, the NCNR uses several different mechanisms to work with participants from outside NIST, including a competitive proposal process, instrument partnerships, and collaborative research with NIST.

Proposal System

Most of the time on NCNR instruments is made available through a competitive, peer-review proposal process. The NCNR issues calls for proposals approximately twice a year. Proposals are reviewed at several different levels. First, expert external referees evaluate each proposal on merit and provide us with written comments and ratings. This is a very thorough process where several different referees review each proposal. Second, the proposals are evaluated on technical feasibility and safety by NCNR staff. Third, we convene our Beam Time Allocation Committee (BTAC) to assess the reviews and to allocate the available instrument time. Using the results of the external peer review and their own judgment, the BTAC makes recommendations to the NCNR Director on the amount of beam time to allocate to each approved experiment. Approved experiments are scheduled by NCNR staff members in consultation with the experimenters.

The current BTAC members are:

- Andrew Allen (NIST Ceramics Division)
- Jeffrey Allen (Michigan Technological University)
- Collin Broholm (Johns Hopkins University)
- Leslie Butler (Louisiana State University)
- Kushol Gupta (University of Pennsylvania)
- Hye-Jung Kang (Clemson University)
- Ramanan Krishnamoorti (University of Houston)
- Valery Kiryukhin (Rutgers University)
- Raul Lobo (University of Delaware)
- Janna Maranas (The Pennsylvania State University)
- Steven May (Drexel University)
- Alan Nakatani (Dow Chemical Company)
- Danilo Pozzo (University of Washington)
- Stephan Rosenkranz (Argonne National Laboratory)
- Lynn Walker (Carnegie-Mellon University)

Partnerships

The NCNR may form partnerships with other institutions to fund the development and operation of selected instruments. These partnerships, or “Participating Research Teams”, may have access to as much as 75 % of the available beam time on the instrument depending on the share of total costs borne by the team. A minimum of 25 % of the available beam time is always made available through the NCNR proposal program to all users. Partnerships are negotiated for a fixed period (usually three years) and may be renewed if there is mutual interest and a continued need. These partnerships have proven to be an important and effective way to expand the research community’s access to NCNR capabilities and have been very successful in developing new instruments.

Collaboration With NIST

Some time on all instruments is available to NIST staff in support of our mission. This time is used to work on NIST research needs, instrument development, and promoting the widespread use of neutron measurements in important research areas, particularly by new users. As a result of these objectives, a significant fraction of the time available to NIST staff is used collaboratively by external users, who often take the lead in the research. Access through such collaborations is managed through written beam time requests. In contrast to proposals, beam time requests are reviewed and approved internally by NCNR staff. We encourage users interested in exploring collaborative research opportunities to contact an appropriate NCNR staff member.

Research Participation And Productivity

The NCNR continued its strong record of serving the U.S. research community this year. Over the 2012 reporting year, 1976 research participants benefited from use of the NCNR. (Research participants include users who come to the NCNR to use the facility as well as active collaborators, including co-proposers of approved experiments, and co-authors of publications resulting from work performed at the NCNR.) As the number of participants has grown, the number of publications per year has increased in proportion. The quality of the publications has been maintained at a very high level. The trend of the past few years, however, suggests that the number of participants and publications is beginning to saturate, as one might expect as the capacity of the facility is reached. The Expansion Initiative full-power reactor shutdown from April 2011 to April 2012 temporarily reduced participant numbers,

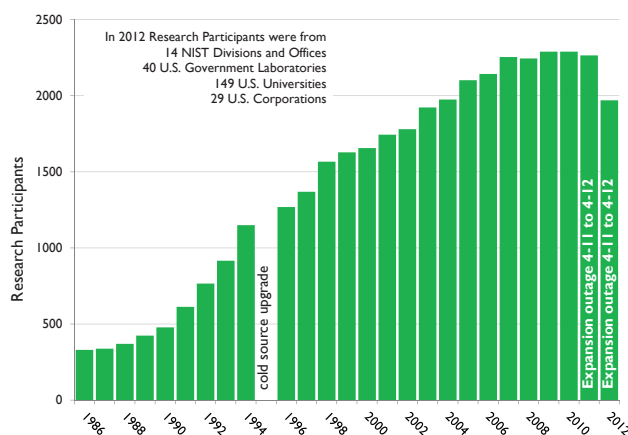


FIGURE 1: Research participants at the NCNR 1986 - 2012.

as shown in Fig. 1. Increasing activity and productivity can be expected as the Expansion continues towards completion.

2012 NCNR Proposal Program

Two calls for proposals for instrument time were issued in the past year. We received 705 proposals, of which 354 were approved and received beam time. The oversubscription, *i.e.*, the ratio of days requested on all proposals to the days available, was 2.3 on the average, but as high as 3.0 for specific instruments in one call. Proposal demand has grown constantly since the NCNR first began accepting proposals in 1991, and has doubled in the past ten years. The following table shows the data for several instrument classes.

Instrument class	Proposals	Days requested	Days allocated
SANS and USANS	258	982	449
Reflectometers	105	653	294
Spectrometers	281	1909	788
Diffraction	30	99	50
Imaging	31	153	74
Total	705	3796	1655

NCNR Users Group

The NCNR Users Group (NUG) provides an independent forum for all facility users to raise issues to NCNR management, working through its executive officers to carry out this function. The current officers are Mark Dadmun (University of Tennessee, chair), John Katsaras (Oak Ridge National Laboratory), Michel Kenzelmann (Paul Scherrer Institute, Switzerland), Despina Louca (University of Virginia), Dale Schaefer (University of Cincinnati), Lynn Walker (Carnegie-Mellon University), and Erik Watkins (University of California, Davis and ILL, Grenoble). The NUG plans to conduct its next election of officers in late 2012.

Panel Of Assessment

The major organizational components of NIST are evaluated annually for quality and effectiveness by the National Research Council (NRC), the principal operating agency of both the National Academy of Sciences and the National Academy of Engineering. A panel appointed by the NRC last reported on the NIST Center of Neutron Research in March 2011. Their findings are summarized in a document that may be viewed online at <http://www.nist.gov/director/nrc/upload/nr-panel-2011-final-report.pdf>. The panel members included Tonya Kuhl of the University of California, Davis (chair), Meigan Aronson, Stony Brook University, Frank Bates, University of Minnesota, Donald Engelmann, Yale University, Paul Fleury, Yale University, Christopher Gould, North Carolina State University, Peter Green, University of Michigan, Alan Hurd, Los Alamos National Laboratory, James Lee, Sandia National Laboratory, John Parise, Stony Brook University, and Sunil Sinha, University of California, San Diego.

The Center For High Resolution Neutron Scattering (CHRNS)

CHRNS is a national user facility that is jointly funded by the National Science Foundation and the NCNR. Its primary goal is to maximize access to state-of-the-art neutron scattering instrumentation for the research community. It operates six neutron scattering instruments at the NCNR, enabling users from around the nation to observe dynamical phenomena involving energies from ≈ 30 neV to ≈ 100 meV, and to obtain structural information on length scales from 1 nm to ≈ 10 μ m. A more detailed account of CHRNS activities may be found on pp 60-63 of this report.

Partnerships For Specific Instruments NG-7 SANS Consortium

A consortium that includes NIST, the Industrial Partnership for Research in Interfacial and Materials Engineering (IPRIME) led by the University of Minnesota, and the ExxonMobil Research and Engineering Company, operates, maintains, and conducts research at the NG-7 30 m SANS instrument. The consortium uses 57 % of the beam time on this instrument, with the remaining 43 % allocated to the general scientific community through the NCNR's proposal system. Consortium members conduct independent research programs primarily in the area of large-scale structure in soft matter. For example, ExxonMobil has used this instrument to deepen their understanding of the underlying nature of ExxonMobil's products and processes, especially in the fields of polymers, complex fluids, and petroleum mixtures.

The nSoft Consortium

Formed in August 2012, the nSoft Consortium allows member companies to participate with NIST in the development of advanced measurements of materials and manufacturing processes, and develop their own expertise in state-of-the-art measurement technologies to include in their analytical research programs. nSoft develops new neutron-based measurement science for manufacturers of soft materials including plastics, composites, protein solutions, surfactants, and colloidal fluids. Members receive access to leading expertise and training support in neutron technology and soft materials science at the NIST Center for Neutron Research, the NIST Polymers Division, and the University of Delaware. Contact: Ron Jones, nSoft Director, rljones@nist.gov, 301-975-4624.

NIST / General Motors – Neutron Imaging

An ongoing partnership and collaboration between General Motors and NIST continues to yield exciting results using neutron imaging. Neutron imaging has been employed to visualize the operation of fuel cells and lithium-ion batteries for automotive vehicle applications. Neutron imaging is an ideal method for visualizing both hydrogen and lithium, the fuel of electric vehicles engines. These unique, fundamental measurements, provide valuable material characterizations that will help improve the performance, increase the reliability, and reduce the time to market introduction of the next generation electric car engines. The GM/NIST partnership is entitled to 25 % of the time on the BT-2 Neutron Imaging Facility.

Interagency Collaborations

The Smithsonian National Museum of Natural History has had a productive 34 year partnership with the NCNR, during which time it has chemically analyzed over 43 100 archaeological artifacts by Instrumental Neutron Activation Analysis (INAA), drawing extensively on the collections of the Smithsonian, as well as on those of many other institutions in this country and abroad. Such chemical analyses provide a means of linking these diverse collections together in order to study continuity and change involved in the production of ceramic and other artifacts.

The Center for Food Safety and Applied Nutrition, U.S. Food and Drug Administration (FDA), directs and maintains a multi-laboratory facility at the NCNR that provides agency-wide analytical support for food safety and food defense programs. Neutron activation (instrumental, neutron-capture prompt-gamma, and radiochemical), x-ray fluorescence spectrometry, and low-level gamma-ray detection techniques provide diverse multi-element and radiological information about foods and related materials. Current studies include validation of swordfish in-house reference material, revalidation of cocoa powder in-house reference material, measuring cesium levels in soil to study cesium uptake behavior into food products, rapid screening of food for dangerous levels of toxic elements (arsenic, cadmium, mercury, and lead), and optimizing neutron activation procedures for determination of arsenic and silver in foods and iodine in dietary supplements.

The Center for High Resolution Neutron Scattering (CHRNS)

The Center for High Resolution Neutron Scattering is a national user facility that is jointly funded by the National Science Foundation through its Division of Materials Research (grant number DMR-0944772), and by the NCNR. The primary purpose of this partnership is to maximize access to state-of-the-art neutron scattering instrumentation for the research community using the NCNR's proposal system. Proposals to use the CHRNS instruments are critically reviewed on the basis of scientific merit and/or technological importance.

The core mission of CHRNS is fourfold: (i) to develop and operate neutron scattering instrumentation, with broad application in materials research, for use by the general scientific community; (ii) to promote the effective use of the CHRNS instruments by having an identifiable staff whose primary function is to assist users; (iii) to conduct research that advances the capabilities and utilization of CHRNS facilities; and (iv) to contribute to the development of human resources through educational and outreach efforts.

Scattering Instruments and Research

During FY 2012, CHRNS supported operation of the following instruments:

- the NG-3 30 m Small Angle Neutron Scattering (SANS) instrument,
- the Ultra-Small Angle Neutron Scattering (USANS) instrument,
- the Spin-Polarized Inelastic Neutron Scattering (SPINS) spectrometer,
- the Multi-Angle Crystal Spectrometer (MACS),
- the Disk Chopper Spectrometer (DCS),
- the High Flux Backscattering Spectrometer (HFBS), and
- the Neutron Spin-Echo (NSE) spectrometer.

The small angle scattering instruments together provide structural information over length scales from ≈ 1 nm to ≈ 10 μ m. The spectrometers collectively yield dynamical information over time scales from $\approx 3 \times 10^{-14}$ s to $\approx 10^{-7}$ s (energy scales from ≈ 100 meV to ≈ 30 neV). These wide ranges of accessible distances and times support a very diverse scientific program, allowing researchers in materials science, chemistry, biology, and condensed matter physics to investigate materials such as polymers, metals, ceramics, magnetic materials, porous media, fluids and gels, and biological molecules.

In the most recent Call for Proposals (call 29), 209 proposals requested CHRNS instruments, and 122 of these proposals received beam time. Of the 1070 days requested for the CHRNS instruments, 503 were awarded. Corresponding numbers for all instruments were 320 proposals received, 201 proposals approved, 1723 days requested, and 842 days awarded. Roughly half of the users of neutron scattering techniques at the NCNR use CHRNS-funded instruments, and more than one third of NCNR publications (see the "Publications" section on p. 66), over the current one-year period, are based on research performed using these instruments. This reports contains several highlights on CHRNS publications (pp. 66-85) In 2012 more than 25 Ph.D. dissertations were completed using results from CHRNS-sponsored instruments.

Scientific Support Services

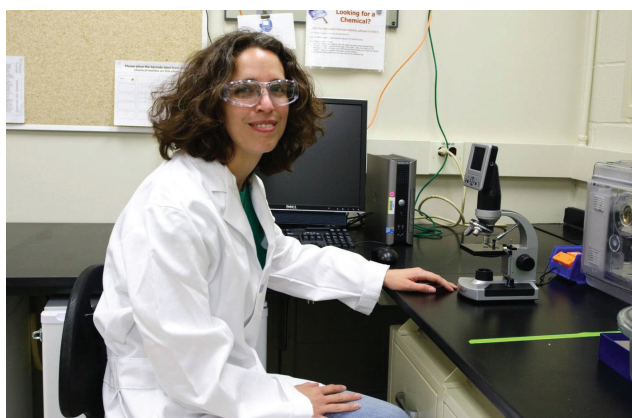
The NCNR Sample Environment team provides users the equipment and training required to make measurements in special conditions of temperature, pressure, magnetic field, and fluid flow. The team recently acquired new equipment to benefit and expand these options:

- three new bottom-loading closed cycle refrigerators (CCRs) that rapidly cool to 4 K,
- an attachment for a CCR that can operate from 25 K to 800 K,
- a new rheometer for uSANS that has the appropriate height for the instrument and is compatible with the existing SANS rheometer, and
- three 6 kbar and three 10 kbar high pressure cells.

During the outage from April, 2011 through February, 2012 the team undertook several projects to ensure that properly working equipment was ready to meet the needs of CHRNS users at startup. Some of these projects are listed below.

- New variable-temperature inserts were installed and tested in the 10 T magnet. This equipment has since been successfully used for experiments approved by the Beam Time Allocation Committee (BTAC).
- Preparations for re-commissioning the 11.5 T magnet and dilution refrigerator have been completed; installation of the new Intelligent Gas Handling System is imminent.
- Cryostats have been inspected and/or refurbished to ensure optimal performance.

- All of the bottom-loading and top-loading CCRs were inspected, new sensors installed, cold heads refurbished, systems tested, and other measures taken to ensure that they are fully functional.
- Sample sticks were refurbished. Concentricity spacers and over-pressure safety systems were added to the sticks. The staff also assured the operation of wires, sensors and heaters.
- The sample environment team and lab personnel worked with the NCNR staff to recover sample cans stored in lockers that were then added to the general supply available to users.
- The team investigated temperature relaxation and equilibration behavior within the range of 5 K to 300 K in a variety of environments, samples and sample cells used on NCNR instruments to provide much-needed information.
- A new gas loading rig was built to improve capabilities to perform gas adsorption studies.
- A new humidity cell for SANS and reflectometry experiments is being prepared for users. New hardware and software are included in the improvements.



NCNR's user lab support staff's Kim Tomasi checks out a Barska digital microscope.

The NCNR offers well-equipped and well-supplied laboratories for CHRNS users to prepare samples in a safe environment.



NCNR's Sarah Parks and Juscelino Leão lower the 10 T magnet into the DCS sample well.

Laboratory staff members have developed training materials and provide regular advice to users as needed. To meet users' demands, and to address the future growth of the user community, the NCNR has acquired new equipment, including a Dynamic Light Scattering system and UV-VIS spectrometer, and expanded laboratory space.

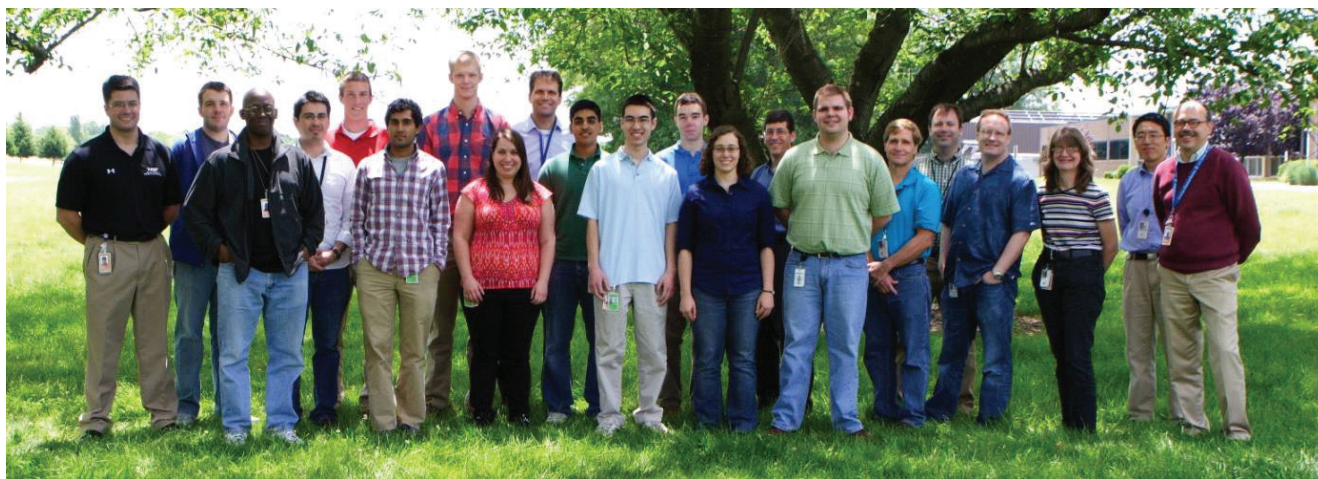
The new users' chemical laboratory was completed before the reactor startup. This laboratory features a wet glove box, fume hood, and vacuum ovens. During the shutdown all the user laboratories were readied with equipment and space, and restocked with supplies.

Education and Outreach

This year the Center for High Resolution Neutron Scattering sponsored a variety of educational programs and activities tailored to specific age groups and professions. The annual summer school, held June 18-23, was entitled "Summer School on Methods and Applications of Small Angle Neutron Scattering, Neutron Reflectivity and Spin Echo". Thirty two graduate and postdoctoral students from 15 states and 23 universities participated in the school. Lectures, research seminars and



2012 NCNR summer school participants and staff.



2012 SURF students and NCNR staff gather for a traditional group photo.

hands-on instruction on data reduction and analysis techniques were highlighted for a wide variety of neutron measurement techniques. The guest lecturers were Prof. Bryan Vogt from the University of Akron and Dr. Hideki Seto from KEK, Japan. The evaluations were excellent and student feedback was very positive.

As part of its expanding education and outreach effort, CHRNS offers to university-based research groups with BTAC-approved experimental proposals the opportunity to request travel support for an additional graduate student to participate in the experiment. This support is intended to enable prospective thesis students, for example, to acquire first-hand experience with a technique that they may later use in their own research. Announcements of this program are sent to all of the university groups whose experimental proposals receive beam time from the BTAC. Recipients of the announcement are encouraged to consider graduate students from under-represented groups for this opportunity. The program is also advertised on the NCNR's website at <http://www.ncnr.nist.gov/outreach.html>.

As in previous years, CHRNS participated in NIST's Summer Undergraduate Research Fellowship (SURF) program. In 2012 CHRNS hosted 10 SURF students. The students participated in areas such as thin-film deposition, x-ray characterization, studies of biological samples and the rheological properties of polymers, diffraction studies of magnetic materials and metal organic frameworks, web-based data reduction techniques, and reactor control systems development. They presented their work at the NIST SURF colloquium. At least four papers co-authored by a former SURF student, and one with a SHIP student (see below), were published in the reporting period.

The Summer High school Intern Program (SHIP) was started in 2008 with the participation of Vikas Bhatia from Gaithersburg High School (MD). Bhatia returned and was joined by Pavan Bhargava from Poolesville High School (MD) the following summer, and both students, now in college, returned as SURF



SHIP student Priyanka Patel presents her work with NCNR's William Ratcliff on calculating neutron structure factors on the web.

students in 2010, 2011 and 2012. The SHIP program is now NIST-wide, and this year we had seven students from high schools in Maryland and Virginia. The students worked on such projects as web-based data reduction, studies of the magnetic properties of defect dicubane lanthanide clusters, and optimizing the smoothness of thin film samples. The results of the students' summer investigations were highlighted in a NIST-wide poster session in early August.

NCNR initiated a Research Experiences for Teachers (RET) program in the summer of 2010. Wootton High School teacher Michael Thompson (Montgomery County, MD) was selected for the program for the summer of 2012. He collaborated with NCNR's Joe Dura and SURF student Pavan Bhargava on a project involving thin carbon films for battery and fuel cell applications.

The annual Summer Institute for Middle School Science Teachers brings middle school science teachers to NIST for two weeks in order to give them a better understanding of the scientific process. In 2012 the Institute included teachers from Maryland, Florida, South Carolina, and New York. Each year,



In the RET program, Wootton High School teacher Michael Thompson (right) worked on carbon-based thin films for fuel cells and batteries with NCNR's Joe Dura.

CHRS hosts the teachers for a one-day introduction to neutron scattering with a presentation that describes how neutrons are produced and how they are used to improve our understanding of materials at the atomic scale. Having toured the neutron guide hall, and having seen several neutron instruments, the teachers learn about the types of experiments performed at the NCNR. To bring home projects suitable for middle school students, they then learn how to grow crystals of “alum” (hydrated aluminum potassium sulfate), and how to make “shake gels”. Throughout the day, the teachers have the opportunity to interact with staff members and SURF students. The feedback from the teachers is consistently positive, and their comments help to improve the CHRS program.

Elementary, Middle, and High School Activities

- As part of NIST's activities for the annual “Take Your Daughters and Sons to Work Day”, CHRS staff gave a presentation on what neutrons can do and offered a tour of the facility. The children, whose ages ranged from 12 to 15 years old, enjoyed watching the “Neutron Mouse Trap” (which demonstrates a “chain reaction” with mouse traps and ping pong balls).
- 15 tours for Middle School, High School, and University students were offered.
- “Adventures in Science” is a hands-on science program for middle school students with classes in physics, chemistry, computers, biology, astronomy, etc., taught by scientists, engineers, and technical professionals. Classes meet for about two hours on Saturday mornings from October through March. NCNR's Dan Neumann led a class this year.
- Boy Scouts Nuclear Science Merit Badge - The NCNR and CHRS staff developed a program to help Boy Scout troops around the NIST area earn their merit badge in nuclear science.
- Montgomery County, MD School System - CHRS staff members gave talks at local schools, teaching students about neutrons and materials studies at the NCNR, from making ice cream with liquid nitrogen (small crystals) to making “slime” using glue, water and sodium borate. Staff also served as judges at local science fairs. NCNR's Yamali Hernandez is an advisor to the Montgomery County Board of Education's Math and Science Curriculum Committee.
- USA Science Festival - NCNR staff members in conjunction with scientists from the National High Magnetic Field Laboratory were in charge of one of the NSF booths at the USA Science Festival in Washington, DC.



Summer Institute for Middle School Science Teachers assemble on the “dance floor” of the NSE instrument during a tour.

2012 Awards



NCNR's **Jeff Lynn** received the **Presidential Rank Award of Distinguished Senior Professional**. This prestigious honor recognizes *individuals with an exceptional record of achieving major program goals and is consistently recognized nationally or internationally as a leader in a field*. Jeff has developed and applied triple-axis neutron spectroscopy to many areas of condensed matter physics, with multiple contributions to the understanding of high-temperature superconductors, colossal magneto-resistance in materials, and magnetism across a wide range of crystalline solids. Such materials are fundamentally important to present and future technologies.



NCNR's **Craig Brown** is one of this year's recipients of the **Arthur S. Flemming Award** honoring outstanding federal employees. He was recognized "For his seminal contributions to our understanding of new materials suited for hydrogen energy storage in next-generation, clean automobiles."



NCNR's **John Barker, Paul Butler, and James Moyer** have received NIST's **Jacob Rabinow Applied Research Award**. They are being recognized "For the design, development, and stewardship of USANS: An ultra-high resolution, small-angle, neutron-scattering instrument."



Thomas Gentile, of NIST's Ionizing Radiation Division at the NCNR, received NIST's **Allen V. Astin Award for Measurement in Science**. He was recognized "For excellence, innovation, and leadership in polarized ^3He ."



NCNR's **Julie Borchers** was elected a **Fellow of the Neutron Scattering Society of America**. She was recognized "For insightful neutron investigations of magnetic materials, particularly interlayer exchange interactions phenomena in magnetic thin films and superlattices".



Cindi Dennis, NIST Metallurgy Div., along with **Julie Borchers** and **Andrew Jackson** of the NCNR received the **NIST Bronze Medal**.

They were recognized for "showing complete tumor regression in 75 % of cancerous mice occurs only after hyperthermia treatment using magnetically – interacting nanoparticles."



NCNR's **Tanya Burke** has received the **NIST Bronze Medal**. She is being recognized "For administrative and technical leadership in the execution of critical, time-sensitive facility modifications supporting the NCNR expansion project."



NCNR's **Polly McCarty** has received the **Organizational Award for Safety**. She was recognized "in recognition of her efforts as part of the Engineered Nanoparticle Safety Committee in helping to ensure a safe working environment for nanoparticle research here at NIST."



NCNR's **Wendy Queen** received **first place of Sigma Xi's** Annual Post-doc Poster Presentation in the area of Materials for her poster entitled "Reducing energy costs of industrial gas separations using metal-organic framework based solid adsorbents." Wendy is now a staff member at the Molecular Foundry at Lawrence Berkley National Laboratory.



Steve DeCaluwe, post-doc at the NCNR, received **first place for Sigma Xi's** annual NIST Post-doc Poster Presentation in the area of Chemistry for his poster titled "*In situ* neutron reflectometry for the direct measurement of cyclic and evolving structures in the lithium battery solid electrolyte interphase." Steve is now an Assistant Professor at the Colorado School of Mines.



NCNR's **Ken Qian** received **second place for Sigma Xi's** annual NIST Post-doc Poster Presentation in the area of Materials, for his poster entitled "Probing the interaction and structural arrangement of medicinal compounds confined in novel, amorphous drug delivery systems."



Prof. Samuel Werner of NIST and University of Missouri has been selected as a **Fellow of the Neutron Scattering Society of America**

“For elegant neutron experiments contributing to the understanding of quantum physics and for his sustained efforts to promote neutron science.” Sam was also recognized with an award by the NSSA as one of its founders for exceptional service to the neutron community.



Charles Glinka was elected a **Fellow of the Neutron Scattering Society of America**,

recognized “For development and operation of world-class capabilities for small angle neutron scattering in America.” Glinka retired from the NCNR and is currently a guest researcher.



Antony Van Dyk and **Alan Nakatani** of Dow Coatings Materials have been selected as the winner of the **American Coatings Award 2012** for the best paper entitled “Shear Rate

Dependent Structure of Polymer Stabilized TiO_2 Dispersions” which highlights their work using USANS (ultra-high resolution small angle neutron scattering) at the NCNR to understand the interaction of TiO_2 slurries under shear. Nakatani and Van Dyk have long championed the utility of the USANS technique for improving understanding of coatings.



Prof. Robert J. Cava of Princeton University received the **Royal Society of Chemistry's Stephanie L. Kwolek Award** “For outstanding contributions to the understanding of the electronic structure and magnetic properties of solid state inorganic materials.” Prof. Cava was

also selected as a **Fellow of the Neutron Scattering Society of America** “For outstanding applications of neutron diffraction to the understanding of complex materials, and advocacy for the field, particularly among young scientists.” He has published more than 100 papers containing neutron data from the NCNR.



Prof. Matt Helgeson of UC Santa Barbara has been named a **Distinguished Young Rheologist** by TA Instruments. Helgeson was invited to talk on “Gelable Gels: Rheology of Soft Nanocomposites from Crosslinkable, Thermoresponsive Emulsions” at the TA

Instruments Annual User Meeting. His work on soft matter is featured in this issue on p. 36.



Prof. Rachel Segalman of the University of California, Berkeley won the 2012 **John H. Dillon Medal** “For fundamental and technological contributions to the field of polymer science and engineering, especially in the area of rod-coil block copolymers.” Prof.

Segalman's group are users of the NCNR.



Prof. Sankar Nair of Georgia Tech, former NCNR post-doc, was selected for 2012 American Institute of Chemical Engineers Separations **Division Fractionation Research, Inc./John G. Kunes Award** and presented an

invited lecture at the AIChE meeting entitled “Metal-Organic Framework (MOF) Materials and Membranes for Molecular Separations.”



Dr. Guangyong Xu of Brookhaven National Laboratory, a frequent collaborator and user of the facilities at the NCNR, was the recipient of the **2012 Science Prize** from the **Neutron Scattering Society of America** “for his work on relaxor ferroelectrics that have provided

new insights into the role of polar nano-regions in determining the extreme electromechanical properties of these materials.”

Xu gave an invited talk on his work at the June 2012 **American Conference on Neutron Scattering**.



Brett Guralnick, a graduate student at the University of Delaware working with Prof. Michael Mackay, was awarded an outstanding student poster prize by the **Neutron Scattering Society of America** at the June 2012 **American Conference on Neutron Scattering** for his

presentation “*In Situ* Annealing Study of Organic Photovoltaic Morphology via Non-invasive Polarized Neutron Reflectivity”, which was based on measurements made at the NCNR.



Jeffrey J. Richards, a graduate student working with Prof. Danilo Pozzo at the University of Washington, was awarded an outstanding student poster prize by the Neutron Scattering Society of America at the June 2012 American Conference on Neutron Scattering for his

presentation “Structure and Properties of Porous Poly(3-hexylthiophene) Gel Particles in Aqueous Dispersion”, which was based on measurements made at the NCNR.

Publications: August 1, 2011 to July 31, 2012

- Abakumov, A.M., Tsirlin, A.A., Perez-Mato, J.M., Petříček, V., Rosner, H., Yang, T., Greenblatt, M., "Spiral Ground State against Ferroelectricity in the Frustrated Magnet $\text{BiMnFe}_2\text{O}_6$," *Phys. Rev. B* **83**(21), 214402 (2011).
- Alexander, M., Nieh, M.-P., Ferrer, M.A., Corredig, M., "Changes in the Calcium Cluster Distribution of Ultrafiltered and Diafiltered Fresh Skim Milk as Observed by Small Angle Neutron Scattering," *J. Dairy Res.* **78**, 349 (2011).
- Alvine, K.J., Tyagi, M., Brown, C.M., Udovic, T.J., Jenkins, T., Pitman, S.G., "Hydrogen Species Motion in Piezoelectrics: A Quasi-Elastic Neutron Scattering Study," *J. Appl. Phys.* **111**(5), 053505 (2012). [CHNRNS]
- Anderson, D.L., Cunningham, W.C., "Analysis of FDA in-house Food Reference Materials with Anticoincidence INAA," *J. Radioanal. Nucl. Chem.*, in press.
- Anderson, D.L., "Anticoincidence INAA Capabilities for Analysis of FDA Total Diet Study Seafoods," *J. Radioanal. Nucl. Chem.*, in press.
- Anderson, D.L., "INAA Study of Hg, Se, As, and Br Irradiation Losses from L-cysteine Treated and Untreated Reference Materials," *J. Radioanal. Nucl. Chem.*, in press.
- Angelova, L.V., Terech, P., Natali, I., Dei, L., Carretti, E., Weiss, R.G., "Cosolvent Gel-like Materials from Partially Hydrolyzed Poly(vinyl acetate)s and Borax," *Langmuir* **27**, 11671 (2011).
- Asada, M., Gin, P., Endoh, M.K., Satija, S.K., Taniguchi, T., Koga, T., "Directed Self-Assembly of Nanoparticles at the Polymer Surface by Highly Compressible Supercritical Carbon Dioxide," *Soft Matter* **7**, 9231 (2011).
- Asada, M., Gin, P., Endoh, M.K., Satija, S.K., Koga, T., "Surface Segregation of Nanoparticles Driven by Supercritical Carbon Dioxide," *J. Phys.: Conf. Ser.* **272**, 012013 (2011).
- Bai, M., Miskowiec, A., Hansen, F.Y., Taub, H., Jenkins, T., Tyagi, M., Diallo, S.O., Mamontov, E., Herwig, K.W., Wang, S.-K., "Study of Water Diffusion on Single-supported Bilayer Lipid Membranes by Quasielastic Neutron Scattering," *Europhys. Lett.* **98**(4), 48006 (2012). [CHNRNS]
- Bailey, M.M., Kline, S.R., Anderson, M.D., Staymates, J.L., Berkland, C., "Chemically Modifiable Fluorinated Copolymer Nanoparticles for ^{19}F -MRI Contrast Enhancement," *J. Appl. Polym. Sci.* **126**, 1218 (2012). [CHNRNS]
- Balzar, D., "Coherency Strain and Dislocations in Copper-Rich-Precipitate Embrittled A710 Ferritic Steels," *Metal Mater Trans A* **43A**, 1462 (2012).
- Bao, W., Huang, Q.-Z., Chen, G.-F., Green, M.A., Wang, D.-M., He, J.-B., Qiu, Y.-M., "A Novel Large Moment Antiferromagnetic Order in $\text{K}_{0.8}\text{Fe}_{1.6}\text{Se}_2$ Superconductor," *Chin. Phys. Lett.* **28**(8), 086104-1 (2011).
- Barsan, M.M., Butler, I.S., Gilson, D.F.R., Moyer, Jr., R. O., Zhou, W., Wu, H., Udovic, T.J., "Raman, FTIR, Photoacoustic-Infrared, and Inelastic Neutron Scattering Spectra of Ternary Metal Hydride Salts A_2MH_5 , (A=Ca, Sr, Eu; Ir, Rh) and Their Deuterides," *J. Phys. Chem. A* **116**, 2490 (2012).
- Behrouzi, R., Roh, J.H., Kilburn, D., Briber, R.M., Woodson, S.A., "Cooperative Tertiary Interaction Network Guides RNA Folding," *Cell* **149**, 348 (2012).
- Bhatia, V., Rodriguez, E.E., Butch, N.P., Paglione, J., Green, M.A., "Phase Separation and Superconductivity in $\text{Fe}_{1+x}\text{Te}_{0.5}\text{Se}_{0.5}$," *Chem. Commun.* **47**, 11297 (2011).
- Bhatti, K.P., El-Khatib, S., Srivastava, V., James, R.D., Leighton, C., "Small-Angle Neutron Scattering Study of Magnetic Ordering and Inhomogeneity Across the Martensitic Phase Transformation in $\text{Ni}_{50-x}\text{Co}_x\text{Mn}_{40}\text{Sn}_{10}$ Alloys," *Phys. Rev. B* **85**(13), 134450 (2012). [CHNRNS]

- Bloch, E.D., Queen, W.L., Krishna, R., Zadrozny, J.M., Brown, C.M., Long, J.R., "Hydrocarbon Separations in a Metal-Organic Framework with Open Iron(II) Coordination Sites," *Science* **335**, 1606 (2012).
- Bloch, E.D., Murray, L.J., Queen, W.L., Chavan, S., Maximoff, S.N., Bigi, J.P., Krishna, R., Peterson, V.K., Grandjean, F., Long, G.J., Smit, B., Bordiga, S., Brown, C.M., Long, J.R., "Selective Binding of O₂ over N₂ in Redox-Active Metal-Organic Framework with Open Iron(II) Coordination Sites," *J. Am. Chem. Soc.* **133**, 14814 (2011).
- Braisted, J., Schneider, E., O'Kelly, S., van der Hoeven, C., "Design of an Irradiation Facility with a Real-Time Radiation Effects Monitoring Capability," *Nucl. Instrum. Methods Phys. Res., Sect. A* **660**, 83 (2011).
- Cappelletti, R.L., "The Acceleration of a Neutron in a Static Electric Field," *Phys. Lett. A* **376**, 2096 (2012).
- Cappelletti, R.L., editor, "2011 NIST Center for Neutron Research Accomplishments and Opportunities," NIST SP 1127 (2011).
- Chen, W., Xu, T., He, F., Wang, W., Wang, C., Strzalka, J., Liu, Y., Wen, J., Miller, D.J., Chen, J., Hong, K., Yu, L., Darling, S.B., "Hierarchical Nanomorphologies Promote Exciton Dissociation in Polymer/Fullerene Bulk Heterojunction Solar Cells," *Nano Lett.* **11**, 3707 (2011).
- Chen, W., Wang, J.-Y., Zhao, W., Li, L., Wei, X., Balazs, A.C., Matyjaszewski, K., Russell, T.P., "Photocontrol over the Disorder-to-Order Transition in Thin Films of Polystyrene-*block*-poly(methyl methacrylate) Block Copolymers Containing Photodimerizable Anthracene Functionality," *J. Am. Chem. Soc.* **133**(43), 17217 (2011).
- Cheng, X., Prask, H.J., Gnaeupel-Herold, T., Luzin, V., Fisher, J.W., "Neutron Diffraction Measurements for Residual Stresses in AL-6XN Stainless Steel Welded Beams," in "Neutron Diffraction," edited by Khidirov, I. (Intech Open Access Publisher, Manhattan, New York) Chap. 2, 25 (2012).
- Chi, S., Rodriguez-Rivera, J.A., Lynn, J.W., Zhang, C., Phelan, D., Singh, D.K., Paul, R., Dai, P., "Common Origin of the Two Types of Magnetic Fluctuations in Iron Chalcogenides," *Phys. Rev. B* **84**(21), 214407 (2011). [CHNRNS]
- Chiang, C.-C., Tsai, W.-C., Wang, L.-W., Hou, H.-C., Liao, J.-W., Lin, H.-J., Chang, F.-H., Kirby, B.J., Lai, C.-H., "(001) FePt Graded Media with PtMn Underlayers," *Appl. Phys. Lett.* **99**(21), 212504 (2011).
- Choi, D., Moon, J.H., Kim, H., Sung, B.J., Kim, M.W., Tae, G.Y., Satija, S.K., Akgun, B., Yu, C.-J., Lee, H.W., Lee, D.R., Henderson, J.M., Kwong, J.W., Lam, K.L., Lee, K.Y.C., Shin, K., "Insertion Mechanism of Cell-penetrating Peptides into Supported Phospholipid Membranes Revealed by X-ray and Neutron Reflection," *Phys. Rev. Lett.*, in press.
- Chou, S.G., Soper, A.K., Khodadadi, S., Curtis, J.E., Krueger, S., Cicerone, M.T., Fitch, A.N., Shalae, E.Y., "Pronounced Microheterogeneity in a Sorbitol-Water Mixture Observed through Variable Temperature Neutron Scattering," *J. Phys. Chem. B* **116**, 4439 (2012). [CHNRNS]
- Chua, Y.S., Wu, H., Zhou, W., Udovic, T.J., Wu, G., Xiong, Z., Wong, M.W., Chen, P., "Monoammoniate of Calcium Amidoborane: Synthesis, Structure and Hydrogen-Storage Properties," *Inorg. Chem.* **51**, 1599 (2012).
- Cicerone, M.T., Douglas, J.F., "β-Relaxation Governs Protein Stability in Sugar-Glass Matrices," *Soft Matter* **8**, 2983 (2012). [CHNRNS]
- Clarkson, C.R., Solano, N., Bustin, R.M., Bustin, A.M.M., Chalmers, G.R.L., He, L., Melnichenko, Y.B., Radliński, A.P., Blach, T.P., "Pore Structure Characterization of North American Shale Gas Reservoirs using USANS/SANS, Gas Adsorption, and Mercury Intrusion," *Fuel*, in press. [CHNRNS]
- Clarkson, C.R., Freeman, M., He, L., Agamalian, M., Melnichenko, Y.B., Mastalerz, M., Bustin, R.M., Radlinski, A.P., Blach, T.P., "Characterization of Tight Gas Reservoir Pore Structure using USANS/SANS and Gas Adsorption Analysis," *Fuel* **95**(1), 371 (2012). [CHNRNS]
- Cooper, R.L., Alarcon, R., Bales, M.J., Bass, C.D., Beise, E.J., Breuer, H., Byrne, J., Chupp, T.E., Coakley, K.J., Dewey, M.S., Fu, C., Gentile, T.R., Mumm, H.P., Nico, J.S., O'Neill, B., Pulliam, K., Thompson, A.K., Wietfeldt, F.E., "A Gamma- and X-ray Detector for Cryogenic, High Magnetic Field Applications," *Nucl. Instrum. Methods Phys. Res., Sect. A*, in press.

- Copley, J.R.D., "Acceptance Diagram Calculations of the Performance of Neutron Removal Mirrors," *Nucl. Instrum. Methods Phys. Res., Sect. A* **659**, 403 (2011).
- Couet, A., Motta, A.T., Comstock, R.J., Paul, R.L., "Cold Neutron Prompt Gamma Activation Analysis, a Non-destructive Technique for Hydrogen Level Assessment in Zirconium Alloys," *J. Nucl. Mater.* **425**, 211 (2012).
- Cui, J., Lackey, M.A., Madkour, A.E., Saffer, E.M., Griffin, D.M., Bhatia, S.R., Crosby, A.J., Tew, G.N., "Synthetically Simple, Highly Resilient Hydrogels," *Biomacromolecules* **13**, 584 (2012).
- Curtis, J.E., McAuley, A., Nanda, H., Krueger, S., "Protein Structure and Interactions in the Solid State Studied by Small-Angle Neutron Scattering," *Faraday Discuss.*, in press. [CHNRNS]
- Curtis, J.E., Nanda, H., Khodadadi, S., Cicerone, M., Lee, H.J., McAuley, A., Krueger, S., "Small-Angle Neutron Scattering Study of Protein Crowding in Liquid and Solid Phases: Lysozyme in Aqueous Solution, Frozen Solution, and Carbohydrate Powders," *J. Phys. Chem. B*, in press. [CHNRNS]
- Curtis, J.E., Raghunandan, S., Nanda, H., Krueger, S., "SASSIE: A Program to Study Intrinsically Disordered Biological Molecules and Macromolecular Ensembles using Experimental Scattering Restraints," *Comput. Phys. Commun.* **183**, 382 (2012). [CHNRNS]
- Das, M.C., Xu, H., Wang, Z., Srinivas, G., Zhou, W., Yue, Y.-F., Nesterov, V.N., Qian, G., Chen, B., "A Zn_4O -Containing Doubly Interpenetrated Porous Metal-Organic Framework for Photocatalytic Decomposition of Methyl Orange," *Chem. Commun.* **47**, 11715 (2011).
- Das, P., Rastovski, C., O'Brien, T.R., Schlesinger, K.J., Dewhurst, C.D., DeBeer-Schmitt, L., Zhigadlo, N.D., Karpinski, J., Eskildsen, M.R., "Observation of Well-Ordered Metastable Vortex Lattice Phases in Superconducting MgB_2 Using Small-Angle Neutron Scattering," *Phys. Rev. Lett.* **108**(16), 167001 (2012). [CHNRNS]
- Dee, D.R., Myers, B., Yada, R.Y., "Dynamics of Thermodynamically Stable, Kinetically Trapped, and Inhibitor-Bound States of Pepsin," *Biophys. J.* **101**, 1699 (2011). [CHNRNS]
- Dee, D.R., Yada, R.Y., "Neutron Scattering and the Folding and Dynamics of the Digestive Enzyme Pepsin," *Neutron News* **23**(2), 29 (2012). [CHNRNS]
- Deka, U., Juhin, A., Eilertsen, E.A., Emerich, H., Green, M.A., Korhonen, S.T., Weckhuysen, B.M., Beale, A.M., "Confirmation of Isolated Cu^{2+} Ions in SSZ-13 Zeolite as Active Sites in NH_3 -Selective Catalytic Reduction," *J. Phys. Chem. C* **116**, 4809 (2012).
- Delaire, O., Stone, M.B., Ma, J., Huq, A., Gout, D., Brown, C., Wang, K.F., Ren, Z.F., "Anharmonic Phonons and Magnons in $BiFeO_3$," *Phys. Rev. B* **85**(6), 064405 (2012). [CHNRNS]
- de Souza, R.A., Staub, U., Scagnoli, V., Garganourakis, M., Bodenthin, Y., Huang, S.W., García-Fernández, M., Ji, S., Lee, S.H., Park, S., Cheong, S.-W., "Magnetic Structure and Electric Field Effects in Multiferroic YMn_2O_5 ," *Phys. Rev. B* **84**(10), 104416 (2011).
- Dhaubhadel, R., Rieker, T.P., Chakrabarti, A., Sorensen, C.M., "Synthesis of Silica Aerosol Gels via Controlled Detonation," *Aerosol Sci. Technol.* **46**, 596 (2012).
- Diallo, S.O., Azuah, R.T., Abernathy, D.L., Rota, R., Boronat, J., Glyde, H.R., "Bose-Einstein Condensation in Liquid 4He Near the Liquid-Solid Transition Line," *Phys. Rev. B* **85**(14), 140505 (2012).
- Diao, Y., Helgeson, M.E., Siam, Z.A., Doyle, P.S., Myerson, A.S., Hatton, T.A., Trout, B.L., "Nucleation Under Soft Confinement: Role of Polymer-Solute Interactions," *Cryst. Growth Des.* **12**(1), 508 (2012). [CHNRNS]
- Ding, L., Wang, C., Chu, L., Yan, J., Na, Y., Huang, Q., Chen, X., "Near Zero Temperature Coefficient of Resistivity in Antiperovskite $Mn_3Ni_{1-x}Cu_xN$," *Appl. Phys. Lett.* **99**(25), 251905 (2011).
- Dissanayake, S.E., Chan, C., Ji, S., Lee, J., Qiu, Y., Rule, K.C., Lake, B., Green, M., Hagihala, M., Zheng, X.G., Ng, T.K., Lee, S.-H., "Magnetic-field-Induced Instability of the Cooperative Paramagnetic State in $Zn_xCo_{4-x}(OD)_6Cl_2$," *Phys. Rev. B* **85**(17), 174435 (2012). [CHNRNS]

- Dufour, C., Fitzsimmons, M.R., Borchers, J.A., Laver, M., Krycka, K.L., Dumesnil, K., Watson, S.M., Chen, W.C., Won, J., Singh, S., "Nanometer-Size Magnetic Domains and Coherent Magnetization Reversal in a Giant Exchange Bias System," *Phys. Rev. B* **84**(6), 064420 (2011).
- Dumas, R.K., Fang, Y., Kirby, B.J., Zha, C., Bonanni, V., Nogués, J., Åkerman, J., "Probing Vertically Graded Anisotropy in FePtCu Films," *Phys. Rev. B* **84**(5), 054434 (2011).
- Dutton, S.E., Huang, Q., Tchernyshyov, O., Broholm, C.L., Cava, R.J., "Sensitivity of the Magnetic Properties of the ZnCr_2O_4 and MgCr_2O_4 Spinels to Nonstoichiometry," *Phys. Rev. B* **83**(6), 064407 (2011).
- Dutton, S.E., Kumar, M., Mourigal, M., Soos, Z.G., Wen, J.-J., Broholm, C.L., Andersen, N.H., Huang, Q., Zbiri, M., Toft-Petersen, R., Cava, R.J., "Quantum Spin Liquid in Frustrated One-Dimensional LiCuSbO_4 ," *Phys. Rev. Lett.* **108**(18), 187206 (2012).
- Eberle, A.P.R., Ortman, K., Baird, D.G., "Structure and Rheology of Fiber Suspensions," in "Applied Polymer Rheology: Polymeric Fluids with Industrial Applications," edited by Kontopoulou, M. (John Wiley & Sons, Inc., Hoboken, NJ) **4**, 113 (2011).
- Eberle, A.P.R., Castañeda-Priego, R., Kim, J.M., Wagner, N.J., "Dynamical Arrest, Percolation, Gelation, and Glass Formation in Model Nanoparticle Dispersions with Thermoreversible Adhesive Interactions," *Langmuir* **28**, 1866 (2011).
- Eberle, A.P.R., Porcar, L., "Flow-SANS and Rheo-SANS Applied to Soft Matter," *Curr. Opin. Colloid Interface Sci.* **17**, 33 (2012).
- Ehlers, G., Huq, A., Diallo, S.O., Adriano, C., Rule, K.C., Cornelius, A.L., Fouquet, P., Pagliuso, P.G., Gardner, J.S., "Low Energy Spin Dynamics in the Spin Ice $\text{Ho}_2\text{Sn}_2\text{O}_7$," *J. Phys.: Condens. Matter* **24**, 076005 (2012).
- Espinal, L., Wong-Ng, W., Kaduk, J.A., Allen, A.J., Snyder, C.R., Chiu, C., Siderius, D.W., Li, L., Cockayne, E., Espinal, A.E., Suib, S.L., "Time-Dependent CO_2 Sorption Hysteresis in a One-Dimensional Microporous Octahedral Molecular Sieve," *J. Am. Chem. Soc.* **134**, 7944 (2012). [CHRNA]
- Falus, P., Porcar, L., Fratini, E., Chen, W.-R., Faraone, A., Hong, K., Baglioni, P., Liu, Y., "Distinguishing the Monomer to Cluster Phase Transition in Concentrated Lysozyme Solutions by Studying the Temperature Dependence of the Short-Time Dynamics," *J. Phys.: Condens. Matter* **24**, 064114 (2012). [CHRNA]
- Faraone, A., Hong, K., Kneller, L.R., Ohl, M., Copley, J.R.D., "Coherent Dynamics of *meta*-Toluidine Investigated by Quasielastic Neutron Scattering," *J. Chem. Phys.* **136**(10), 104502 (2012). [CHRNA]
- Ferguson, P.P., Fleischauer, M.D., LaForge, J.M., Todd, A.D.W., Li, P., Dahn, J.R., "Studies of CoSn Grains in the Carbon Matrix Structure of Nanostructured Tin-Cobalt-Carbon," *J. Alloys Compd.*, in press. [CHRNA]
- Fisher, B.M., Abdurashitov, J.N., Coakley, K.J., Gavrin, V.N., Gilliam, D.M., Nico, J.S., Shikhin, A.A., Thompson, A.K., Vecchia, D.F., Yants, V.E., "Fast Neutron Detection with ^6Li -Loaded Liquid Scintillator," *Nucl. Instrum. Methods Phys. Res., Sect. A* **646**, 126 (2011).
- Fitzgerald, P.A., Chatjaroenporn, K., Zhang, X., Warr, G.G., "Micellization of Monomeric and Poly- ω -methacryloyloxyundecyltrimethylammonium Surfactants," *Langmuir* **27**, 11852 (2011).
- Ford, K.M., Konzman, B.G., Robinson, J.F., "A More Informative Approach for Characterization of Polymer Monolithic Phases: Small Angle Neutron Scattering/ Ultrasmall Angle Neutron Scattering," *J. Anal. Chem.* **83**, 9201 (2011). [CHRNA]
- Frontzek, M., Haraldsen, J.T., Podlesnyak, A., Matsuda, M., Christianson, A.D., Fishman, R.S., Sefat, A.S., Qiu, Y., Copley, J.R.D., Barilo, S., Shiryaev, S.V., Ehlers, G., "Magnetic Excitations in the Geometric Frustrated Multiferroic CuCrO_2 ," *Phys. Rev. B* **84**(9), 094448- 1 (2011). [CHRNA]
- Furdyna, J.K., Leiner, J., Liu, X., Dobrowolska, M., Lee, S., Chung, J.-H., Kirby, B.J., "Exchange Coupling in Magnetic Semiconductor Multilayers and Superlattices," *Acta Phys. Pol., A* **5-6**, 973 (2012).
- Gadipelli, S., Calizo, I., Ford, J., Cheng, G., Hight Walker, A.R., Yildirim, T., "A Highly Practical Route for Large-Area, Single Layer Graphene from Liquid Carbon Sources such as Benzene and Methanol," *J. Mater. Chem.* **21**, 16057 (2011).

- Gardner, J.S., Ehlers, G., Diallo, S.O., "Neutron Studies of $\text{Tb}_2\text{Mo}_2\text{O}_7$," *Chin. J. Phys.* **50**(2), 256 (2012). [CHNRNS]
- Garg, S., Porcar, L., Hamill, A.C., Butler, P.D., Perez-Salas, U., "Response to "How Slow is the Transbilayer Diffusion (Flip-Flop) of Cholesterol?,"" *Biophys. J.* **102**(4), 947 (2012). [CHNRNS]
- Gaulin, B.D., Gardner, J.S., McClarty, P.A., Gringras, M.J.P., "Lack of Evidence for a Singlet Crystal-Field Ground State in the Magnetic Pyrochlore $\text{Tb}_2\text{Ti}_2\text{O}_7$," *Phys. Rev. B* **84**(14), 140402 (2011). [CHNRNS]
- Gaulin, B.D., Gardner, J.S., "Experimental Studies of Pyrochlore Antiferromagnets," in "Introduction to Frustrated Magnetism Materials, Experiments, Theory," edited by Lacroix, C., Mendels, P., Mila, F. (Springer Berlin Heidelberg), Chap. 8, 177 (2011). [CHNRNS]
- Gehring, P.M., "Neutron Diffuse Scattering in Lead-Based Relaxor Ferroelectrics and its Relationship to the Ultra-High Piezoelectricity," *J. Adv. Dielect.* **2**(2), 1241005 (2012). [CHNRNS]
- Gentile, T.R., Bass, C.D., Nico, J.S., Breuer, H., Farrell, R., "Magnetic Field Effects on Large Area Avalanche Photodiodes at Cryogenic Temperatures," *Nucl. Instrum. Methods Phys. Res., Sect. A* **652**, 520 (2011).
- Gentile, T.R., Bales, M., Arp, U., Dong, B., Farrell, R., "Response of Large Area Avalanche Photodiodes to Low Energy X-Rays," *Rev. Sci. Instrum.* **83**(5), 053105-1 (2012).
- Glyde, H.R., Diallo, S.O., Azuah, R.T., Kirichek, O., Taylor, J.W., "Atomic Momentum Distribution and Bose-Einstein Condensation in Liquid ^4He under Pressure," *Phys. Rev. B* **84**(18), 184506-1 (2011).
- Gnäupel-Herold, T.H., "A Software for Diffraction Stress Factor Calculations for Textured Material," in "Advances in X-ray Analysis," edited by Blanton, T., (60th Denver X-ray Conf. Proc., August 2011, Colorado Springs, CO) **55**, 123 (2012).
- Gnäupel-Herold, T.H., "ISODEC: Software for Calculating Diffraction Elastic Constants," *J. Appl. Crystallogr.* **45**, 573 (2012).
- Gnäupel-Herold, T.H., Creuziger, A.A., Iadicola, M., "A Model for Calculating Diffraction Elastic Constants," *J. Appl. Crystallogr.* **45**, 197 (2012).
- Gnäupel-Herold, T.H., "A Software for Diffraction Stress Factor Calculations for Textured Materials," *Powder Diffr.* **27**(2), 114 (2012).
- Gnäupel-Herold, T.H., Creuziger, A., Iadicola, M.A., "An Investigation of the Accuracy of Diffraction Stress Evaluation of Textured Materials," in "Advances in X-ray Analysis," edited by Blanton, T., (60th Denver X-ray Conf. Proc., August 2011, Colorado Springs, CO) **55**, 128 (2012).
- Gnäupel-Herold, T.H., Creuziger, A.A., Iadicola, M., "Evolution of Anisotropic Stress Factors with Texture in the Biaxial Deformation of HSLA50 Steel," in "Plasticity 2012," edited by Khan, A., (International Symp. On Plasticity and its Current Appl. Conf. Proc., January 2012, Rio Grande, PR.), 13 (2012).
- Gu, Y., Wang, C., Russell, T.P., "Multi-Length-Scale Morphologies in PCPDTBT/PCBM Bulk-Heterojunction Solar Cells," *Adv. Energy Mater.* **2**, 683 (2012).
- Guidi, T., "Neutron Spectroscopy of Molecular Nanomagnets," in "Molecular Cluster Magnets, Volume 3" edited by Winpenny, R. (World Scientific Series in NanoScience and Nanotechnology), Chap. 4, 181 (2011). [CHNRNS]
- Gupta, S., Dura, J.A., Freites, J.A., Tobias, D.J., Blasie, J.K., "Structural Characterization of the Voltage Sensor Domain and Voltage-gated K^+ Channel Proteins Vectorially-oriented within a Single Bilayer Membrane at the Solid/Vapor and Solid/Liquid interfaces via Neutron Interferometry," *Langmuir* **28**(28), 10504 (2012).
- Habersberger, B.M., Bates, F.S., Lodge, T.P., "Hierarchical Microphase Separation in Bicontinuous Ternary Polymer Blends," *Soft Matter* **8**, 3429 (2012).
- Hammouda, B., "Small-Angle Scattering from Branched Polymers," *Macromol. Theory Simul.* **21**, 372 (2012).
- Hardy, G.J., Nayak, R., Munir Alam, S., Shapter, J.G., Heinrich, F., Zauscher, S., "Biomimetic Supported Lipid Bilayers with High Cholesterol Content Formed by α -helical Peptide-induced Vesicle Fusion," *J. Mater. Chem.*, in press.

- He, L., Melnichenko, Y.B., Mastalerz, M., Sakurovs, R., Radlinski, A.P., Blach, T., "Pore Accessibility by Methane and Carbon Dioxide in Coal as Determined by Neutron Scattering," *Energy Fuels* **26**, 1975 (2012). [CHRNA]
- He, T., Wu, H., Wu, G., Wang, J., Zhou, W., Xiong, Z., Chen, J., Zhang, T., Chen, P., "Borohydride Hydrazines: High Hydrogen Content Materials for Hydrogen Storage," *Energy Environ. Sci.* **5**, 5686 (2012).
- He, Y., Zhang, Z., Xiang, S., Wu, H., Franczek, F.R., Zhou, W., Krishna, R., O'Keeffe, M., Chen, B., "High Separation Capacity and Selectivity of C₂ Hydrocarbons over Methane within a Microporous Metal-Organic Framework at Room Temperature," *Chem. Eur. J.*, **18** 1901 (2012).
- Helgeson, M.E., Wagner, N.J., "Colloidal Interactions Mediated by End-adsorbing Polymer-Like Micelles," *J. Chem. Phys.* **135**(8), 084901 (2011).
- Helgeson, M.E., Moran, S.E., An, H.Z., Doyle, P.S., "Mesoporous Organohydrogels from Thermogelling Photocrosslinkable Nanoemulsions," *Nature Materials* **11**(4), 344 (2012). [CHRNA]
- Helton, J.S., Stone, M.B., Shulyatev, D.A., Mukovskii, Y.M., Lynn, J.W., "Paramagnetic Spin Correlations in Colossal Magnetoresistive La_{0.7}Ca_{0.3}MnO₃," *Phys. Rev. B* **85**(14), 144401 (2012).
- Helton, J.S., Singh, D.K., Nair, H.S., Elizabeth, S., "Magnetic Order of the Hexagonal Rare-Earth Manganite Dy_{0.5}Y_{0.5}MnO₃," *Phys. Rev. B* **84**(6), 064434 (2011). [CHRNA]
- Helton, J.S., Chen, Y., Bychkov, G.L., Barilo, S.N., Rogado, N., Cava, R.J., Lynn, J.W., "Evolution of the Commensurate and Incommensurate Magnetic phases of the $S = 3/2$ Kagome Staircase Co₃V₂O₈ in an Applied Field," *J. Phys.: Condens. Matter* **24**, 016003 (2012).
- Her, J.-H., Wu, H., Verdal, N., Zhou, W., Stavila, V., Udovic, T.J., "Structures of the Strontium and Barium Dodecahydro-*closo*-dodecaborates," *J. Alloys Compd.* **514**, 71 (2012).
- Hoarfrost, M.L., Tyagi, M., Segalman, R.A., Reimer, J.A., "Proton Hopping and Long-Range Transport in the Protic Liquid [Im][TFSI], Probed by Pulsed-Field Gradient NMR and Quasi-Elastic Neutron Scattering," *J. Phys. Chem. B* **116**(28), 8201 (2012). [CHRNA]
- Hoarfrost, M.L., Tyagi, M.S., Segalman, R.A., Reimer, J.A., "Effect of Confinement on Proton Transport Mechanisms in Block Copolymer/Ionic Liquid Membranes," *Macromolecules* **45**, 3112 (2012). [CHRNA]
- Hong, K., Liu, Y., Porcar, L., Liu, D., Gao, C.Y., Smith, G.S., Herwig, K.W., Cai, S., Li, X., Wu, B., Chen, W.-R., Liu, L., "Structural Response of Polyelectrolyte Dendrimer Towards Molecular Protonation: The Inconsistency Revealed by SANS and NMR," *J. Phys.: Condens. Matter* **24**, 064116 (2012).
- Hong, L., Smolin, N., Lindner, B., Sokolov, A.P., Smith, J.C., "Three Classes of Motion in the Dynamic Neutron-Scattering Susceptibility of a Globular Protein," *Phys. Rev. Lett.* **107**(14), 148102 (2011). [CHRNA]
- Hong, L., Cheng, X., Glass, D.C., Smith, J.C., "Surface Hydration Amplifies Single-Well Protein Atom Diffusion Propagating into the Macromolecular Core," *Phys. Rev. Lett.* **108**(23), 238102 (2012). [CHRNA]
- Hopkins, A.R., Tomczak, S.J., Vij, V., Jackson, A.J., "Small Angle Neutron Scattering (SANS) Characterization of Electrically Conducting Polyaniline Nanofiber/Polyimide Nanocomposites," *Thin Solid Films* **520**, 1617 (2011). [CHRNA]
- Horkay, F., Cho, S.H., Tathireddy, P., Rieth, L., Solzbacher, F., Magda, J., "Thermodynamic Analysis of the Selectivity Enhancement Obtained by Using Smart Hydrogels that are Zwitterionic when Detecting Glucose with Boronic Acid Moieties," *Sensors and Actuators B* **160**, 1363 (2011). [CHRNA]
- Horkay, F., Basser, P.J., Hecht, A.-M., Geissler, E., "Hierarchical Organization of Cartilage Proteoglycans," *Macromol. Symp.* **306-307**, 11 (2011). [CHRNA]
- Horkay, F., Basser, P.J., Hecht, A.-M., Geissler, E., "Chondroitin Sulfate in Solution: Effects of Mono- and Divalent Salts," *Macromolecules* **45**, 2882 (2012).

- Hu, N., Borkar, N., Kohls, D., Schaefer, D.W.,
“Characterization of Porous Materials Using Combined
Small-Angle X-ray and Neutron Scattering Techniques,”
J. Membr. Sci. **379**, 138 (2011). [CHNRNS]
- Huang, Q., Cai, J., Wu, H., He, Y., Chen, B., Qian, G.,
“A Robust Microporous Metal-Organic Framework
Constructed from a Flexible Organic Linker for Highly
Selective Sorption of Methanol over Ethanol and
Water,” J. Mater. Chem. **22**, 10352 (2012).
- Hudson, M.R., Queen, W.L., Mason, J.A., Fickel, D.W.,
Lobo, R.F., Brown, C.M., “Unconventional, Highly
Selective CO₂ Adsorption in Zeolite SSZ-13,” J. Am.
Chem. Soc. **134**, 1970 (2012).
- Hussey, D.S., Jacobson, D.L., Baltic, E., “Changing Optical
Axis due to Reactor Operation,” Nucl. Instrum.
Methods Phys. Res., Sect. A **651**, 73 (2011).
- Hyland, L.L., Taraban, M.B., Hammouda, B., Yu, Y.B.,
“Mutually Reinforced Multicomponent Polysaccharide
Networks,” Biopolymers **95**(12), 840 (2011).
- Hyland, L.L., Taraban, M.B., Feng, Y., Hammouda, B., Yu,
Y.B., “Viscoelastic Properties and Nanoscale Structures
of Composite Oligopeptide-Polysaccharide Hydrogels,”
Biopolymers **97**(3), 177 (2012). [CHNRNS]
- Iadicola, M., Gnäupel-Herold, T.H., “Effective X-ray Elastic
Constant Measurement for *In situ* Stress Measurement
of Biaxially Strained AA5754-O,” Mater. Sci. Eng.,
A **545**, 168 (2012).
- Iida, K., Lee, S.-H., Cheong, S.-W., “Coexisting Order
and Disorder Hidden in a Quasi-Two-Dimensional
Frustrated Magnet,” Phys. Rev. Lett. **108**(21), 217207
(2012). [CHNRNS]
- Iida, K., Qiu, Y., Sato, T.J., “Dzyaloshinsky-Moriya
Interaction and Long Lifetime of the Spin State in
the Cu₃ Triangular Spin Cluster by Inelastic Neutron
Scattering Measurements,” Phys. Rev. B **84**(9), 094449
(2011). [CHNRNS]
- Iwata-Harms, J.M., Wong, F.J., Alaan, U.S., Kirby, B.J.,
Borchers, J.A., Toney, M.F., Nelson-Cheeseman, B.B.,
Liberati, M., Arenholz, E., Suzuki, Y., “Controlling
Spin Ordering in Frustrated Magnets via Thin Film
Heteroepitaxy,” Phys. Rev. B **85**(21), 214424-1 (2012).
- Jacobson, D.L., Hussey, D.S., Baltic, E., “*In Situ* Imaging at
the NIST Neutron Imaging Facility,” Mater. Res. Soc.
Symp. Proc. **1318**, 3 (2011).
- Jang, Y., Akgun, B., Kim, H., Satija, S., Char, K.,
“Controlled Release from Model Blend Multilayer
Films Containing Mixtures of Strong and Weak
Polyelectrolytes,” Macromolecules **45**, 3542 (2012).
- Jendrzewska, I., Zajdel, P., Goryczka, T., Goraus, J., Kita,
A., Mydlarz, T., “Influence of Covalency and Anion
Polarization on Magnetic and Electronic Properties of
ZnCr_{2-x}Ni_xSe₄,” J. Alloys Compd. **520**, 153 (2012).
- Ju, H., Heuser, B.J., Abernathy, D.L., Udovic, T.J.,
“Comparison of FANS and ARCS Incoherent Inelastic
Neutron Scattering Measurements of Hydrogen
Trapped at Dislocations in Deformed Pd,” Nucl.
Instrum. Methods Phys. Res., Sect. A **654**, 522 (2011).
- Kamitakahara, W.A., Faraone, A., Liu, K.-H., Mou, C.-Y.,
“Temperature Dependence of Structure and Density
for D₂O Confined in MCM-41-S,” J. Phys.: Condens.
Matter **24**, 064106 (2012).
- Kang, X., Wu, H., Luo, J., Zhou, W., Wang, P., “A Simple
and Efficient Approach to Synthesize Amidoborane
Ammoniates: Case Study for Mg(NH₂BH₃)₂(NH₃)₃
with Unusual Coordination Structure,” J. Mater.
Chem. **22**, 13174 (2012).
- Karhu, E.A., Kahwaji, S., Robertson, M.D., Fritzsche, H.,
Kirby, B.J., Majkrzak, C.F., Monchesky, T.L., “Helical
Magnetic Order in MnSi Thin Films,” Phys. Rev. B:
Condens. Matter **84**(6), 060404-1 (2011).
- Karhu, E.A., Rößler, U., Bogdanov, A.N., Kahwaji, S.,
Kirby, B.J., Fritzsche, H., Robertson, M.D., Majkrzak,
C.F., Monchesky, T.L., “Chiral Modulations and
Reorientation Effects in MnSi Thin Films,” Phys. Rev.
B **85**(9), 094429-1 (2012).
- Katayama, N., Matsubayashi, K., Nomura, Y., Ji, S., Leao,
J., Green, M.A., Sato, T.J., Uwatoko, Y., Fujita, M.,
Yamada, K., Arita, R., Lee, S.-H., “Conductivity
and Incommensurate Antiferromagnetism of
Fe_{1.02}Se_{0.10}Te_{0.90} Under Pressure,” Europhys. Lett. **98**,
37002 (2012).

- Kauffman, K.L., Culp, J.T., Allen, A.J., Espinal, L., Wong-Ng, W., Brown, T.D., Goodman, A., Bernardo, M.P., Pancoast, R.J., Chirdon, D., Matranga, C., "Selective Adsorption of CO₂ from Light Gas Mixtures by Using a Structurally Dynamic Porous Coordination Polymer," *Angew. Chem. Int. Ed.* **50**, 10888 (2011). [CHRN]
- Khatami, E., Helton, J.S., Rigol, M., "Numerical Study of the Thermodynamics of Clinoatacamite," *Phys. Rev. B* **85**(6), 064401 (2012).
- Kim, F.S., Penumadu, D., Hussey, D.S., "Water Distribution Variation in Partially Saturated Granular Materials Using Neutron Imaging," *J. Geotech. Geoenviron. Eng.* **138**(2), 147 (2012).
- Kim, J.-H., van der Vegte, M.A., Scaramucci, A., Artyukhin, S., Chung, J.-H., Park, S., Cheong, S.-W., Mostovoy, M., Lee, S.-H., "Magnetic Excitations in the Low-Temperature Ferroelectric Phase of Multiferroic YMn₂O₅ Using Inelastic Neutron Scattering," *Phys. Rev. Lett.* **107**(9), 097401 (2011). [CHRN]
- Kim, M.-H., Doh, J.-M., Han, S.C., Chae, K.H., Yu, B.-Y., Hong, K.T., Jackson, A., Anovitz, L.M., "The Pore Wall Structure of Porous Semi-Crystalline Anatase TiO₂," *J. Appl. Crystallogr.* **44**(6), 1238 (2011).
- Kim, S.Y., Schweizer, K.S., Zukoski, C.F., "Multiscale Structure, Interfacial Cohesion, Adsorbed Layers, and Thermodynamics in Dense Polymer-Nanoparticle Mixtures," *Phys. Rev. Lett.* **107**(22), 225504-1 (2011).
- Kim, S.Y., Zukoski, C.F., "Role of Polymer Segment-Particle Surface Interactions in Controlling Nanoparticle Dispersions in Concentrated Polymer Solutions," *Langmuir* **27**, 10455 (2011).
- Kim, S.Y., Meyer, H.W., Saalwächter, K., Zukoski, C.F., "Polymer Dynamics in PEG-Silica Nanocomposites: Effects of Polymer Molecular Weight, Temperature and Solvent Dilution," *Macromolecules* **45**, 4225 (2012).
- Kim, S.W., Kim, S.-H., Halasyamani, P.S., Green, M.A., Bhatti, K.P., Leighton, C., Das, H., Fennie, C.J., "RbFe²⁺Fe³⁺F₆: Synthesis, Structure, and Characterization of a New Charge-Ordered Magnetically Frustrated Pyrochlore-Related Mixed-Metal Fluoride," *Chem. Sci.* **3**, 741 (2012).
- Kim, Y.-J., Sorini, A.P., Stock, C., Perring, T.G., van den Brink, J., Devereaux, T.P., "Probing High-Energy Electronic Excitations in NiO Using Inelastic Neutron Scattering," *Phys. Rev. B* **84**(8), 085132-1 (2011).
- Kintzel, Jr., E.J., Kidder, M.K., Buchanan, III, A.C., Britt, P.F., Mamontov, E., Zamponi, M., Herwig, K.W., "Dynamics of 1,3-Diphenylpropane Tethered to the Interior Pore Surfaces of MCM-41," *J. Phys. Chem. C* **116**, 923 (2011).
- Kirby, B.J., Kienzle, P.A., Maranville, B.B., Berk, N.F., Krycka, J., Heinrich, F., Majkrzak, C.F., "Phase-Sensitive Specular Neutron Reflectometry for Imaging the Nanometer Scale Composition Depth Profile of Thin-Film Materials," *Curr. Opin. Colloid Interface Sci.* **17**, 44 (2012).
- Kirschner, S.B., Smith, N.P., Wepasnick, K.A., Katz, H.E., Kirby, B.J., Borchers, J.A., Reich, D.H., "X-ray and Neutron Reflectivity and Electronic Properties of PCBM-poly(bromo)styrene Blends and Bilayers with Poly(3-hexylthiophene)," *J. Mater. Chem.* **22**, 4364 (2012).
- Klimczuk, T., Wang, C.H., Lawrence, J.M., Xu, Q., Durakiewicz, T., Ronning, F., Llobet, A., Trouw, F., Kurita, N., Tokiwa, Y., Lee, H.-O., Booth, C.H., Gardner, J.S., Bauer, E.D., Joyce, J.J., Zandbergen, H.W., Movshovich, R., Cava, R.J., Thompson, J.D., "Crystal Fields, Disorder, and Antiferromagnetic Short-Range Order in Yb_{0.24}Sn_{0.76}Ru," *Phys. Rev. B* **84**(7), 075152 (2011).
- Klose, C., Khaire, T.S., Wang, Y., Pratt, Jr., W.P., Birge, N.O., McMorran, B.J., Ginley, T.P., Borchers, J.A., Kirby, B.J., Maranville, B.B., Unguris, J., "Optimization of Spin-Triplet Supercurrent in Ferromagnetic Josephson Junctions," *Phys. Rev. Lett.* **108**(12), 127002-1 (2012).
- Kofu, M., Someya, T., Tatsumi, S., Ueno, K., Ueki, T., Watanabe, M., Matsunaga, T., Shibayama, M., García Sakai, V., Tyagi, M., Yamamuro, O., "Microscopic Insights into Ion Gel Dynamics using Neutron Spectroscopy," *Soft Matter* **8**, 7888 (2012). [CHRN]
- Koga, T., Gin, P., Yamaguchi, H., Endoh, M.K., Asada, M., Sendogdular, L., Kobayashi, M., Takahara, A., Akgun, B., Satija, S.K., Sumi, T., "Generality of Anomalous Expansion of Polymer Chains in Supercritical Fluids," *Polymer* **52**, 4331 (2011).

- Krueger, S., Shin, J.-H., Raghunandan, S., Curtis, J.E., Kelman, Z., "Atomistic Ensemble Modeling and Small-Angle Neutron Scattering of Intrinsically Disordered Protein Complexes: Applied to Minichromosome Maintenance Protein," *Biophys. J.* **101**, 2999 (2011). [CHNRNS]
- Krueger, S., Huie, J.L., Kuzmanovic, D.A., "Small Angle Scattering Analysis of Virus-like Particles for Biomedical Diagnostic Assays," in "Neutron Scattering Methods and Studies," edited by Lyons, M. J. (NOVA Science Publishers, Inc.), Chap. 2, 35 (2011).
- Krycka, K., Borchers, J., Ijiri, Y., Booth, R., Majetich, S., "Polarization-Analyzed Small-Angle Neutron Scattering. II. Mathematical Angular Analysis," *J. Appl. Crystallogr.* **45**, 554 (2012). [CHNRNS]
- Krycka, K., Chen, W., Borchers, J., Maranville, B., Watson, S., "Polarization-Analyzed Small-Angle Neutron Scattering. I. Polarized Data Reduction using *Pol-Corr*," *J. Appl. Crystallogr.* **45**, 546 (2012). [CHNRNS]
- Kučerka, N., Holland, B.W., Gray, C.G., Tomberli, B., Katsara, J., "Scattering Density Profile Model of POPG Bilayers as Determined by Molecular Dynamics Simulations and Small-Angle Neutron and X-ray Scattering Experiments," *J. Phys. Chem. B* **116**, 232 (2011). [CHNRNS]
- Kučerka, N., Nieh, M.-P., Katsaras, J., "Fluid Phase Lipid Areas and Bilayer Thickness of Commonly used Phosphatidylcholines as a Function of Temperature," *Biochim. Biophys. Acta* **1808**, 2761 (2011). [CHNRNS]
- Kulkarni, M.M., Yager, K.G., Sharma, A., Karim, A., "Combinatorial Block Copolymer Ordering on Tunable Rough Substrates," *Macromolecules* **45**(10), 4303 (2012). [CHNRNS]
- Kumari, H., Kline, S.R., Atwood, J.L., "Investigation of Encapsulation of Insulin Biotemplate within *C*-methylresorcin[4]arenes," *Chem. Commun.* **48**, 3599 (2012).
- Kumari, H., Mossine, A.V., Kline, S.R., Dennis, C.L., Fowler, D.A., Teat, S.J., Barnes, C.L., Deakyne, C.A., Atwood, J.L., "Controlling the Self-Assembly of Metal-Seamed Organic Nanocapsules," *Angew. Chem. Int. Ed.* **51**, 1452 (2012).
- Kumari, H., Kline, S.R., Wycoff, W.G., Paul, R.L., Mossine, A.V., Deakyne, C.A., Atwood, J.L., "Solution-Phase Structures of Gallium-Containing Pyrogallol[4]arene Scaffolds," *Angew. Chem. Int. Ed.* **51**, 5086 (2012).
- Kumari, H., Kline, S.R., Schuster, N.J., Barnes, C.L., Atwood, J.L., "Exploring the Ellipsoidal and Core-Shell Geometries of Copper-Seamed C-alkylpyrogallol[4]arene Nanocapsules in Solution," *J. Am. Chem. Soc.* **133**, 18102 (2011).
- Kumari, H., Kline, S.R., Schuster, N.J., Atwood, J.L., "Solution Structure of Copper-seamed C-alkylpyrogallol[4]arene Nanocapsules with Varying Chain Lengths," *Chem. Commun.* **47**, 12298 (2011). [CHNRNS]
- Kumi, B.C., Greer, S.C., "Micelles of Polybutadiene-*b*-poly(ethylene oxide) in Deuterated Methanol and Deuterated Cyclohexane," *J. Colloid Interface Sci.*, in press. [CHNRNS]
- Larson-Smith, K., Jackson, A., Pozzo, D.C., "SANS and SAXS Analysis of Charged Nanoparticle Adsorption at Oil-Water Interfaces," *Langmuir* **28**(5), 2493 (2012). [CHNRNS]
- Lauw, Y., Horne, M.D., Rodopoulos, T., Lockett, V., Akgun, B., Hamilton, W.A., Nelson, A.R.J., "Structure of [C₄mpyr][NTf₂] Room-Temperature Ionic Liquid at Electrified Gold Interfaces," *Langmuir* **28**, 7374 (2012).
- Lee, H., Kim, D.H., Witte, K.N., Ohn, K., Choi, J., Akgun, B., Satija, S.K., Won, Y.-Y., "Water is a Poor Solvent for Densely Grafted Poly(ethylene oxide) Chains: A Conclusion Drawn from a Self-Consistent Field Theory- Based Analysis of Neutron Reflectivity and Surface Pressure-Area Isotherm Data," *J. Phys. Chem. B* **116**, 7367 (2012).
- Lee, W., Kofinas, P., Briber, R.M., "Structure Investigation of Poly((2-dimethylamino)ethyl Methacrylate)/Sodium Dodecylsulfate Complexes in Concentrated Poly((2-dimethylamino)ethyl Methacrylate) Solutions using Small Angle Neutron Scattering," *Polymer* **53**, 2942 (2012).
- Levasseur, B., Ebrahim, A.M., Burrell, J., Bandosz, T.J., "Interactions of NO₂ at Ambient Temperature with Cerium-Zirconium Mixed Oxides Supported on SBA-15," *J. Hazard. Mater.* **197**, 294 (2011).

- Li, H., Chiang, W.-S., Fratini, E., Ridi, F., Bausi, F., Baglioni, P., Tyagi, M., Chen, S.-H., "Dynamic Crossover in Hydration Water of Curing Cement Paste: The Effect of Superplasticizer," *J. Phys.: Condens. Matter* **24**, 064108 (2012).
- Li, W.-H., Wang, C.-W., Hsu, D., Lee, C.-H., Wu, C.-M., Chou, C.-C., Yang, H.-D., Zhao, Y., Chang, S., Lynn, J.W., Berger, H., "Interplay Between the Magnetic and Electric Degrees of Freedom in Multiferroic Co_3TeO_6 ," *Phys. Rev. B* **85**(9), 094431 (2012).
- Li, X., Wu, B., Liu, Y., Pynn, R., Shew, C.-Y., Smith, G.S., Herwig, K.W., Robertson, J.L., Chen, W.-R., Liu, L., "Contrast Variation in Spin-Echo Small Angle Neutron Scattering," *J. Phys.: Condens. Matter* **24**, 064115 (2012).
- Lindstrom, R.M., "Hydrogen Measurement in Steel: A Query," *J. Radioanal. Nucl. Chem.* **289**(3), 289 (2011).
- Lindstrom, R.M., "A Second-Generation Low-Background Gamma Spectrometer," *Transactions of the American Nuclear Society* **105**, 349 (2011).
- Lindstrom, R.M., Fischbach, E., Buncher, J.B., Jenkins, J.H., Yue, A., "Absence of a Self-Induced Decay Effect in ^{198}Au ," *Nucl. Instrum. Methods Phys. Res., Sect.* **659**, 269 (2011).
- Lioudyno, M.I., Broccio, M., Sokolov, Y., Rasool, S., Wu, J., Alkire, M.T., Liu, V., Kozak, J.A., Dennison, P.R., Glabe, C.G., Lösche, M., Hall, J.E., "Effect of Synthetic A β Peptide Oligomers and Fluorinated Solvents on Kv1.3 Channel Properties and Membrane Conductance," *PloS ONE* 7(4), e35090 (2012).
- Liu, C.K., Warr, G.G., "Resiliently Spherical Micelles of Alkyltrimethylammonium Surfactants with Multivalent, Hydrolyzable Counterions," *Langmuir* **28**, 11007 (2012). [CHRNNS]
- Liu, J., Kirby, B.J., Gray, B., Kareev, M., Habermeier, H.-U., Cristiani, G., Freeland, J.W., Chakhalian, J., "Interfacial Electronic and Magnetic Properties of a $\text{Y}_{0.6}\text{Pr}_{0.4}\text{Ba}_2\text{Cu}_3\text{O}_7/\text{La}_{2/3}\text{Ca}_{1/3}\text{MnO}_3$ Superlattice," *Phys. Rev. B* **84**(9), 092506 (2011).
- Liu, X., Smith, D.J., Fan, J., Zhang, Y.-H., Cao, H., Chen, Y.P., Leiner, J., Kirby, B.J., Dobrowolska, M., Furdyna, J.K., "Structural Properties of Bi_2Te_3 and Bi_2Se_3 Topological Insulators Grown by Molecular Beam Epitaxy on GaAs(001) Substrates," *Appl. Phys. Lett.* **99**(17), 171903 (2011).
- Liu, X., Smith, D.J., Fan, J., Zhang, Y.-H., Cao, H., Chen, Y.P., Kirby, B.J., Sun, N., Ruggiero, S.T., Leiner, J., Pimpinella, R.E., Hagmann, J., Tivakornsasithorn, K., Dobrowolska, M., Furdyna, J.K., "Topological Insulators Bi_2Te_3 and Bi_2Se_3 Grown by MBE on (001) GaAs Substrates," *AIP Cong. Proc.* **1416**, 105 (2011).
- Liu, Y., Brown, C.M., Neumann, D.A., Geohegan, D.B., Puretzky, A.A., Rouleau, C.M., Hu, H., Styers-Barnett, D., Krasnov, P.O., Yakobson, B.I., "Metal-Assisted Hydrogen Storage on Pt-Decorated Single-Walled Carbon Nanohorns," *Carbon*, in press.
- López-Barrón, C.R., Basavaraj, M.G., DeRita, L., Wagner, N.J., "Sponge-to-Lamellar Transition in a Double-Tail Cationic Surfactant/Protic Ionic Liquid System: Structural and Rheological Analysis," *J. Phys. Chem. B* **116**, 813 (2012).
- López-Barrón, C.R., Porcar, L., Eberle, A.P.R., Wagner, N.J., "Dynamics of Melting and Recrystallization in a Polymeric Micellar Crystal Subjected to Large Amplitude Oscillatory Shear Flow," *Phys. Rev. Lett.* **108**(25), 258301 (2012).
- Lu, H., Akgun, B., Russell, T.P., "Morphological Characterization of a Low-Bandgap Crystalline Polymer:PCBM Bulk Heterojunction Solar Cells," *Adv. Energy Mater.* **1**, 870 (2011).
- Lu, H., Akgun, B., Wei, X., Li, L., Satija, S.K., Russell, T.P., "Temperature-Triggered Micellization of Block Copolymers on an Ionic Liquid Surface," *Langmuir* **27**, 12443 (2011).
- Lu, Y., Kwan, A.H., Trehella, J., Jeffries, C.M., "The C0C1 Fragment of Human Cardiac Myosin Binding Protein C Has Common Binding Determinants for Both Actin and Myosin," *J. Mol. Biol.* **413**, 908 (2011).

- Luo, H., Zhang, R., Laver, M., Yamani, Z., Wang, M., Lu, X., Wang, M., Chen, Y., Li, S., Chang, S., Lynn, J.W., Dai, P., "Coexistence and Competition of the Short-Range Incommensurate Antiferromagnetic Order with Superconducting in $\text{BaFe}_{2-x}\text{Ni}_x\text{As}_2$," *Phys. Rev. Lett.* **108**(24), 247002 (2012).
- Luo, J., Wu, H., Zhou, W., Kang, X., Fang, Z., Wang, P., "LiBH₄•NH₃BH₃: A New Lithium Borohydride Ammonia Borane Compound with a Novel Structure and Favorable Hydrogen Storage Properties," *Int. J. Hydrogen Energy* **37**, 10750 (2012).
- Lynn, J.W., Chen, Y., Chang, S., Zhao, Y., Chi, S., Ratcliff, II, W., Ueland, B.G., Erwin, R.W., "Double-Focusing Thermal Triple-Axis Spectrometer at the NCNR," *The Journal of Research of NIST* **117**, 61 (2012).
- Maiti, T., Guo, R., Bhalla, A.S., "Evaluation of Experimental Resume of $\text{BaZr}_x\text{Ti}_{1-x}\text{O}_3$ with Perspective to Ferroelectric Relaxor Family: An Overview," *Ferroelectrics* **425**, 4 (2011).
- Maitland, C.F., Buckley, C.E., O'Connor, B.H., Butler, P.D., Hart, R.D., "Characterization of the Pore Structure of Metakaolin-derived Geopolymers by Neutron Scattering and Electron Microscopy," *J. Appl. Crystallogr.* **44**(4), 697 (2011). [CHNRNS]
- Majkrzak, C.F., Carpenter, E., Heinrich, F., Berk, N.F., "When Beauty is Only Skin Deep; Optimizing the Sensitivity of Specular Neutron Reflectivity for Probing Structure Beneath the Surface of Thin Films," *J. Appl. Phys.* **110**(10), 102212 (2011).
- Malherbe, J., Isaure, M.-P., Séby, F., Watson, R.P., Rodriguez-Gonzalez, P., Stutzman, P.E., Davis, C.W., Maurizio, C., Unceta, N., Sieber, J.R., Long, S.E., Donard, O.F.X., "Evaluation of Hexavalent Chromium Extraction Method EPA Method 3060A for Soils using XANES Spectroscopy," *Environ. Sci. Technol.* **45**, 10492 (2011).
- Malingowski, A.C., Stephens, P.W., Huq, A., Huang, Q., Khalid, S., Khalifah, P.G., "Substitutional Mechanism of Ni into the Wide-Band-Gap Semiconductor InTaO_4 and its Implications for Water Splitting Activity in the Wolframite Structure Type," *Inorg. Chem.* **51**, 6096 (2012).
- Mallia, V.A., Terech, P., Weiss, R.G., "Correlations of Properties and Structures at Different Length Scales of Hydro- and Organo-gels Based on *N*-Alkyl-(*R*)-12-Hydroxyoctadecylammonium Chlorides," *J. Phys. Chem. B* **115**, 12401 (2011).
- Mang, J.T., Hjelm, R.P., "Small-Angle Neutron Scattering and Contrast Variation Measurement of the Interfacial Surface Area in PBX 9501 as a Function of Pressing Intensity," *Propellants Explos. Pyrotech.* **36**(5), 439 (2011). [CHNRNS]
- Maranas, J.K., "Solid Polymer Electrolytes", in "Dynamics of Soft Matter Neutron Applications and Techniques," edited by Sakai, V., Chen, S.-H., Alba-Simionesco, C.(Springer Science & Business Media, LLC, New York, NY) Chap, 5, 123 (2012). [CHNRNS]
- Mastalerz, M., He, L., Melnichenko, Y.B., Rupp, J.A., "Porosity of Coal and Shale: Insights from Gas Adsorption and SANS/USANS Techniques," *Energy Fuels*, in press. [CHNRNS]
- Melnichenko, Y.B., He, L., Sakurovs, R., Kholodenko, A.L., Blach, T., Mastalerz, M., Radliński, A.P., Cheng, G., Mildner, D.F.R., "Accessibility of Pores in Coal to Methane and Carbon Dioxide," *Fuel* **91**(1), 200 (2012). [CHNRNS]
- Mildner, D.F.R., Barker, J. G., Kline, S.R., "The Effect of Gravity on the Resolution of Small-Angle Neutron Diffraction Peaks," *J. Appl. Crystallogr.* **44**(5), 1127 (2011).
- Mildner, D.F.R., "Modeling the Transmission of Curved Neutron Guides with Non-Perfect Reflectivity," *Nucl. Instrum. Methods Phys. Res., Sect. A* **656**, 96 (2011).
- Mildner, D.F.R., Cubitt, R., "The Effect of Gravity on the Debye-Scherrer Ring in Small-Angle Neutron Scattering," *J. Appl. Crystallogr.* **45**(1), 124 (2012).
- Mishler, J., Wang, Y., Mukherjee, P.P., Mukundan, R., Borup, R.L., "Subfreezing Operation of Polymer Electrolyte Fuel Cells: Ice Formation and Cell Performance Loss," *Electrochim. Acta* **65**, 127 (2012).
- Mishler, J., Wang, Y., Mukundan, R., Spendelow, J., Hussey, D.S., Jacobson, D.L., Borup, R.L., "Probing the Water Content in Polymer Electrolyte Fuel Cells using Neutron Radiography," *Electrochim. Acta* **75**, 1 (2012).

- Mossine, A.V., Kumari, H., Fowler, D.A., Maerz, A.K., Kline, S.R., Barnes, C.L., Atwood, J.L., "Ferrocene as a Hydrophobic Templating Agent with Pyrogallol[4]arenes," *Isr. J. Chem.* **51**, 840 (2011).
- Mossine, A.V., Kumari, H., Fowler, D.A., Shih, A., Kline, S.R., Barnes, C.L., Atwood, J.L., "Ferrocene Species Included within a Pyrogallol[4]arene Tube," *Eur. J. Org. Chem.*, in press.
- Mumm, H.P., Chupp, T.E., Coulter, K.P., Cooper, R.L., Freedman, S.J., Fujikawa, B.K., García, A., Jones, G.L., Nico, J.S., Thompson, A.K., Trull, C.A., Wietfeldt, F.E., Wilkerson, J.F., "A New Limit on Time-Reversal-Invariance Violation in Beta Decay: Results of the emiT-II Experiment," in "Proceedings of Science," edited by unknown, (The 2011 Europhysics Conf. on High Energy Physics, July 2011, Grenoble, France) 1 (2011).
- Mumm, H.P., Chupp, T.E., Cooper, R.L., Coulter, K.P., Freedman, S.J., Fujikawa, B.K., García, A., Jones, G.L., Nico, J.S., Thompson, A.K., Trull, C.A., Wilkerson, J.F., Wietfeldt, F.E., "New Limit on Time-Reversal Violation in Beta Decay," *Phys. Rev. Lett.* **107**(10), 102301 (2011).
- Nagao, M., "Temperature and Scattering Contrast Dependencies of Thickness Fluctuations in Surfactant Membranes," *J. Chem. Phys.* **135**(7), 074704 (2011). [CHRN]
- Nagpure, S.C., Downing, R.G., Bhushan, B., Babu, S.S., "Discovery of Lithium in Copper Current Collectors used in Batteries," *Scripta Mater.*, in press.
- Nakatsuji, S., Kuga, K., Kimura, K., Satake, R., Katayama, N., Nishibori, E., Sawa, H., Ishii, R., Hagiwara, M., Bridges, F., Ito, T.U., Higemoto, W., Karaki, Y., Halim, M., Nugroho, A.A., Rodriguez-Rivera, J.A., Green, M.A., Broholm, C., "Spin-Orbital Short Range-Order on a Honeycomb-Based Lattice," *Science* **336**, 559 (2012).
- Newbloom, G.M., Weigandt, K.M., Pozzo, D.C., "Electrical, Mechanical, and Structural Characterization of Self-Assembly in Poly(3-hexylthiophene) Organogel Networks," *Macromolecules* **45**(8), 3452 (2012). [CHRN]
- Nickels, J.D., Curtis, J.E., O'Neill, H., Sokolov, A.P., "Role of Methyl Groups in Dynamics and Evolution of Biomolecules," *J. Biol. Phys.* **38**(3), 497 (2012). [CHRN]
- Nieh, M.-P., Dolinar, P., Kučerka, N., Kline, S.R., Debeer-Schmitt, L.M., Littrell, K.C., Katsaras, J., "Formation of Kinetically Trapped Nanoscopic Unilamellar Vesicles from Metastable Nanodiscs," *Langmuir* **27**, 14308 (2011). [CHRN]
- O'Malley, M.A., Helgeson, M.E., Wagner, N.J., Robinson, A.S., "Toward Rational Design of Protein Detergent Complexes: Determinants of Mixed Micelles That Are Critical for the *In Vitro* Stabilization of a G-Protein Coupled Receptor," *Biophys. J.* **101**, 1938 (2011).
- Oleson, T.A., Sahai, N., Wesolowski, D.J., Dura, J.A., Majkrzak, C.F., Giuffrè, A.J., "Neutron Reflectivity Study of Substrate Surface Chemistry Effects on Supported Phospholipid Bilayer Formation on (1120) Sapphire," *J. Colloid Interface Sci.* **370**, 192 (2012).
- Owejan, J.E., Owejan, J.P., DeCaluwe, S.C., Dura, J.A., "Solid Electrolyte Interphase in Li-Ion Batteries: Evolving Structures Measured *in situ* by Neutron Reflectometry," *Chem. Mater.* **24**, 2133 (2012).
- Owejan, J.P., Gagliardo, J.J., Harris, S.J., Wang, H., Hussey, D.S., Jacobson, D.L., "Direct Measurement of Lithium Transport in Graphite Electrodes using Neutrons," *Electrochim. Acta.* **66**, 94 (2012).
- Pai, S.S., Heinrich, F., Canady, A.L., Przybycien, T.M., Tilton, R.D., "Coverage-Dependent Morphology of PEGylated Lysozyme Layers Adsorbed on Silica," *J. Colloid Interface Sci.* **370**, 170 (2012).
- Pai, S.S., Hammouda, B., Hong, K., Pozzo, D.C., Przybycien, T.M., Tilton, R.D., "The Conformation of Poly(ethylene glycol) Chain in Mono-PEGylated Lysozyme and Mono-PEGylated Human Growth Hormone," *Bioconjugate Chem.* **22**, 2317 (2011). [CHRN]
- Pajerowski, D.M., Hallock, S.J., "Demagnetization in Photomagnetic Films," *J. Magn. Magn. Mater.* **324**, 1818 (2012).

- Pajerowski, D.M., Yamamoto, T., Einaga, Y.,
“Photomagnetic $K_{0.25}Ni_{1-x}Co_x[Fe(CN)_6] \cdot nH_2O$ and $K_{0.25}Co[Fe(CN)_6]_{0.75(1-y)} \cdot nH_2O$ Prussian Blue Analogue Solid Solutions,” *Inorg. Chem.* **51**, 3648 (2012).
- Pan, J., Heberle, F.A., Tristram-Nagle, S., Szymanski, M., Koepfinger, M., Katsaras, J., Kučerka, N., “Molecular Structures of Fluid Phase Phosphatidylglycerol Bilayers as Determined by Small Angle Neutron and X-ray Scattering,” *Biochim. Biophys. Acta*, in press.
- Peng, H.-G., Tyagi, M., Page, K. A., Soles, C. L., “Inelastic Neutron Scattering on Polymer Electrolytes for Lithium-Ion Batteries,” in “Polymers for Energy Storage and Delivery: Polyelectrolytes for Batteries and Fuel Cells, Volume 1096,” edited by Page, K. A., Soles, C. L., Runt, J. (ACS Publications, Washington, D.C.), Chap. 5, 67 (2012). [CHNRNS]
- Peri, S.R., Akgun, B., Satija, S.K., Jiang, H., Enlow, J., Bunning, T.J., Foster, M.D., “Control of Interface Nanoscale Structure Created by Plasma-Enhanced Chemical Vapor Deposition,” *ACS Appl. Mater. Interfaces* **3**, 3375 (2011).
- Perry, N.H., Mason, T.O., Ma, C., Navrotsky, A., Shi, Y., Bettinger, J.S., Toney, M.F., Paudel, T.R., Lany, S., Zunger, A., “ $Co_3O_4 \cdot Co_2ZnO_4$ Spinels: The Case for a Solid Solution,” *J. Solid State Chem.* **190**, 143 (2012).
- Pfefferkorn, C.M., Heinrich, F., Sodt, A.J., Maltsev, A.S., Pastor, R.W., Lee, J.C., “Depth of α -Synuclein in a Bilayer Determined by Fluorescence, Neutron Reflectometry, and Computation,” *Biophys. J.* **102**, 613 (2012).
- Porcar, L., Pozzo, D., Langenbacher, G., Moyer, J., Butler, P.D., “Rheo-Small-Angle Neutron Scattering at the National Institute of Standards and Technology Center for Neutron Research,” *Rev. Sci. Instrum.* **82**(8), 083902 (2011).
- Prabhu, V.M., Kang, S., Sha, J., Bonnesen, P.V., Satija, S., Wu, W.L., Ober, C.K., “Neutron Reflectivity Characterization of the Photoacid Reaction-Diffusion Latent and Developed Images of Molecular Resists for Extreme Ultraviolet Lithography,” *Langmuir* **28**, 7665 (2012).
- Prabhu, V.M., Kang, S., Kline, R.J., DeLongchamp, D.M., Fischer, D.A., Wu, W.-L., Satija, S.K., Bonnesen, P.V., Sha, J., Ober, C.K., “Characterization of the Non-uniform Reaction in Chemically Amplified Calix[4] Resorcinarene Molecular Resist Thin Films,” *Aust. J. Chem.* **64**(8), 1065 (2011).
- Prabhu, V.M., Reipa, V., “*In situ* Electrochemical Small-Angle Neutron Scattering (*e*SANS) for Quantitative Structure and Redox Properties of Nanoparticles,” *J. Phys. Chem. Lett.* **3**, 646 (2012). [CHNRNS]
- Pushin, D.A., Huber, M.G., Arif, M., Cory, D.G., “Experimental Realization of Decoherence-Free Subspace in Neutron Interferometry,” *Phys. Rev. Lett.* **107**(15), 150401 (2011).
- Qian, B., Lee, J., Hu, J., Wang, G.C., Kumar, P., Fang, M.H., Liu, T.J., Fobes, D., Pham, H., Spinu, L., Wu, X.S., Green, M., Lee, S.H., Mao, Z.Q., “Ferromagnetism in CuFeSb: Evidence of Competing Magnetic Interactions in Iron-Based Superconductors,” *Phys. Rev. B* **85**(14), 144427 (2012).
- Qian, K.K., Bogner, R.H., “Application of Mesoporous Silicon Dioxide and Silicate in Oral Amorphous Drug Delivery Systems,” *J. Pharm. Sci.* **101**(2), 444 (2012).
- Qian, K.K., Wurster, D.E., Bogner, R.H., “Spontaneous Crystalline-to-Amorphous Phase Transformation of Organic or Medicinal Compounds in the Presence of Porous Media, Part 3: Effect of Moisture,” *Pharm. Res.*, in press.
- Qian, K.K., Zhou, W., Xu, X., Udovic, T.J., “Characterization of Medicinal Compounds Confined in Porous Media by Neutron Vibrational Spectroscopy and First-Principles Calculations: A Case Study with Ibuprofen,” *Pharm. Res.*, in press.
- Queen, W.L., Brown, C.M., Britt, D.K., Zajdel, P., Hudson, M.R., Yaghi, O.M., “Site-Specific CO_2 Adsorption and Zero Thermal Expansion in an Anisotropic Pore Network,” *J. Phys. Chem. C* **115**, 24915 (2011).
- Queen, W.L., Bloch, E.D., Brown, C.M., Hudson, M.R., Mason, J.A., Murray, L.J., Ramirez-Cuesta, A.J., Peterson, V.K., Long, J.R., “Hydrogen Adsorption in the Metal-Organic Frameworks $Fe_2(dobdc)$ and $Fe_2(O_2)(dobdc)$,” *Dalton Trans.* **41**, 4180 (2012).

- Ramachandran, R., Beaucage, G., Rai, D.K., Lohse, D.J., Sun, T., Tsou, A.H., Norman, A., Hadjichristidis, N., "Quantification of Branching in Model Three-Arm Star Polyethylene," *Macromolecules* **45**(2), 1056 (2012).
- Ramazanoglu, M., Ratcliff, II, W., Yi, H.T., Sirenko, A.A., Cheong, S.-W., Kiryukhin, V., "Giant Effect of Uniaxial Pressure on Magnetic Domain Populations in Multiferroic Bismuth Ferrite," *Phys. Rev. Lett.* **107**(6), 067203 (2011).
- Ramazanoglu, M., Laver, M., Ratcliff, II, W., Watson, S.M., Chen, W.C., Jackson, A., Kothapalli, K., Lee, S., Cheong, S.-W., Kiryukhin, V., "Local Weak Ferromagnetism in Single-Crystalline Ferroelectric BiFeO₃," *Phys. Rev. Lett.* **107**(20), 207206 (2011).
- Reynga, Jr., G.J., "NCNR Control Room Modernization Phase I" in "Proc. of the American Nuclear Society," edited by unknown, (American Nuclear Society 2011 Winter Meeting, Washington, D.C., October 2011), in press.
- Richards, J.J., Weigandt, K.M., Pozzo, D.C., "Aqueous Dispersions of Colloidal Poly(3-hexylthiophene) Gel Particles with High Internal Porosity," *J. Colloid Interface Sci.* **364**, 341 (2011). [CHRNA]
- Rikkou-Kalourkoti, M., Loizou, E., Porcar, L., Matyjaszewski, K., Patrickios, C.S., "End-linked, Amphiphilic, Degradable Polymer Conetworks: Synthesis by Sequential Atom Transfer Radical Polymerization using a Bifunctional, Cleavable Initiator," *Polym. Chem.* **3**, 105 (2012).
- Ripley, E.M., Li, C., Moore, C.H., Elswick, E.R., Maynard, J.B., Paul, R.L., Sylvester, P., Seo, J.H., Shimizu, N., "Analytical Methods for Sulfur Determination in Glasses, Rocks, Minerals and Fluid Inclusions," in "Reviews in Mineralogy and Geochemistry, Volume 73," edited by Behrens, H., Webster, J.D. (The Mineralogical Society of America, Chantilly, VA), Chap. 2, 9 (2011).
- Ro, H.W., Akgun, B., O'Connor, B.T., Hammond, M., Kline, R.J., Snyder, C.R., Satija, S.K., Ayzner, A.L., Toney, M.F., Soles, C.L., DeLongchamp, D.M., "Poly(3-hexylthiophene) and [6,6]-Phenyl-C₆₁-Butyric Acid Methyl Ester Mixing in Organic Solar Cells," *Macromolecules*, in press.
- Rodriguez, E.E., Stock, C., Zajdel, P., Krycka, K. L., Majkrzak, C.F., Zavalij, P., Green, M.A., "Magnetic- Crystallographic Phase Diagram of the Superconducting Parent Compound Fe_{1+x}Te," *Phys. Rev. B* **84**(6), 064403 (2011). [CHRNA]
- Roh, J.H., Tyagi, M., Briber, R.M., Woodson, S.A., Sokolov, A.P., "The Dynamics of Unfolded Versus Folded tRNA: The Role of Electrostatic Interactions," *J. Am. Chem. Soc.* **133**, 16406 (2011). [CHRNA]
- Rosales, A.M., Murnen, H.K., Kline, S.R., Zuckermann, R.N., Segalman, R.A., "Determination of the Persistence Length of Helical and Non-Helical Polypeptoids in Solution," *Soft Matter* **8**, 3673 (2012). [CHRNA]
- Ross, K.A., Yaraskavitch, L.R., Laver, M., Gardner, J.S., Quilliam, J.A., Meng, S., Kycia, J.B., Singh, D.K., Proffen, Th., Dabkowska, H.A., Gaulin, B.D., "Dimensional Evolution of Spin Correlations in the Magnetic Pyrochlore Yb₂Ti₂O₇," *Phys. Rev. B* **84**(17), 174442 (2011). [CHRNA]
- Ross, K.A., Savary, L., Gaulin, B.D., Balents, L., "Quantum Excitations in Quantum Spin Ice," *Phys. Rev. X* **1**(2), 021002 (2011). [CHRNA]
- Saam, B., Petukhov, A.K., Chastagnier, J., Gentile, T.R., Golub, R., Swank, C.M., "Comment on "Pressure Dependence of Wall Relaxation in Polarized ³He Gaseous Cells"," *Phys. Rev. A* **85**(4), 047401 (2012).
- Saha, S.R., Butch, N.P., Drye, T., Magill, J., Ziemak, S., Kirshenbaum, K., Zavalij, P.Y., Lynn, J.W., Paglione, J., "Structural Collapse and Superconductivity in Rare-Earth-Doped CaFe₂As₂," *Phys. Rev. B* **85**(2), 024525 (2012).
- Şahin, İ., "Random Lines: A Novel Population Set-Based Evolutionary Global Optimization Algorithm." in "Genetic Programming, Volume 6621," edited by Silva, S., Foster, J.A., Nicolau, M., Machado, P., Giacobini, M, (Springer Berlin Heidelberg, Germany) 97 (2011).
- Sakurovs, R., He, L., Melnichenko, Y.B., Radlinski, A.P., Blach, T., Lemmel, H., Mildner, D.F.R., "Pore Size Distribution and Accessible Pore Size Distribution in Bituminous Coals," *International Journal of Coal Geology* **100**, 51 (2012). [CHRNA]

- Sander, L.C., Bedner, M., Tims, M.C., Yen, J.H., Duewer, D.L., Porter, B., Christopher, S.J., Day, R.D., Long, S.E., Molloy, J.L., Murphy, K.E., Lang, B.E., Lieberman, R., Wood, L.J., Payne, M.J., Roman, M.C., Betz, J.M., NguyenPho, A., Sharpless, K.E., Wise, S.A., "Development and Certification of Green Tea-Containing Standard Reference Materials," *Anal. Bioanal. Chem.* **402**, 473 (2012).
- Santos, T.S., Kirby, B.J., Kumar, S., May, S.J., Borchers, J.A., Maranville, B.B., Zarestky, J., te Velthuis, S.G.E., van den Brink, J., Bhattacharya, A., "Delta Doping of Ferromagnetism in Antiferromagnetic Manganite Superlattices," *Phys. Rev. Lett.* **107**(16), 167202 (2011).
- Sarte, P.M., Silverstein, H.J., Van Wyk, B.T.K., Gardner, J.S., Qiu, Y., Zhou, H.D., Wiebe, C.R., "Absence of Long -Range Magnetic Ordering in the Pyrochlore Compound $\text{Er}_2\text{Sn}_2\text{O}_7$," *J. Phys.: Condens. Matter* **23**, 382201 (2011). [CHRN]
- Selvam, P., Bharatwaj, B., Porcar, L., da Rocha, S.R.P., "Reverse Aqueous Microemulsions in Hydrofluoroalkane Propellants and their Aerosol Characteristics," *Int. J. Pharm.* **422**, 428 (2012).
- Shekhar, P., Nanda, H., Lösche, M., Heinrich, F., "Continuous Distribution Model for the Investigation of Complex Molecular Architectures near Interfaces with Scattering Techniques," *J. Appl. Phys.* **110**(10), 1022161 (2011).
- Shenoy, S., Shekhar, P., Heinrich, F., Daou, M.-C., Gericke, A., Ross, A.H., Lösche, M., "Membrane Association of the PTEN Tumor Suppressor: Molecular Details of the Protein-Membrane Complex from SPR Binding Studies and Neutron Reflection," *PloS ONE* **7**(4), e32591 (2012).
- Shew, C.-Y., Do, C., Hong, K., Liu, Y., Porcar, L., Smith, G.S., Chen, W.-R., "Conformational Effect on Small Angle Neutron Scattering Behavior of Interacting Polyelectrolyte Solutions: A Perspective of Integral Equation Theory," *J. Chem. Phys.* **137**(2), 024907 (2012).
- Shi, X., Yang, J., Salvador, J.R., Chi, M., Cho, J.Y., Wang, H., Bai, S., Yang, J., Zhang, W., Chen, L., "Multiple-Filled Skutterudites: High Thermoelectric Figure of Merit through Separately Optimizing Electrical and Thermal Transports," *J. Am. Chem. Soc.* **134**, 2842 (2012). [CHRN]
- Siderius, D.W., Krekelberg, W.P., Roberts, C.J., Shen, V.K., "Osmotic Virial Coefficients for Model Protein and Colloidal Solutions: Importance of Ensemble Constraints in the Analysis of Light Scattering Data," *J. Chem. Phys.* **136**(17), 175102 (2012).
- Siegel, J.B., Lin, X., Stefanopoulou, A., "On the Accuracy and Simplifications of Battery Models using *In Situ* Measurements of Lithium Concentration in Operational Cells," in "2012 American Control Conference" edited by unknown, (Fairmont Queen Elizabeth, Montreal, QC, Canada June 2012), 1362 (2012).
- Siegel, J.B., Lin, X., Stefanopoulou, A.G., Hussey, D.S., Jacobson, D.L., Gorisch, D., "Neutron Imaging of Lithium Concentration in LFP Pouch Cell Battery," *J. Electrochem. Soc.* **158**(5), A523 (2011).
- Simmons, J.M., Yildirim, T., Hamaed, A., Antonelli, D.M., Webb, M.I., Walsby, C.J., "Direct Observation of Activated Hydrogen Binding to a Supported Organometallic Compound at Room Temperature," *Chem. Eur. J.* **18**, 4170 (2012).
- Simonson, J.W., Yin, Z.P., Pezzoli, M., Guo, J., Liu, J., Post, K., Efimenko, A., Hollmann, N., Hu, Z., Lin, H.-J., Chen, C.-T., Marques, C., Leyva, V., Smith, G., Lynn, J.W., Sun, L.L., Kotliar, G., Basov, D.N., Tjeng, L.-H., Aronson, M.C., "From Antiferromagnetic Insulator to Correlated Metal in Pressurized and Doped LaMnPo ," *PNAS* **109**(27), 10751 (2012).
- Singh, D.K., Thamizhavel, A., Lynn, J.W., Dhar, S., Rodriguez-Rivera, J., Herman, T., "Field-induced Quantum Fluctuations in the Heavy Fermion Superconductor CeCu_2Ge_2 ," *Scientific Reports* **1**(117), 1 (2011). [CHRN]
- Singh, D.K., Thamizhavel, A., Chang, S., Lynn, J.W., Joshi, D.A., Dhar, S.K., Chi, S., "Coupling of Field-Induced Spin Fluctuations and Spin-Density Wave in Intermetallic CeAg_2Ge_2 ," *Phys. Rev. B* **84**(5), 052401 (2011). [CHRN]

- Sinha, K., Wang, W., Winey, K.I., Maranas, J.K., "Dynamic Patterning in PEO-Based Single Ion Conductors for Li Ion Batteries," *Macromolecules* **45**, 4354 (2012). [CHRNS]
- Skiprov, A.V., Mushnikov, N.V., Terent'ev, P.B., Gaviko, V.S., Udovic, T.J., Rush, J.J., "Hydrogen Dynamics in $\text{Ce}_2\text{Fe}_{17}\text{H}_5$: Inelastic and Quasielastic Neutron Scattering Studies," *J. Phys.: Condens. Matter* **23**, 405402 (2011). [CHRNS]
- Sobkowicz, M.J., Jones, R.L., Kline, R.J., DeLongchamp, D.M., "Effect of Fullerenes on Crystallization-Induced Aggregation in Polymer Photovoltaics Casting Solutions," *Macromolecules* **45**, 1046 (2011). [CHRNS]
- Song, X., Sun, Z., Huang, Q., Rettenmayr, M., Liu, X., Seyring, M., Li, G., Rao, G., Yin, F., "Adjustable Zero Thermal Expansion in Antiperovskite Manganese Nitride," *Adv. Mater.* **23**, 4690 (2011).
- Sora, I.N., Caronna, T., Fontana, F., de Julián Fernández, C., Caneschi, Green, M., "Crystal Structures and Magnetic Properties of Strontium and Copper Doped Lanthanum Ferrites," *J. Solid State Chem.* **191**, 33 (2012).
- Srinivas, G., Ford, J., Zhou, W., Yildirim, T., "Zn-MOF Assisted Dehydrogenation of Ammonia Borane: Enhanced Kinetics and Clean Hydrogen Generation," *Int. J. Hydrogen Energy* **37**, 3633 (2012).
- Srinivas, G., Burrell, J., Yildirim, T., "Graphene Oxide Derived Carbons (GODCs): Synthesis and Gas Adsorption Properties," *Energy Environ. Sci.* **5**(4), 6453 (2012).
- Stein, D.M., Grinberg, I., Rappe, A.M., Davies, P.K., "Multiple Dielectric Transitions in the PbTiO_3 - $\text{Bi}(\text{Zn}_{1/2}\text{Ti})\text{O}_3$ - $\text{Bi}(\text{Mg}_{1/2}\text{Ti}_{1/2})\text{O}_3$ System," *J. Appl. Phys.* **110**(7), 074110 (2011).
- Stewart, J.R., Ehlers, G., Wills, A.S., Bramwell, S.T., Gardner, J.S., "Comment on "Magnetic Structure of $\text{Gd}_2\text{Ti}_2\text{O}_7$," *Phys. Rev. B* **85**(10), 106401 (2012).
- Stock, C., Sokolov, D.A., Bourges, P., Tobash, P.H., Gofryk, K., Ronning, F., Bauer, E.D., Rule, K.C., Huxley, A.D., "Anisotropic Critical Magnetic Fluctuations in the Ferromagnetic Superconductor UCoGe ," *Phys. Rev. Lett.* **107**(18), 187202 (2011). [CHRNS]
- Stock, C., Cowley, R.A., Taylor, J.W., Bennington, S.M., "Reply to "Comment on 'High-Energy Neutron Scattering from Hydrogen using a Direct Geometry Spectrometer,'" *Phys. Rev. B* **84**(5), 056302 (2011).
- Stock, C., Rodriguez, E.E., Green, M.A., "Spin Fluctuations and Superconductivity in Powders of $\text{Fe}_{1+x}\text{Te}_{0.7}\text{Se}_{0.3}$ as a Function of Interstitial Iron Concentration," *Phys. Rev. B* **85**(9), 094507 (2012). [CHRNS]
- Sturgeon, R.E., Lam, J.W., Windust, A., Grinberg, P., Zeisler, R.L., Oflaz, R., Paul, R.L., Lang, B.E., Fagan, J.A., Simard, B., Kingston, C.T., "Determination of Moisture Content of Single-wall Carbon Nanotubes," *Anal. Bioanal. Chem.* **402**, 429 (2012).
- Sun, L., Chen, X.-J., Guo, J., Gao, P., Huang, Q.-Z., Wang, H., Fang, M., Chen, X., Chen, G., Wu, Q., Zhang, C., Gu, D., Dong, X., Wang, L., Yang, K., Li, A., Dai, X., Mao, H.-K., Zhao, Z., "Re-emerging Superconductivity at 48 Kelvin in Iron Chalcogenides," *Nature* **483**, 67 (2012).
- Sun, Y., Wang, C., Huang, Q., Guo, Y., Chu, L., Arai, M., Yamaura, K., "Neutron Diffraction Study of Unusual Phase Separation in the Antiperovskite Nitride Mn_3ZnN ," *Inorg. Chem.* **51**(13), 7232 (2012).
- Takatsu, H., Kadowaki, H., Sato, T.J., Lynn, J.W., Tabata, Y., Yamazaki, T., Matsuhira, K., "Quantum Spin Fluctuations in the Spin Liquid State of $\text{Tb}_2\text{Ti}_2\text{O}_7$," *J. Phys.: Condens. Matter* **24**, 052201 (2011). [CHRNS]
- Tao, R., "Electrorheology for Efficient Energy Production and Conservation," *J. Intell. Mater. Syst. Struct.* **22**, 1667 (2011).
- Taraban, M.B., Feng, Y., Hammouda, B., Hyland, L.L., Yu, Y.B., "Chirality-Mediated Mechanical and Structural Properties of Oligopeptide Hydrogels," *Chem. Mater.* **24**, 2299 (2012).
- Thampy, V., Kang, J., Rodriguez-Rivera, J.A., Bao, W., Savici, A.T., Hu, J., Liu, T.J., Qian, B., Fobes, D., Mao, Z.Q., Fu, C.B., Chen, W.C., Ye, Q., Erwin, R.W., Gentile, T.R., Tesanovic, Z., Broholm, C., "Friedel-like Oscillations from Interstitial Iron in Superconducting $\text{Fe}_{1+y}\text{Te}_{0.62}\text{Se}_{0.38}$," *Phys. Rev. Lett.* **108**(10), 107002 (2012). [CHRNS]

- Thomas, J.J., James, S., Ortega, J.A., Musso, S., Auzeais, F., Krakowiak, S.K.J., Akono, A., Ulm, F., Pellenq, R.J.M., "Fundamental Investigation of the Chemical and Mechanical Properties of High-Temperature-Cured Oilwell Cements," in "Offshore Technology Conference Proc." editor unknown, (Offshore Tech. Conf., April 2012, Houston, TX.), (2012).
- Thomas, J.J., Allen, A.J., Jennings, H.M., "Density and Water Content of Nanoscale Solid C-S-H Formed in Alkali-Activated Slag (AAS) Paste and Implications for Chemical Shrinkage," *Cem. Concr. Res.* **42**, 377 (2012). [CHRS]
- Thompson, S.M., Ma, H.B., Wilson, C., "Investigation of a Flat-Plate Oscillating Heat Pipe with Tesla-Type Check Valves," *Exp. Therm. Fluid Sci.* **35**, 1265 (2011).
- Toft-Petersen, R., Andersen, N.H., Li, H., Li, J., Tian, W., Bud'ko, S.L., Jensen, T.B.S., Niedermayer, C., Laver, M., Zaharko, O., Lynn, J.W., Vaknin, D., "Magnetic Phase Diagram of Magnetoelectric LiMnPO_4 ," *Phys. Rev. B* **85**(22), 224415 (2012).
- Tomiyasu, K., Crawford, M.K., Adroja, D.T., Manuel, P., Tominaga, A., Hara, S., Sato, H., Watanabe, T., Ikeda, S.I., Lynn, J.W., Iwasa, K., Yamada, K., "Molecular Spin-Orbit Excitations in the $J_{\text{eff}} = 1/2$ Frustrated Spinel GeCo_2O_4 ," *Phys. Rev. B* **84**(5), 054405 (2011).
- Top, A., Zhong, S., Yan, C., Roberts, C.J., Pochan, D.J., Kiick, K.L., "Controlling Assembly of Helical Polypeptides *via* PEGylation Strategies," *Soft Matter* **7**, 9758 (2011).
- Toppozini, L., Armstrong, C.L., Kaye, M.D., Tyagi, M., Jenkins, T., Rheinstädter, M.C., "Hydration Water Freezing in Single Supported Lipid Bilayers," *ISRN Biophysics* **2012**, 520307 (2012). [CHRS]
- Trivelpiece, C.L., Petrunis, J.H., Pantano, C.G., Downing, R.G., "Glass Surface Layer Density by Neutron Depth Profiling," *International Journal of Applied Glass Science* **3**(2), 137 (2012).
- Tsao, C.-S., Liu, Y., Chuang, H.-Y., Tseng, H.-H., Chen, T.-Y., Chen, C.-C., Yu, M.-S., Li, Q., Lueking, A., Chen, S.-H., "Hydrogen Spillover Effect of Pt-Doped Activated Carbon Studied by Inelastic Neutron Scattering," *J. Phys. Chem. Lett.* **2**, 2322 (2011).
- Valenza, II, J.J., Thomas, J.J., "Permeability and Elastic Modulus of Cement Paste as a Function of Curing Temperature," *Cem. Concr. Res.* **42**, 440 (2012). [CHRS]
- Verdal, N., Wu, H., Udovic, T.J., Stavila, V., Zhou, W., Rush, J.J., "Evidence of a Transition to Reorientational Disorder in the Cubic Alkali-metal Dodecahydro-*closo*-dodecaborates," *J. Phys. Chem. Solids* **184**, 3110 (2011).
- Verdal, N., Zhou, W., Stavila, V., Her, J.-H., Yousufuddin, M., Yildirim, T., Udovic, T.J., "Alkali and Alkaline-Earth Metal Dodecahydro-*closo*-Dodecaborates: Probing Structural Variations *via* Neutron Vibrational Spectroscopy," *J. Alloys Compd.* **509S**, S694 (2011).
- Verdal, N., Udovic, T.J., Rush, J.J., "The Nature of BH_4^- Reorientations in Hexagonal LiBH_4 ," *J. Phys. Chem. C* **116**, 1614 (2011).
- Verdal, N., Udovic, T.J., Rush, J.J., "Correction to "The Nature of BH_4^- Reorientations in Hexagonal LiBH_4 ," *J. Phys. Chem. C* **116**, 5275 (2012). [CHRS]
- Von White, II, G., Mohammed, F.S., Kitchens, C.L., "Small-Angle Neutron Scattering Investigation of Gold Nanoparticle Clustering and Ligand Structure Under Antisolvent Conditions," *J. Phys. Chem. C* **115**, 18397 (2011).
- Wang, C., Chu, L., Yao, Q., Sun, Y., Wu, M., Ding, L., Yan, J., Na, Y., Tang, W., Li, G., Huang, Q., Lynn, J.W., "Tuning the Range, Magnitude, and Sign of the Thermal Expansion in Intermetallic $\text{Mn}_3(\text{Zn}, \text{M})\text{N}$ ($M = \text{Ag}, \text{Ge}$)," *Phys. Rev. B* **85**(22), 220103 (2012).
- Wang, H., Downing, R.G., Dura, J.A., Hussey, D.S., "In situ Neutron Techniques for Studying Lithium Ion Batteries," in "Polymers for Energy Storage and Delivery: Polyelectrolytes for Batteries and Fuel Cells, Volume 1096," edited by Page, K., *et al.*, (American Chemical Society, Washington, D.C.) Chap. 6, 91 (2012).
- Wang, M., Wang, M., Li, G.N., Huang, Q., Li, C.H., Tan, G.T., Zhang, C.L., Cao, H., Tian, W., Zhao, Y., Chen, Y.C., Lu, X.Y., Sheng, B., Luo, H.Q., Li, S.L., Fang, M.H., Zarestky, J.L., Ratcliff, W., Lumsden, M.D., Lynn, J.W., Dai, P., "Antiferromagnetic Order and Superlattice Structure in Nonsuperconducting and Superconducting $\text{RbFe}_{1.6+x}\text{Se}_2$," *Phys. Rev. B* **84**(9), 094504 (2011).

- Wang, S.-C., Mirarefi, P., Faraone, A., Lee, Jr., C.T., "Light-Controlled Protein Dynamics Observed with Neutron Spin Echo Measurements," *Biochemistry* **50**, 8150 (2011). [CHRSN]
- Wang, X.-M., Wang, C.-H., Wu, M.M., Wang, Y.X., Jing, X.-P., "O/N Ordering in the Structure of $\text{Ca}_3\text{Si}_2\text{O}_4\text{N}_2$ and the Luminescence Properties of the Ce^{3+} Doped Material," *J. Mater. Chem.* **22**, 3388 (2012).
- Watson, B.J., Hammouda, B., Briber, R.M., Hutcheson, S.W., "Influence of Organic Liquids on the Nanostructure of Precipitated Cellulose," *J. Appl. Polym. Sci.*, in press. [CHRSN]
- Weber, F., Rosenkranz, S., Castellan, J.-P., Osborn, R., Zheng, H., Mitchell, J.F., Chen, Y., Chi, S., Lynn, J.W., Reznik, D., "Response of Acoustic Phonons to Charge and Orbital order in the 50 % Doped Bilayer Manganite $\text{LaSr}_2\text{Mn}_2\text{O}_7$," *Phys. Rev. Lett.* **107**(20), 207202 (2011).
- Weigandt, K.M., Porcar, L., Pozzo, D.C., "In situ Neutron Scattering Study of Structural Transitions in Fibrin Networks under Shear Deformation," *Soft Matter* **7**, 9992 (2011).
- Weinrich, M., Nanda, H., Worcester, D.L., Majkrzak, C.F., Maranville, B.B., Bezrukov, S.M., "Halothane Changes the Domain Structure of a Binary Lipid Membrane," *Langmuir* **28**, 4723 (2012).
- Wen, J., Xu, Z., Xu, G., Jie, Q., Hücker, M., Zheludev, A., Tian, W., Winn, B.L., Zarestky, J.L., Singh, D. K., Hong, T., Li, Q., Gu, G., Tranquada, J.M., "Probing the Connections Between Superconductivity, Stripe Order, and Structure in $\text{La}_{1.905}\text{Ba}_{0.095}\text{Cu}_{1-y}\text{Zn}_y\text{O}_4$," *Phys. Rev. B* **85**(13), 134512 (2012). [CHRSN]
- Wen, J., Jie, Q., Li, Q., Hücker, M., Zimmermann, M.v., Han, S.J., Xu, Z., Singh, D.K., Konik, R.M., Zhang, L., Gu, G., Tranquada, J.M., "Uniaxial Linear Resistivity of Superconducting $\text{La}_{1.905}\text{Ba}_{0.095}\text{CuO}_4$ Induced by an External Magnetic Field," *Phys. Rev. B* **85**(13), 134513 (2012). [CHRSN]
- White, J.S., Heslop, R.W., Holmes, A.T., Forgan, E.M., Hinkov, V., Egetenmeyer, N., Gavilano, J.L., Laver, M., Dewhurst, C.D., Cubitt, R., Erb, A., "Magnetic-Field- Induced Nonlocal Effects on the Vortex Interactions in Twin-Free $\text{YB}_2\text{Cu}_3\text{O}_7$," *Phys. Rev. B* **84**(10), 104519 (2011).
- Williams, J.G., Gilliam, D.M., "Thermal Neutron Standards," *Metrologia* **48**, S254 (2011).
- Wolff, M., Pálsson, G.K., Korelis, P.T., Dura, J.A., Majkrzak, C., Hjörvarsson, B., "Hydrogen Distribution in Nb/Ta Superlattices," *J. Phys.: Condens. Matter* **24**, 255306 (2012).
- Wong-Ng, W., Yang, Z., Liu, G., Huang, Q., Cook, L.P., Diwanji, S., Lucas, C., Jang, M.-H., Kaduk, J.A., "Chemical Interactions of the $\text{Ba}_2\text{YCu}_3\text{O}_{6+x}$ Superconductor with Coated Conductor Buffer Layers," in "Advances and Applications in Electroceramics, Volume 226," edited by Nair, K.M., Jia, Q., Pryia, S. (John Wiley & Sons, Inc. Hoboken, NJ), Chap. 19, 173 (2012).
- Wong-Ng, W., Kaduk, J.A., Espinal, L., Suchomel, M.R., Allen, A.J., Wu, H., "High-Resolution Synchrotron X-ray Powder Diffraction Study of bis(2-methylimidazolyl)-zinc $\text{C}_8\text{H}_{10}\text{N}_4\text{Zn}$ (ZIF-8)," *Powder Diffr.* **26**(3), 234 (2011).
- Wong-Ng, W., Lu, T., Xie, W., Tang, W.H., Kaduk, J.A., Huang, Q., Yan, Y., Chattopadhyay, S., Tang, X., Tritt, T., "Phase Diagram, Crystal Chemistry and Thermoelectric Properties of Compounds in the Ca-Co-Zn-O System," *J. Solid State Chem.* **184**, 2159 (2011).
- Wong-Ng, W., Huang, Q., Levin, I., Woicik, J.C., Shi, X., Yang, J., Kaduk, J.A., "Crystal Structure and Powder Diffraction Reference Pattern of Type I Clathrate $\text{Ba}_8\text{Ni}_4\text{Ge}_{42}$," *Powder Diffr.* **27**(1), 25 (2012).
- Woodka, A.C., Butler, P.D., Porcar, L., Farago, B., Nagao, M., "Lipid Bilayers and Membrane Dynamics: Insight into Thickness Fluctuations," *Phys. Rev. Lett.* **109**(5), 058102 (2012). [CHRSN]
- Wright, N.T., Raththagala, M., Hemmis, C.W., Edwards, S., Curtis, J.E., Krueger, S., Schildbach, J.F., "Solution Structure and Small Angle Scattering Analysis of Tral (381-569)," *Proteins*, in press.
- Wu, B., Li, X., Do, C., Kim, T.-H., Shew, C.-Y., Liu, Y., Yang, J., Hong, K., Porcar, L., Chen, C.-Y., Liu, E.L., Smith, G.S., Herwig, K.W., Chen, W.-R., "Spatial Distribution of Intra-Molecular Water and Polymeric Components in Polyelectrolyte Dendrimers Revealed by Small Angle Scattering Investigations," *J. Chem. Phys.* **135**(14), 144903 (2011).

- Wu, B., Kerkeni, B., Egami, T., Do, C., Liu, Y., Wang, Y., Porcar, L., Hong, K., Smith, S.C., Liu, E.L., Smith, G.S., Chen, W.-R., "Structured Water in Polyelectrolyte Dendrimers: Understanding Small Angle Neutron Scattering Results through Atomistic Simulation," *J. Chem. Phys.* **136**(14), 14490 (2012).
- Wu, H., Zhou, W., Pinkerton, F.E., Udovic, T.J., Yildirim, T., Rush, J.J., "Metal Hydrazinoborane $\text{LiN}_2\text{H}_3\text{BH}_3$ and $\text{LiN}_2\text{H}_3\text{BH}_3 \cdot 2\text{N}_2\text{H}_4\text{BH}_3$: Crystal Structures and High-Extent Dehydrogenation," *Energy Environ. Sci.* **5**, 7531 (2012).
- Wu, L.S., Janssen, Y., Marques, C., Bennett, M.C., Kim, M.S., Park, K., Chi, S., Lynn, J.W., Lorusso, G., Biasiol, G., Aronson, M.C., "Magnetic Field Tuning of Antiferromagnetic Yb_3Pt_4 ," *Phys. Rev. B* **84**(13), 134409 (2011).
- Xiang, S., He, Y., Zhang, Z., Wu, H., Zhou, W., Krishna, R., Chen, B., "Microporous Metal-Organic Framework with Potential for Carbon Dioxide Capture at Ambient Conditions," *Nat. Commun.* **3**(954), 1 (2012).
- Xu, Z., Wen, J., Xu, G., Chi, S., Ku, W., Gu, G., Tranquada, J.M., "Local-moment Magnetism in Superconducting $\text{FeTe}_{0.35}\text{Se}_{0.65}$ as Seen via Inelastic Neutron Scattering," *Phys. Rev. B* **84**(5), 052506 (2011).
- Yamada, T., Yonamine, R., Yamada, T., Kitagawa, H., Tyagi, M., Nagao, M., Yamamuro, O., "Quasi-elastic Neutron Scattering Studies on Dynamics of Water Confined in Nanoporous Copper Rubinate Hydrates," *J. Phys. Chem. B* **115**, 13563 (2011). [CHRNS]
- Yamamuro, O., Yamada, T., Kofu, M., Nakakoshi, M., Nagao, M., "Hierarchical Structure and Dynamics of an Ionic Liquid 1-Octyl-3-methylimidazolium Chloride," *J. Chem. Phys.* **135**(5), 054508 (2011). [CHRNS]
- Yáñez-Vilar, S., Mun, E.D., Zapf, V.S., Ueland, B.G., Gardner, J.S., Thompson, J.D., Singleton, J., Sánchez-Andújar, M., Mira, J., Biskup, N., Seánarís-Rodríguez, M.A., Batista, C.D., "Multiferroic Behaviour in the New Double-Perovskite $\text{Lu}_2\text{MnCoO}_6$," *Phys. Rev. B* **84**(13), 134427 (2011).
- Yang, J.B., Yang, Y.B., Chen, X.G., Ma, X.B., Han, J.Z., Yang, Y.C., Guo, S., Yan, A.R., Huang, Q. Z., Wu, M.M., Chen, D.F., "Anisotropic Nanocrystalline MnBi with High Coercivity at High Temperature," *Appl. Phys. Lett.* **99**(8), 082505 (2011).
- Yang, K., Xu, C., Huang, L., Zou, L., Wang, H., "Hybrid Nanostructure Heterojunction Solar Cells Fabricated using Vertically Aligned ZnO Nanotubes Grown on Reduced Graphene Oxide," *Nanotechnology* **22**, 405401 (2011).
- Yang, Y.-Q., Li, G.-N., Wang, T., Huang, Q.-Z., Gao, Q.-Q., Li, J.-B., Liu, G.-Y., Luo, J., Rao, G.-H., "Neutron Diffraction Study on Composite Compound Nd_2Co_7 ," *Chin. Phys. B* **20**(10), 106101 (2011).
- Yankova, T., Huvonen, D., Mühlbauer, S., Schmidiger, D., Wulf, E., Zhao, S., Zheludev, A., Hong, T., Garlea, V.O., Custelcean, R., Ehlers, G., "Crystals for Neutron Scattering Studies of Quantum Magnetism," *Philos. Mag.* **92**(19-21), 2629 (2012).
- Yao, J., Brunetta, C.D., Aitken, J.A., "Suppression of Antiferromagnetic Interactions through Cu Vacancies in Mn-Substituted CuInSe_2 Chalcopyrites," *J. Phys.: Condens. Matter* **24**(8), 086006 (2012).
- Yao, J., Rudyk, B.W., Brunetta, C.D., Knorr, K.B., Figore, H.A., Mar, A., Aitken, J.A., "Mn Incorporation in CuInS_2 Chalcopyrites: Structure, Magnetism and Optical Properties," *Mater. Chem. Phys.*, in press.
- Yaron, P.N., Holt, B.D., Short, P.A., Lösche, M., Islam, M.F., Dahl, K.N., "Single Wall Carbon Nanotubes Enter Cells by Endocytosis and not Membrane Penetration," *Journal of Nanobiotechnology* **9**(45), 1 (2011).
- Ye, F., Fishman, R.S., Haraldsen, J., Lorenz, B., Chu, C.W., Kimura, T., "Spin Dynamics in the Multiferroic Materials (invited)," *J. Appl. Phys.* **111**(7), 07E137 (2012). [CHRNS]
- Yeo, J., Kim, S.Y., Kim, S., Ryu, D.Y., Kim, T.-H., Park, M.J., "Mechanically and Structurally Robust Sulfonated Block Copolymer Membranes for Water Purification Applications," *Nanotechnology* **23**, 245703 (2012).

- Yeon, J., Kim, S.-H., Green, M.A., Bhatti, K.P., Leighton, C., Halasyamani, P.S., "Syntheses, Crystal Structures, and Characterization of Two New Tl^+ - Cu^{2+} - Te^{6+} Oxides: Tl_4CuTeO_6 and $Tl_6CuTe_2O_{20}$," *J. Solid State Chem.*, in press.
- Yi, Z., Miao, Y., Baudry, J., Jain, N., Smith, J.C., "Derivation of Mean-Square Displacements for Protein Dynamics from Elastic Incoherent Neutron Scattering," *J. Phys. Chem. B* **116**, 5028 (2012).
- Yi, Z., Nagao, M., Bossev, D.P., "Effect of Charged Lidocaine on Static and Dynamic Properties of Model Bio- Membranes," *Biophys. Chem.* **160**, 20 (2012). [CHRNNS]
- Yoon, I., Wilson, C., Borgmeyer, B., Winholtz, R.A., Ma, H.B., Jacobson, D.L., Hussey, D.S., "Neutron Phase Volumetry and Temperature Observations in an Oscillating Heat Pipe," *International Journal of Thermal Sciences*, in press.
- Yoonessi, M., Heinz, H., Dang, T.D., Bai, Z., "Morphology of Sulfonated Polyarylenethioethersulfone Random Copolymer Series as Proton Exchange Fuel Cells Membranes by Small Angle Neutron Scattering," *Polymer* **52**, 5615 (2011).
- Yu, J., Phelan, D., Louca, D., "Spin-state Transitions in $PrCoO_3$ Investigated by Neutron Scattering," *Phys. Rev. B* **84**(13), 132410 (2011).
- Yu, L.L., Jarrett, J.M., Davis, W.C., Kilpatrick, E.L., Oflaz, R., Turk, G.C., Leber, D.D., Valentin, L., Morel-Espinosa, M., Blount, B.C., "Characterization of Perchlorate in a New Frozen Human Urine Standard Reference Material," *Anal. Bioanal. Chem.*, in press.
- Yun, S.I., Cao, L., Kang, T.-B., Huh, M., Gauthier, M., "Morphology of Polystyrene Core-*d*Poly(ethylene oxide) Shell Arborescent Copolymer Micelles from Small-Angle Neutron Scattering Analysis," *J. Macromol. Sci., Phys.* **50**, 2318 (2011).
- Zeisler, R., Oflaz, R., Paul, R.L., Fagan, J. A., "Use of Neutron Activation Analysis for the Characterization of Single-Wall Carbon Nanotube Materials," *J. Radioanal. Nucl. Chem.* **291**, 561 (2012).
- Zhao, J., Niestemski, F.C., Kunwar, S., Li, S. Steffens, P. Hiess, A. Kang, H.J., Wilson, S.D., Wang, Z., Dai P. and Madhavan, V. "Electron-Spin Excitation Coupling in an Electron-Doped Copper Oxide Superconductor," *Nature Physics* **7**, 719 (2011). [CHRNNS]
- Zhang, C., Wang, M., Luo, H., Wang, M., Liu, M., Zhao, J., Abernathy, D.L., Maier, T.A., Marty, K., Lumsden, M.D., Chi, S., Chang, S., Rodriguez-Rivera, J.A., Lynn, J.W., Xiang, T., Hu, J., Dai, P., "Neutron Scattering Studies of Spin Excitations in Hole-Doped $Ba_{0.67}K_{0.33}Fe_2As_2$ Superconductor," *Scientific Reports* **1**(115), 1 (2011). [CHRNNS]
- Zhang, Y., Faraone, A., Kamitakahara, W.A., Liu, K.-H., Mou, C.-Y., Leão, J.B., Chang, S., Chen, S.-H., "Reply to Soper: Density Measurement of Confined Water with Neutron Scattering," *PNAS* **108**(47), E1193 (2011). [CHRNNS]
- Zhang, Y., Tyagi, M., Mamontov, E., Chen, S.-H., "Quasi-Elastic Neutron Scattering Studies of the Slow Dynamics of Supercooled and Glassy Aspirin," *J. Phys.: Condens. Matter* **24**, 064112 (2012). [CHRNNS]
- Zhou, H.D., Bramwell, S.T., Cheng, J.G., Wiebe, C.R., Li, G., Balicas, L., Bloxson, J.A., Silverstein, H.J., Zhou, J.S., Goodenough, J.B., Gardner, J.S., "High Pressure Route to Generate Magnetic Monopole Dimers in Spin Ice," *Nat. Commun.* **2**(478), 1 (2011).
- Zhou, H.D., Cheng, J.G., Hallas, A.M., Wiebe, C.R., Li, G., Balicas, L., Zhou, J.S., Goodenough, J.B., Gardner, J.S., Choi, E.S., "Chemical Pressure Effects on Pyrochlore Spin Ice," *Phys. Rev. Lett.* **108**(20), 207206 (2012).

Instruments and Contacts

Instruments and Contacts: (name, tel. (301) 975-XXXX, email address)

High resolution powder diffractometer (BT-1):

J.K. Stalick, 6223, judith.stalick@nist.gov

H. Wu, 2387, hui.wu@nist.gov

Q.Z. Huang, 6164, qing.huang@nist.gov

Residual stress diffractometer (BT-8):

T. Gnaeupel-Herold, 5380, thomas.gnaeupel-herold@nist.gov

30-m SANS instrument (NG-7):

Yun Liu, 6235, yun.liu@nist.gov

Paul Butler, 2028, paul.butler@nist.gov

Jeff Krzywon, 6650, jkrzywon@nist.gov

30-m SANS instrument (NG-3) (CHRS):

Boualem Hammouda, 3961, hammouda@nist.gov

Steve Kline, 6243, steven.kline@nist.gov

Susan Krueger, 6734, susan.krueger@nist.gov

Cedric Gagnon, 2020, cedric.gagnon@nist.gov

10-m SANS instrument (nSoft) (NGBI):

Ron Jones, 4624, ronald.jones@nist.gov

Katie Weigandt, 8396, kathleen.wiegandt@nist.gov

USANS, Perfect Crystal SANS (BT-5) (CHRS):

David Mildner, 6366, david.mildner@nist.gov

Matt Wasbrough, 6017, matthew.wasbrough@nist.gov

Paul Butler, 2028, paul.butler@nist.gov

Polarized Beam Reflectometer/Diffractometer (NG-D):

B.J. Kirby, 8395, brian.kirby@nist.gov

J.A. Borchers, 6597, julie.borchers@nist.gov

C.F. Majkrzak, 5251, cmajkrzak@nist.gov

MAGIK, Off-Specular Reflectometer (NG-D):

B.B. Maranville, 6034, brian.maranville@nist.gov

J.A. Dura, 6251, joseph.dura@nist.gov

Neutron reflectometer-horizontal sample (NG-7):

S.K. Satija, 5250, satija@nist.gov

B. Akgun, 6469, bulent.akgun@nist.gov

Double-focusing triple-axis Spectrometer (BT-7):

Y. Zhao, 2164, yang.zhao@nist.gov

J. Helton, 4899, joel.helton@nist.gov

J.W. Lynn, 6246, jeff.lynn@nist.gov

SPINS, Spin-polarized triple-axis spectrometer (NG-5):

D. Singh, 4863, deepak.singh@nist.gov

L. Harriger, 8360, leland.harriger@nist.gov

Triple-axis spectrometer (BT-4):

W. Ratcliff, 4316, william.ratcliff@nist.gov

FANS, Filter-analyzer neutron spectrometer (BT-4):

T.J. Udovic, 6241, udovic@nist.gov

DCS, Disk-chopper time-of-flight spectrometer (NG-4)(CHRS):

J.R.D. Copley, 5133, jcopley@nist.gov

Y. Qiu, 3274, yiming.qiu@nist.gov

C. M. Brown, 5134, craig.brown@nist.gov

HFBS, High-flux backscattering spectrometer (NG-2) (CHRS):

M. Tyagi, 2046, madhusudan.tyagi@nist.gov

W. Zhou, 8169, wei.zhou@nist.gov

NSE, Neutron spin echo spectrometer (NG-5) (CHRS):

A. Faraone, 5254, antonio.faraone@nist.gov

J.S. Gardner, 8396, jason.gardner@nist.gov

M. Nagao, 5505, michihiro.nagao@nist.gov

MACS, Multi-angle crystal spectrometer (BT-9) (CHRS):

J. Rodriguez, 6019, jose.rodriguez@nist.gov

Cold-neutron prompt-gamma neutron activation analysis (NG-D):

R.L. Paul, 6287, rpaul@nist.gov

Thermal-neutron prompt-gamma activation analysis (VT-5):

G. Downing, 3782, gregory.downing@nist.gov

Other activation analysis facilities:

G. Downing, 3782, gregory.downing@nist.gov

Cold neutron depth profiling (NG-1):

G. Downing, 3782, gregory.downing@nist.gov

Neutron Imaging Station (BT-2):

D. Jacobson, 6207, david.jacobson@nist.gov

D. Hussey, 6465, daniel.hussey@nist.gov

M. Arif, 6303, muhammad.arif@nist.gov

Neutron interferometer (NG-7):

M. Arif, 6303, muhammad.arif@nist.gov

D. Jacobson, 6207, david.jacobson@nist.gov

D. Hussey, 6465, daniel.hussey@nist.gov

Fundamental neutron physics station (NG-6):

NG-6M: M.S. Dewey, 4843, mdewey@nist.gov

NG-6U: H.P. Mumm, 8355, pieter.mumm@nist.gov

NG-6: J. Nico, 4663, nico@nist.gov

Theory and modeling:

J.E. Curtis, 3959, joseph.curtis@nist.gov

T. Yildirim, 6228, taner@nist.gov

Instruments Under Development

vSANS instrument:

J. Barker, 6732, john.barker@nist.gov

C. Glinka, 6242, charles.glinka@nist.gov

CANDOR, White-beam reflectometer/diffractometer:

F. Heinrich, 4507, frank.heinrich@nist.gov

C. Majkrzak, 5251, charles.majkrzak@nist.gov

NIST Center For Neutron Research Contacts

Copies of annual reports, facility information, user information, And research proposal guidelines are available electronically.

Please visit our website:
<http://www.ncnr.nist.gov>

For a paper copy of this report:

Ron Cappelletti
301-975-6221
ron.cappelletti@nist.gov

For general information on the facility:

Rob Dimeo
301-975-6210
robert.dimeo@nist.gov

Dan Neumann
301-975-5252
dan.neumann@nist.gov

For information on visiting the facility and/or user access questions:

Julie Keyser
301-975-8200
julie.keyser@nist.gov

Mary Ann FitzGerald
301-975-8200
maryann.fitzgerald@nist.gov

For information on performing research at the facility:

Bill Kamitakahara
301-975-6878
william.kamitakahara@nist.gov

Facility address:

NIST Center for Neutron Research
National Institute of Standards and Technology
100 Bureau Drive, Mail Stop 6100
Gaithersburg, MD 20899-6100 USA

NIST CENTER FOR NEUTRON RESEARCH
National Institute of Standards and Technology
100 Bureau Drive, MS 6100
Gaithersburg, MD 20899-6100

www.ncnr.nist.gov